Modelling of tropospheric ozone and radical chemistry

- Modellierung der troposphärischen Ozon- und Radikalchemie-

Vom Fachbereich für Physik und Elektrotechnik
der Universität Bremen

Zur Erlangung des akademischen Grades eines
Doktor der Naturwissenschaften (Dr. rer. nat.)
genehmigte Dissertation

von
Dipl. Phys. Jörn Burkert
aus Bremen

1. Gutachter: Prof. Dr. rer. nat. John Phillip Burrows
2. Gutachter: Prof. Dr. rer. nat. Russel R. Dickerson

Eingereicht am: 10.03.2003
Tag des Promotionskolloquiums 16.04.2003

Abstract

This work describes in detail the photochemistry of O_3 and radicals in both remote "clean air" and "heavily polluted" regions. The results of two field studies are presented: the Indian Ocean Experiment (INDOEX) and the Peroxy Radical Initiative for Measurements in the Environment (PRIME).

The **INDOEX** campaign, an international research initiative, studied the chemistry of remote areas of the Indian Ocean and the influence of the outflow from the Indian subcontinent on these regions. Within the INDOEX campaign the first measurements of peroxy radicals were successfully performed above the Indian Ocean. These, together with other relevant trace gases (NMHC, O_3, CO, HCHO, NO, O_3 soundings, and satellite data of O_3, HCHO, and NO_2) and parameters ($j(NO_2)$, $j(O(^1D)$, and meterological data) have been compared with the results of a 0-dimensional chemistry model. The comparison between measurements and simulations revealed large discrepancies, which indicated the presence of significant levels of Cl (10^4-10^5 molecule cm^{-3}).

In addition, a radiative transfer model has been modified and used to calculate the influence of highly absorbing aerosols on the energy budget of the Earth. The results of the RTM calculations of the warming rates caused by the aerosols' absorption of solar radiation showed temperature increases up to 1 K. This temperature increase particularly above the MBL stabilised the atmosphere significantly. Therefore, the presence of aerosols in the layer above the MBL leads to enhanced stability during the day and less stability during the night.

Satellite and sonde data were used for the investigation macro and mesoscale processes and for the identification of all relevant processes responsible for the amount of O_3 present above the Indian Ocean. The combination of vertical profiles, satellite pictures of tropospheric columns of O_3, NO_2, HCHO, and meterological data, indicated that the amount of O_3 resultant from the STE is the major source for tropospheric O_3 in the SH Indian Ocean.

The **PRIME** campaign took place during July and August 1999 near London, UK. Ambient measurements of trace gases (HO_2, RO_2^*, NO_2, NO, PAN, CO, CH_3OOH, H_2O_2, OH) were carried out.

During daylight the maximum RO_2^* mixing ratios varied between 15 and 70 pptv during "polluted episodes". At night non negligible amounts of RO_2^* were observed, varying between 5 to 20 pptv.

The comparison between simulated and measured daytime trace gas concentrations showed good agreement for RO_2^*, H_2O_2, OH and large discrepancies for HO_2. The measured RO_2^* to HO_2 ratio varied between 5 to 10, which is in total disagreement with the model results where this ratio varied between 1.1 and 2.3 even when the model was run with unrealistically high amounts of volatile organic compounds. The measured H_2O_2 mixing ratios are also in disagreement with the observed HO_2 amounts assuming that H_2O_2 is exclusively produced via the HO_2 self reaction.

The actual measurements of RO_2^*, HO_2, and NO taken during the early morning hours showed that these three species coexisted in high amounts. This cannot be explained by the known chemistry.

TABLE OF CONTENTS

1 Introduction and overview 1

1.1 Introduction 1
1.2 Overview 5

2 Theoretical background 7

2.1 Physics of the atmosphere 7
2.1.1 Radiation and energy processes 7
2.1.1.1 Basics of the radiative transfer 7
2.1.1.2 Radiation/Energy budget 10
2.1.1.3 Aerosol scattering and absorption 13
2.1.2 Dynamics of the atmosphere 15
2.1.2.1 Atmospheric Boundary layer 17
2.1.2.2 Free atmosphere 31
2.1.2.3 Stratospheric/tropospheric exchange 31
2.2 Chemistry of the troposphere 35
2.2.1 Chemistry of the clean marine troposphere 35
2.2.1.1 Hydroxyl radical (OH) 35
2.2.1.2 Peroxy radicals (RO_2^*) 37
2.2.1.3 Formaldehyde (HCHO) 39
2.2.1.4 Radical balance 40
2.2.1.5 Ozone (O_3) 41
2.2.1.6 Methane (CH_4) 42
2.2.1.7 Non methane hydrocabons (NMHC) 43
2.2.1.8 Halogens (Br, Cl, I) 43
2.2.1.9 Influence of halogens and radicals on the O_3 balance 48
2.2.2 Chemistry of the polluted troposphere 49
2.2.2.1 Nitrogen oxides (NO, NO_2) 49
2.2.2.2 Nitrate radical (NO_3) 54
2.2.2.3 Nitrous acid (HONO) 56
2.2.2.4 Non methane hydrocarbons (NMHC) 56
2.3 Atmospheric chemistry modelling 63
2.3.1 Basics 63
2.3.2 Different model types 65
2.3.3 The structure of chemical models 69
2.3.3.1 The reaction rate coefficients 69
2.3.3.2 Solving of the differential equations 75

3 Experimental 79

3.1 INDOEX campaign 79

3.1.1 RO_2^* measurement technique 81
3.1.2 CO measurement technique 83
3.1.3 O_3 measurement technique 83
3.1.4 NO measurement technique 83
3.1.5 NMHC measurement technique 84
3.1.6 $j(NO_2)$ measurement technique 84
3.1.7 $j(O(^1D))$ measurement technique 85
3.1.8 O_3 soundings 85
3.1.9 Satellite data 86
3.1.10 Other supporting measurements 87
3.1.11 Modelling 87

3.2 PRIME campaign 89

3.2.1 Overview of all measurement techniques 89
3.2.2 RO_2^* measurement technique 89
3.2.3 OH and HO_2 measurement techniques 90
3.2.4 CO measurement technique 90
3.2.5 NO and NO_2 measurement techniques 90
3.2.6 PAN measurement technique 91
3.2.7 H_2O_2 and CH_3OOH measurement techniques 91
3.2.8 Other supporting measurements 92
3.2.9 Modelling 92

4 INDOEX campaign 95

4.1 Definition of air masses 95

4.2 Trace gas and radical behaviour 99

4.2.1 Introduction 99
4.2.2 Results 100
4.2.2.1 Characteristics of the different air masses observed 100
4.2.2.2 Measurements trace constituents and parameters 102
4.2.3 Discussion and Interpretation 108
4.2.3.1 Simulation of photolysis frequencies 108
4.2.3.2 Interpretation of the MBL chemistry 120
4.2.4 Summary 136

4.3 Photochemistry and radiative effects of aerosols 139

4.3.1 Introduction 139
4.3.2 Results 139
4.3.2.1 Characteristics of the different air masses observed 139
4.3.2.2 Measurements of trace constituents and parameters 141
4.3.3 Discussion 159
4.3.3.1 O_3 depletion 159
4.3.3.2 O_3 recovery 163
4.3.4 Interpretation 170

5 PRIME campaign 173

5.1 Introduction 173

5.2 Results and discussion 175

5.2.1 Air mass classification and measurement site description 175

5.2.2 Trace gas measurements 177

5.2.2.1 General diurnal behaviour of trace gases 183

5.2.2.2 Peroxy radical diurnal variation 184

5.2.2.3 Nocturnal radical mixing ratios 185

5.2.3 Model results 186

5.2.3.1 Base case 187

5.2.3.2 CO variation 190

5.2.3.3 CH_4 variation 191

5.2.3.4 C_2H_4 variation 193

5.2.3.5 C_2H_6 variation 195

5.2.3.6 C_3H_6 variation 197

5.2.3.7 C_3H_6 variation with 10 times higher reactivity with O_3 199

5.2.3.8 RO_2^* to HO_2 ratio 201

5.2.4 Comparison between model and measurements 201

5.2.4.1 RO_2^* to HO_2 ratio 201

5.2.4.2 H_2O_2 mixing ratio 202

5.2.4.3 OH mixing ratio 205

5.2.5 Comparison with other datasets 206

5.2.6 Interpretation 210

5.3 Conclusions 213

6 Epitome 215

6.1 Summary 215

6.1.1 Trace gas and radical behaviour [Burkert et al., 2003a] 215

6.1.2 Photochemistry and radiative effects of aerosols [Burkert et al., 2003b] 215

6.1.3 Peroxy radicals and peroxides in the urban troposphere [Burkert et al., 2003c] 216

6.2 Conclusion 219

6.2.1 Evidence for Cl in the atmosphere 220

6.2.2 Influence of aerosol absorption in the dynamics of the atmosphere 227

6.2.3 Importance of the STE as a source of O_3 over the Indian Ocean 227

6.2.4 Open questions in the radical chemistry of the “polluted” atmosphere 228

6.3 Outlook 231

References 233

Acknowledgements 275

Appendendix 277

Appendix 1 277

Appendix 2 281

LIST OF FIGURES

Figure 1: Solar and terrestrial radiation and atmospheric absorption spectrum for a beam reaching the ground [http://envisat.estec.esa.nl/instruments /sciamachy/index.html]..... 11

Figure 2: The greenhouse effect [colour image adapted from Kiehl and Trenberth, 1997]. The Earth's radiation energy balance which controls the way the greenhouse effect works, can here be seen graphically. Note that nearly half the incoming solar radiation penetrates the clouds (and greenhouse gases) to reach the Earth's surface. Greenhouse gases and clouds reradiate most of the absorbed energy back down toward the surface. 12

Figure 3: The vertical temperature profile of the Earth's atmosphere. The different regions are labelled. 15

Figure 4: Theoretical diurnal evolution of the atmospheric boundary layer over land. 18

Figure 5: Change in the mixing depth, Los Angeles, July 23, 2000 [Jacobson, 2002].. 19

Figure 6: Formation of a subsidence inversion [Jacobson, 1998]..... 21

Figure 7: a) Smoke layer trapped in an inversion following a fire in Menlo Park, California (June, 2001), b) Elevated pollution layer (Los Angeles, July 22, 2000) [Jacobson, 2002]..... 23

Figure 8: Stability of air. Different regions of stability are marked by the black arrows. The red dotted line represents the dry adiabatic temperature profile (G_D), the blue dotted line is the wet adiabatic temperature profile (G_W), and the green lines show four possible environmental temperature profiles (G_E). 28

Figure 9: Schematic picture of a sea breeze circulation [Batt, 1995]..... 30

Figure 10: Global circulation cells and winds [Jacobson, 1998]..... 32

Figure 11: Dynamical aspects of stratosphere–troposphere exchange. The tropopause is shown by the thick line. Thin lines are isentropic or constant potential temperature surfaces labelled in Kelvin. The heavily shaded region is the "lowermost stratosphere" where isentropic surfaces span the tropopause and isentropic exchange by tropopause folding occurs. The region above the 380 K surface is the "overworld", in which isentropes lie entirely in the stratosphere. Light shading in the overworld denotes wave-induced forcing (the extratropical "pump"). The wiggly double headed arrows denote meridional transport by eddy motions, which include tropical upper-tropospheric troughs and their cut off cyclones as well as their midlatitude counterparts including folds. Not all eddy transports are shown; and the wiggly arrows are not meant to imply any two-way symmetry. The broad arrows show transport by the globalscale circulation, which is driven by the extratropical pump. This global-scale circulation is the primary contribution

to exchange across isentropic surfaces (e. g. the ~380 K surface) that are entirely in the over world [Holton et al., 1995]. 33

Figure 12: O_3 loss and radical chemistry in a NOx free atmosphere. The Figure shows the radical balance of two initially produced OH radicals. The numbers in the boxes indicate the change of the number of free radicals [Schultz et al., 1996]..... 40

Figure 13: Net cycles for the possible oxidation pathways of methane. 43

Figure 14: A simplified scheme of the bromine cycling between homogeneous and heterogeneous phase [Color image adapted from Sander and Crutzen, 1996]..... 45

Figure 15: Different groups of volatile organic compounds found in the Earth's atmosphere, with typical examples for each group. 56

Figure 16: Temporal scale of dynamical processes and of the lifetimes of several trace gases [P.S. Monks, Uni-Leicester] 68

Figure 17: The Indian Ocean Experiment (INDOEX) 1999 [http://www-indoex.ucsd.edu /index.html]..... 80

Figure 18: INDOEX cruise tracks for leg 1-3, numbers along the track indicate day of the year (DOY). 96

Figure 19: Cruise track of the RV Ronald H. Brown during the 1999 INDOEX campaign and the cluster trajectories (950 hPa) showing the origin of the air masses encountered during the different segments of the cruise. The flow regimes are labelled SHmE, Southern Hemisphere marine equatorial; NHmE, Northern Hemisphere marine equatorial; NHcT, Northern Hemisphere continental tropical (subdivided in the sub-regimes Bengal and West); and NHcX, Northern Hemisphere continental extra-tropical. 97

Figure 20: Plots of the individual diurnal variation of RO_2^*, O_3, and CO observed on legs 1 to 3 of INDOEX. The classification of the air masses encountered are written above, the days and vertical lines separate the different types of air masses. 103

Figure 21: a) Measured $j(O(^1D))$ photolysis rates for leg 2 (DOY 63 – 80) during INDOEX. b) Diurnal variation in the photolysis rate coefficient for NO_2; only cloud-free data are shown. Filled squares represent data from the clean, marine atmosphere on DOY 57 at 4°S with an AOD of about 0.07 at 500 nm. Open squares represent data from a polluted atmosphere over the northern Indian Ocean on DOY 65 at 6°N with an AOD of 0.4 at 500 nm.105

Figure 22: NMHC, i.e. alkane and acetylene measurements in the NH during INDOEX (DOY 64 – 78) a) the lighter alkanes and acetylene, b) the heavier alkanes measured. 107

Figure 23: Micropulse Lidar (MPL) average profiles for AOD=0.15, 0.30, 0.45, 0.6. All extinction coefficient profiles are a mixture between the measured and the smooth Lowtran-profile [Welton, et al., 2002]..... 113

Figure 24: Modelled photolysis frequencies of $j(O(^1D))$ and $j(NO_2)$ for different AOD vs. sec(SZA)..... 115

Figure 25: Correlation between measured and modelled $j(O(^1D)$ photolysis rates during INDOEX, separated into different AOD ranges. 116

Figure 26: Diurnal variation in the photolysis rate coefficient for NO_2; only cloud-free data are shown. Filled squares (measurements) and the black curve (model) represent data from the clean, marine atmosphere on DOY 57 at 4°S with an AOD of about 0.07 at 500 nm. Open squares (measurements) and grey curve (model) represent data from a polluted atmosphere over the northern Indian Ocean on DOY 65 at 6°N with an AOD of 0.4 at 500 nm. Crosses represent data from the polluted atmosphere over the Eastern US (Greenbelt, Maryland, 39°N) on July 15, 1995 with an AOD of 0.88 at 520 nm and 1.4 at 380 nm. 118

Figure 27: The same data as Figure 26, but with the photolysis rate coefficients plotted as a function of the secant of the solar zenith angle. Filled squares (measurements) and black curve (model) represent data from the clean marine environment; Crosses represent data from a polluted environment over North America, and open squares (measurements) and grey curve (model) represent data from a polluted environment in the Northern Indian Ocean. 119

Figure 28: Average diurnal variation of measured and modelled RO_2^* mixing ratios for the NH and SH during INDOEX. Local time is given by UTC + ~4 hrs.... 121

Figure 29: Modelled and measured average diurnal behaviour of RO_2^* mixing ratios for different air mass regions during INDOEX. Note: absolute concentrations of measurements and model are in good agreement, but the observations are broader. 125

Figure 30: The required diurnal behaviour of Cl to describe the observed broad shape in the measured RO_2^* diurnal behaviour. 128

Figure 31: Average diurnal variation of measured and modelled RO_2^* mixing ratios for the NH and SH during ALBATROSS (1996) above the Atlantic Ocean. Local time is given by UTC + ~2 hrs..... 130

Figure 32: Average diurnal variation of measured and modelled RO_2^* mixing ratios for the a) NH and b) SH during AEROSOL (1999) above the Atlantic Ocean. Local time approximately UTC a) +4 hrs and b) +2 hrs. 131

Figure 33: Measured and modelled HCHO mixing ratios during INDOEX..... 134

Figure 34: Plots of the individual diurnal variation of O_3 and CO observed on legs 1 to 3 of INDOEX. The classification of the air masses encountered are written above the days, and vertical lines separate the different types of air masses. 143

Figure 35: O_3 soundings (0 to 5 km) grouped into a) leg 1 (23-28 Feb.), b) leg 2 (5-10 March), c) NH leg 2 (11-13 March), d) leg 2 (13-14 March) days with same latitude, e) leg 2 (14-19 March), f) leg 2 (19-22 March), g) leg 3 (26-30 March) [H.G.J. Smit, Research Centre Jülich (ICG 2), Germany]..... 148

Figure 36: O_3 soundings (0 to 20 km) grouped into a) leg 1 (23-28 Feb.), b) leg 2 (5-10 March), c) NH leg 2 (11-13 March), d) leg 2 (13-14 March) days with same latitude, e) leg 2 (14-19 March), f) leg 2 (19-22 March), g) leg 3 (26-30 March) [H.G.J. Smit, Research Centre Jülich (ICG 2), Germany]..... 153

Figure 37: 6 day back trajectories arriving at the ship at 950, 750, and 500 mbar (12Z) for DOY 53 and 54 during leg 1 (INDOEX) [http://saga.pmel.noaa.gov /indoex/traject/]..... 153

Figure 38: Tropospheric O_3 vertical column[DU] measured by GOME (Feb./March 1999)..... 155

Figure 39: Number of fires according to Along Track Scanning Radiometer (ATSR) for Feb. and March 1999. 155

Figure 40: Lightning activity during Feb. and March 1999 [NASA/MSFC]..... 156

Figure 41: Lightning produced tropospheric NO_2 vertical columns Feb. and March 1999. 157

Figure 42: Tropospheric NO_2 vertical column measured by GOME (Feb./March 1999). 158

Figure 43: Tropospheric HCHO vertical column measured by GOME (Feb./March 1999)..... 158

Figure 44: Diurnal variation of measured and modelled O_3 mixing ratios for DOY 72-73 (horizontal transect, no change in the latitude)..... 160

Figure 45: Relative importance of the main first order reactions defining O_3 losses over remote areas of the MBL in the NH (a) and SH (b). The calculations have been made considering the measured amounts of $j(O^1D)$, H_2O, OH and O_3 for DOY 73 (a) and 55 (b) respectively. The following assumptions have been made: HO_2 = ½ RO_2^* (i.e. RO_2+HO_2), Boundary layer height = 1000 m, deposition velocity = 0.045 cm s^{-1} and Br = 0.05 pptv..... 162

Figure 46: Cross section of relative humidity and horizontal winds observed during INDOEX [http://saga.pmel.noaa.gov/indoex/rsonds/hw_a1_lat_5_c.gif]. 165

Figure 47: Modelled warming rates caused by aerosols for different AOD at a SZA of 30°. Composition and vertical distribution are described in Table 5 and Figure 23 respectively. 167

Figure 48: Air mass trajectories at 0.5, 2.5, and 5.5 km are shown for each category defined in the text. The C1, C2, C3, C5, and C6 trajectory patterns are shown in (a), and C4 trajectory patterns are shown in (b) [Welton et al., 2002]..... 167

Figure 49: The average extinction profile for each air mass category is shown in (a), the humidity profile is shown in (b), and the temperature profile is shown in (c). Horizontal bars represent the standard deviation in each average profile [Welton et al., 2002]..... 168

Figure 50: Typical 5-day back trajectories for a) North-West (23.7 – 27.7; 10.8 – 12.8), b) East (28.7 – 3.8; 9.8), c) South-West (4.8 – 8.8) [British Atmospheric Data Centre – Trajectory service, http://www.badc.rl.ac.uk/]..... 176

Figure 51: RO_2, CO, O_3, NO, NO_2, and PAN mixing ratios measured during the PRIME 1999 field campaign. 180*

Figure 52: HO_2 (x 100), H_2O_2, and CH_3OOH mixing ratios measured during the PRIME 1999 field campaign. 182

Figure 53: NO, NO_2, RO_2^*, HO_2 x 6, O_3, and OH x 1000 mixing ratios on the 31st of July between 600 and 1800 (UTC) during the PRIME campaign. 185

Figure 54: Overview of the different cases considered in the sensitivity study..... 187

Figure 55: Modelled (dotted lines) and measured (solid line) HO_2 and RO_2^* mixing ratios for the 31st of July 1999 during the PRIME campaign..... 188

Figure 56: Diurnal variation of modelled HO_2 and RO_2^* mixing ratio for CO 0 ppbv, 4 ppbv, 40 ppbv, base case (400 ppbv), and 4 ppmv..... 190

Figure 57: Diurnal variation of modelled HO_2 and RO_2^* mixing ratios for CH_4 0 ppbv, 400 ppbv, base case (4 ppmv), and 40 ppmv..... 192

Figure 58: Diurnal variation of modelled HO_2 and RO_2^* mixing ratio for C_2H_4 0 pptv, 400 pptv, 4 ppbv (base case), 40 ppbv, and 400 ppbv..... 194

Figure 59: Diurnal variation of modelled HO_2 and RO_2^* mixing ratio for C_2H_6 0 ppbv, 8 ppbv, 80 ppbv, 800 ppbv (base case), 8 ppmv, and 80 ppmv..... 196

Figure 60: Diurnal variation of modelled HO_2 and RO_2^* mixing ratio for C_3H_6 0 pptv, 15 pptv, 150 pptv, 1500 pptv, 15 ppbv (base case), 150 ppbv, and 1500 ppbv. 198

Figure 61: Diurnal variation of modelled HO_2 and RO_2^* mixing ratio for C_3H_6 0 pptv, 15 pptv, 150 pptv, 1500 pptv, 15 ppbv (base case), 150 ppbv, and 1500 ppbv (the O_3 reaction is enhanced by a factor of 10)..... 200

Figure 62: Diurnal variation of H_2O_2 mixing ratios of the base case, the observations, and the base case with additional production of H_2O_2 via reaction (120). 204

Figure 63: Diurnal profiles of measured and simulated amounts of H_2O_2 for different HO_2 mixing ratios. 205

Figure 64: Diurnal variation of measured and simulated (base case (C_3H_6 = 8500 pptv) and base case with a 10 times faster O_3 reaction rate) OH mixing ratios. 206

Figure 65: Comparison between measured and simulated H_2O_2 mixing ratios for the ALBATROSS campaign [Burkert et al., 2001b]. H_2O_2 data were measured by Weller et al. [2000]..... 207

Figure 66: Relative fluxes in the free troposphere calculated by Nic Carslaw – U. York., UK using the Master Chemical Mechanism (MCM, Uni-Leeds) 225

LIST OF TABLES

Table 1: Main compounds of dry air [Brimblecombe, 1986]..... 1

Table 2: Variation in the amount of several trace gases in different parts of the atmosphere [Jacobson, 1998]..... 2

Table 3: Measurements performed by IUP-UB and Uni-Leeds during the PRIME campaign. GFC: Gas filter correlation, PERCA: chemical amplification, CL: chemiluminescence, GC: gas chromatography, HPLC: high performance liquid chromatography..... 89

Table 4: Averaged NO mixing ratios observed in four different air masses. Mixing ratios were computed as day-night differences. 104

Table 5: a) Averaged aerosol composition measured at Kaashidoo during the INDOEX campaign [Lelieveld, et al., 2001] and b) typical sea salt aerosol composition [Shettle and Fenn, 1976]. c) describes the MBL mixing between a) and b) assumed in the model. 110

Table 6: Assumed mixing ratios for C_2H_4, C_3H_6, and C_2H_2 seperated into different air mass regions [according to Jens Mühle, personal communication, 2002] 120

Table 7: Measured daily average and maximum mixing ratios for OH, HO_2, and RO_2^* during the PRIME campaign 1999. 202

Table 8: Overview of different campaigns where HO_2 and/or RO_2^* mixing ratios have been determined..... 209

Table 9: Reaction rate coefficients for Cl, OH, NO_3, and O_3 with VOC [Finnlayson-Pitts and Pitts, 2000]..... 223

1 Introduction and overview

1.1 Introduction

Over the last decades, the growing realisation that human activities influence the chemical composition of the atmosphere has led to more scientific attention towards the physical and chemical processes within the Earth's atmosphere. The ozone hole discovered by Farman et al. [1985], the destruction of forests by acid rain [Brimblecombe, 1977, Cowling, 1982] or the observation of summer smog situations in Los Angeles by Haagen-Smit [1952] are indicative of the extent to which mankind has influenced and been detrimental to life on this planet. Knowledge of the dominant atmospheric processes is essential prerequisite for predicting the anthropogenic influence on the climate system and therefore on the future of our planet Earth.

The "main constituents" of air have been known for a long time, Table 1 gives an overview of the mixing ratios of individual gases. The main components are relatively inert gases, that contribute little to chemical reactions and therefore to the behaviour of the atmosphere.

Gases	Mixing ratio
Nitrogen	78,084 Vol %
Oxygen	20,946 Vol %
Argone	0,934 Vol %
Carbon dioxyde	360 ppmv[1]
Neon	18,18 ppmv
Helium	5,24 ppmv
Methane	1,6 – 1,8 ppmv
Krypton	1,14 ppmv
Hydrogen	0,5 ppmv
Other trace gases	~ 0,3 ppmv

Table 1: Main compounds of dry air [Brimblecombe, 1986].

[1] ppmv = parts per million (v/v)

Because of this the focus is on the so called “trace gases”. Table 2 shows the observed mixing ratios of several trace gases divided into the clean and polluted troposphere and the stratosphere.

		Volume Mixing Ratio [ppbv[2]]		
Gas Name	**Chemical Formula**	**Clean Troposphere**	**Polluted Troposphere**	**Stratosphere**
Inorganic				
Water vapour	H_2O	3000-4.0(+7)	5.0(+6)-4.0(+7)	3000-6000
Carbon dioxide	CO_2	365,000	365,000	365,000
Carbon monoxide	CO	40-200	2000-10,000	10-60
Ozone	O_3	10-100	10-350	1000-12,000
Sulfur dioxide	SO_2	0.02-1	1-30	0.01-1
Nitric oxide	NO	0.005-0.1	0.05-300	0.005-10
Nitrogen dioxide	NO_2	0.01-0.3	0.2-200	0.005-10
CFC-12	CF_2Cl_2	0.55	0.55	0.22
Organic				
Methane	CH_4	1800	1800-2500	150-1700
Ethane	C_2H_6	0-2.5	1-50	---
Ethene	C_2H_4	0-1	1-30	---
Formaldehyde	HCHO	0.1-1	1-200	---
Toluene	$C_6C_5CH_3$	---	1-30	---
Xylene	$C_6H_4(CH_3)_2$	---	1-30	---
Methyl chloride	CH_3Cl	0.61	1-30	0.36

Table 2: Variation in the amount of several trace gases in different parts of the atmosphere [Jacobson, 1998a].

The conversion of trace gases in the atmosphere is dominantly caused by radicals via catalytic cycles. The resultant products are stable species such as carbon dioxide (CO_2) or water soluble compounds like sulphuric acid (H_2SO_4) or nitric acid (HNO_3). The steady increase of anthropogenic emissions of relatively long lived species like methane (CH_4) with an atmospheric lifetime (τ) of ~10.5 years, carbon monoxide (CO) (τ ~ 3 month), and nitrogen oxides (NO, NO_2) (τ ~ few days) [IPCC, 1992] causes

the majority of known effects like global warming (CO_2) or acid rain (H_2SO_4, HNO_3). These effects then in turn exert a lasting influence on the biosphere and the climate. The understanding of the reaction pathways between the mainly anthropogenic emitted gases (CH_4, CO, NO, NO_2) and the stable species like CO_2, H_2SO_4, and HNO_3, is an essential part of the process of developing strategies to reduce the emission of gases harmful for human health and/or climate.

In the troposphere the decomposition of nearly all trace gases is caused by the reaction with OH, O_3, and NO_3. Knowledge of processes like CO oxidation (through the reaction of CO with OH radicals [Weinstock, 1969]) or the production of OH radicals (via the photolysis of O_3 and the subsequent reaction with water (H_2O) [Levy, 1971]), the importance of radicals has become central to the understanding of tropospheric chemistry. Furthermore, peroxy radicals are the key intermediates of all oxidation processes taking place in the Earth's atmosphere, and are therefore the crucial species on which to base any verification of the current knowledge and understanding of processes – for example by comparing model results with observations.

The different levels of anthropogenic pollution found in the troposphere makes it easier to understand the dominant chemical processes. This is why in heavily polluted areas (for example, large conurbations or industrial centres) reactions involving nitrogen oxides are emphasized because of the relatively high amounts of NO_x (=NO+NO_2) mixing ratios (~20 ppbv) present.

Conversely, in less polluted regions (for example, areas of low population and industrial density) trace gas mixing ratios (NO_x ~ 1 ppbv) are mainly influenced by emissions of biochemical degradation products of plants and animals. However it is not possible to neglect this type of reactions in favour of those dominating in polluted areas because reaction rates are often comparable.

The chemistry of remote "clean air" regions (for example above the oceans) is relatively simple. In these areas amounts of NO_x are lowest (NO_x ~ 0-40 pptv[3]). In these

[2] ppbv = parts per 10^9 (v/v)
[3] pptv = parts per 10^{12} (v/v)

"clean air" areas, reactions between O_3, OH, HO_2, and the degradation products of methane can become dominant over the NO_x reactions concerning O_3 production and loss mechanisms. Therefore remote "clean air" regions are of special interest for the total tropospheric O_3 budget.

The absence of anthropogenic sources leads to the fact that the complex chemistry of non methane hydrocarbons (NMHC) and the dynamical processes play only a minor important role. The measurements in remote "clean air" regions provide the opportunity to observe the undisturbed evolution of trace gas concentrations over the time period of several days. This then enables comparisons to be made between measurements and model calculations, the results of which help to identify hitherto unknown processes relevant to the chemistry of the Earth's atmosphere.

1.2 Overview

The aim of this work is to describe in detail the photochemistry of O_3 and radicals in both remote "clean air" and "heavily polluted" regions. The results of two field studies are presented which form the basis for this thesis. These studies were the Indian Ocean Experiment (INDOEX)[4] and the Peroxy Radical Initiative for Measurements in the Environment (PRIME)[5].

Within the INDOEX campaign the first measurements of peroxy radicals $\left(RO_2^* = HO_2 + \sum_i R_i O_2 \right)$ were successfully performed above the Indian Ocean. These, together with other relevant trace gases and parameters have been compared with the results of a 0-dimensional chemistry model developed within this work (for details see Appendix 0). The comparison between measurements and simulations revealed large discrepancies, which lead to the identification of new processes of relevance to the chemistry of the atmosphere. In addition, a radiative transfer model has been modified and used to calculate the influence of highly absorbing aerosols on the energy budget of the Earth. Satellite and sonde data have been used for the investigation of large scale phenomena and for the identification of all relevant processes responsible for the amount of O_3 present above the Indian Ocean.

The measurements of PRIME complement the peroxy radical dataset obtained during the INDOEX campaign by providing radical datasets for polluted urban air mass, i.e. the outflow of London, UK. The PRIME study analysed the measured variability of radical, peroxy radical, and peroxide mixing ratios by the comparison with model results.

[4] The INDOEX campaign, an international research initiative, studied the chemistry of remote areas of the Indian Ocean and the influence of the outflow from the Indian subcontinent on these regions [see Crutzen and Ramanathan, 2001, Ramanathan et al., 2001, Lelieveld et al., 2001, Ball et al., 2003, http://www-indoex.ucsd.edu]. This campaign took place during February, March, and April 1999.

[5] The PRIME campaign took place during July and August 1999 at the Silwood Park Atmospheric Research Station, near London (51°24'53''N, 0°38'48''W). The site offered the opportunity to measure on many days the plume from the city centre of London.

The large discrepancies between measured and simulated hydrogen peroxy radical concentrations and the coexistence of high amounts of nitrogen oxides and peroxy radicals are the two main features observed. Different processes are suggested to explain the disagreement between measured and expected (i.e. by the conventional tropospheric chemistry) concentrations.

The outline of this work is as follows: Chapter 2 presents in some detail the theoretical background of this work. The theoretical background highlights the limitations in the current scientific knowledge and the questions that need to be solved.

Chapter 3 gives an overview of the different measurement techniques and model specifications used within the PRIME and INDOEX campain.

The INDOEX campaign is described in Chapter 4. In the first section the analysis of the peroxy radical and formaldehyde (HCHO) measurements is shown, based on Burkert et al. [2003a]. Diurnal behaviour of O_3 and the responsible meso scale processes follow and finally the chapter ends with a discussion on the possible sources for O_3 and the influence of highly absorbing aerosols on the energy budget of the Earth [Burkert et al., 2003b].

Chapter 5 focuses on the interpretation of the measurements of RO_2^*, HO_2, OH, and H_2O_2 from the PRIME campaign, in particular on the difference between simulations and measurements [Burkert et al., 2003c].

Chapter 6 summarises this work and describes the most striking features found. It also includes a discussion on the limitations of the current understanding of atmospheric chemistry and dynamics concluding with an overview of open questions and recommendations resultant from this work.

2 Theoretical background

The chapter that follows is an overview and discussion on the theoretical background which underpins this research. The material is divided into two main sub-sections - “Physics of the atmosphere” (2.1) and “Chemistry of the troposphere” (2.2).

2.1 Physics of the atmosphere

This section is comprised of two sub-sections - “Radiation and energy processes” (2.1.1) and “Dynamics of the atmosphere” (2.1.2). The intention in this discussion is not to cover everything about these two very large fields of physics, but rather to discuss processes which are later used as the basis for the interpretation and modelling of the natural phenomena encountered during the course of the research.

2.1.1 Radiation and energy processes

Radiation and energy processes are fundamental to even a simplistic understanding of radiative transfer models. Furthermore, radiation and energy budgets are necessary in order to comprehend the dynamical mechanisms described in chapter 2.1.2. One of the more important theoretical concepts is the frequently underestimated role that the scattering and absorption of aerosols play in this budgets.

2.1.1.1 Basics of the radiative transfer

Absorption and scattering are the two most crucial processes influencing the radiation in the atmosphere. Thermal emission plays only a minor role, at least in the UV and visible wavelength region. Thermal emissions are therefore excluded from the following discussions.

Absorption is the interaction between a photon and solid or fluid matter or gases, in a process that results in the photon being picked up by a molecule or atom. The molecule changes its structure and emits excess energy in various ways.

For the molecule AB in the excited state AB^* the ways of emitting excess energy are:

- Fluorescence : $AB^* \longrightarrow AB + h\nu$
- Photoionisation : $AB^* \longrightarrow AB^+ + e^-$
- Reaction : $AB^* + C \longrightarrow AC + B$
- Quenching : $AB^* + M \longrightarrow AB + M$
- Photodissociation : $AB^* \longrightarrow A + B$.

The probability of the absorption of a photon with a certain wavelength by a molecule is dependent on the molecule's structure. The describing parameter for the molecule's structure is the **absorption cross section** $\sigma_a(\lambda)$, measured in units of cm^2 $molec^{-1}$.

A molecule absorbs only photons with certain discrete energies – a phenomena caused by the different energy states of the molecule. In the UV / visible light region of the spectrum continuous spectra are often observed. These spectra are caused by excitation of a molecule by a photon in an unbound state. This excitation leads to dissociation of the molecule and in consequence to non discrete energy differences.

The number density (concentration) N in [molec cm^{-3}] of an atmospheric gas also has a significant influence on the attenuation of sunlight as it passes through the atmosphere. The product of the absorption cross section $\sigma(\lambda)$ and number density N is named **absorption coefficient** $\alpha(\lambda)$ in units of [cm^{-1}].

Scattering is the interaction between light and solid or fluid matter, which occurs whenever a photon changes its direction. If a photon is **elastically scattered**, the energy (i.e. the wavelength) will be conserved. By contrast **inelastic scattering** occurs when change in the direction of the photon is accompanied by an energy transfer between the photon and the scattering molecule.

In the following discussions only elastic scattering is considered. This is because inelastic scattering plays only a minor role in the process under review here.

The two main quantities used to describe scattering are the effective **scattering cross section** $\sigma_s(\lambda)$ and the **phase function** $p(\gamma)$. The scattering cross section has the same units as the absorption cross section and therefore described in units of [molec cm^2].

In analogy to the absorption, the scattering coefficient represents the attenuation of light through the product of the scattering cross section $\beta(\lambda)$ and the number density N of the scattering centres. Each air molecule works as a scattering centre and the scattering coefficient is therefore proportional to the air pressure.

Phase function is a way of representing the directional dependence of the scattered radiation as a function of the **scattering angle** g. It is usual to express phase function by normalising it to unity. Put in another way, phase function is the probability of a photon being scattered in a certain direction, and the scattering angle γ is the angle between incoming and outgoing radiation.

Scattering is divided into two types (Rayleigh and Mie scattering) - defined by the relative proportion between the size of the scattering centre and the wavelength of the light. For both types the resultant scattering cross sections and phase functions are different.

When the scattering particles are small compared to the wavelength, the scattering is described by the **Rayleigh scattering** theory. The theory is based on the assumption that the light is scattered by spherical particles. In the simplest case of spherical particles the phase function for Rayleigh scattering has the form

$$p_r(g) = \frac{3}{4}\left(1+\cos^2 g\right). \qquad (1)$$

However, the two most important scattering particles O_2 and N_2 are linear molecules, therefore a correction factor has to be included. This factor is a function of the so called **depolarisation factor** d.

Taking the formula of Rayleigh and Cabannes for the Rayleigh scattering cross section (note that this formula also includes the refractive index that depends on pressure and temperature [Penndorf, 1957]), the scattering cross section for Rayleigh scattering is approximately proportional to λ^{-4}. Hence the blue colour of a clear sky results from the stronger scattering of shorter wavelengths.

Rayleigh scattering is relatively isotropic (isotropic: $p(\gamma)$=const.). As a result of this, nearly equal amounts of light are scattered forward and backwards, and about half of the forward or backward scattered light is vertical to the incoming radiation scattered.

The second type of scattering is named **Mie scattering**. The Mie theory is used when the size of the scattering particles is in the same range of the wavelength of the light. Examples of Mie scattering particles in the atmosphere are the aerosols or cloud

droplets. The dependence of the scattering coefficient on the wavelength is between λ^{-1} and $\lambda^{-1.5}$, depending on the particle size. Compared to the Rayleigh scattering the wavelength dependence is much smaller. The most visible consequence of this type of scattering is the white colour of clouds. In addition the phase function of Mie scattering by contrast to Rayleigh scattering has a distinct forward scattering behaviour.

The **extinction coefficient** $\sigma_e(\lambda)$ results from the effective coefficient from the absorption ($a(\lambda)$) and scattering ($b(\lambda)$).

$$\sigma_e(\lambda) = a(\lambda) + b(\lambda) \tag{2}$$

The integral of $\sigma_e(\lambda)$ over the optical path (usually the height z) is called **optical depth** $\tau(\lambda, z)$

$$\tau(\lambda, z) = \int_z^\infty \sigma_e(\lambda, z')\, dz' \tag{3}$$

and in several formulations of the radiative transport the optical depth is used as an independent variable instead of the geometrical height [e.g. Sobolev, 1975, Meier et al., 1982, Stamnes et al., 1988].

Resultant from the optical depth there comes the **optical thickness** $\tau(\lambda)$, defined as the specific integral of the optical depth between z_1 and z_2 for a given medium.

The ratio between scattering and extinction coefficient is named **single scattering albedo**

$$\nu_0(\lambda) = \frac{b(\lambda)}{\sigma_e(\lambda)}. \tag{4}$$

This parameter represents the probability of scattering occurring when a photon interacts with a molecule in the atmosphere. Media with $\nu_0(\lambda) = 1$ (i.e. no scattering), are conservative.

2.1.1.2 Radiation/Energy budget

The radiation from the Sun is the ultimate source of energy which drives the Earth's climate. About 90% of the sun's radiant energy lies within the 0.4 to 4 μm wavelengths - maximum intensity being in the green part of the visible spectrum (at 0.48 μm – Figure 1).

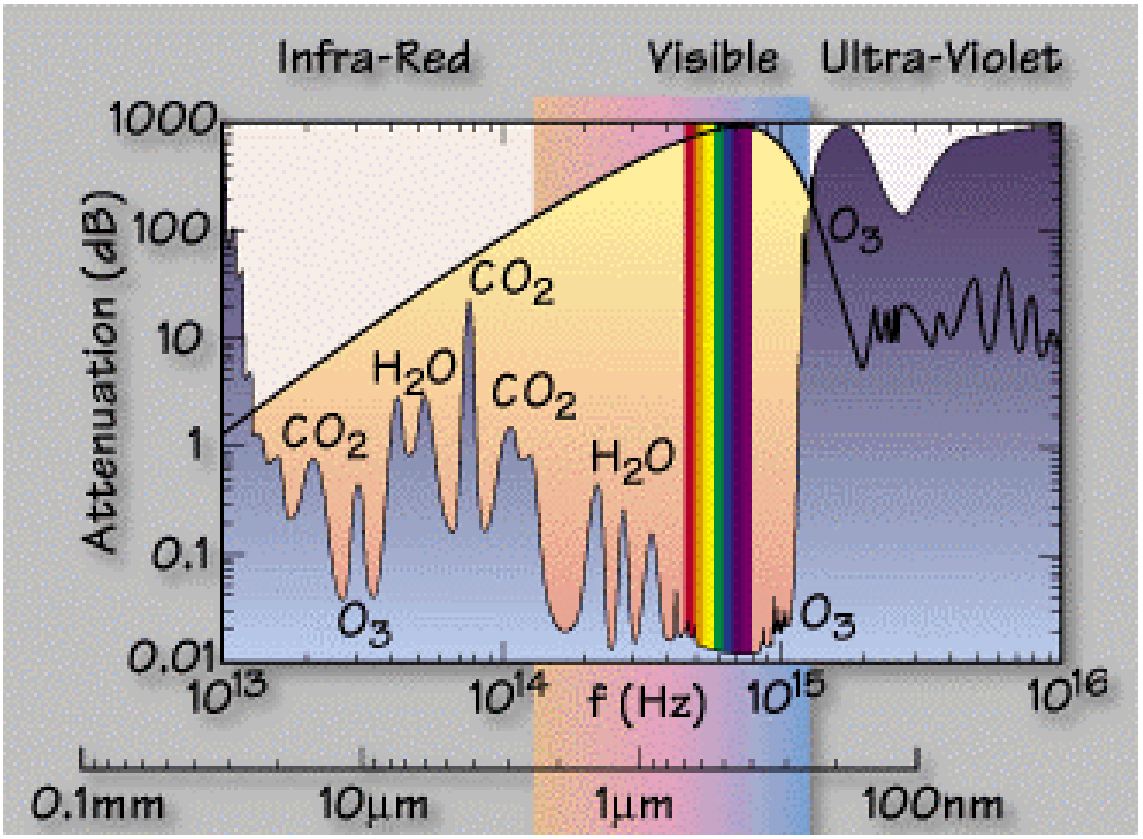

Figure 1: Solar and terrestrial radiation and atmospheric absorption spectrum for a beam reaching the ground [http://envisat.estec.esa.nl/instruments/sciamachy/index.html].

Assuming the Earth had no atmosphere and a spherical surface, each square metre would receive on average 342 Watts of solar radiation throughout the year. The atmosphere approximately halves this number, because about 30% of the incoming solar energy is reflected back into space by clouds, the atmosphere, and by the Earth's surface. Approximately 20% of the sun's incoming energy is absorbed by the atmosphere but most of it (~168 Wm^{-2}) penetrates the atmosphere and warms the Earth's surface: both the land and the oceans.

Energy returns to the atmosphere from the Earth's surface by means of infrared radiation, sensible heat, and as water vapour - which releases its heat to the atmosphere as it rises and condenses.

The mean global temperature near the ground which results from these processes is about 14°C. This decreases rapidly with increasing altitude, reaching a mean temperature of –58°C at the top of the troposphere.

Energy balance is achieved when the climate system itself radiates on average 235 Wm^{-2} back to space. Figure 2 details these energy balancing processes - the left hand side shows what happens to the incoming solar radiation, with the right hand side showing how the atmosphere emits the outgoing infrared radiation.

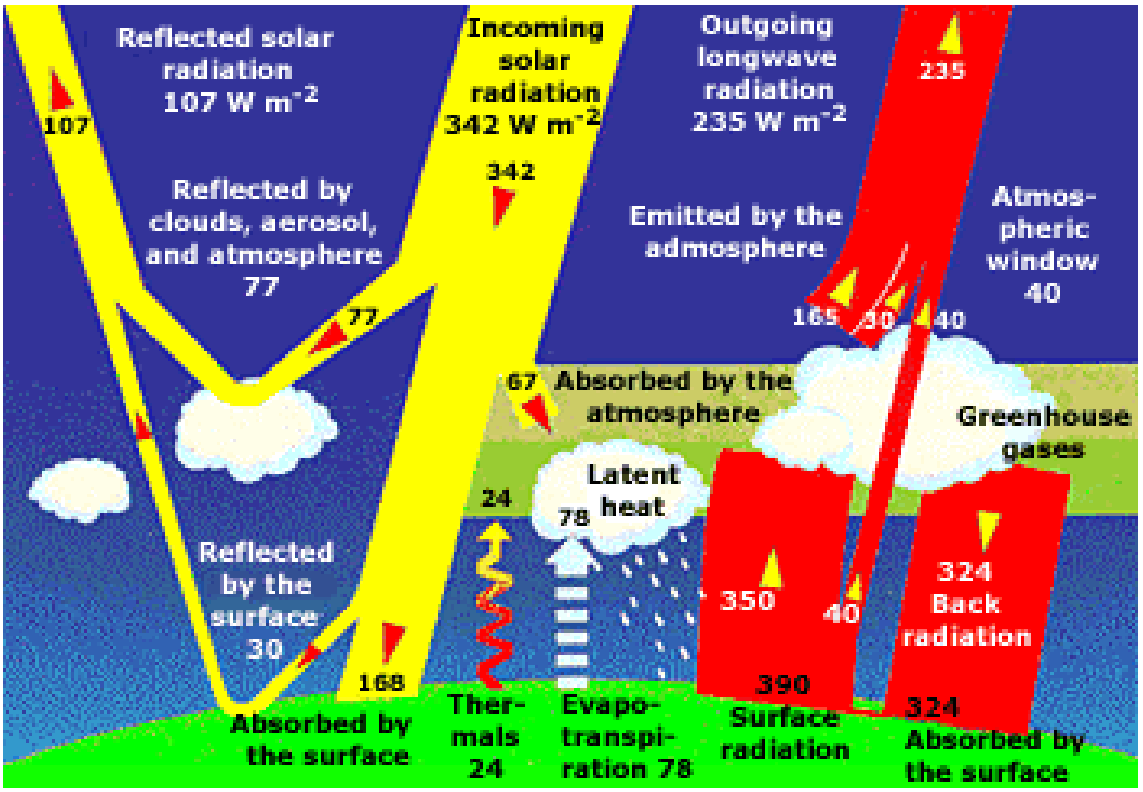

Figure 2: The greenhouse effect [colour image adapted from Kiehl and Trenberth, 1997]. The Earth's radiation energy balance which controls the way the greenhouse effect works, can here be seen graphically. Note that nearly half the incoming solar radiation penetrates the clouds (and greenhouse gases) to reach the Earth's surface. Greenhouse gases and clouds reradiate most of the absorbed energy back down toward the surface.

The Earth's energy balance leads to an equilibrium climate state with a zero average net radiation at the top of the atmosphere (TOA). In practice, the top of the troposphere is taken as the top of the atmosphere. This is because the stratosphere responds faster (in the order of months) to changes in the radiative balance, in contrast to the Earth's surface-troposphere system (with its large thermal inertia caused by the oceans).

Changes in either solar radiation or infrared radiation affect the net radiation, and therefore leads to an imbalance called "radiative forcing" – defined by IPCC as follows:

"The **radiative forcing** of the surface-troposphere system due to the perturbation in, or the introduction of, an agent (say, a change in greenhouse gas concentrations) is the change in net (down minus up) irradiance (solar plus long-wave; in Wm^{-2}) at the tropopause AFTER allowing for stratospheric temperatures to readjust to radiative equilibrium, but with surface and tropospheric temperatures, and state held fixed at the unperturbed values" [Intergovernmental Panel on Climate Change (IPCC), 1996].

2.1.1.3 Aerosol scattering and absorption

Atmospheric aerosol particles are of major importance for solar radiative transfer and thus affect the Earth's climate. As a result, the so called direct aerosol effect refers to the reflection and absorption of solar radiation by these aerosols [e.g. Charlson and Heintzenberg, 1995]. Several studies have assessed the direct effect of aerosol particles in terms of their radiative forcing at the top of the atmosphere [for examples see IPCC, 1996].

The scattering and absorption of aerosols leads to differences in vertical temperature profiles. It is not possible to distinguish whether there is a positive or a negative feedback on the radiative forcing, because several parameters have to be considered (e.g. albedo, solar zenith angle, vertical profiles of the aerosols). In general scattering processes in the atmosphere control the portion of incoming radiation scattered back to space, and absorption processes control the transfer light to other energy forms, mainly heat. Consequently an increasing burden of scattering particles (e.g. sulfates) induces a net cooling effect [Charlson et al., 1991].

However if absorbing aerosols are also present in the atmosphere, cooling caused by an increase in scattering particles can be offset or even changed into a heating effect [Chylek and Coakley, 1974, Haywood and Shine, 1995].

One of the strongest absorbing components in the solar spectral range is black carbon (BC) [Bohren and Huffman, 1983]. BC is responsible for a significant fraction of light extinction in urban [Shah et al., 1984], rural [Trijonis, 1982], and remote continental areas [Malm et al., 1994]. As the average lifetime of BC particles is in the

range of a week (depending on the rate of mixing with other compounds and the rain rate), BC can also be found in remote polar and oceanic regions [Heintzenberg, 1982, Hansen and Novakov, 1988, Clarke, 1985].

Significant radiative forcing due to particle absorption can be expected in regions with high BC concentrations [Smith et al., 1989, Cadle and Dasch, 1988]. If the BC particles are embedded in nonabsorbing particles, they absorb solar radiation more efficiently than they could as separate BC particles [e.g. Fuller, 1999, Horvath, 1997, Heintzenberg and Wendisch, 1996].

In order to make quantitative estimates of the radiative forcing of the absorbing component of the particles, radiative transfer calculations have to be based on detailed measurements. Studies based on ground-based particle absorption measurements [e.g. Müller et al., 2000] can give estimates of the forcing for certain atmospheric conditions (e.g. well-mixed boundary layer).

The assessment of the radiative forcing of aerosol particles from the measured aerosol absorption properties is of special importance in climatic studies. As shown by Haywood and Shine [1997] and Haywood and Ramaswamy [1998], the direct radiative forcing is strongly dependent on BC vertical profiles. For example, BC in higher altitudes, above highly reflecting clouds, can induce a much higher forcing than BC located below clouds.

In addition to the direct radiative forcing at the TOA, the warming of different layers within the atmosphere is important. Absorption of aerosols is particularly important when investigating local dynamics, as it can lead to either a stabilising or destabilising effect dependent on the vertical structure and composition of the atmosphere. In polluted areas where absorbing aerosols are emitted within the lowest layers absorption by direct sunlight leads to increased heating in these layers (i.e. compared to the heating of air parcels above). As a consequence, absorbing aerosols can lead to an enhanced ascent of the lowest atmospheric layer, together with increased entrainment of free tropospheric air.

The opposite effect is observed in remote areas over the northern Indian Ocean. The marine boundary layer (MBL) contains mainly scattering aerosols (e.g. sea salt aerosols), which lead to a cooling effect. The layer above the MBL is characterised by highly absorbing aerosols. Thus the cooling in the MBL and the heating in the free troposphere lead to a stabilising effect, which results in entrainment being suppressed.

This effect was neglected in the past, but the calculations by Burkert et al. [2003b] indicate the importance of this effect when modelling at both local and global scales (especially in the Indian outflow region above the ocean).

A secondary effect of aerosols is called “indirect forcing”. This process involves the role of aerosol particles as cloud condensation nuclei [Ramanathan et al, 2001].

2.1.2 Dynamics of the atmosphere

This section focuses on an experimental view of the atmospheric dynamics. The following subsections consider the different parts of the troposphere separately: The boundary layer (chapter 2.1.2.1), the free troposphere (chapter 2.1.2.2), and the tropopause region (chapter 2.1.2.3).

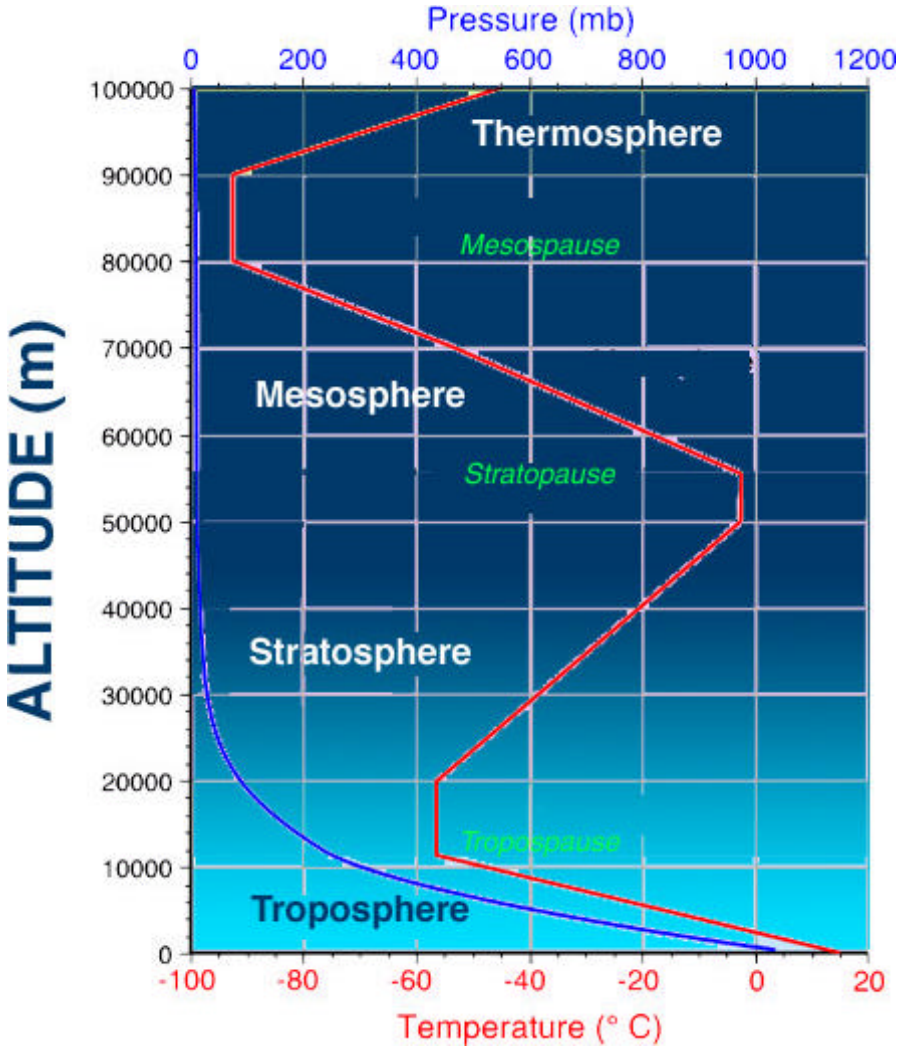

Figure 3: The vertical temperature profile of the Earth’s atmosphere. The different regions are labelled.

The troposphere extends from the surface up to an altitude of 8 to 18 km (Figure 1). The transition zone between the troposphere and the stratosphere is named tropopause. The height of the tropopause is defined by the World Meteorological Organization (WMO) as the lowest level at which the rate of decrease of temperature with height (i.e. temperature lapse rate) decreases to 2 K km^{-1} or less and the lapse rate averaged between this level and any level within the next 2 km does not exceed 2 K km^{1} [Holton et al., 1995]. The height of the troposphere is minimal at the pole and slopes upward towards the inter tropical convergence zone (ITCZ).

The temperature lapse rate within the troposphere is 9.8 K km^{-1} for dry air (**dry adiabatic lapse rate (Γ_D)**). The reason for this progressive decline is the increasing distance from the Earth's surface.

Vertical motion of air is caused by either (a) convection from solar heating of the Earth´s surface, (b) convergence or divergence of horizontal flows, (c) horizontal flow over topographic features at the Earth's surface, and/or (d) buoyancy caused by the release of latent heat as water condenses [Seinfeld and Pandis, 1998].

As air moves vertically, its temperature changes in response to the local pressure. The "Ideal Gas Law" is a combination of Boyle's law, Charles' law, and Avogadro's law, and describes the change of temperature and pressure as follows,

$$p = \frac{nR^*T}{V} = \frac{nA}{V}\left(\frac{R^*}{A}\right)T = Nk_BT \qquad (5)$$

where R^* is the universal gas constant (8.314 x 10^4 cm^3 mbar $mole^{-1}$ K^{-1}), A is the Avogadro's number, A = 6.02252 x 10^{23} molecules $mole^{-1}$, N=nA/V is the number concentration of gas molecules (molecules of gas per cubic centimetre of air), and k_B = R^*/A is Boltzmann's constant in units of 1.3807 x 10^{-19} cm^3 mbar K^{-1}.

The rate of change of temperature with height is dependent on the water content of the air parcel and therefore can vary between 5 (**wet adiabatic lapse rate (Γ_W)**) and 10 K km^{-1} (dry adiabatic lapse rate). The vertical motion of air parcels accompanied with the strong dependence of the saturation vapour pressure on temperature can lead to an increase of the relative humidity (r.h.). This increase can cause the air to reach saturation (r.h. = 100%) or even supersaturation. The saturation of air leads to formation of clouds and therefore to additional energy win for the rising air parcel through the latent heat release as water condenses.

2.1.2.1 Atmospheric Boundary layer

The atmospheric boundary layer (ABL) is defined as the part of the troposphere that is directly influenced by the presence of the Earth's surface and responds to surface forcing with a timescale of about an hour or less [Stull, 1988]. This forcing includes frictional drag, evaporation and transpiration, heat transfer, pollutant emission, and terrain induced flow modification. The ABL is capped by a statically stable layer of air or temperature inversion. The height of the inversion layer is variable in time and space, ranging from tens of metres in strongly statically stable situations, to several kilometres in convective conditions over deserts and oceans. Within the ABL strong turbulence is common.

The following discussion differentiates the characteristics of the ABL over land from those of the ABL over the ocean. The definition of the different meteorological parameters are according to the Glossary of Meteorology, 2nd Edition, American Meteorological Society [2000].

The ABL over land has a marked diurnal cycle during fair weather situations (Figure 4). During daytime, a mixed layer of vigorous turbulence grows in depth, typically capped by a statically stable inversion layer. The inversion layer also called entrainment zone is characterised by intermittent turbulence and overshooting thermals. The free atmosphere is entrained into the top of the boundary layer.

The entrainment zone is thinner when a stronger temperature inversion caps the boundary layer and thicker when higher turbulence and more active thermals are present. Near sunset, turbulence decays leave a weakly mixed residual layer in place of the mixed layer. At night, the bottom of the residual layer is transformed into a statically stable boundary layer. This **nocturnal boundary layer** is typically observed under clear sky conditions. Radiation to space cools the land surface, which therefore cools the adjacent air mainly through the process of molecular conduction and turbulence, and to a lesser extent through radiative transfer. The depth of the nocturnal boundary layer can grow up to a few hundreds of metres, depending on the season.

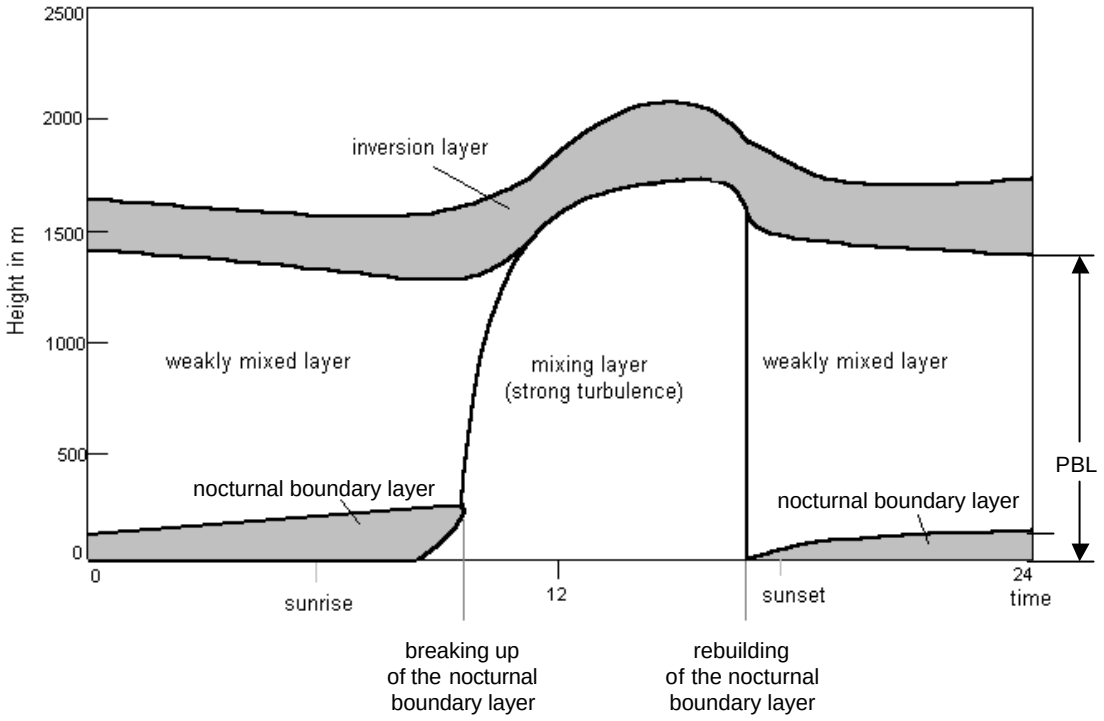

Figure 4: Theoretical diurnal evolution of the atmospheric boundary layer over land.

Figure 5 shows as an example the change in the mixing depth of the ABL during a day in the Los Angeles basin. Figure 5a shows the hazy layer of pollution in the morning hours. The same layer approximately doubles its depth in the late afternoon (Figure 5b).

a)

b)

Figure 5: Change in the mixing depth, Los Angeles, July 23, 2000 [Jacobson, 2002].

The ABL over the ocean (also called marine boundary layer (MBL)), in contrast to the ABL over land, is characterised by a nearly constant height throughout the day. The roughly constant temperature of the ocean surface (i.e. sea surface temperature (SST)) leads to a steady heat flux to the adjacent air parcels to the ocean surface. Therefore, no nocturnal boundary layer is built, and due to the constant SST the depth of the MBL is stable throughout a day.

The **mixed layer** in the ABL is characterised by a homogeneous mainly vertical distribution of quantities such as conservative tracers (i.e. trace gases with a longer lifetime than the transport process, absolute humidity, equivalent potential temperature, radioactivity, and CCN composition), and momentum or wind speed.

Turbulence within a mixed layer can be caused by either strong winds or wind shears that generate forced convection, or by free convection associated with large thermals. **Forced convection** is typically induced by mechanical forces such as deflection by a large-scale surface irregularity (i.e. buildings, mountains, waves, etc.). The mixed layers generated by **free convective** are typically caused by heating at the bottom boundary such as the Earth's surface or radiative cooling at the tops of cloud or fog layers.

Temperature inversions as the upper limit of the mixed layer of the ABL can be caused by different processes. The different notations used to describe temperature inversions are named according to their origin.

The **turbulence inversion** is built by strong turbulence within the surface layer, typically caused by strong winds. For example, starting with an initial condition of calm winds and a lapse rate of 6 K km^{-1}, wind speed increases within the first 800 m, then air parcels start to move upwards and downwards, while their temperature changes dry adiabatically by 10 K km^{-1}.

In the turbulence inversion the total heat energy of the mixed layer does not change. The average temperature also remains constant, therefore the resulting vertical temperature gradient of 10 K km^{-1} leads to a decrease in the temperature at the top of the mixed layer together with an increase in the temperature at its bottom. Consequently an inversion on top of the mixed layer is built.

Turbulence inversions are typically found in high pressure zones above the oceans, where strong trade winds are present. Furthermore, subsiding air in high

pressure systems leads to trade inversions, which enhance the building (or maintaining) of the temperature inversion.

The **subsidence inversion** is found in cases when large scale downward motion of air is observed, for example in high pressure systems. Starting from initial conditions with a vertical temperature gradient of 7 K km^{-1} and no vertical movement of the air an air parcel starts descending for example 1 km above the height H and arrives at that height H 3 K warmer than its surrounding air having been consequently subjected to adiabatic warming. In Figure 6 the typical formation of a subsidence inversion is shown.

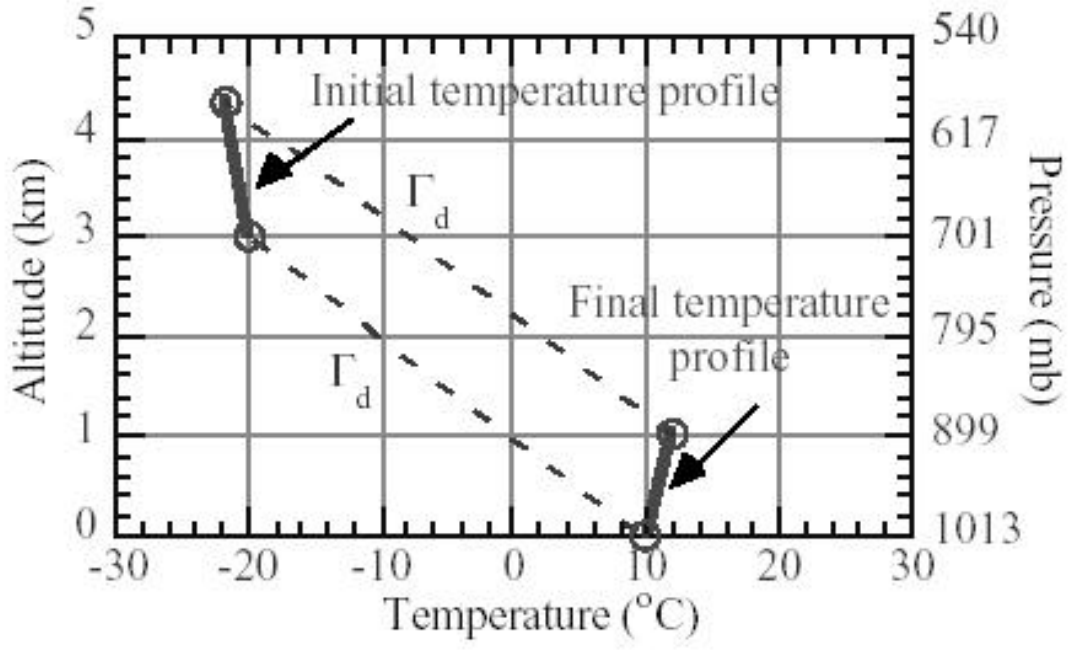

Figure 6: Formation of a subsidence inversion [Jacobson, 1998a].

The **trade inversion** is a specific form of the more general subsidence inversion. It is usually found in large-scale subsiding flows which constitute the descent branches of the Hadley cell and Walker circulation. This type of inversion is commonly found in trade-wind streams over the eastern portions of the tropical oceans.

The subsidence warming in the inversion layer is balanced by radiative cooling and evaporation from the tops of trade cumuli. The height of this inversion's base varies from about 500 m at the eastern extremities of subtropical highs, to about 2000 m at the western and equatorial extremities. In the equatorial trough zone and over the western

portions of the trade-wind belt, the inversion does not exist as a mean condition, although it appears in certain weather patterns.

The strength of trade inversions varies enormously, occasionally being more than 10°C over 1 km, but sometimes being absent altogether, especially in the Northern Hemisphere. The inversion is generally strongest when the height of its base is lowest, and vice versa. The thickness of the inversion layer varies from only a few metres to more than 1000 metres. On the average its thickness is about 400 metres.

Airflow below a trade inversion is very moist and filled with cumulus clouds (trade cumuli). Above it, the air is warm and exceedingly dry; this structure is so characteristic of the trade current that tropical analysts think of the tropical troposphere as consisting of a lower moist and an upper dry layer [Riehl, 1954].

Overall, atmospheric conditions in general are typically a combination of several processes, and the air in the lower layers is vivid and also moves upwards and downwards. Therefore, air parcels in one layer sometimes subside much faster than in other layers leading to multiple temperature inversions.

Figure 7 shows how pollution is caped within two inversion layers in a certain height.

a)

b)

Figure 7: a) Smoke layer trapped in an inversion following a fire in Menlo Park, California (June, 2001), b) Elevated pollution layer (Los Angeles, July 22, 2000) [Jacobson, 2002].

Stability:

This study focuses on the static stability, therefore in the context of this thesis the word "stability" should be taken to mean "static stability" throughout. Knowledge about the stability of air parcels is essential to understand the possible influence of transport (i.e. horizontal and/or vertical) processes on the amounts of trace gases in different parts of the atmosphere. Many descriptions are given in the literature of how stability is defined in terms of temperature or energy.

The atmosphere is defined as being stable when a parcel of air which has been displaced vertically, returns to its original position. The atmosphere is unstable when a displaced air parcel continues to move in the same direction as it was when initially displaced. The atmosphere is neutral when a parcel remains still after being displaced.

These simple definitions lead to several different approaches to determining whether or not an atmosphere is stable. The most common approach is to take the potential temperature as the key indicator for stability. In general all the various approaches are self consistent, but there are differences in the cause and effect assumption [Stull, 1988, Jacob, 1999]. The main question that needs to be addressed is: Is the observed temperature profile the cause or the effect of the dynamical processes of the atmosphere?

The temperature profile is actually both the cause and the effect. This is because the actual temperature change of air with height (Environmental Lapse Rate (Γ_E)) as measured for example by radiosondes is only a snap-shot in time of the atmosphere. The actual temperature profile is dynamic and is continuously evolving. The environmental lapse rate plotted on a thermodynamic diagram is a snap shot in time of the atmosphere. The environmental lapse rate can be positive or negative and switch from one to the other with height. The average environment lapse rate is 6 K km^{-1}. But this is just the average, and the lapse rate will always vary from this average.

Therefore, analyse of stability do not include the history of the investigated air, but it can state the future. However, the history of an air parcel can be determined by other long lived tracers such as potential vorticity, certain trace gas concentrations, etc.

Different temperatures are usually used to define the stability of the atmosphere. There are several sub divisions corresponding to different strengths of the atmosphere's stability/instability, which are defined afterwards. The decision which temperature is useful to determine stability depends on whether clouds are present or not (i.e. does

condensation release latent heat or not) and on the amount of water vapour (i.e. is the amount of water vapour negligible for the density of an air parcel).

Potential temperature (θ) is the temperature of an unsaturated parcel of dry air brought adiabatically and reversibly from its initial state to a standard pressure, p_0, typically 1000 mbar.

$$q = T_0 \left(p_0 / p \right)^k \tag{6}$$

$$k = \frac{\mathrm{R_d}}{\mathrm{c_{pd}}} \frac{1 + r_v / e}{1 + r_v c_{pv} / c_{pd}} \approx 0.2854 \left(1 - 0.24 r_v\right) \tag{7}$$

where θ is the potential temperature, T is the temperature, κ (=0.2854 for dry air) is the Poisson constant, R_d and c_{pd} are the gas constant and specific heat of dry air, ε is the ratio of the gas constant for water vapour and for dry air, c_{pv} is the specific heat of water vapour, and r_v is the water vapour mixing ratio.

Equivalent temperature is the temperature of an air parcel when all its water vapour condenses at constant pressure and the released energy is used to heat the air:

$$T_{ie} = T \left(1 + \frac{Lw}{c_p T} \right) \tag{8}$$

where T_{ie} is the isobaric equivalent temperature, T the temperature, w the mixing ratio, L the latent heat, and c_p the specific heat of air at constant pressure.

Adiabatic equivalent temperature is the temperature that an air parcel has after undergoing a dry-adiabatic expansion until it is saturated, followed by a pseudoadiabatic expansion until all moisture is precipitated out, and finally brought back to the initial pressure with dry-adiabatic compression.

$$T_{ae} = T \exp \left(\frac{Lw}{c_p T} \right) \tag{9}$$

being T_{ae} the adiabatic equivalent temperature.

Equivalent potential temperature (θ_e**)** is the temperature of an air parcel undergoing a dry-adiabatic expansion until it is saturated, followed by a pseudoadiabatic expansion until all moisture is precipitated out adiabatically and finally brought back to standard pressure with dry-adiabatic compression, p_0, typically 1000 mbar.

It is given most accurately as

$$q_e = T\left(\frac{p_0}{p_d}\right)^{R_d/\left(c_{pd}+r_t c\right)} r.h.^{-r_v R_v/\left(c_{pd}+r_t c\right)} \exp\left[\frac{L_v r_v}{\left(c_{pd}+r_t c\right)T}\right] \qquad (10)$$

where θ_e is the equivalent potential temperature, c_{pd} is the heat capacity at constant pressure of dry air, r_t is the total water mixing ratio, c is the heat capacity of liquid water, T is the temperature, R_d is the gas constant for dry air, p_d is the partial pressure of dry air, p_0 is a reference pressure (usually 1000 mbar), L_v is the latent heat of vaporization, r_v is the vapour mixing ratio, R_v is the gas constant for water vapor, and r.h. is the relative humidity [Paluch, 1979, Emanuel, 1994].

Virtual temperature is a fictitious temperature that takes into account moisture in the air. The formal definition of virtual temperature is the temperature that dry air would have if its pressure and specific volume were equal to those of a given sample of moist air. Virtual temperature allows meteorologists to use the equation of state for dry air even though moisture is present.

$$T_v = \frac{T\left(1+\frac{r_v}{e}\right)}{\left(1+r_v\right)} \qquad (11)$$

where r_v is the mixing ratio, and ε is the ratio of the gas constants of air and water vapour, ≈0.622.

The stability of the atmosphere can be determined from the environmental lapse rate. Comparison with the dry and wet adiabatic lapse rates enables the estimation of the current stability. The temperatures above can be used to more easily investigate stability and to account for different processes occurring (i.e. condensation and/or density changes depending on the water content of the air parcel).

Any layer in the atmosphere is called **absolute stable**, if the environmental lapse rate decrease (or increase) with height is less than the cooling rate of the moist adiabatic lapse rate. The most stable layers are inversions where temperature increases with height.

The opposite, an **absolute unstable** atmosphere layer, is encountered where the environmental lapse rate decreases with height more than 9.8 K km^{-1} (rapid cooling with height).

Any layer defined as **conditional unstable** has an environmental lapse rate which decreases with height between the moist and dry adiabatic lapse rate. The air is unstable if saturated but stable if unsaturated. Saturated air cools less with height due to latent heat release thus allowing the parcel to be warmer than the environment if lifting occurs in a conditionally unstable environment.

Environmental lapse rate:

$$\Gamma_E = -\frac{\Delta T}{\Delta z} \tag{12}$$

Stability criteria for moist air:

$\Gamma_E > \Gamma_D$	absolute unstable
$\Gamma_E = \Gamma_D$	dry neutral
$\Gamma_D > \Gamma_E > \Gamma_W$	conditional unstable
$\Gamma_E = \Gamma_W$	wet neutral
$\Gamma_E < \Gamma_W$	absolute stable

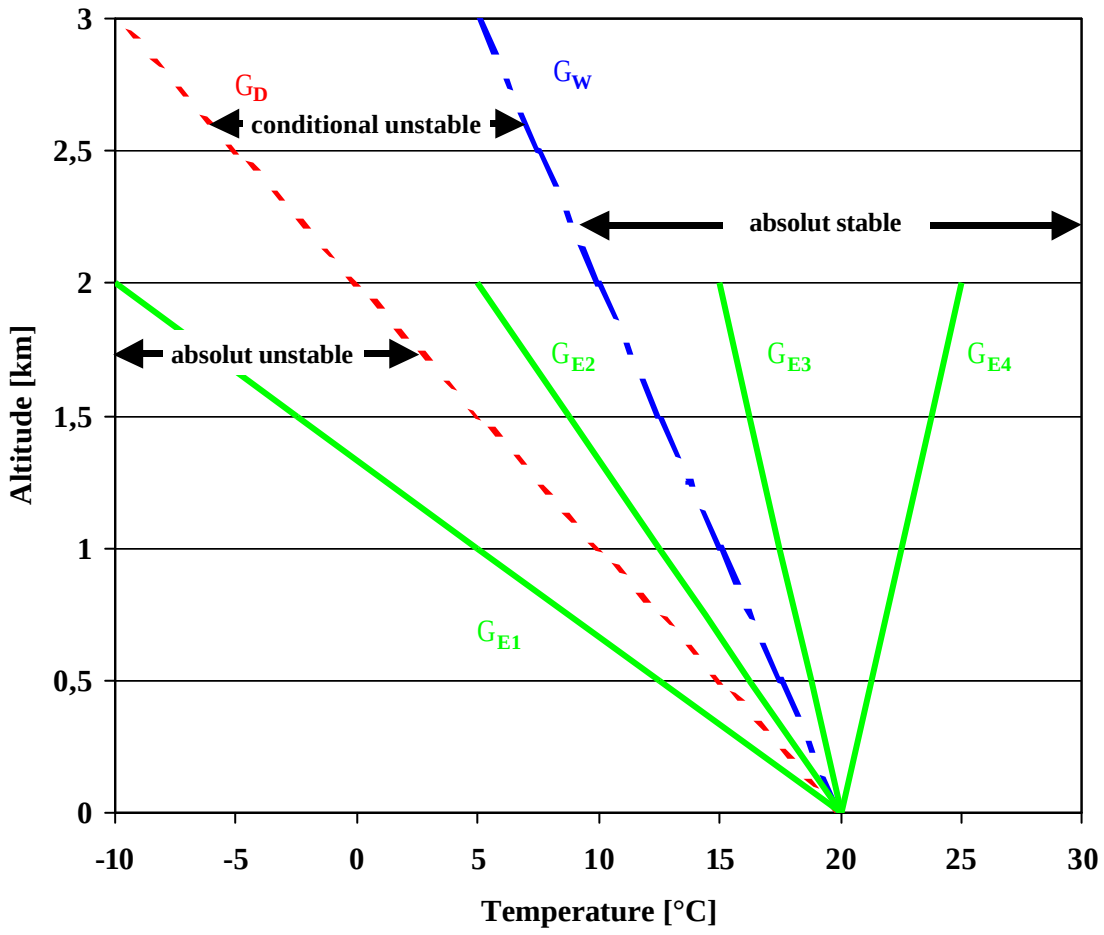

Figure 8: Stability of air. Different regions of stability are marked by the black arrows. The red dotted line represents the dry adiabatic temperature profile (Γ_D), the blue dotted line is the wet adiabatic temperature profile (Γ_W), and the green lines show four possible environmental temperature profiles (Γ_E).

The **level of free convection** (LFC) is often found in the literature describing the level at which a parcel of air lifted dry-adiabatically until saturated and moist-adiabatically thereafter would first become warmer than its surroundings. This means that the parcel is now free to continue rising without the need of any additional energy input from the environment - hence it is "free" to continue convecting.

These preceding definitions are crucial elements in describing atmospheric dynamics.

Another important process involving horizontal transport of air masses is the sea (land) breeze. The same basic process can also be superimposed on, for example, large scale frontal systems arriving in coastal regions.

The sea (land) breeze is the notation for a horizontal process leading to a change of the vertical temperature profile. The process itself can be superimposed by for example large scale frontal systems arriving in coastal regions, however this process still takes place. **Sea (and land) breezes** are caused by unequal heating and cooling of adjacent land and sea surfaces. A sea breeze is wind with its direction from the sea to the land (and vice versa for the land breeze) in consequence of this differential heating.

The warmed air rises over the land surface, and a local circulation commences, with cool air from the sea being drawn in over the land. At the same time the ascending air returns seaward in what is known as the upper return current (Figure 9).

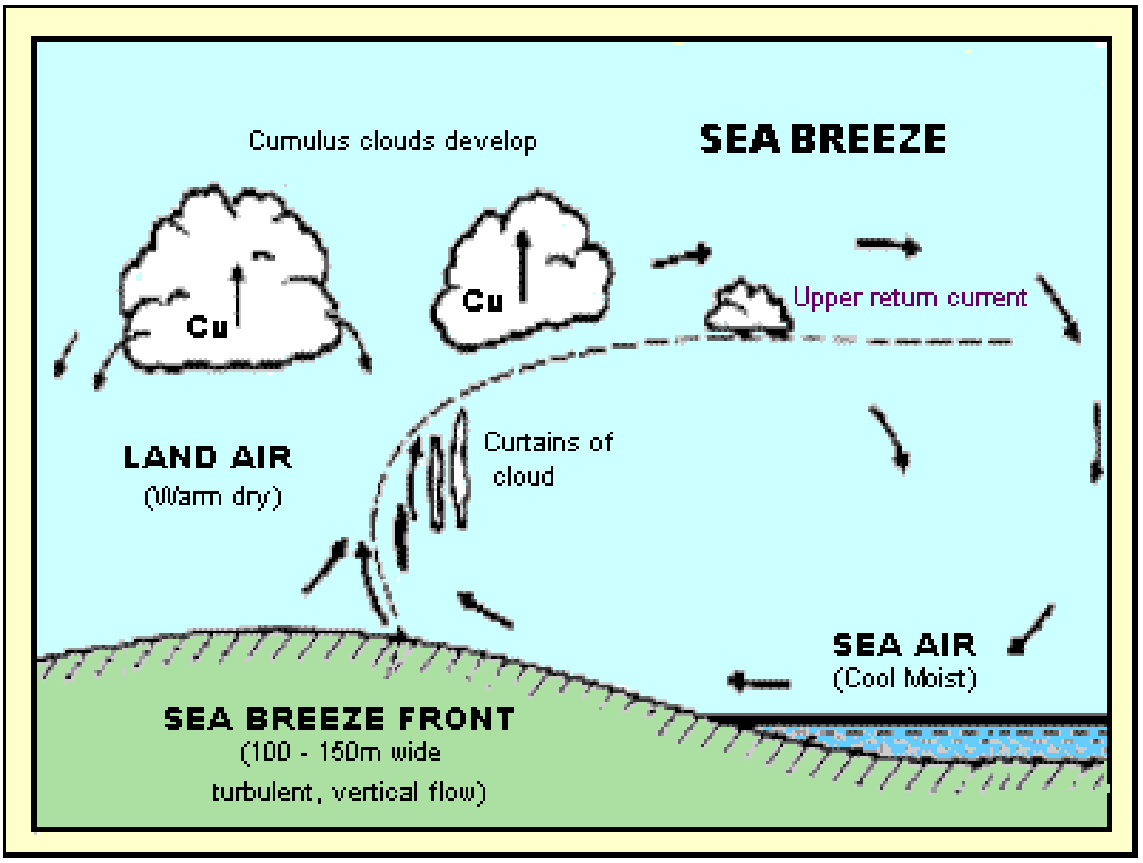

Figure 9: Schematic picture of a sea breeze circulation [Batt, 1995].

With weak general wind circulations (around the centre of a high for example), a sea breeze (pure sea breeze) moves over the coastline soon after the land temperature has exceed the sea temperature (late morning to early afternoon). As the difference increases, the sea breeze becomes stronger and extends farther inland. It also increases in depth from about 100 metre to as much as 450 to 800 metre in a well developed breeze. Maximum wind speed occurs a few hours after the maximum temperature is reached, generally during the mid to the late afternoon.

A weak sea breeze dies away soon after sunset, but a better developed sea breeze persists at the coast till 8 to 10 pm., usually dying away fairly suddenly at the coast and slowly moving seawards as a cut-off sea breeze circulation.

With stronger general wind circulations, coupled with the required temperature gradient, the development of the sea breeze becomes complicated. For example, a moderate to strong prevailing off-shore surface wind can delay the onset of the sea breeze. If strong enough, it can even prevent the sea breeze from developing at all. On-shore surface winds are generally enhanced by the sea breeze component.

2.1.2.2 Free atmosphere

The free atmosphere is commonly defined as the part of the atmosphere where the effect of the Earth's surface friction on air motion is negligible. The base of the free atmosphere usually taken as the point where the wind becomes geostrophic, or the top of the ABL.

2.1.2.3 Stratospheric/tropospheric exchange

The **stratospheric/tropospheric exchange (STE)** received attention in the early 1960's when radioactive fallout from atmospheric nuclear test explosions became a major concern. The tropopause was expected to be impermeable at that time. However, the presence of different trace gases (e.g. H_2O, SO_2, CH_4, CO, etc.) within the stratosphere, which are primarily found in the troposphere, suggested that an upward flux towards the stratosphere of intruding anthropogenic and natural chemical constituents was occurring, which could therefore lead to global effects on the radiative balance and budget of different trace gases [Junge, 1962]. For example, the transport of chlorofluorocarbons into the stratosphere leads to O_3 destruction [Molina and Rowland, 1974].

Furthermore, the exchange between stratosphere and troposphere does not only occur in an upward direction. Conversely, the STE represents an important source of tropospheric O_3. This is achieved by entrainment from the stratosphere into the troposphere and contributes significantly to the removal of many other stratospheric species.

The intrusion of stratospheric air into the troposphere is largest where the Hadly cell meets the Ferrel cell, i.e. the border between the tropics and the extratropics (Figure 10).

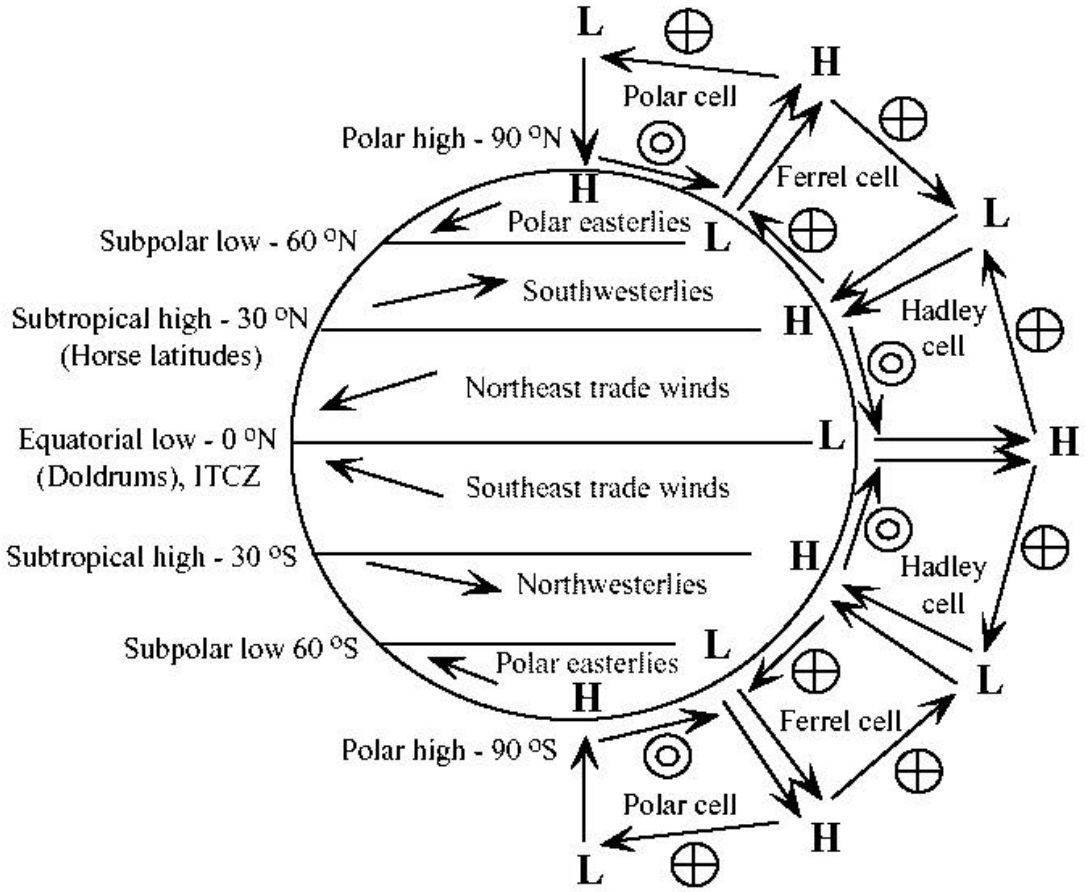

Figure 10: Global circulation cells and winds [Jacobson, 1998a].

The STE is pronounced as large latitudinal displacements occur. The shaded area in Figure 11 shows the region within the lower stratosphere most directly affected by these large scale motions. The STE mechanism is a cycle (Figure 11) in which tropospheric air at the inter tropospheric convergence zone (ITCZ) is lifted by cumulus convective turrets. The latent heat energy gained through condensation enables air parcels to penetrate into the stratosphere. Within the stratosphere the air of the lower tropical stratosphere is sucked by the extratropical stratosphere and transported towards the polar regions. Large scale subsidence and tropopause folding offers a thin band of stratospheric air the opportunity to enter into the troposphere along strongly tilted isentropes. Part of the stratospheric air in the fold returns reversibly to the stratosphere and part is drawn irreversibly into the troposphere [Holton et al., 1995]. Much of the O_3 transport from the lowermost stratosphere into the troposphere is believed to occur in connection with tropopause folding events.

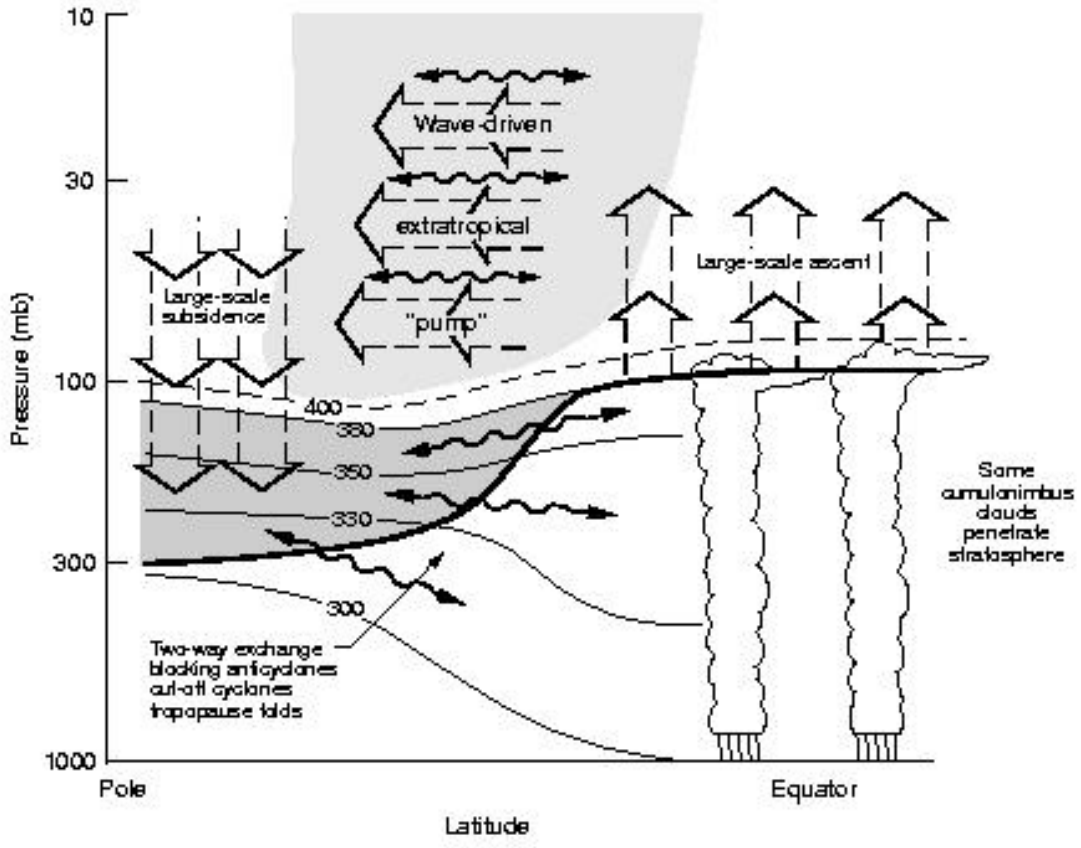

Figure 11: Dynamical aspects of stratosphere–troposphere exchange. The tropopause is shown by the thick line. Thin lines are isentropic or constant potential temperature surfaces labelled in Kelvin. The heavily shaded region is the "lowermost stratosphere" where isentropic surfaces span the tropopause and isentropic exchange by tropopause folding occurs. The region above the 380 K surface is the "overworld", in which isentropes lie entirely in the stratosphere. Light shading in the overworld denotes wave-induced forcing (the extratropical "pump"). The wiggly double headed arrows denote meridional transport by eddy motions, which include tropical upper-tropospheric troughs and their cut off cyclones as well as their midlatitude counterparts including folds. Not all eddy transports are shown; and the wiggly arrows are not meant to imply any two-way symmetry. The broad arrows show transport by the globalscale circulation, which is driven by the extratropical pump. This global-scale circulation is the primary contribution to exchange across isentropic surfaces (e. g. the ~380 K surface) that are entirely in the over world [Holton et al., 1995].

2.2 Chemistry of the troposphere

The Chapter focuses on the tropospheric photochemistry relevant for this study. In subsection (2.2.1) the "clean" atmosphere is described. The assumption of a nitrogen oxides (NO_x) free troposphere, although hypothetical, is used to emphasize the dominant reactions in the marine boundary layer (MBL) and to illustrate the differences with the polluted atmosphere.

In the second subsection (2.2.2) the photochemical production of tropospheric ozone is outlined. This includes the discussion of the interaction of nitrogen oxide (NO) and nitrogen dioxide (NO_2) with radicals, the oxidising steps of the NMHC, and the reactions of radicals and O_3.

2.2.1 Chemistry of the clean marine troposphere

This chapter describes the chemistry of the "clean" (free of nitrogen oxides) boundary layer. As the chemistry of the troposphere is dominated by highly complex reaction chains, the reactions are thematically separated.

2.2.1.1 Hydroxyl radical (OH)

The photochemical reactions of ozone and the production of OH belong to the most important processes in the atmosphere. Ozone absorbs energy from the sunlight over a large spectral region. In the visible and ultraviolet spectral region the ozone molecule is photodissociated into an oxygen molecule and an oxygen atom. The photodissociation is here, for reasons of simplicity, divided into two different wavelength regions. In the first case the resultant oxygen atom is in the electronic ground state ($O(^3P)$) whereas in the second case the atom is in the first excited state ($O(^1D)$).

$$O_3 + h\nu \left(\lambda < 420nm \right) \rightarrow O\left(^3P \right) + O_2 \quad (13)$$

$$O_3 + h\nu \left(\lambda < 320nm \right) \rightarrow O\left(^1D \right) + O_2\left(^1\Delta \right) \quad (14)$$

In practice the $O(^3P)$ atoms in the troposphere react completely with O_2 to form O_3.

$$O\left(^3P \right) + O_2 + M \rightarrow O_3 + M \quad (15)$$

The excited oxygen atoms ($O(^1D)$) are mainly quenched into the ground state (^3P) through collision with air molecules (M) (78% nitrogen (N_2); 21% oxygen (O_2)). The residue react with water (H_2O) to form hydroxy radicals (OH).

$$O(^1D) + N_2 \rightarrow O(^3P) + N_2 \quad (16)$$

$$O(^1D) + O_2 \rightarrow O(^3P) + O_2 \quad (17)$$

$$O(^1D) + H_2O \rightarrow OH + OH \quad (18)$$

The rate of production of OH radicals depends on the relative rates of the reactions (16) (17), and (18). The branching ratio can be determined as follows:

$$a_{(2.4),(2.5),(2.6)} = \frac{k_{(2.6)} \cdot [H_2O]}{k_{(2.6)} \cdot [H_2O] + k_{(2.4)} \cdot [N_2] + k_{(2.5)} \cdot [O_2]} \approx 7m[H_2O] \quad (19)^6$$

where $\mu[H_2O]=[H_2O]/[M]$, H_2O is the vapour mixing ratio and M the total number of molecules per volume.

In the case of an atmospheric H_2O mixing ratio of ~ 1% (which corresponds to 50% relative humidity (r.h.) at 20°C) around 10% of the $O(^1D)$ atoms react with H_2O to form OH.

The significance of the OH radical in the chemical composition of the troposphere is caused by its high reactivity with nearly all gases that are emitted into the atmosphere by natural and/or anthropogenic activities.

For example, the reaction of OH with hydrocarbons, carbon monoxide (CO), the most abundant sulphuric and partially halogenated compounds, and nitrogen dioxide (NO_2) represents the most dominant loss process for these trace gases. As a consequence the lifetime of a large amount of trace gases is defined by their reactivity with OH.

This lifetime varies between a few hours for gases like e.g. isoprene (C_5H_8) or NO_x (= NO + NO_2), to 1-2 months for CO and ~ 10 years for methane (CH_4). In the troposphere there are several trace gases that do not react with OH, like e.g. chloro

[6] From the reactions (14) and (16)-(18), it is possible to estimate the average residence time of O_3 in the clean troposphere. The reaction of the $O(^1D)$ atoms with H_2O (equation (19)) leads to a net O_3 destruction of 0.2 ozone molecules for every absorbed photon with a wavelength below 320 nm and maximum r.h. (i.e. $\mu(H_2O)\approx 3\%$ under normal conditions). The half-life of O_3 is ~4 days considering a daily averaged photolysis frequency of $j_{(O(^1D))}$ of $1 \cdot 10^{-5}$ s^{-1} (middle latitude, summer). The photochemical lifetime in the free troposphere with significantly reduced H_2O vapour mixing ratios increases to several weeks.

fluorocarbons ($CFCl_3$, CF_2Cl_2) and N_2O, these gases can reach the stratosphere and disturb the chemistry there e.g., Molina and Rowland [1974].

2.2.1.2 Peroxy radicals (RO_2^*)

Production of RO_2^*

The peroxy radicals $\left(RO_2^* = HO_2 + \sum_i R_i O_2 \right)$ play a comparable role in the chemistry of the troposphere to the OH radical, although they are not as reactive. They achieve their importance in the MBL chemistry by destroying O_3. In addition, they are the key intermediates in the oxidation of long lived species and the production of peroxides and formaldehyde.

The production of RO_2^* radicals takes place in the marine troposphere mainly via the oxidation of CO and CH_4 by the OH radical produced in reaction (18).

$$OH + CO \rightarrow H + CO_2 \qquad (20)^7$$

$$OH + CH_4 \rightarrow CH_3 + H_2O \qquad (21)$$

Around 60% of the OH radicals react in the unpolluted atmosphere with CO (90 ppbv, typical value in the remote northern hemisphere (NH)) and 40% with CH_4 (1,8 ppmv, average of the NH) [Gautrois et al., 1998]. In both reactions radicals are formed which react with O_2 to form RO_2^* radicals.

$$H + O_2 + M \rightarrow HO_2 + M \qquad (22)$$

$$CH_3 + O_2 + M \rightarrow CH_3O_2 + M \qquad (23)$$

---

[7] The oxidation of CO with OH is one of the most important reactions in the tropospheric chemistry. The reaction shows some interesting kinetic features, which have to be taken into account, while developing a tropospheric model. First, the temperature dependence of the reaction differs significantly from the Arrhenius theory. The activation energy is close to zero at temperatures below 300 K. Secondly, the kinetic constant of the reaction is pressure dependent, and the reaction rate coefficient increases with increasing pressure. A possible explanation of this kinetical behaviour is the formation of a HOCO complex in a discrete substep of the reaction:

$CO + OH \rightleftharpoons HOCO^*$ (a)

$HOCO^* \rightarrow H + CO_2$ (b)

$HOCO^* + M \rightleftharpoons HOCO + M$ (c)

$HOCO + O_2 \rightarrow HO_2 + CO_2$ (d)

Reaction (c) followed by (d) leads to the possibility of a pressure dependent reaction path, which is not resulting into the products H + CO_2 from reaction (20). This reaction path takes place in the presence of O_2. The reaction (a) is favoured at low temperature, leading to a slightly negative temperature dependence of the reaction rate constant.

Loss of RO_2^*

The RO_2^* are key intermediates in the photochemical processes generating peroxides (e.g. H_2O_2 and CH_3O_2H) and in the subsequent production of HCHO. The loss reactions of HO_2 and CH_3O_2 produce peroxides via reactions (24) and (25).

$$HO_2 + HO_2 \rightarrow H_2O_2 + O_2 \quad (24)$$

$$HO_2 + CH_3O_2 \rightarrow CH_3O_2H + O_2 \quad (25)$$

The reactions (26), (27), and (28) are radical loss reactions of minor importance, since the CH_3O_2 self reactions ((26) and (27)) have reaction rate coefficients one order of magnitude smaller than the HO_2 self reaction. However, the CH_3O_2 concentration can be significantly higher than the concentration of HO_2, and consequently gain importance.

$$CH_3O_2 + CH_3O_2 \rightarrow HCHO + CH_3OH + O_2 \quad (26)$$

$$CH_3O_2 + CH_3O_2 \rightarrow 2 \cdot CH_3O + O_2 \quad (27)$$

$$CH_3O_2 + OH \rightarrow CH_3OH + O_2 \quad (28)$$

The reaction pathways of radicals are highly complicated, and for simplicity only the most important pathways are shown. The methoxy radicals (CH_3O) and the hydroxymethyl radicals (CH_2OH) react with O_2 to form formaldehyde (HCHO) and HO_2 (see reactions (29) und (31)). The methanol (CH_3OH) can react with an OH radical (see reactions (30) and (31)) and therefore produce HCHO and HO_2.

$$CH_3O + O_2 \rightarrow HCHO + HO_2 \quad (29)$$

$$OH + CH_3OH \rightarrow H_2O + CH_2OH \quad (30)$$

$$CH_2OH + O_2 \rightarrow HO_2 + HCHO \quad (31)$$

The peroxides are a reservoir for radicals when they photodissociate (see reactions (32) and (33)), this means that they are neutral referring to the radical balance (i.e. they produce radicals back). Net losses of radicals are caused by the reactions of the peroxides with OH ((34), (35), and (36)). In these reactions are up to two radicals lost.

$$H_2O_2 + h\nu \rightarrow OH + OH \quad (32)$$

$$CH_3O_2H + h\nu \rightarrow HCHO + H + OH \quad (33)$$

$$H_2O_2 + OH \rightarrow HO_2 + H_2O \quad (34)$$

$$CH_3O_2H + OH \rightarrow CH_3O_2 + H_2O \quad (35)$$

$$CH_3O_2H + OH \rightarrow HCHO + OH + H_2O \quad (36)^8$$

The photolysis frequencies $j_{(H_2O_2)}$ and $j_{(CH_3O_2H)}$ are in the same order of magnitude as the reaction rate coefficients ($k_{(34),\,(35),\,(36)}$) for the reaction with OH.

The dry and wet deposition rates of peroxides are high. This is especially true for the hydroperoxide being hydrophilic. The wash out of hydroperoxides is an important loss process for radicals in the troposphere.

2.2.1.3 Formaldehyde (HCHO)

Since the HCHO represents a similar reservoir substance as the peroxides, the HCHO reactions are of special interest for radicals. HCHO reacts with OH, decomposes, and photolyses in the same manner as the peroxides. The photolysis rate $j_{(HCHO)}$ is about one order of magnitude higher than the photolysis frequency of H_2O_2 $j_{(H_2O_2)}$. The reaction rate coefficient of the reaction (37) of HCHO and OH is ~ 5 times higher than the respective value for the H_2O_2 reaction (34). The resultant lifetime of HCHO is one order of magnitude lower than the lifetime of H_2O_2 and amounts to a few hours during daytime.

$$HCHO + OH \rightarrow CHO + H_2O \quad (37)$$

$$HCHO + h\nu \rightarrow H_2 + CO \quad (38)$$

$$HCHO + h\nu \rightarrow H + CHO \quad (39)$$

The subsequent products of the oxydation and the photolysis of HCHO further react as follows:

$$CHO + O_2 \rightarrow HO_2 + CO \quad (40)$$

$$H_2 + OH \rightarrow H_2O + H \quad (41)$$

The photochemical processes of HCHO form radicals and can positively influence the radical balance (39).

[8] The reaction (36) involves two steps: First an intermediate product CH_3OOH is formed, which under typical atmospheric conditions decomposes very rapidly into HCHO and OH.

2.2.1.4 Radical balance

Figure 12 shows the most important pathways of the radical reactions in the NO_x free troposphere. Mechanisms leading to both recycling and net losses of radicals are represented.

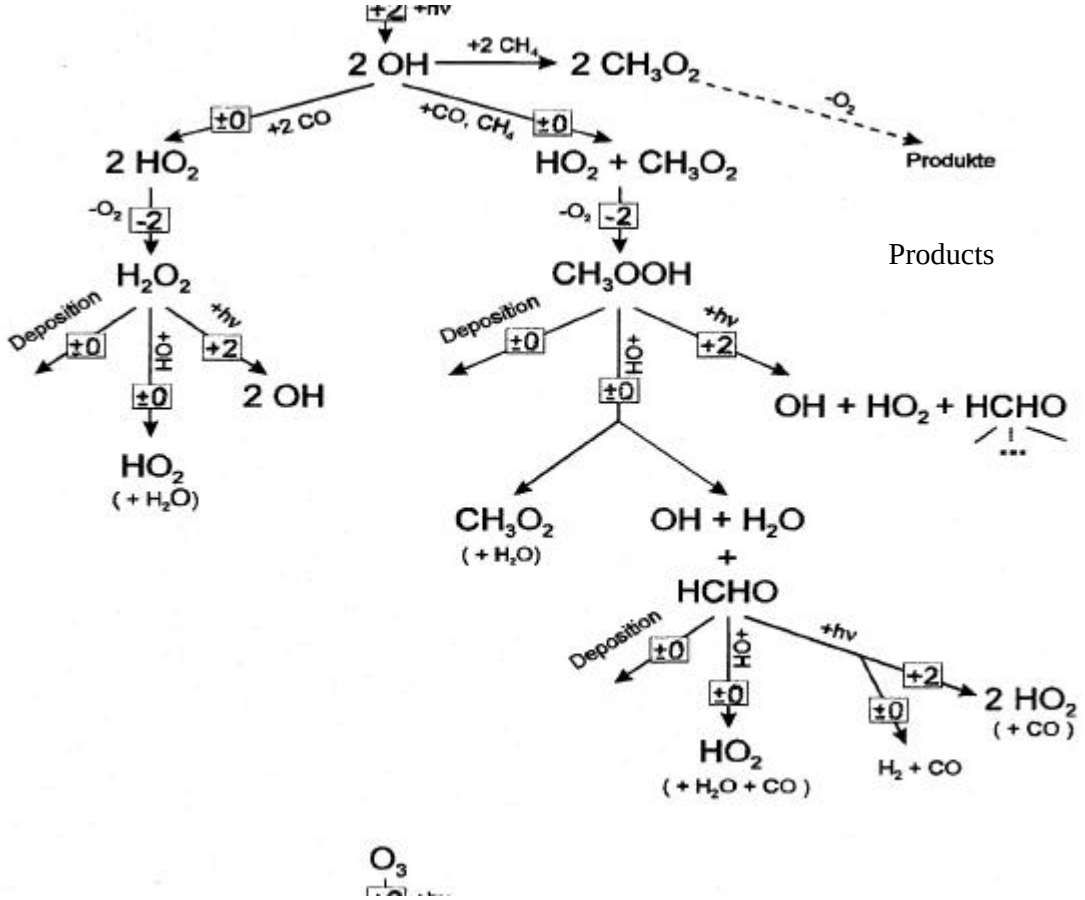

Figure 12: O_3 loss and radical chemistry in a NOx free atmosphere. The Figure shows the radical balance of two initially produced OH radicals. The numbers in the boxes indicate the change of the number of free radicals [Schultz et al., 1996].

2.2.1.5 Ozone (O_3)

The analysis of ozone and radical loss processes in marine areas has recently received attention within the scientific community. High daytime O_3 losses have been observed over the ocean [Dickerson et al., 1999]. In the Indian Ocean e.g. O_3 losses of up to 50% and minimum O_3 mixing ratios around 5 ppbv in the MBL have been observed [Stehr et al., 2002]. There still remains considerable speculation about the processes possibly explaining the observations.

The dominant first order loss processes for O_3 during daytime are the photolysis, the dry deposition, and the reaction with OH and HO_2 (assuming NO_x, and halogen free conditions). When trying to determine the significance of these primary losses of O_3 it is assumed that the back reaction of $O(^3P)$ with O_2 proceeds instantaneously. This implies that the photolytical losses are equivalent to the production of OH through reaction (18).

$$OH + O_3 \rightarrow HO_2 + O_2 \quad (42)$$

$$HO_2 + O_3 \rightarrow OH + 2 \cdot O_2 \quad (43)$$

$$O_3 + h\nu \left(l < 320nm \right) \rightarrow O\left(^1D \right) + O_2 \quad (14)$$

Revering to the radical balance (Figure 12) the reactions (42) and (43) are neutral, because the radicals interconvert themselves while transforming O_3 to O_2.

HO_x(=OH+HO_2)-cycle:

$$OH + O_3 \rightarrow HO_2 + O_2 \quad (42)$$

$$\underline{HO_2 + O_3 \rightarrow OH + 2 \cdot O_2} \quad (43)$$

net: $$2 \cdot O_3 \rightarrow 3 \cdot O_2$$

The reaction chain is only terminated by radical-radical reactions. The following loss reactions are dominant for the HO_x cycle under NO_x free atmospheric conditions:

$$OH + OH \rightarrow H_2O + O\left(^3P \right) \quad (44)$$

$$OH + OH \rightarrow H_2O_2 \quad (45)$$

$$OH + HO_2 \rightarrow H_2O + O_2 \quad (46)$$

$$HO_2 + HO_2 \rightarrow H_2O_2 + O_2 \quad (47)$$

From the above mentioned reactions the net balance equation for O_3 related to HO_x results:

Cycle A:

$$O_3 + hn\,(l < 420nm) \rightarrow O(^3P) + O_2 \quad (13)$$

$$O(^1D) + N_2 \rightarrow O(^3P) + N_2 \quad (16)$$

$$O(^1D) + O_2 \rightarrow O(^3P) + O_2 \quad (17)$$

$$3 \cdot \left(O(^3P) + O_2 + M \rightarrow O_3 + M\right) \quad (15)$$

$$2 \cdot \left(HO_2 + O_3 \rightarrow OH + 2 \cdot O_2\right) \quad (43)$$

$$2 \cdot \left(OH + O_3 \rightarrow HO_2 + O_2\right) \quad (42)$$

$$2 \cdot \left(OH + CO \rightarrow H + CO_2\right) \quad (20)$$

$$2 \cdot \left(H + O_2 + M \rightarrow HO_2 + M\right) \quad (22)$$

$$3 \cdot \left(O_3 + hn\,(l < 320nm) \rightarrow O(^1D) + O_2\right) \quad (14)$$

net: $$3 \cdot O_3 + CO \rightarrow 4 \cdot O_2 + CO_2$$

Cycle A has a negative effect on the O_3 balance, three O_3 molecules and one CO molecule are converted into four O_2 molecules and one CO_2 molecule.

2.2.1.6 Methane (CH_4)

The variety of possible reaction pathways for the oxydation of methane clearly shows the complexity of the chemistry even in remote unpolluted areas. Each possible reaction pathway, starting from the top of

Figure 13 to the bottom describes the influence on the O_3 and radical balance. It is difficult to identify which pathway is predominant because the absolute reaction rates variing throughout the day.

Cycle B:

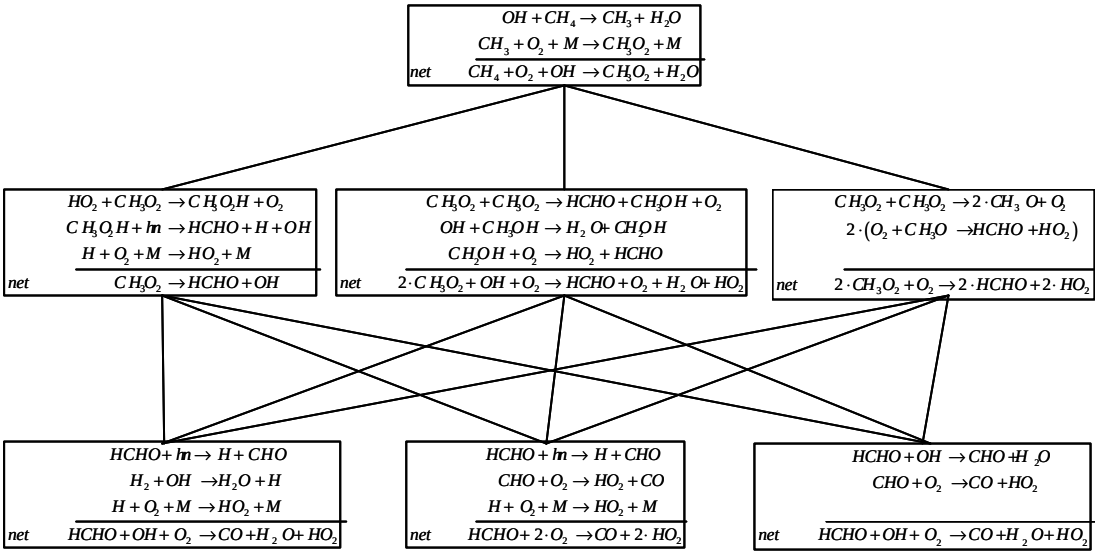

Figure 13: Net cycles for the possible oxidation pathways of methane.

2.2.1.7 Non methane hydrocabons (NMHC)

In the chemistry of the remote MBL the oxydation of the NMHC can in a first approximation be considered as negligible. In spite of their partially higher reactivity, the NMHC have no important influence on the chemistry because their concentrations are significantly lower than the concentrations of CH_4 [Rudolph and Johnen, 1990]. The discussion of the reactions involving NMHC has been deferred to chapter 2.2.2 focusing on the chemistry of polluted atmospheres, where they play an important role.

2.2.1.8 Halogens (Br, Cl, I)

Several hypothesis regarding the possible noticeable influence of halogens on the photochemistry of the MBL have been reported in the literature [e.g. Keene et al., 1990, Pszenny et al., 1993, Fan and Jacob, 1992, Finlayson-Pitts, 1993, Parrish et al., 1993, McKeen and Liu, 1993, Graedel and Keene, 1995, Keene et al., 1996, Ariya et al., 1998].

Vogt et al. [1996], Sander and Crutzen [1996], and Sander et al. [1997] have concluded from observations of O_3 losses, which cannot be explained by the known chemistry, that another loss cycle is needed. The cycle should not involve high NO_x concentrations, because the O_3 losses have been observed in remote regions without anthropogenic sources.

They proposed a cycle removing O_3 as follows:

$$Br + O_3 \rightarrow BrO + O_2 \quad (48)$$

$$BrO + HO_2 \rightarrow HOBr + O_2 \quad (49)$$

$$\underline{HOBr + h\nu \rightarrow OH + Br} \quad (50)$$

net: $$O_3 + HO_2 \rightarrow OH + 2 \cdot O_2$$

In recent laboratory experiments the formation of Br_2 through the reaction of sodium bromide (NaBr) particles was reported by Hirokawa et al. [1998]. Spicer et al. [1998] observed relevant amounts of Cl_2 and Br_2 during the night, however there still remain large uncertainties over the origin and the whereabouts of the tropospheric halogens.

One possibility for the origin of Br was postulated by Vogt et al. [1996]. They propose an auto catalytic mechanism for the emission of halogens from sea salt aerosols into the gas phase. The mechanism is initiated by the adsorption of HOBr in the gas phase on aerosols, which is then converted into hydrophobic BrCl and Br_2 (Figure 14). Afterwards the BrCl and Br_2 turn into the gaseous phase.

$$HOBr + Cl^- + H^+ \rightleftharpoons BrCl + H_2O \quad (51)$$

$$BrCl + Br^- \rightleftharpoons Br_2Cl^- \quad (52)$$

$$Br_2Cl^- \rightleftharpoons Br_2 + Cl^- \quad (53)$$

$$Br_2 + h\nu \rightarrow 2Br \quad (54)$$

$$2 \cdot (Br + O_3 \rightarrow BrO + O_2) \quad (48)$$

$$\underline{2 \cdot (BrO + HO_2 \rightarrow HOBr + O_2)} \quad (49)$$

net: $$2HO_2 + H^+ + 2O_3 + Br^- + h\nu \rightarrow HOBr + 4O_2 + H_2O$$

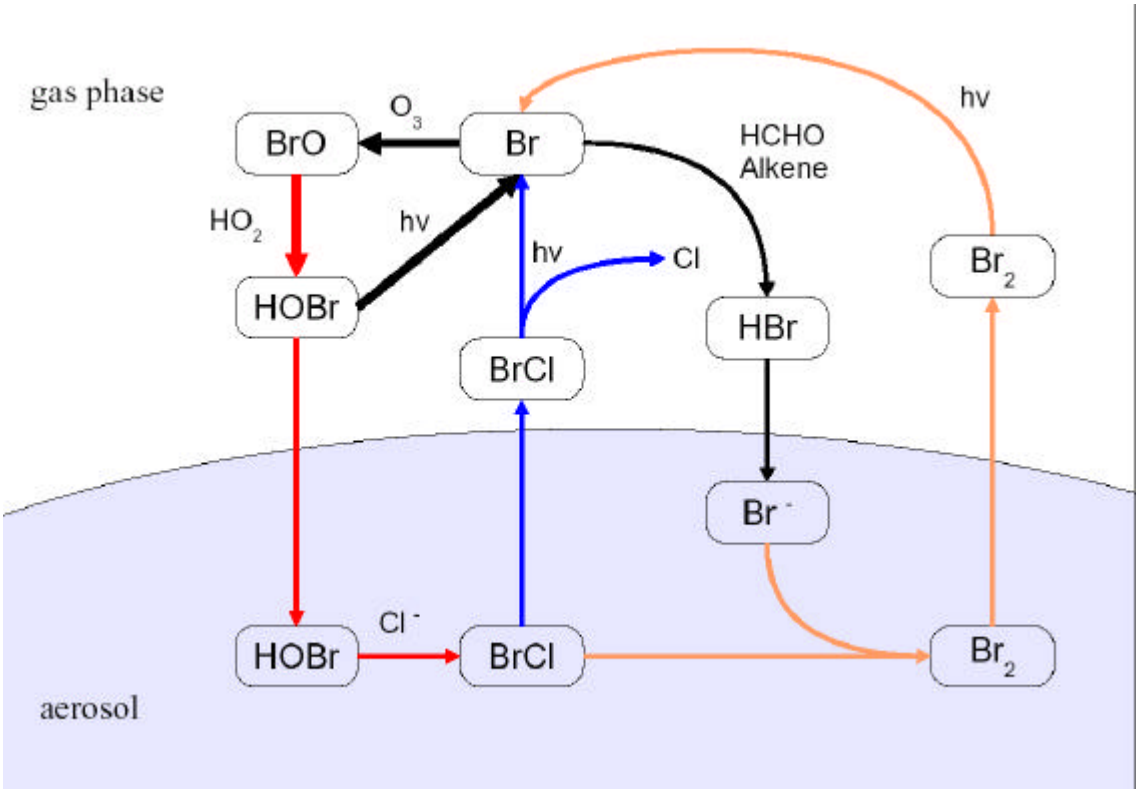

Figure 14: A simplified scheme of the bromine cycling between homogeneous and heterogeneous phase [Color image adapted from Sander and Crutzen, 1996].

The most recent atmospheric models reveal that larger amounts of Cl radicals are unlikely, because their presence would reduce the hydrocarbon concentrations to levels unrealistically low [Finlayson-Pitts, 1993, Parrish et al., 1993, McKeen and Liu, 1993, Graedel and Keene, 1995, Wingenter et al., 1996]. Conversely, the observed amounts of HCHO [Wagner et al., 2001, 2002], the observed isotopic fractionation of CH_4 [Allan et al., 2001], and the diurnal evolution of the RO_2^* concentration [Burkert et al., 2003a] suggest that the presence of low amounts of Cl are responsible for the differences between measurements and calculations.

The presence of both chlorine and bromine is predicted to come from sea salt aerosols by the MOCCA model [Sander and Crutzen, 1996, Dickerson et al., 1999, Vogt et al., 1996]. Others have speculated that Cl can be generated from sea salt particles in the presence of sufficient amounts of NO_2, N_2O_5 or $ClONO_2$ with reactions (57) and (58) [Finlayson-Pitts, 1993, Graedel and Keene, 1995, Vogt et al., 1996].

$$2NO_{2(g)} + NaCl_{(s)} \rightarrow ClNO_{(g)} + NaNO_{3(s)} \quad (55)$$

$$2NO_{2(g)} + NaBr_{(s)} \rightarrow BrNO_{(g)} + NaNO_{3(s)} \quad (56)$$

$$N_2O_{5(g)} + NaCl_{(s)} \rightarrow ClNO_{2(g)} + NaNO_{3(s)} \quad (57)$$

$$ClONO_{2(g)} + NaCl_{(s)} \rightarrow Cl_{2(g)} + NaNO_{3(s)} \quad (58)$$

Photolysis then generates chlorine atoms, e.g.

$$ClNO_2 + h\nu \rightarrow Cl + NO_2 \quad (59)$$

$$Cl_2 + h\nu \rightarrow 2Cl \quad (60)$$

An alternative potential explanation for the presence of significant amounts of Cl in the atmosphere is by the enhanced emissions of halogenated carbon compounds such as CH_3Cl in coastal regions. The Cl is produced through the following oxidation pathways.

$$CH_3Cl + OH \rightarrow CH_2Cl + H_2O \quad (61)$$

$$CH_2Cl + O_2 + M \rightarrow CH_2ClO_2 + M \quad (62)$$

$$CH_2ClO_2 + NO \rightarrow CH_2ClO + NO_2 \quad (63)$$

$$CH_2ClO + O_2 \rightarrow CHOCl + HO_2 \quad (64)$$

$$CH_2ClO_2 + HO_2 \rightarrow CH_2ClOOH + O_2 \quad (65)$$

$$CH_2ClO_2 + RO_2 \rightarrow CH_2ClO + RO + O_2 \quad (66)$$

$$CH_2ClO_2 + RO_2 \rightarrow CHOCl + ROH + O_2 \quad (67)$$

$$CH_2ClO_2 + RO_2 \rightarrow CH_2ClOH + R'(R' = R_{H-1})O + O_2 \quad (68)$$

$$CH_2ClOOH + OH \rightarrow CH_2ClO_2 + H_2O \quad (69)$$

$$CH_2ClOOH + OH \rightarrow CHOCl + OH + H_2O \quad (70)$$

$$CH_2ClOOH + h\nu \rightarrow CH_2ClO + OH \quad (71)$$

$$CHOCl + OH \rightarrow CO + Cl + H_2O \quad (72)$$

$$CHOCl + h\nu \rightarrow CO + Cl + H \quad (73)$$

$$CH_2ClOH + OH + O_2 \rightarrow CHOCl + HO_2 + H_2O \quad (74)$$

Several studies [Khalil and Rasmussen, 1999, Moore et al., 1996] have shown that the ocean is not a significant source CH_3Cl. However, Yokouchi et al. [2000]

observed up to 2100 pptv of CH_3Cl on islands in the tropics, but these high mixing ratios might be related to emissions from forested land.

Cl reacts in the same way as Br with O_3 and leads through its catalytic cycle to a net loss of O_3. In addition, the reaction rate coefficient of Cl with O_3 is one order of magnitude higher compared to the equivalent for Br.

The **iodine (I)** halogen is supposed to be dominantly emitted via biological activities as a hydrocarbon complex [Cicerone, 1981, Rasmussen et al., 1982, Singh et al., 1983, Class and Ballschmiter, 1988, Carlier et al., 1991, Reifenhäuser and Heumann, 1992, Schall and Heumann, 1993, Carpenter et al., 1998]. The emission is strongly dependent on the tide and therefore higher amounts of I are expected in coastal regions [Carpenter et al., 1999, 2000]. By contrast to Br and Cl halogens, I is supposed not to be produced by heterogeneous chemistry on aerosols. However, Vogt et al. [1999] suggested that I compounds partly go into the aqueous phase, but are cycled back. There remain many unknowns about the reactions and sources producing I atoms. However, I contributes to the loss of O_3. Three catalytic cycles are proposed, first by Chameides and Davis [1980] for low I concentrations.

Cycle 1:

$$I + O_3 \rightarrow IO + O_2 \tag{75}$$

$$IO + HO_2 \rightarrow HOI + O_2 \tag{76}$$

$$\underline{HOI + h\nu \rightarrow OH + I} \tag{77}$$

net: $$O_3 + HO_2 \rightarrow OH + 2 \cdot O_2$$

The IO self reaction becomes more important at higher iodine concentrations and the reaction cycle changes [Chameides and Davis, 1980, Chatfield and Crutzen, 1990, Jenkin, 1992].

Cycle 2:

$$2\left(I + O_3\right) \rightarrow 2\left(IO + O_2\right) \tag{75}$$

$$IO + IO \rightarrow 2I + O_2 \tag{78}$$

$$IO + IO \rightarrow I_2O_2 \tag{79}$$

$$\underline{I_2O_2 + h\nu \rightarrow 2I + O_2} \tag{80}$$

net: $$2O_3 \rightarrow 3O_2$$

The third catalytic cycle suggested by Solomon et al. [1994] needs higher amounts of BrO to recycle IO.

Cycle 3:

$$I + O_3 \rightarrow IO + O_2 \tag{75}$$

$$Br + O_3 \rightarrow BrO + O_2 \tag{48}$$

$$BrO + IO \rightarrow Br + I + O_2 \tag{81}$$

net: $$2O_3 \rightarrow 3O_2$$

2.2.1.9 Influence of halogens and radicals on the O_3 balance

Considering the above mentioned reaction paths, the chemical and photolytical reactions lead to a depletion of O_3 in the NO_x free atmosphere. Exemplary, the case of Br is considered, the loss processes by Cl and I can be treated in the same way.

The temporal variation of O_3 can be calculated with equation (82).

$$\begin{aligned}\frac{d[O_3]}{dt} = {} & k_{(2.3)}\left[O\left(^3P\right)\right][O_2] - k_{(2.12)}[HO_2][O_3] - k_{(2.11)}[OH][O_3] \\ & - k_{(2.33)}[Br][O_3] - j\left(O\left(^1D\right)\right)[O_3] - j\left(O\left(^3P\right)\right)[O_3]\end{aligned} \tag{82}$$

Assuming that reaction (15) proceeds instantaneously the equation (82) can be approximated to

$$\frac{d[O_3]}{dt} = -k_{(2.12)}[HO_2][O_3] - k_{(2.11)}[OH][O_3] - k_{(2.34)}[Br][O_3] - a_{(2.4),(2.5),(2.6)} \cdot j\left(O\left(^1D\right)\right)[O_3].$$

Another loss process for O_3 not yet quantified is the dry and wet deposition on surfaces, see Ganzeveld and Lelieveld [1995].

The importance of the different loss processes of O_3 is illustrated in chapter 4.3.3.1, where losses of relevant trace gases are quantified.

2.2.2 Chemistry of the polluted troposphere

In contrast to the chemistry of the marine troposphere, described in chapter 2.2.1, reactions involving nitrogen oxides are of great relevance in polluted atmospheres (i.e. NO_x > 40pptv). These reactions lead to O_3 production and are responsible for the formation of e.g. nitrates. Under special topographical and meteorological circumstances the O_3 mixing ratios can reach extremely high values in the lower troposphere. The first evidence was found while investigating the summer smog phenomena in Los Angeles [Haagen-Smit, 1952, Cadle and Johnston, 1952].

2.2.2.1 Nitrogen oxides (NO, NO_2)

The reactive molecules NO and NO_2 play a key role in the photochemistry of O_3. The main source of NO_x (=NO+NO_2) in the troposphere is anthropogenic (~80%) [Müller, 1992], with 20% originating naturally from plants, surface emissions, and from lightning [Dickerson, 1984, Galbally et al., 1985, Kaplan et al., 1988, Williams et al., 1992].

Nitrogen oxide emissions consist mainly (>90%) of NO, especially in urban areas with high traffic events („rush hours“) with high concentrations of NO_x being observed in the early morning. The NO reacts rapidly with O_3 to form NO_2. Therefore high NO concentrations are accompanied with high NO_2 concentrations, when sufficient amounts of O_3 are present.

$$NO + O_3 \rightarrow NO_2 + O_2 \qquad (83)$$

The lifetime τ of NO can be calculated in a first approach from the reaction rate coefficient for reaction (83) and an O_3 mixing ratio. A typical mixing ratio for the polluted lower troposphere is 60 ppbv leads to $\tau \sim 34$s.

$$t = \frac{1}{k_{(2.43)}[O_3]},$$

During the night the reaction (83) represents a net sink for O_3, because the subsequent reactions (described in chapter 2.2.2.2), are the initiators for the so called "nighttime chemistry” and they lead to additional losses of the produced NO_2. This is in contrast to the NO_2 produced during the day, which is immediately photodissociated to form a NO molecule back. In addition an O atom in the electronical ground state (^{3}P) is produced, reacting together with O_2 back to form an O_3 molecule (15).

$$NO_2 + h\nu\,(315nm < l < 420nm) \rightarrow NO + O\left(^3P\right) \quad (84)$$

$$O\left(^3P\right) + O_2 + M \rightarrow O_3 + M \quad (15)$$

2.2.2.1.1 Photostationary state (PSS)

The photolysis frequency $j_{(NO_2)}$ from reaction (84) reaches values up to $1{\cdot}10^{-2}\,s^{-1}$ (i.e. at noon, during summer, at the surface, in middle latitudes). The absolute rate for reaction (84) is in that case of the same order of magnitude as for reaction (83). According to these reactions between NO and NO_2 a quasi stationary equilibrium (PSS = photostationary state) is achieved within 1 to 2 minutes. Assuming the PSS for the involved species,

$$\frac{d[O_3]}{dt} = \frac{d[NO_2]}{dt} = \frac{d[NO]}{dt} = \frac{d\left[O\left(^3P\right)\right]}{dt} = 0$$

results in

$$j_{(NO_2)}[NO_2] - k_{(2.43)}[NO][O_3] = 0\,. \quad (85)$$

Cycle C:

$$NO + O_3 \rightarrow NO_2 + O_2 \quad (83)$$

$$O\left(^3P\right) + O_2 + M \rightarrow O_3 + M \quad (15)$$

$$NO_2 + h\nu\,(315nm < l < 420nm) \rightarrow NO + O\left(^3P\right) \quad (84)$$

net: $0 \rightarrow 0$

The net equation from cycle C reveals that within this cycle no net O_3 is produced, only the PSS between NO and NO_2 is achieved [Leighton, 1961].

The equation (85) assumes that all other reactions are of minor importance. However, the absolute reaction rates (i.e. the total amount of molecules cm^{-3} s^{-1} produced by a reaction, e.g. $k_{A+B}[A][B]$) of the peroxy radicals with NO are in comparison slow, but they have an important impact. They disturb the PSS between NO, NO_2 and O_3 leading therefore to a higher amount of O_3 than in the undisturbed case.

NO is oxidised with the peroxy radicals via the following reactions,

$$NO + HO_2 \rightarrow NO_2 + OH \quad (86)$$

$$NO + RO_2 \rightarrow NO_2 + RO\,. \quad (87)$$

The additional amount of NO_2 produced leads to a net production of O_3 via reaction (84) and the subsequent reaction (15), where R represents the corresponding hydrocarbon group. During daytime conditions the reactions (86) and (87) are rate determining for the O_3 production rate, and to a good approximation the following reaction can be applied (for the derivation of this equation see Appendix 0).

$$\frac{d[O_3]}{dt} = [NO] \cdot \left(\sum_i \left(k_i \cdot [R_i O_2] \right) + k_{(2.45)} \cdot [HO_2] \right) \qquad (88)$$

The index i represents the different hydrocarbon groups. In principle they all react at different velocities with NO. The kinetic investigations of peroxy radical reactions with NO, however, have revealed large discrepancies in the last decade. In the past, it was assumed that all the peroxy radicals react at the same velocity with NO [e.g. Finlayson-Pitts and Pitts, 1986, and references therein]. In recent years several authors have revised this assumption [e.g. Kirchner et al., 1990, Moortgard et al., 1989, Peeters et al., 1992, Sehested and Nielsen, 1993, Le Bras et al., 1994]. However, the most recent investigations [Eberhard and Howard, 1997] confirmed that the C3-C5 and to a large extent also the larger peroxy radicals react at the same velocity with NO. Thus, an average reaction rate coefficient for reaction ((86) und (87)) of $k_{average} = 8 \cdot 10^{-12} \frac{cm^3}{molecules \cdot s}$ can be assumed. With this and the simultaneous knowledge of O_3, NO, NO_2, and $j_{(NO_2)}$, the total concentration of all peroxy radicals can be calculated.

$$RO_2^{*PSS} = RO_2^{PSS} + HO_2^{PSS} = \frac{j_{(NO_2)}}{k_{average}} \cdot \frac{NO_2}{NO} - \frac{k_{(2.43)}}{k_{average}} \cdot [O_3]$$

2.2.2.1.2 Nitrogen oxides in the ozone balance

As described in cycle C (see section 2.2.2.1.1), there is no net production of O_3 from the reactions (15), (83), and (84). The presence of peroxy radicals as shown in equation (88) leads to a net production of O_3. The formed NO_2 molecules from the reactions (86) and (87) are not produced by the destruction of an O_3 molecule. The O_3 production goes into competition with the reactions (42), (43), and (14) (chapter 2.2.1). Whereat the $O(^1D)$ atoms formed by reaction (14) mainly relaxate by quenching (reaction (16) and (17)) into the ground state and form back O_3 via reaction (15). The net loss is only caused by the $O(^1D)$ atoms leading to the formation of OH. This part is represented by the factor $a_{(2.4),(2.5),(2.6)}$ (section 2.2.1.1).

The extent of O_3 production depends on the amount of NO_x present. Lightfoot et al. [1992] calculated a NO_x mixing ratio threshold of 40 pptv (assuming 20 ppbv O_3), by which O_3 is neither produced nor destroyed. If assuming a PSS for NO_2, O_3, $O(^3P)$, and $O(^1D)$ the reactions (13)-(18), (42), (43), (86), and (87) provide the time dependent variation of the O_3 concentration.

$$\frac{\partial[O_3]}{\partial t} = k_{average} \cdot [NO]\left[RO_2^*\right] - a_{(2.4),(2.5),(2.6)} \cdot j_{(O(^1D))}[O_3] - k_{(2.12)} \cdot [HO_2][O_3] - k_{(2.11)} \cdot [OH][O_3]$$

The threshold value for NO at which a net O_3 production starts can be calculated by a simple transformation.

$$[NO] > \frac{a_{(2.4),(2.5),(2.6)} \cdot j_{(O(^1D))}[O_3] + k_{(2.12)} \cdot [HO_2][O_3] + k_{(2.11)} \cdot [OH][O_3]}{k_{average} \cdot \left[RO_2^*\right]}$$

If typical values for $a_{(2.4),(2.5),(2.6)}$ 7μ(H_2O), μ(H_2O) (1%), $j_{(O(^1D))}$ ($3{,}2 \cdot 10^{-5} s^{-1}$), O_3 (40 ppbv), HO_2 (20 pptv), and CH_3O_2 (20 pptv) are considered the NO mixing ratio of 20 pptv represents the threshold NO value.

The ratio between NO_2 and NO, necessary for the calculation of the NO_x mixing ratio, can be estimated from the simple PSS (of reactions (15), (83), and (84)).

$$\frac{[NO_2]}{[NO]} = \frac{k_{(2.43)}[O_3]}{j_{(NO_2)}}$$

Assuming a typical photolysis rate for mid latitudes for NO_2 of $j_{(NO_2)}$=0,01s^{-1} a NO_2/NO ratio of ~2 results, implying NO_x ~ 40 pptv. The amount of NO_x depends on the O_3, H_2O vapour concentration and photolysis frequencies.

2.2.2.1.3 Loss processes of nitrogen oxides

Nitrogen oxides are predominantly removed by the reactions involving NO_2 and the subsequent wet and dry deposition of the products. For NO, only reactions with some organic peroxy radicals (see chapter 2.2.2.2) can compete with the fast photochemical cycle (83) - (87). The share of nitrate production to the total turnover is below 30% for the most radicals [Becker and Wirtz, 1989, Roberts, 1990].

Main loss processes are the following:

- The reaction of NO_2 with OH during the day represents the most dominant loss for NO_x.

$$NO_2 + OH + M \rightarrow HNO_3 + M \quad (89)$$

The nitric acid (HNO_3) formed in reaction (89) is highly water soluble and reacts rapidly with surfaces (dry deposition). Therefore, HNO_3 can easily be washed out or deposed from the atmosphere.

- NO_2 reacts with HO_2 or organic peroxy radicals (RO_2), in both cases the formed peroxy nitrates are thermal unstable and frequently decompose within a short period of time back to the educts.

$$NO_2 + HO_2 \rightleftharpoons HO_2NO_2 \quad (90)$$

$$NO_2 + RO_2 \rightleftharpoons RO_2NO_2 \quad (91)$$

The hydroperoxy nitrate (HO_2NO_2) and the alkylperoxy nitrates (RO_2NO_2) formed via alkylperoxy radicals (e.g. CH_3O_2, $C_2H_5O_2$, ...) which typically react with NO_2 in the lower troposphere have only a lifetime of a few seconds. In contrast to the peroxy acetyl nitrates (PAN), due to their essential higher activation energy, which can have lifetimes up to several months at lower temperatures, when it is transported into the free troposphere. PAN as a reservoir for NO_x can therefore have a significant influence on the local amounts of reactive nitrogen oxides, even in unpolluted regions [Singh et al., 1990, 1992]. The formation reactions (90) and (91) of organic nitrates are not a sink for the total amount of NO_x, because the deposition velocities are very low compared with the thermal decomposition.

- In layers close to the surface the dry deposition of NO_2 is important. The deposition velocities vary between 0,2 and 0,4 cm s^{-1} [Hanson and Lindberg, 1991].

- The reaction with O_3 constitutes an additional NO_2 loss mechanism.

$$NO_2 + O_3 \rightarrow NO_3 + O_2 \quad (92)$$

The formed NO_3 radical is very rapidly photodissociated during daytime into NO or NO_2 (see reaction (93)). The nocturnal chemistry is described in more detail in section 2.2.2.2.

2.2.2.2 Nitrate radical (NO_3)

The NO_3 radical, produced within reaction (92), plays an important role during the night. During daytime it is rapidly photodissociated being the amounts of NO_3 negligible.

$$NO_3 + h\nu \xrightarrow{a} NO_2 + O\left(^3P\right) \qquad \xrightarrow{b} NO + O_2 \qquad (93)^9$$

NO_3 is produced by the dissociation of N_2O_5.

$$NO_2 + NO_3 + M \rightarrow N_2O_5 + M \qquad (94)$$

$$N_2O_5 + M \rightarrow NO_3 + NO_2 + M \qquad (95)$$

N_2O_5 is a reservoir substance not a net source, because N_2O_5 is exclusively produced by reaction (94) [Wayne et al., 1990].

The NO_3 radical oxidises several organic compounds present in the troposphere. During daytime the OH radical is the dominant reaction partner for the oxidation of organic compounds. Conversely, during the night the NO_3 radical is for almost all organic compounds the most important oxidising agent in the troposphere. For a few compounds, e.g. CH_3SCH_3, the reaction with NO_3 during the night can be even more significant than the daytime reaction with OH.

The rate coefficients for the reaction of hydrocarbons with NO_3 are clearly smaller than the corresponding reaction rate coefficients with OH. For instance, the relative reactivity of OH with hydrocarbons for example for butane and 1-butene are in the order of 10^5 and 3000 respectively higher than the corresponding for NO_3 at temperatures around 20°C. The importance of the separate pathways is emphasized when the concentrations of NO_3 during the night (~10^9 molecules cm^{-3}) and of OH during the day (~10^6 molecules cm^{-3}) are taken into account. The absolute reaction rates of NO_3 with alkenes during the night are of the same order of magnitude compared with the rates of OH during the day.

Terpenes have comparatively much higher reaction rate coefficients with NO_3. The rate coefficients are only two orders of magnitude smaller than the corresponding for OH. In this case the reactions of natural terpenes with NO_3 during the night can be more significant than with OH during daytime.

[9] The part of channel a to reaction (93) amount to ~ 90%.

Two typical reaction mechanisms can be identified: the hydrogen abstraction and the addition to an unsaturated bonding.

$$NO_3 + RH \rightarrow HNO_3 + R \quad (96)$$

$$NO_3 + C_2H_4 \rightarrow C_2H_4ONO_2 \quad (97)$$

HNO_3 is a direct product of the hydrogen abstraction of the NO_3 radical. The produced R radical in reaction (96) reacts predominantly with O_2 to form RO_2^* in the troposphere. The other aldehyde precursors produce an acyl peroxy radical ($RCOO_2$) as a product of reaction (96) and therefore are a potential source for PAN.

The product from reaction (97) can be a NO_2 sink, because of its reaction with NO_2 producing epoxides. However, in the troposphere the reaction with O_2 dominates. For example propene reacts with O_2:

$$CH_3CHCH_2ONO_2 + O_2 \rightarrow CH_3CHOOCH_2ONO_2 \quad (98)$$

and produces nitrated acetone by reactions (99) and (100).

$$CH_3CHOOCH_2ONO_2 + NO \rightarrow CH_3CHOCH_2ONO_2 + NO_2 \quad (99)$$

$$CH_3CHOCH_2ONO_2 + O_2 \rightarrow CH_3COCH_2ONO_2 + HO_2 \quad (100)$$

These reactions underline, the analogy to the reaction (87) and (106). They constitute a source of HO_2 radicals during the night enabling the conversion of NO to NO_2.

Of special interest is the production of α-(nitroxy)-acetone, reported as a mutagen. Other products are di-nitrates which also have noxious reactions.

The role of NO_3 in the tropospheric chemistry can be summarised as follows:

- Organic compounds can be oxidised and removed from the atmosphere during the night.
- HNO_3 can be produced, either by the hydrolysis of N_2O_5 or as a product of the H abstraction from reaction (96).
- Free radicals from the reaction of NO_3 with organic compounds can rapidly be converted into HO_2 und RO_2, and therefore initiate oxidising chain reactions, which lead to a source of OH radicals.
- Toxic compounds, other nitrates, and oxidised compounds can be formed.

2.2.2.3 Nitrous acid (HONO)

HONO is of great interest because of its absorption of light in the actinic region and rapid photolysis to generate OH radicals ((101)).

$$HONO + h\nu \rightarrow OH + NO \qquad (101)$$

This reaction can have a major impact on the production of OH especially in the early morning hours, because HONO is mainly produced and accumulated during the night by heterogeneous reactions of NO_2. During the day it can also be formed by the reaction of OH with NO:

$$OH + NO + M \rightarrow HONO + M \qquad (102)$$

Winer and Biermann [1994] observed HONO mixing ratios up to 15 ppbv in the early morning hours at Long Beach, California. However, the impact of these two reactions on the production of radicals during daytime can be neglected.

2.2.2.4 Non methane hydrocarbons (NMHC)

2.2.2.4.1 OH oxidation of NMHC

The oxidation of NMHC in polluted regions plays a significant role among the production of RO_2^* radicals. The NMHC are a large group of different substances which have both anthropogenic and natural origin (Figure 15).

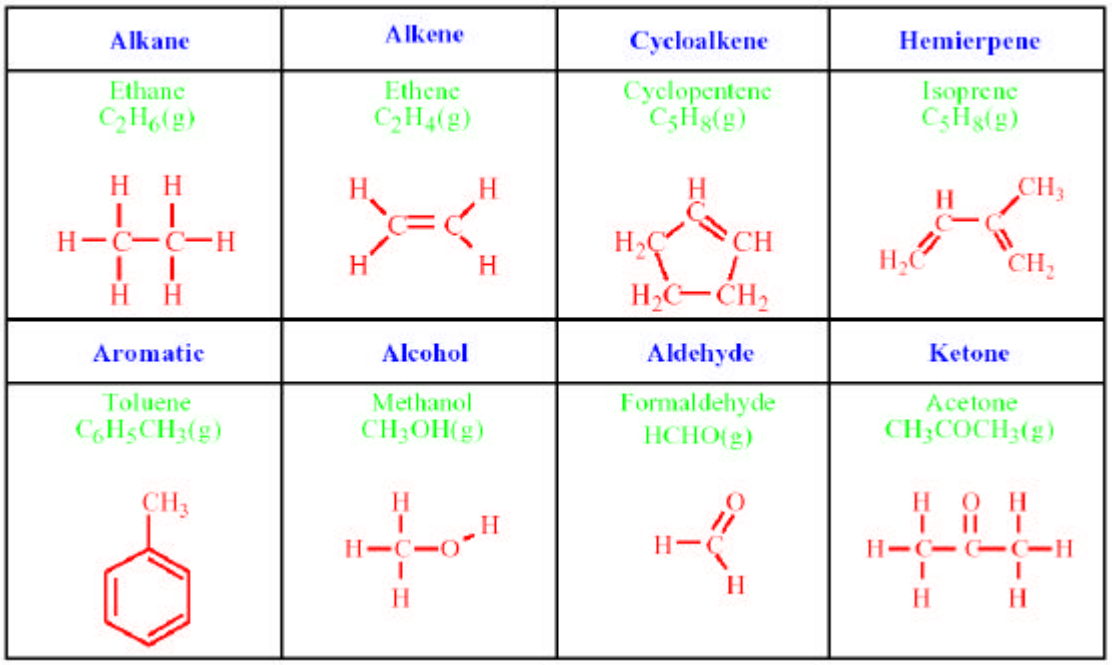

Figure 15: Different groups of volatile organic compounds found in the Earth's atmosphere, with typical examples for each group.

In order to keep the discussion at a reasonable degree of complexity only reactions with OH as initialising step are included (the NO_3, O_3, and Cl oxidation is described in chapters 2.2.2.2, 2.2.2.4.2, and 2.2.2.4.3, respectively). The reactions of NMHC with HO_2, O, and O_3 play a minor role and will be neglected here, except for the reactions of alkenes with O_3. In addition, the further discussion will only focus on the oxidations of simple alkanes and alkenes. These pathways are representative for most of the NMHC.

The reaction with OH is the dominant loss process for alkanes within the troposphere, where the H atom is separated from the C-H bond ((103)) and forms an alkyl (R) radical. The subsequent reaction of the R radical with O_2 forms a RO_2 radical.

$$RH + OH \rightarrow R + H_2O \quad (103)$$

$$R + O_2 \rightarrow RO_2 \quad (104)$$

If R is CH_3 a third reaction partner is needed (reaction (23)). Ethane and propane can react in the following steps:

$$RO_2 + NO \rightarrow NO_2 + RO \quad (87)$$

$$RO \rightarrow R' + R''CHO \quad (105)$$

$$RO + O_2 \rightarrow R'R''CO + HO_2 \quad (106)$$

R´ and R´´ represent smaller alkyl radicals or organic groups. The aldehydes and ketones (R´´CHO, R´R´´CO) can be photolysed, as described for HCHO (see reactions (38) and (39)), or further oxidised. For instance the OH radical abstracts one H atom from the acetaldehyd and forms CH_3CO, which then reacts with O_2 to produce an acetyl peroxy radical (CH_3COO_2).

$$CH_3CHO + OH \rightarrow CH_3CO + H_2O \quad (107)$$

$$CH_3CO + O_2 \rightarrow CH_3COO_2 \quad (108)$$

The reaction of CH_3COO_2 with NO_2 is important, because it produces PAN.

$$CH_3COO_2 + NO_2 \rightleftharpoons CH_3COO_2NO_2 \quad (109)$$

The importance of PAN is based on the thermal equilibrium of reaction (109), which is shifted to the products side at lower temperatures. PAN represents a reservoir substance for NO_x. Under convective conditions air parcels can rise. This is in conjunction with lower temperatures in the free troposphere and the corresponding shift of the equilibrium of reaction (109) can favour the transport of NO_x over large distances.

The subsidence of air parcels and the corresponding temperature increase moves the equilibrium back to the side of the educts. Resulting from this effect enhanced amounts of NO_x molecules can be transported into remote areas.

Another important pathway for CH_3COO_2 is the reaction with NO (110). Through this reaction the resultant CH_3COO radical can be further fragmented (111):

$$CH_3COO_2 + NO \rightarrow CH_3COO + NO_2 \quad (110)$$

$$CH_3COO \rightarrow CH_3 + CO_2 \quad (111)$$

In the described reaction pathway larger alkyl radicals are fragmented to smaller alkyl radicals, until they are converted from CH_3 into CO and CO_2.

Ethene (C_2H_4) and propene (C_3H_6) react differently with OH. The alkenes form a complex with OH.

$$OH + C_2H_4 \rightarrow HOC_2H_4 \quad (112)$$

$$OH + C_3H_6 \rightarrow HOC_3H_6 \quad (113)$$

Both reactions show an intermediate state. In contrast to reaction (113), reaction (112) needs a stabilising collision partner (M). The two reactions show a negative temperature coefficient for the reaction rate constant, which is typical for an addition process.

In the case of reaction (113) a stabilised collision product was observed. The production of an OH-ethene adduct is exothermic (~ 134 $kJmol^{-1}$). However, the breaking of the C-H bond is endothermic (~ 30$kJmol^{-1}$), therefore the preferred reaction path is the decomposition back into the educts of reaction (112). The excess energy of the formed product from the propene with OH reaction (113) is comparable to reaction (112), but the abstraction of CH_3 is energetically possible.

The alkene OH adducts predominantly react in analogy to the alkyl radicals. The subsequent oxydation steps of the propene OH adduct are following:

$$CH_3CHCH_2OH + O_2 \rightarrow CH_3CH(O_2)CH_2OH \quad (114)$$

$$CH_3CH(O_2)CH_2OH + NO \rightarrow CH_3CH(O)CH_2OH + NO_2 \quad (115)$$

$$CH_3CH(O)CH_2OH \rightarrow CH_3CHO + CH_2OH \quad (116)$$

The reaction mechanism presented above is comparable to this formed by reactions (87), (105), and (106) for the R-, RO_2, and RO radicals. In the atmosphere, the CH_2OH reacts exclusively with O_2, to form HCHO and HO_2.

$$CH_2OH + O_2 \rightarrow HCHO + HO_2 \quad (31)$$

The final products of the reaction of OH with propene, i.e. the aldehydes HCHO and CH_3CHO, are oxidised and photolysed as mentioned earlier. These reactions combined with the reaction of HO_2 with NO lead to a chain reaction.

In general the oxidation of hydrocarbons is summarised as follows.

Cycle D:

$$OH + RH \rightarrow H_2O + R \quad (103)$$

$$R + O_2 + M \rightarrow RO_2 + M \quad (104)$$

$$RO_2 + NO \rightarrow RO + NO_2 \quad (87)$$

$$RO + O_2 \rightarrow R'COR'' + HO_2 \quad (106)$$

$$HO_2 + NO \rightarrow OH + NO_2 \quad (86)$$

$$2 \cdot \left(NO_2 + h\nu \rightarrow NO + O\left({}^3P \right) \right) \quad (84)$$

$$2 \cdot \left(O\left({}^3P \right) + O_2 + M \rightarrow O_3 + M \right) \quad (15)$$

net: $$RH + 4O_2 \rightarrow R'COR'' + 2O_3 + H_2O$$

The chain carrier HO_2 and OH are converted into one another. The hydrocarbon RH will be oxidised under the consumption of four O_2 molecules to form two O_3 molecules. Finally, the net equation reveals the importance for the tropospheric O_3 production.

2.2.2.4.2 O_3 oxidation of NMHC

The mechanisms of the reactions of O_3 with alkenes are still not well understood. The initial step in the reaction is the addition of O_3 across the double bond to form what is known as a primary ozonide ((117)). The primary ozonide is not stable. One of the two peroxy O-O bonds and the C-C bond cleave simultaneously to give an aldehyde or ketone and a Criegee intermediate ((118)). The Criegee intermediate has excess energy, and can either be stabilized ((119)) or decomposed in a variety of ways.

Several studies in the literature [Horie et al., 1994, Gäb et al., 1995, Neeb et al., 1997, Wolff et al., 1997, Sauer et al., 1999] discuss the possible H_2O_2 production through the ozonolysis of alkenes and the subsequent reaction.

$$CH_2 = CHR + O_3 \rightarrow primary - ozonide \quad (117)$$

$$primary - ozonide \rightarrow CH_2OO^* + RCHO \quad (118)$$

$$CH_2OO^* + M \rightarrow CH_2OO + M \quad (119)$$

$$CH_2OO + H_2O \rightarrow CH_2O + H_2O_2 \quad (120)$$

R represents the organic group and corresponds to H in the case of ethene. These reactions (117) to (120) are not the dominant pathways, but can contribute significantly to the total amount of H_2O_2.

In the recent literature there is some controversial discussion which questions whether production of H_2O_2 via this reaction path takes place at all [Geert Moortgat, personal communication, 2002]. Neeb et al. [1997] observed no significant production of H_2O_2, and the formation of HCHO linearly coupled to the consumption of alkenes. This indicates that HCHO is formed only as a primary product from the primary ozonide [Hatakeyama and Akimoto, 1994].

2.2.2.4.3 Cl oxidation of NMHC

In contrast to OH, Cl reacts only with the hydrocarbons and not with CO. The Cl with hydrocarbon reactions can either proceed by abstraction of a hydrogen atom from a C-H bond or proceed by addition to a for example double bond in the case of the hydrocarbon being an alkene. The most reaction rate coefficients of Cl with alkanes reactions ((121)) are up to 2 orders of magnitude faster than the corresponding OH. The reaction rate coefficients of the Cl and alkenes are approximately up to one order of magnitude faster than the corresponding OH.

$$RH + Cl \rightarrow HCl + R \quad (121)$$

Cl also reacts with aromatic hydrocarbons, but only at a significant rate with those having saturated chains from which the Cl can abstract a hydrogen or unsaturated side chains where it can add. For example, the reaction of Cl with benzene is slow (k = 1.3×10^{-15} cm^3 $molecule^{-1}$ s^{-1}) [Shi and Bernhard, 1997]. On the other hand, the rate constants for the reactions with toluene, p-xylene, and p-cymene are high (0.59×10^{-10} cm^3 $molecule^{-1}$ s^{-1}, 1.5×10^{-10} cm^3 $molecule^{-1}$ s^{-1}, and 2.1×10^{-10} cm^3 $molecule^{-1}$ s^{-1}) [Shi and Bernhard, 1997, Finlayson-Pitts et al., 1999]. Hence reactions of aromatic

hydrocarbons with chlorine atoms will be primarily significant for those species having reactive groups attached to the ring.

Several atmospheric models have shown that larger amounts of Cl radicals are unlikely, because their presence would reduce the hydrocarbon concentrations to levels unrealistically low [Finlayson-Pitts, 1993b, Parrish et al., 1993, McKeen and Liu, 1993, Graedel and Keene, 1995, Wingenter et al., 1996].

Conversely, other scientists have estimated halogen concentrations in the order of 10^3 to 10^6 molecules cm^{-3} on account of hydrocarbon measurements [Singh et al., 1996, Jobson et al., 1994, Wingenter et al., 1996].

2.3 Atmospheric chemistry modelling

The basis and the different approaches for the modelling of the atmosphere are presented within this section. The description of different chemical reaction types is followed by their numerical treatment. The main purpose is to show the general theoretical approach and to present in a transparent way the motivation to reduce the modelling efforts within this work towards a zero dimensional chemistry model.

2.3.1 Basics

All models which simulate atmospheric processes calculate, starting with the initial value, the time dependent variation of the concentrations of the individual gases y_i. The concentration for the time T = t + dt results from the following mathematical expression:

$$[y_i](T) = [y_i](t) + \left(\frac{d[y_i]}{dt}\right)_{total} dt \,. \tag{122}$$

The concentration of a certain species y_i is indicated by the cornered brackets. The unit of concentration is [molec cm^{-3}]. This equation has to be solved for every species and for every considered location. The variations of the concentrations are calculated by an equation, which accounts for the variation caused by chemical processes as well as by transport, emission, and deposition (continuity equation):

$$\left(\frac{d[y_i]}{dt}\right)_{total} = \left(\frac{d[y_i]}{dt}\right)_{transport} + \left(\frac{d[y_i]}{dt}\right)_{chemistry/deposition} + \left(\frac{d[y_i]}{dt}\right)_{emission} \tag{123}$$

As this work focuses on the chemical evolution of the concentrations of different species, the transport and emission processes are not further described. The description of the atmospheric dynamics and their mathematical treatment can be found in Trenberth [1992] and Seinfeld and Pandis [1998].

The continuity equation for the variation of the concentration of species by chemical processes is:

$$\left(\frac{d[y_i]}{dt}\right)_{chemistry} = P_i - L_i[y_i] \tag{124}$$

where P_i is the chemical production and L_i is the chemical loss rate of the species y_i at the considered location. The chemical loss processes are proportional to the concentration $[y_i]$ of that species. As deposition processes can be treated according to the k-theory like effective first order loss processes, there is no longer any separation between the chemical and the deposition mechanisms.

For the calculation of the chemical loss and production terms, the reaction rate coefficients of the involved reactions of each species y_i are needed. They are determined within laboratory experiments and can be found in DeMoore et al. [1997], National Institute of Standards and Technology (NIST) Chemical Kinetics Database, Atkinson et al. [2000, International Union of Pure and Applied Chemistry (IUPAC)].

There are three different types of reactions:

a) bimolecular reactions: $A + B \xrightarrow{k_b} C + D$

b) termolecular reactions: $A + B + M \xrightarrow{k_t} C + D + M$

c) unimolecular reactions: $A(+M) \xrightarrow{k_{uni}} C + D(+M)$

In addition the two following reaction types are described explicitly, due to their particularity.

d) photolysis reactions: $A + h\nu \xrightarrow{j} C + D$

e) heterogeneous reactions: $A + B \xrightarrow{k_{het}} C + D$.

The reaction rate coefficients k_b, k_t, and k_{uni} can be found in the literature mentioned above and models are typically in agreement with each other due to the relatively small uncertainty of the values the models use. Conversely, the calculation of the rate coefficients for the photolysis reactions and the heterogeneous reactions are more complicated and usually vary from model to model, because there is no conventional approach for neither of these processes.

The knowledge of the composition of the aerosols is essential for calculating the heterogenous reaction rate coefficients k_h in chemical models [Carslaw et al., 1995, Hanson et al., 1994]. As this work focuses on the gas phase chemistry, the heterogeneous chemistry is not considered. Nevertheless, the heterogeneous reactions involving the halogen production are discussed qualitatively, and assumptions are made for the resultant amounts of halogens in the gas phase. Different approaches for the

calculation of the composition of liquid aerosols are discussed in Carslaw et al. [1997]. A compendium of laboratory data and their implementation into chemical models is described in Ravishankara [1995, 1997], Sander and Crutzen [1996],Vogt et al. [1996, 1999].

The calculation of the reaction rate coefficient of the photodissociation, the photolysis frequency j, needs an even higher expenditure, because the rate of the pholoysis reaction depends on the intensity of the light present in the atmosphere. The photolysis frequency depends predominantly on the solar zenith angle and consequently on the geographical position, the time of the day and on the time of the season. In addition the radiation itself is affected by the composition of the Earth's atmosphere. The photolysis frequencies are necessary input parameters for atmospheric models and are typically independently calculated. Due to the very time consuming calculation of the photolysis frequencies, large models typically use simplified calculation schemes.

The calculation of the photolysis frequencies typically consumes more time than the equation (124) does. As a consequence, the photolysis reactions are only approximated within larger models.

The calculation of the photolysis frequencies is a main focus of this work. Therefore the validation and the limitations of the used model are extensively discussed in chapter 4.2.3.1.

2.3.2 Different model types

The present understanding of atmospheric processes has achieved a level at which it is possible to realistically simulate the behaviour of the atmosphere. The use of models and their validation with measurements gives the opportunity to identify deficits of the current knowledge of atmospheric mechanisms, and in combination with specific laboratory studies and atmospheric observations, to solve these deficits.

For the description of the Earth's atmosphere several different types of models are used. Any particular type of model is selected according to the initial purpose. The limitation of the computing power restricts the complexity of a model.

The simplest models are the so called box models or 0-D-models. These models assume that the chemical reactions take place in an isolated area (box). Simple concepts are used for the parameterisation of the entrainment of other air masses into the box.

The main application of box models is to investigate the influence of specific reactions, reaction cycles [Crutzen et al., 1992, Danilin et al., 1996, Sander and Crutzen, 1996, Vogt et al., 1996, Dickerson et al., 1999], or different approximations on the results like the calculation of photolysis frequencies [Lary and Pyle, 1991, DeMajistre et al., 1995]. In the latter case the Box is fixed at a certain location, and the parameter pressure and the temperature are varied (Eulerian model). The importance of the individual reactions can be determined with different model runs. The combination of both applications is described in Finkbeiner et al. [1995].

The first extension of the box models leads to the 1-D-models. Typically, several boxes are piled up, and the atmosphere is simulated simultaneously in different altitudes. In addition, there is vertical exchange between the boxes. Typical applications are the investigation of the effect of different emission scenarios of chlorofluorocarbons (CFCs) on the amount of stratospheric O_3 [Brühl and Crutzen, 1988], or the comparison of vertical profiles of measurements with model results [Froidevaux et al., 1985, Allen and Delitsky, 1991, Wagner et al., 2002]. Based on their measurement geometry especially balloon soundings are frequently used for comparisons with 1-D-models [Chance et al., 1996, Renard et al., 1996]. The horizontal transport is commonly ignored in 1-D-models, because it is negligible on the small time intervals used in the simulations.

Beside this application there are 1-D-models adapted to the measurement geometry of certain measurement techniques. For example, the atmospheric zenith sky measurements determine the trace gas concentrations along the light path of the sunlight through the atmosphere (slant column). The interpretation of results requires the conversion of slant into vertical columns. Therefore, the boxes are arranged in order to fit the path of the sunlight [Solomon et al., 1987, Fish et al., 1995].

The 2-D-models are the next step in the development of atmospheric models. These models calculate individual boxes in two directions in space, typically the altitude and the latitude. The models average in the zonal direction, which means that they assume the variation in zonal direction is smaller than the variation in meridional and vertical direction. Since the 80's several models of this type exist, and they are continuously improved [Jackman et al., 1988, WMO 1995].

Accounting for transport within the 2-D-models enables the investigation of other aspects, like for example the global ozone distribution of the past decades [Solomon et al., 1996] and the impact of aircraft emissions [Tie et al., 1994]. However,

the required computing time increases strongly compared with 1-D-models, proportionally to the number of boxes considered. In addition, the zonal averaging makes the comparison with observations difficult.

3-D models are designed to solve the latter problem. There are two different approaches:

- Uncoupled 3-D-models are models in which the dynamics are calculated or meteorological data are measured, before they are used as input variables for the chemical model. As a consequence, it is possible to simulate a specific region (or globally) for a limited time period and to validate the results with measurements. Two famous models of this type are SLIMCAT [Chipperfield et al., 1997] and REPROBUS [Lefèvre et al., 1994]. The forecast ability of these models is reliable only as long as the chemical change has no impact on the dynamics.

- Coupled 3-D-models are models in which a general circulation model is coupled with a chemistry model. As a consequence, while the confidence of forecasting longer time intervals is enhanced, the overall precision of the model is reduced. The latter is caused by the uncertainty of the general circulation model compared with uncoupled dynamic calculations involving measurements of meteorological parameters. The development of the coupled 3-D-models is not very advanced [Steil et al., 1998]. Especially the needed computing capacity exceeds the available computing capacity by far.

All models which account for the horizontal transport, have to simplify the chemical description of the atmosphere due to insufficient computing capacity. These partly rough approximations are typically made in the calculation of the photolysis frequencies, in the reaction rate coefficients for heterogeneous reactions, sometimes in the numerical solving of the chemical equations, and in certain reaction cycles.

The observed discrepancies between simulations and observations might therefore be caused by the approximations in the model and can hardly be a proof for missing reactions. As a consequence, the multi dimensional models are not appropriate for the detailed investigation of the chemistry of the atmosphere.

Exclusively the 0-D-models enable the implementation of all relevant chemical processes without rough approximations, and therefore the investigation of their impact on the composition of the atmosphere. The influence of transport processes on the results of the simulation can be minimised, when the simulations are constrained to the measurements of the long lived species. The different temporal scales of dynamic processes and lifetimes of several trace gases are shown in Figure 16.

Figure 16 indicates which trace gases have to be constrained to the measurements depending on the time of simulation and the possible influence of the different dynamical processes.

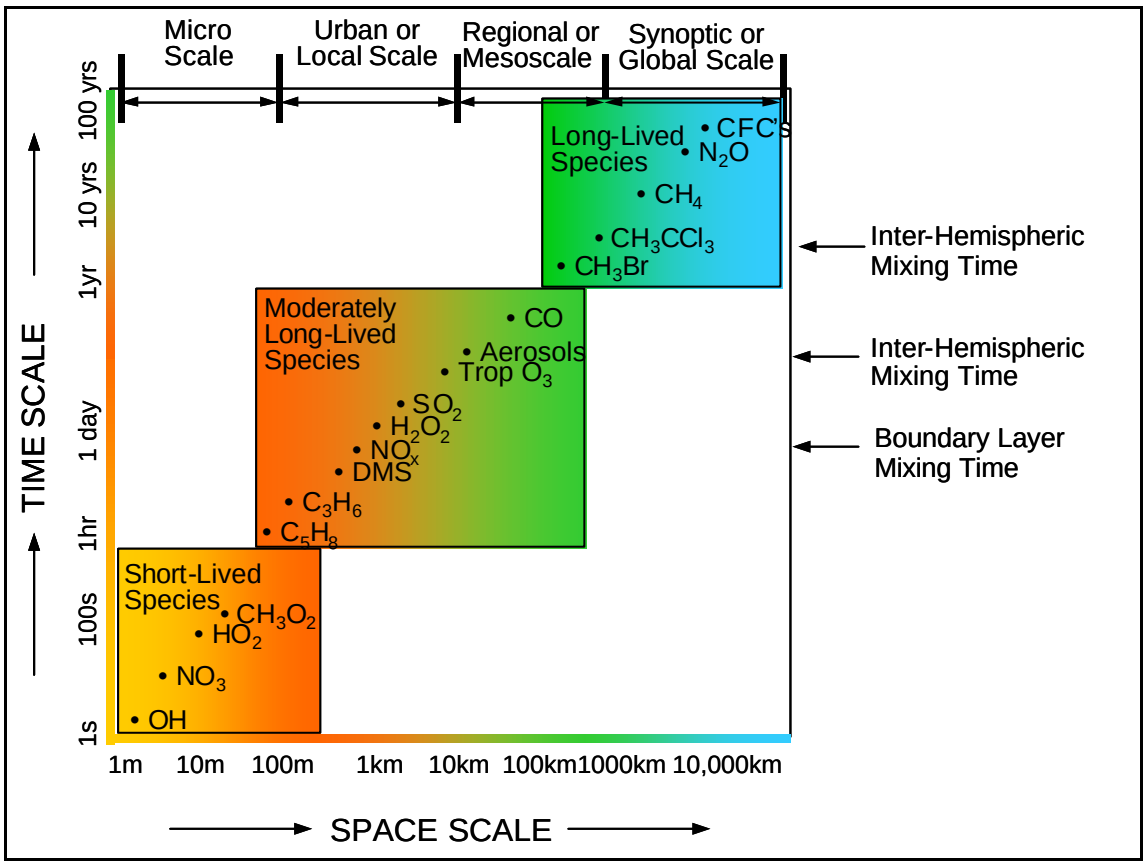

Figure 16: Temporal scale of dynamical processes and of the lifetimes of several trace gases [P.S. Monks, Uni-Leicester]

2.3.3 The structure of chemical models

As it is already described in chapter 2.3.1, the chemical evolution of the concentration of the species y_i is expressed by the continuity equation

$$\frac{d[y_i]}{dt} = P_i - L_i[y_i]. \tag{124}$$

To calculate the evolution of the species y_i, the production and loss terms have to be known. There are five different reaction types, which is discussed in the following.

2.3.3.1 The reaction rate coefficients

2.3.3.1.1 Bimolecular reacions

Bimolecular reactions can be represented as:

$$A + B \xrightarrow{k_b} C + D\,.$$

Bimolecular reactions are the most important ones within the Earth's atmosphere. They are second order reactions, which means that their velocity is proportional to the product of two concentrations. The variation of the concentration of A, B, C, and D results from the following expression:

$$\frac{d[A]}{dt} = \frac{d[B]}{dt} = -\frac{d[C]}{dt} = -\frac{d[D]}{dt} = -k_b[A][B] \tag{125}$$

where k_b is the reaction rate coefficient for this reaction.

The value and the temperature and pressure dependence of the reaction rate coefficient is determined in laboratory studies. The temperature dependence of most of the bimolecular reactions can be described with the Arrhenius law:

$$k_b = Ae^{\frac{E_a}{RT}} \tag{126}$$

where A is the Arrhenius factor, E_a the activation energy, R the gas constant, and T the temperature. The unit of the of k_b is [cm^3 $molec^{-1}$ s^{-1}] resultant from equation (125). The values for A and E_a or E_a/R for the most important atmospheric reactions are tabulated in DeMoore et al. [1997], National Institute of Standards and Technology (NIST) Chemical Kinetics Database [1998], Atkinson et al. [2000, International Union of Pure and Applied Chemistry (IUPAC)].

There are two different categories of bimolecular reactions: the direct and the indirect reactions.

Direct bimolecular reactions

The course of the direct bimolecular reaction can be explained by a collision process, which activates an excited state which falls apart into the final products.

$$A + B \longrightarrow (AB)^* \longrightarrow C + D$$

The Arrhenius factor depends on both the collision frequency and the geometry of the participating molecules. This is because a reaction can only occur when the molecules are orientated to each other in the right direction. The maximum value for the Arrhenius factor ($3x10^{-10}$ cm^3 $molec^{-1}$ s^{-1} [Wayne, 1991a]) results from the collision theory under the assumption of spherical and solid particles at 300 K. The collision frequency is proportional to the Arrhenius factor with $\sqrt{T}$, but this dependency is neglected within the Arrhenius law.

The temperature dependence of k_b is caused by the necessary overcome of the positiv activation energy E_a, in order to achieve the intermediate state $(AB)^*$. The fraction of molecules with sufficient energy is given by the Maxwell distribution and therefore is proportional to $e^{-\frac{E_a}{T}}$.

Direct bimolecular reactions are not pressure dependent. The Arrhenius law can well describe the temperature dependence of the reaction rate coefficients between 200 and 300 K [DeMoore et al., 1997].

Indirect bimolecular reactions

The indirect bimolecular reactions are characterised by their negative activation energy. This property cannot be explained by a simple theory. In the course of the reaction a relatively stable intermediate is formed

$$A + B \rightleftharpoons [AB]^* \longrightarrow C + D$$

where $[AB]^*$ is stable, and can therefore exist for a longer period of time, than $(AB)^*$, which is unstable and cannot be determined experimentally.

The dependence of the reaction rate coefficients of indirect bimolecular reactions on the temperature and pressure can be much more complicated than for direct bimolecular reaction rate coefficients. If [AB]* reacts to form C and D or if it falls apart back into A and B, it will be a function of the energy of $[AB]^*$, which will therefore

strongly depend on the temperature and pressure (i.e. for example [AB]* is more stable at lower temperatures, thus tends to produce more C and D).

An example for an indirect bimolecular reaction, where the temperature dependence resultant from the laboratory studies fits with the Arrhenius law, is

$$ClO + NO \longrightarrow NO_2 + Cl, \quad k_b = 6.4 \cdot 10^{-12} e^{\frac{290}{T}}$$

where neither pressure nor complex temperature dependence was observed.

An example for an indirect bimolecular reaction with a complex temperature and pressure dependence is

$$HNO_3 + OH \longrightarrow H_2O + NO_3, \quad k_b = k_0 + \frac{k_3[M]}{1 + \frac{k_3[M]}{k_2}},$$

where k_0, k_2, and k_3 are experimentally determined.

2.3.3.1.2 Termolecular reactions

Termolecular reactions are described by the following expression,

$$A + B + M \longrightarrow C + M$$

where M is a collision partner, typically N_2 or O_2 in the Earth's atmosphere. The collision partner is needed to conserve the impulse, but also to energetically stabilise the intermediate. The variation in the concentration of the participating species can be determined by

$$\frac{d[A]}{dt} = \frac{d[B]}{dt} = -\frac{d[C]}{dt} = -k_t[A][B] \qquad (127)$$

However, the calculation of the termolecular reaction rate coefficient k_t is not as simple as it is with the Arrhenius law, because the dependence on pressure and temperature is, due to the need of a collision partner, complex.

The termolecular reaction can be described by two sub steps:

1. activation: $A + B \longrightarrow C^*$

2a. stabilisation: $C^* + M \longrightarrow C + M$

2b. back reaction: $C^* \longrightarrow A + B$.

First of all the intermediate C^* has to be formed (1.). Then the intermediate can either be stabilised (2a.), which means that the excess energy is transferred to the

collision partner M, or can react back to the initial products (2b.). Only if the excited state C^* is stabilised the reaction will take place.

The theory for describing termolecular reactions has been developed by Rice, Ramsberger, Kassel, and Marcus (RRKM) [Wayne, 1991a] and is based on the exact calculation of the different excited states of the molecules. This method excellently expresses the measured reaction rate coefficients and their pressure and temperature dependences. However this theory is not suitable for being implemented into a model. Therefore, an appropriate parameterisation of the reaction rate coefficient has been developed [Troe, 1983]. The equation for the reaction rate coefficient is as follows:

$$k_t(M,T) = \frac{k_0(T)[M]}{1+\left(\frac{k_0(T)[M]}{k_\infty(T)}\right)} \cdot F\left(M, k_0(T), k_\infty(T)\right) \tag{128}$$

where k_0 is the threshold for the reaction rate coefficient for low pressure:

$$k_0 = \lim_{[M]\to 0} k_t(M,T). \tag{129}$$

In the low pressure range k_t is proportional with [M] and therefore with the pressure. k_∞ is the threshold of the reaction rate coefficient for high pressure:

$$k_\infty = \lim_{[M]\to \infty} k_t(M,T). \tag{130}$$

For this conditions k_t is independent on the pressure. The function F(M, k_0(T), k_∞(T)) is called broadening factor. It describes the turnover between the two pressure regions. F can be analytically solved for atmospheric temperatures as follows:

$$\log_{10} F \cong \frac{\log_{10} F_C}{1+\left[\frac{\log_{10}\left(k_0(T)[M]\right)}{k_\infty(T)}\right]^2} \tag{131}$$

where the value for F_C has to be given. The equation includes a simplification, which under special circumstances can lead to significant discrepancies in comparison with the exact calculation (RRKM).

The temperature dependence is fitted to the measured data by the following relation:

$$k_{0(\infty)}(T) = k_{0(\infty)}^{300}\left(\frac{T}{300}\right)^{-n(m)} \tag{132}$$

The exponent n is selected for k_0 and the exponent m is used for k_∞. The reaction rate coefficients k_t for the termolecular reaction can also analytically be calculated with k_0^{300}, n, k_∞^{300}, m, and F_C. In DeMoore et al. [1997] F_C has a constant value for all reactions, so that only four parameters are tabulated. The values for k_0^{300}, n, k_∞^{300}, m, and F_C do either come from measurements or from model calculations with the RRKM theory.

All four respectively five parameters can be found in DeMoore et al. [1997], National Institute of Standards and Technology (NIST) Chemical Kinetics Database [1998], Atkinson et al. [2000, International Union of Pure and Applied Chemistry (IUPAC)]. An investigation of the simplifications made in the broadening function in equation (131) showed differences between 10 and 30% for k_t at atmospheric pressures in comparison with measurements and exact model calculations [Donahue et al., 1997].

A very important termolecular reaction is the production of O_3 by the reaction of $O(^3P)$ with O_2.

$$O_2 + O\left(^3P\right) + M \longrightarrow O_3 + M, \quad k_t = 6 \cdot 10^{-34} \left[M\right] \cdot \left(\frac{T}{300}\right)^{-2.3}$$

Within the range of atmospheric pressures this reaction is linearly dependent on the pressure.

Another termolecular reaction of major importance in the Earth's atmosphere is the reaction of NO_2 with OH.

$$NO_2 + OH + M \longrightarrow HNO_3 + M$$

2.3.3.1.3 Unimolecular reactions

Unimolecular reactions, e.g. thermal decomposition reactions can be described by

$$A(+M) \longrightarrow C + D(+M).$$

The variation of [A] results from

$$\frac{d\left[A\right]}{dt} = -k_{th}\left[A\right] \tag{133}$$

These reactions are pseudo first order, because the reaction rate coefficient k_{uni} is strongly dependent on temperature and pressure. The unit for k_{uni} is $[s^{-1}]$. Obviously the reaction is faster at higher temperatures and higher pressures, because the number of

collisions increases. In addition the many species are thermally unstable, thus a higher temperature enhances their decomposition.

These reactions are the back reactions of the termolecular reactions, which means they can be parameterised in the same way as used in Atkinson et al. [2000]. The temperature dependence of k_0 and k_∞ is parameterised with the Arrhenius equation.

In DeMore et al. [1997] the equilibrium constants K_{eq} for the termolecular reaction are given, where the reaction rate coefficients can be calculated from.

$$k_{uni} = \frac{k_t}{K_{eq}} \tag{134}$$

An important thermal decomposition reaction is the breakdown of N_2O_5.

$$N_2O_5 + M \longrightarrow NO_2 + NO_3, \quad K_{eq} = 2.7 \cdot 10^{-27} e^{\frac{11000}{T}}$$

This equilibrium constant was determined in several independent experiments [DeMore et al., 1997].

The experimental errors of the reaction rate coefficients of the uni-, bi-, and termolecular reactions are always above 20% [DeMore et al., 1997]. Especially the determination of the temperature dependence is associated with larger errors.

2.3.3.1.4 Photolysis reactions

The photolysis reactions

$$A + h\nu \longrightarrow C + D$$

are first order reactions, which means that the temporal variation can be calculated by

$$\frac{d[A]}{dt} = -j[A]. \tag{135}$$

j is the photolysis frequency in units of [s^{-1}]. The reaction constant depends on the light intensity as well as the molecule properties (absorbtion cross section and quantum yield).

2.3.3.1.5 Heterogeneous reactions

Heterogeneous reactions take place at the liquid and solid particles (aerosols) in the atmosphere.

$$A + B \xrightarrow{het} C + D$$

Typically, these reactions are treated as first order reactions. Therefore the temporal variation can be expressed as

$$\frac{d[A]}{dt} = -k_{het}[A]. \tag{136}$$

The reaction rate constant can be calculated with

$$k_{het} = \frac{w A g}{4} \tag{137}$$

where ω is the thermal velocity, A the surface of the particle and γ the uptake coefficient [Ravishankara, 1997]. The uptake coefficient is the probability that the reaction takes place in the case of a collision between the molecule and the particle happenes. The calculation of the available surface and the uptake coefficient have large uncertainties. The experimental determination of γ and the determination of the basis of the physicochemical parameters, as the Henry-Law's-Constant to calculate γ in models, belong to the most extensive laboratory studies within this field. An detailed discussion of heterogeneous chemistry can be found in Ravishankara [1997].

2.3.3.2 Solving of the differential equations

For calculating the temporal evolution of the concentrations, the equation (124) has to be solved for each participating species y. As a consequence a coupled non-linear system of n equation results, where n is the number of considered species.

A problem occurs while solving this system, because the reaction rate coefficients vary by several orders of magnitude. The concentrations of single gases therefore vary with different velocities, in particular the photolysis frequencies change additionally with the time of the day. This is called a system of stiff differential equations.

In general, a system of ordinary differential equations (ODE) with given initial values can easily be solved. It starts with

$$\frac{dy_i(t)}{dt} = f_i(t, y_1, .., y_n), \quad i = 1, .., n, \tag{138}$$

where the functions $f_i(t,y_1,..,y_n)$ are known. When the initial values $y_i(t_0)$ are known, it is possible to solve the system by changing the infinite dy_i's and dt into finite steps Δy and Δt. One obtains $y_i(t=t_0+\Delta t)$ as the sum of $y_i(t_0)$ and $\Delta y_i(t_0)= f_i(t_0,y_1,..,y_n)\Delta t$. This method with a suitable step size for Δt leads in a good approximation to the exact solution of the differential equations, and the step size determines the accuracy.

To achieve an acceptable accuracy, the step size has to be smaller than the time in which the solution varies significantly, i.e. smaller than the time constants. This circumstance leads to problems within stiff differential equation systems as they appear in the atmospheric chemistry. Some reactions need small time steps for their fast reaction rate coefficients whereas smaller reaction rate coefficients need larger integration intervals. This can lead to numerical instabilities of the solution.

There are two different solution methods for ODE's, the explicit and the implicit. The explicit solutions are described with the following formula:

$$y(t+\Delta t) = y(t) + \Delta t y'(t). \tag{139}$$

The new value $y(t+\Delta t)$ results from the derivation at the time t, therefore from $f_i(t,y_1,..,y_n)$. The usage of explicit solution methods is inappropriate to solve stiff differential equations [Press et al., 1992].

Stiff differential equation systems can only be solved by implicit methods. The implicit method calculates the value for $y(t+\Delta t)$ not from the derivation at the time t, but at the time $t+\Delta t$.:

$$y(t+\Delta t) = y(t) + \Delta t y'(t+\Delta t) \tag{140}$$

This method does not guarantee stability, but is much more reliable than the explicit method. The problem of the implicit method is that the derivation at the time $t+\Delta t$ is unknown, which means that the derivation has to be either calculated or approximated.

There are several different approaches for implicit solution methods to solve stiff differential equation systems [Press et al., 1992].

A frequently used implicit method for solving stiff differential equations is the Predictor-Corrector-method, where the derivation at the time $t+\Delta t$ is calculated with an iterative technique. An advantage of this method is that the time step Δt is determined by the algorithm itself dependent on the needed accuracy.

The method given by Gear [1971] is based on this technique. The Gear's method determines the derivation at the time $t+\Delta t$ considering and extrapolating the earlier derivation with the help of the Backward Differential Formular (BDF) with fixed coefficients. This method has been used within the atmospheric chemistry since decades and has established itself as a reference for other methods used for solving chemical differential equations. The Gear's method is used for example in FACSIMILE [AEA Technology, 1994] and in ASAD (A Self-contained Atmospheric chemistry coDe) [Carver et al., 1997]. The latter code is used in the present work for solving the reaction schemes in the developed model.

3 Experimental

This section gives an overview of all the techniques and analysis procedures for the measurement, determination and/or modelling of the species and parameters used for the inerpretation of the present work. Some of the measurements were provided by other scientific groups involved in the corresponding experimental campaigns. The section is divided into the “INDOEX campaign” and for the “PRIME campaign”.

3.1 INDOEX campaign

The INDOEX campaign, an international research initiative, studied the chemistry of remote areas of the Indian Ocean and the influence of the outflow from the Indian subcontinent on these regions. This campaign took place during February, March, and April 1999.

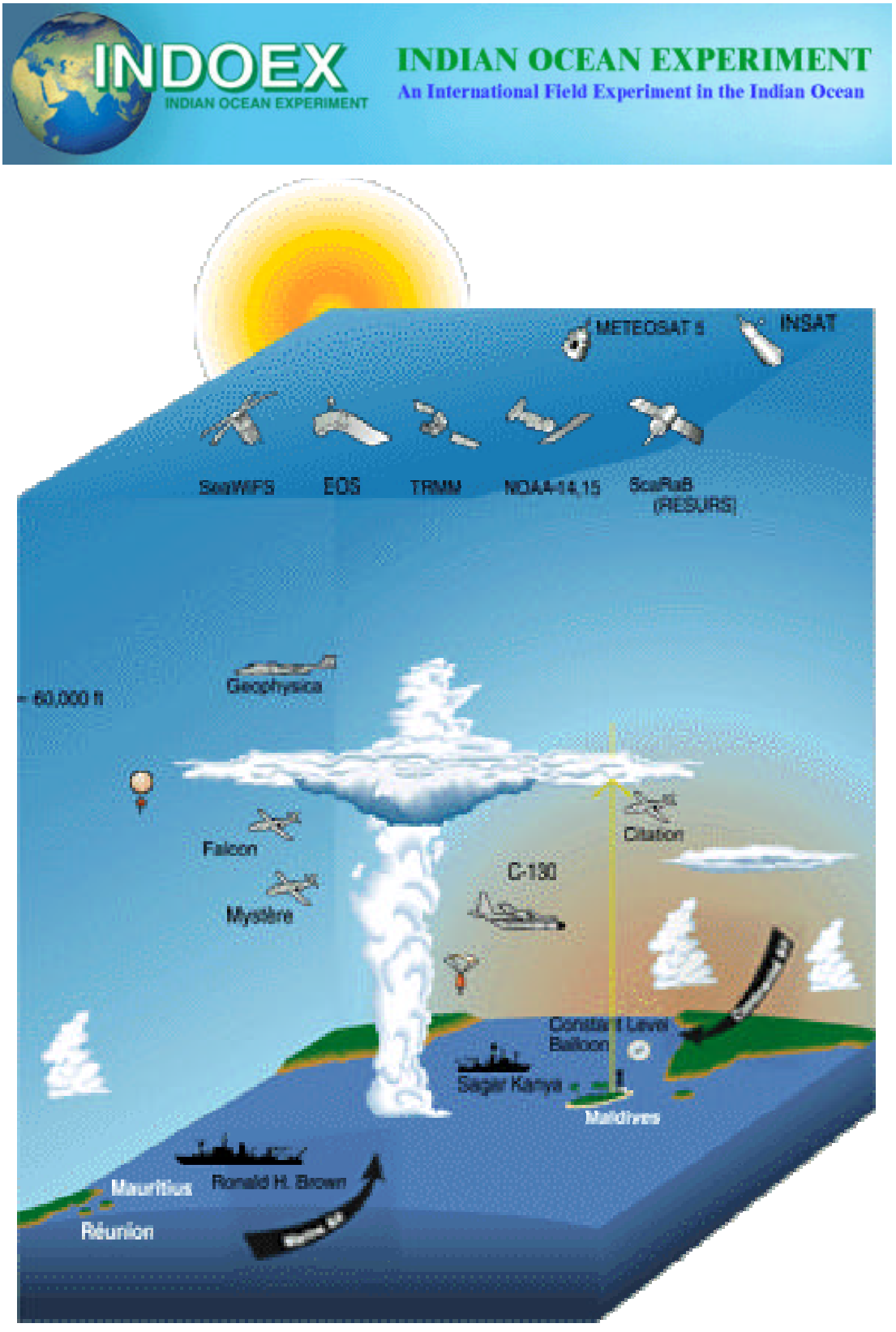

Figure 17: The Indian Ocean Experiment (INDOEX) 1999 [http://www-indoex.ucsd.edu/index.html].

3.1.1 RO_2^* measurement technique

Peroxy radicals were measured continuously during the INDOEX campaign by using the chemical amplification technique (PERCA). This measurement technique is based on the conversion of peroxy and oxy radicals into an amplified, NO_2-modulated signal. The latter is detected by the chemiluminiscence produced from the reaction of NO_2 with a Luminol solution [Hastie et al., 1991, Clemitshaw et al., 1997, Burkert et al., 2001a]. The PERCA measures the sum of HO_2, OH, RO and RO_2 radicals, which to a good approximation can be considered to be equivalent to RO_2^*. The amplification of the signal, i.e. the chain length (CL) of the chain reactions, and the conversion factor for the individual organic radicals must be determined by adequate calibrations. The radical calibration source utilises the photolysis of H_2O in air at 185 nm [Schultz et al., 1995]. The PERCA and the calibration technique have been described in more detail elsewhere [Hastie et al, 1991, Volz-Thomas et al., 1998, Burkert et al., 2001b].

The response of the instrument is calibrated regularly by adding different dilutions of the NO_2 flow emitted from permeation tubes held at constant temperature. The PERCA used at the IUP-UB has been described more in detail elsewhere [Volz-Thomas et al., 1998, Stöbener, 1999, Burkert et al., 2001b, 2002a]. In this system, 3.3 ppmv NO and 9.9 % v/v CO are mixed with a flow of outside air in a glass reactor. This reactor comprises a 3 cm long nose of 4 mm internal diameter which expands into a cylinder of 2 cm diameter and 22 cm length. The air sampled is pumped through a homemade NO_2 luminol detector at a constant flow rate of 2 $sLmin^{-1}$. The chemiluminiscence is produced from the reaction of NO_2 with a $5x10^{-4}$ M luminol solution on a Whatman glass fibre filter paper. The number of photons produced via the chemilumiscence is measured by a photomultiplier tube. In order to assure that the sampled concentrations lie within the linear response regime of the NO_2 detector, the output of a NO_2 permeation tube is continuously added to the flow of air CO and NO, prior to the detector. This provides an offset NO_2 concentration, which is a convenient measure of the instrument response.

Data are acquired at 1 Hz using a Data Translation interface and Agilent Vee software which switches three way valves in the inlet system every 30 s. This yields an alternating signal comprising the radical amplification and the radical destruction modes, hereafter called signal and background modes respectively. Fifteen seconds of each mode are used to determine the average signal. Successive background modes are

averaged and subtracted from the signal mode. Finally, one minute averages of the radical signal are stored.

The whole system is mounted in a portable rack. Gas flow rates are controlled by MKS mass flow controllers. Both input and exhaust gas flows are purified using appropriate chemical converters: e.g. charcoal/iodine remove iron and nickel carbonyls from CO, $FeSO_4$ removes traces of NO_2 in NO, and activated charcoal with Pt/Al pellets at a temperature T > 100 °C converts the CO in the exhaust to CO_2.

The chain length (CL) of the conversion reaction is determined with the aid of a calibration system based on the production of radicals from the UV photolysis of H_2O [Schultz et al., 1995].

The CL has recently been shown to be dependent on the relative humidity of the air sampled [Mihele and Hastie, 1998]. Therefore, the CL values obtained from a calibration under dry conditions were corrected according to the water dependency characterised in laboratory experiments for the IUP-UB set up. The reason for this dependency is still a subject under research [Mihele et al., 1999, Salisbury et al., 2001, Reichert et al., 2003].

During INDOEX, NO_2 and radical calibrations for the PERCA were performed twice a day and once a week respectively. The average CL, determined from all the radical calibrations performed in dry air during the measurement period, was 159 for the first leg, 136±13 for the second leg and 122±13 for the third leg. The steady decrease of the CL, observed during the whole campaign, is most probably caused by increasing contamination of the 20m long inlet system with sea salt, in spite of the regular cleaning of the reactor.

The temperature and the relative humidity of air entering the PERCA were assumed to be that provided by the data system of the ship. The detection limit is estimated to be 3-5 pptv RO_2^* for 1-min values. The precision of peroxy radical calibrations is ~15%, and a maximum uncertainty of ± 30% is estimated for 1σ and 1 minute RO_2^* values.

The inlet of the system was mounted on a mast located at the bow of the ship approximately 20 m above the sea level. The PERCA detector was inside an air-conditioned container on the deck.

3.1.2 CO measurement technique

CO was measured with a modified commercial nondispersive infrared gas filter correlation analyser (TEI model 48C, Franklin, MA) [Dickerson and Delany, 1988, Parsons and Dickerson, 1999] acquired at 1-min resolution.

3.1.3 O_3 measurement technique

O_3 was measured with a commercial UV photometer (TEI Model 49C, Franklin, MA), acquired at 1-min resolution. The complete dataset is reported by Stehr et al. [2002].

3.1.4 NO measurement technique

Nitrogen oxide was measured by a chemiluminescence detector built according to established protocols [e.g. Carroll et al., 1985]. The instrument is described in previous publications [Rhoads et al., 1997; Carsey, et al., 1997]. The detector was housed together with the PERCA, both inlets were fixed on the sampling tower. To avoid contamination by sea salt aerosols, the inlet line was capped by a 37-mm diameter 1-µm pore size Teflon filter (Gelman), replaced frequently during the cruise.

Airflow through the system was set to 1.2 L min^{-1}. The flow rate was calibrated periodically throughout the cruise with a bubble-flow meter (Sensidyne, Clearwater, Florida). A needle valve in the air line at the instrument rack further reduced the pressure and decreased gas travel time from the sampling point to the detector to less than 5 seconds. The NO was detected by measuring the chemiluminescent emission resulting from the reaction of NO with O_3 within a gold-coated stainless steel reaction chamber. Blank count rates were determined by reacting the gas stream with excess O_3 prior to entering the reaction chamber. The emitted photons were recorded by a 9658R photomultiplier tube (Thorn EMI) held at a potential of 1250 volts and contained in a cooled housing (Products For Research) maintained nominally at -40°C. Photon counting intervals of 10 seconds were recorded for the duration of the cycle. The first 2-3 minutes of each measure and calibrate count segments were ignored to allow the system to equilibrate. Each run was scanned for spikes or other anomalies due to other shipboard instrumentation. For the calibration a commercial calibration gas mixture (4.94 ppbv NO in N_2, Scott Specialty Gas) was injected into the inlet stream. Background count rates were higher than in previous experiments. The mixing ratios of

NO were obtained by subtracting the daytime (10 a. m. to 2 p. m. local time) average mixing ratios, from that obtained at night (10 p. m. to 2 a. m. local time).

3.1.5 NMHC measurement technique

Altogether 59 air samples, each having a volume of 9 L (STP), were collected in 2.5 L electropolished stainless steel canisters for the laboratory based analysis of NMHC. The air was sucked from the top of the bow tower (10 m height) via a stainless steel tube. Except during transport (~6 days) to the analytical laboratory (MPI-C, Mainz, Germany) the canisters were kept at −18°C and then equilibrated at ambient temperature for 12 h before gas chromatographic analysis. The condensable compounds (encompassing the NMHC) were first cryogenically concentrated at −170°C in a microtrap packed with porous silica beads, and thereafter were separated on a Al_2O_3/KCl porous layer open tubular (PLOT) column connected to a quadrupole mass spectrometer (HP 5973). Laboratory tests indicated detection limits (3σ variation of a blank sample) of 0.2-6.8 pptv for ethane, propane, butane, iso-butane, pentane and iso-pentane, and 14-26 pptv for acetylene. The precision for all species is 5-10 %. Comparisons with other laboratories showed agreements within ~20% for all species addressed here. For details, see Muehle et al. [2002].

3.1.6 j(NO_2) measurement technique

The frequency of photodissociation of NO_2 to NO and $O(^3P)$ was measured by determining the production of NO in a flow of NO_2 through a glass reactor of length 20cm and volume 10 cm^3 (Kelley et al., 1995). In the standard manner, a black surface beneath the detector, yields the photolysis frequency of NO_2, j(NO_2):

$$j(NO_2) = \int I(2\pi).\phi(NO_2, \lambda)\sigma(NO_2, \lambda)d\lambda$$

Where $I(2\pi)$ is the down-welling light flux at the surface, $\phi(NO_2, \lambda)$ the quantum yield for the dissociation of NO_2 and $\sigma(NO_2, \lambda)$ the absorption cross section of NO_2.

2 l min^{-1} of a mixture of NO_2 and air flowed constantly through the system. The NO and NO_2 mixing ratios were determined using a commercial detector (TEI model 42, Franklin, MA). The uncertainty with 95% confidence is estimated to be +/- 7% for values above $3x10^{-3}$ $s^{-1}$for 1 min average.

3.1.7 j($O(^1D)$) measurement technique

The actinic UV flux was measured using a 2π sr filter radiometer with isotropic sensitivity (Meteorologie Consult GmbH, Germany), described by Junkermann et al. [1989] but having a filter combination optimised for cloudy conditions and high solar zenith angles. The O_3 column necessary to convert the recorded actinic UV flux into an O_3 photolysis frequency, j($O(^1D)$), was measured many times each day aboard the RV Ronald H. Brown using a hand-held Microtops II sunphotometer (S/N 3685), having a 1-2% precision [Meywerk and Ramanathan, 2001]. The filter radiometer was compared with a spectroradiometer, described by Hofzumahaus et al. [1999] immediately after the INDOEX campaign. The j($O(^1D)$) values ranged between 0 and $2.2 \times 10^{-5} s^{-1}$. The regression line exhibited a slope of 1.0; the linear correlation coefficient r^2 being 0.9989. The total uncertainty of the j($O(^1D)$) data presented here is 15-20% for solar zenith angles (SZA) below 60°, increasing to 50% at SZA = 80° (including the current uncertainties in the O_3 absorption cross-section and $O(^1D)$ quantum yield).

3.1.8 O_3 soundings

Sixty-one ozone and over sixty rawinsondes were launched twice a day, throughout the intensive field phase of INDOEX. Vertical profiles from 15ºS near Mauritius to 17ºN in the southeastern Arabian Sea were obtained [Herman Smit et al., personal communication, 1999]. The frequency of sampling increased when the ship approached the southwestern Bay of Bengal and during the ITCZ crossings.

The sondes used were balloon-borne ECC (Electrochemical Concentration Cell) ozone sondes (Model SPC-6A, Science Pump Corporation, New Jersey, USA) coupled to Väisälä radiosondes (Model RS80-15 H, Väisälä Finland). The error of the ECC ozone sensor is expected to be ± 1-2 ppbv below 5 km increasing to ± 5 ppbv at 10 km and ± 20 ppbv at 20 km altitude [Smit et al., 1994, 1998]. The response time of the ozone sensor is 25-30 seconds which corresponds to an ascent velocity of 5 m s^{-1} – this gives an altitude resolution of about 125-150 m.

The uncertainties in the temperature and pressure measurements below 20 km are ± 0.3ºC and ± 0.5 hPa respectively. The accuracy of the humidity sensor (HUMICAP-H) increases from ± 2% near the surface to ± 15-30% between 5-15 km altitude [Kley et al., 1997]. At low temperatures the response time of the sensor increases from about 200 sec. at -60ºC to 400 sec. at –70ºC [Antikainen and Paukkunen,

1994]. Above 15 km altitude the performance of the sensor is unreliable anymore [Kley et al., 1997].

3.1.9 Satellite data

The GOME instrument [Burrows et al,. 1999] is a grating pseudo double monochromator covering the spectral range of 240 to 790 nm at a spectral resolution of 0.2 – 0.4 nm. GOME observes light scattered back from the atmosphere and reflected from the ground in near nadir viewing geometry. The GOME instrument was launched on board the European ERS-2 satellite in April 1995 and has been operational since July. The ERS-2 satellite is in a sun-synchronous polar orbit with an equator crossing time of 10:30 local time. The broad spectral coverage of GOME and the moderate spectral resolution allows the retrieval of a number of different trace gases that have structured absorptions in the UV and visible wavelength range. Under clear sky conditions, visible and near UV radiation reaches the surface, and provides GOME with a unique sensitivity towards tropospheric absorbers. In particular, GOME measurements have been used to study tropospheric SO_2 [Eisinger and Burrows, 1998], BrO [Wagner and Platt, 1998, Richter et al. 1998], HCHO [Wittrock et al., 2000, Thomas et al., 1998, Chance et al., 2001] and NO_2 [Leue et al., 2001, Velders et al., 2001].

In this study, tropospheric HCHO, O_3, and NO_2 columns are derived from GOME measurements. The absorption in a single earth-shine spectrum is derived using the Differential Optical Absorption Spectroscopy (DOAS) technique. The stratospheric NO_2 and O_3 contribution to this absorption is estimated using a measurement taken at the same latitude over the Pacific (180°-190° longitude), assuming the tropospheric amount of NO_2 and O_3 to be negligible and 22.5 DU, respectively, in this region. The assumption, however, of longitudinal homogeneity is reasonable only at low and middle latitudes [Richter et al., 2001]. The use of the Pacific region as a clean air reference is supported by results of both air-borne campaigns [Schultz et al., 1999, and references therein] and the GOME measurements themselves, indicated little or no influence of anthropogenic or lightning produced NO_2. The tropospheric O_3 is assumed to be constant, which is in fair agreement with measured O_3 soundings in this region [Thompson and Witte, 1999].

By subtracting the stratospheric column from the total column, a tropospheric slant column is derived that can be converted to a vertical tropospheric column using an

appropriate airmass factor (AMF). The AMF is defined as the ratio of the observed slant column to the vertical column and is calculated with a radiative transfer model SCIATRAN [Rozanov et al., 1997] using a model atmosphere. To minimise the bias introduced by clouds shielding the troposphere, only measurements with a cloud cover fraction below 0.1 are included in the analysis [Richter and Burrows, 2001]. The vertical tropospheric column of HCHO is derived, from the slant column by using an appropriate tropospheric AMF. The stratospheric contribution is neglected.

The lightning produced NO_2 in the troposphere is measured as described above, but instead of using measurements with a cloud friction below 0.1, measurements concurrent with lightning activity are used. Lightning can be detected by NASA/NASDA-satellite project Lightning Imaging Sensor [Christian et al., 1999]. The air mass factor is corrected for influence of clouds, i.e. reflection at the top of cloud, multiple scattering in the clouds, single scattering below the cloud, and reflection at the surface [Hild et al., 2002].

3.1.10 Other supporting measurements

The meteorological parameters and backtrajectory analysis were taken from the INDOEX database and from the NOAA Pacific Marine Environmental Laboratory (PMEL) (for further information see http://www-indoex.ucsd.edu/index.html and http://saga.pmel.noaa. gov/indoex/index.html).

3.1.11 Modelling

The model, developed to simulate and investigate the chemical mechanism of the remote MBL, solves the time dependent set of differential equations using the atmospheric chemistry package ASAD (A Self-contained Atmospheric chemistry coDe) [Carver et al., 1997].

The chemical scheme accounts for 95 species and describes the chemistry of CH_4, CO, dimethylsulfide (DMS) and selected NMHC (C_2H_2, C_2H_4, C_2H_6, C_3H_6, C_3H_8) [Burkert et al., 2001b, 2003a, 2003b. 2003c]. The oxidation of NMHC and DMS was assumed to produce HCHO or peroxy radicals in their reaction pathways, when the products of their reaction are unknown.

The chemistry of the MBL is described by 149 bimolecular, 30 termolecular and 21 photolysis reactions. Additionally the physical deposition of H_2O_2, CH_3OOH and O_3

at the sea surface is appropriately modelled. The reactions and reaction rate coefficients have been collated from the IUPAC [Atkinson et al., 2000], JPL [DeMore et al., 1997] and NIST (National Institute of Standards and Technology) Chemical Kinetics Databases. The model does not take into account the dynamics, for example mixing, advection or convection, and the remote marine boundary layer is considered to be an effectively well mixed chemical reactor.

The photolysis frequencies were calculated by using PHOTOST an improved version of the model PHOTOGT [Blindauer et al., 1996], which is based on the radiative transfer model (RTM) SCIATRAN [Buchwitz, 2000]. To initialise the RTM, in situ measurements of the aerosol optical depth (AOD) were used [Welton et al., 2002]. The total ozone columns used in the model were measured by GOME [Burrows et al., 1999 and references therein]. The aerosol composition used by the model was adapted to measurements performed at Kashidoo Island [Lelieveld et al., 2001]. The comparison of measured and calculated photolysis frequencies indicates that the calculated photolysis frequencies are slightly overestimated for high AOD. The $j(O(^1D))$ and $j(NO_2)$ calculated photolysis frequencies at 30° SZA for AOD of 0 and 0.6 differ by about 30% and 24% respectively [Burkert et al., 2003a]. In all simulations the photolysis frequencies have been constrained to the measurements.

3.2 PRIME campaign

The PRIME campaign took place during July and August 1999 at the Silwood Park Atmospheric Research Station, near London (51°24'53''N, 0°38'48''W). The site offered the opportunity to measure on many days the plume from the city centre of London.

3.2.1 Overview of all measurement techniques

An overview of the measured trace gases together with a short description of the technique, calibration method, detection limit, and the time resolution is shown in Table 3.

Species	Technique	Calibration method	Detection limit	Time resolution
CO	GFC	CO cylinder	20 ppbv	1 min
NO/NO_2	CL	NO + NO_2 cylinders	25 pptv	1 min
RO_2^*	PERCA	NO_2 permeation tubes H_2O photolysis	5-10 pptv	1 min
PAN	GC	CH_3COCH_3 + hν + NO	100 pptv	10 min
H_2O_2, ROOH	HPLC	H_2O_2 cylinder	20 pptv	25 min
HO_2	FAGE	H_2O photolysis		
OH	FAGE	H_2O photolysis		

Table 3: Measurements performed by IUP-UB and Uni-Leeds during the PRIME campaign. GFC: Gas filter correlation, PERCA: chemical amplification, CL: chemiluminescence, GC: gas chromatography, HPLC: high performance liquid chromatography.

3.2.2 RO_2^* measurement technique

The PERCA technique has already been described in detail in 3.1.1. Both NO_2 and RO_2^* calibrations were made regularly during the PRIME experiment. The CL averaged during the period of the campaign had a value of 165 for dry conditions. The detection limit is ~10 pptv for wet conditions (i.e. r.h. > 80%) for 10 min average and

decreases with decreasing relative humidity reaching levels of ~1-2 pptv for dry conditions. The 1 σ relative error is ~10% for 10 min averaged values.

3.2.3 OH and HO_2 measurement techniques

HO_2 was measured by the University of Leeds using the FAGE (Fluorescence Assay with Gas Expansion/Laser-Induced Fluorescence) technique for direct OH measurement. The HO_2 measurement is accomplished by in situ conversion of HO_2 to OH adding NO to the sample air stream [for details see Abram et al., 2000].

3.2.4 CO measurement technique

The Gas Filter Correlation (CFC) CO ambient analyser (Thermo Environmental Instruments Inc. Model 48) was used for the measurement of CO. The GFC spectroscopy is based upon comparison of the detailed structure of the infrared absorption spectrum of the measured gas to that of other gases also present in the sample being analysed. In the case of CO the technique is implemented by using a high concentration sample of CO as a filter for the infrared radiation transmitted through the analyser. CO and N_2 are alternated producing a modulated signal with an amplitude related to the concentration of the CO in the sample cell.

Variations in temperature cause a drifting of the base line which is corrected by programming a zero measurement the first ten minutes of every hour. A five point calibration of the instrument was performed directly before the campaign.

3.2.5 NO and NO_2 measurement techniques

The chemiluminiscent analyser MLU 200 AU was used for the monitoring of NO and NO_2. The instrument measures the light intensity of the chemiluminiscent gas phase reaction of NO and O_3. This reaction results in electronically excited NO_2 molecules which release their excess energy by emitting a photon. The light intensity produced is directly proportional to the NO concentration present. A molybdenum converter, heated at 315°C, is used to reduce any NO_x present to NO. NO_2 is obtained by subtraction of both values. The instrument has a detection limit of ~25 pptv NO for 1 min resolution and a relative error for the 1 σ confidence interval of 5% for 1 min averaged values.

The instrument was calibrated before and during the campaign. Both calibrations agreed within the experimental error.

3.2.6 PAN measurement technique

The PAN instrument (Meterologie Consult GmbH) consists of a gas chromatograph and a calibration unit. The measurement is based on the gas chromatographic separation of trace gases in the air sample followed by determination of PAN using an electron capture detector (ECD). Substances with high electronic affinity cause a decrease in the electronic density at the detector, which is compensated by a variation in the pulse rate at the electrodes of the detector. This variation is proportional to the amount of the substance in the sample. A sample is analysed every ten minutes and the system is calibrated regularly.

The calibration is based on the photolysis of acetone and the reaction of the formed peroxy acetyl radicals with NO to form PAN.

The detection limit is ~100 pptv and the 1 σ rel. error is ~10% for 10 min resolution.

3.2.7 H_2O_2 and CH_3OOH measurement techniques

This analytical technique uses high performance liquid chromatography (HPLC) with post column derivatization to separate and derivatize H_2O_2 and ROOH in any given sample. The peroxidase enzyme fluorescence technique is based on a method of Lazrus et al. [1986]. HPLC separation is achieved using an Merck LiChrospher C-18 reverse phase column with a mobile phase comprised of 10^{-3} M sulphuric acid and 10^{-4} M ethylenediamine tetraacetic acid solution supplied at a flow rate of 0.6 ml min^{-1}.

Samples are manually injected onto a 100 µl sample loop and flushed by mobile phase to the separating column. After separation hydroperoxides are derivatised to the stable dimer of p-hydroxyphenylacetic acid by addition of a reagent via a mixing tee. The reagent consists of 26mM p-hydroxyphenylacetic acid with 10^5 units l^{-1} of horseradish peroxidase in 0.5 M potassium hydrogen phthalate buffer at pH 5.8. After reagent addition, adequate contact time is given for the rapid reaction of hydroperoxides with the derivatization reagent. The pH of the solution is raised to between 10 and 11 to convert the dimer into its fluorescent anionic form using a membrane reactor constructed of Nafion tubing immersed in 30% ammonium hydroxide solution.

Dimer quantification is achieved by fluorescence detection using a fluorescence detector with excitation and emission wavelengths of 310 nm and 405 nm respectively. Calibration of the HPLC is performed twice daily with fresh standards made by serial dilution of a 30% hydrogen peroxide solution in the range of 10^{-7} to 10^{-8}, the concentration of which is determined by titration against potassium permanganate previously standardised with sodium oxilate.

The detection limit is ~20 pptv for 25 min resolution and the rel. error for 1 σ confidence interval is ~15%.

3.2.8 Other supporting measurements

In addition to the measurements made by the IUP-UB and Uni-Leeds, many other relevant trace gases including O_3, HONO, CH_2O, carbonyls, H_2O, NMHCs, SO_2, aerosols, and photolysis rates ($j(NO_2)$ and $j(O(^1D))$ were measured along with standard meteorological parameters. Back trajectories were used for the air mass characterization [British Atmospheric Data Centre – Trajectory service, http://www.badc.rl.ac.uk/].

3.2.9 Modelling

A zero dimensional model was used to simulate the observed trace gas diurnal evolutions. The atmospheric chemistry package ASAD (A Self-contained Atmospheric chemistry coDe) is used for solving the time-dependent chemical reactions [Carver et al., 1997]. It consists of 138 species describing CH_4, CO and a minor set of NMHC oxidations, 243 bimolecular, 32 termolecular and 36 photolysis reactions, and includes the deposition of H_2O_2, CH_3OOH and O_3 [Burkert et al., 2001b, 2003a]. The reactions have been compiled from the NIST (National Institute of Standards and Technology) Chemical Kinetics Database. It is assumed that the partly unknown pathways of NMHC and DMS oxidations lead to HCHO or peroxy radicals. The heterogeneous reactions of NO_3 are not considered in the model.

The photolysis rates are simulated if not measured, using the model PHOTOST, an improved version of the model PHOTOGT, already described 3.1.11. The input data used in PHOTOST are from GOME (Global Ozone Monitoring Experiment) on board the satellite ERS2 [Burrows et al., 1999 and references therein] and aerosol optical depth values calculated from the $j(O(^1D))$ measurements [Univ. Leeds, personal communication, 2002].

The model does not consider any dynamical processes. It has been successfully employed for the simulation of the diurnal evolution of trace gases measured over the Indian Ocean [Burkert et al., 2003a]. The mixing ratios of CH_4, NMHC, NO, NO_2, and CO have been constraint to the measurements on a 10 min base.

4 INDOEX campaign

The chapter that follows focuses on the analysis of the measurements performed during February, March, and April 1999 as a part of the Indian Ocean Experiment (INDOEX). The measurements were carried out on board the research vessel RV Ronald H. Brown above the Indian Ocean. The chapter is divided into two main sub-sections – "Trace gas and radical behaviour" and "Photochemistry and radiative effects of aerosols".

4.1 Definition of air masses

Making use of the 6 days back-trajectories and the measurements of chemical and aerosol composition, four different types of dynamical regimes could be defined during the campaign [Ball et al., 2003]:

- Southern Hemisphere maritime Equatorial (SHmE), characterised as having a long transport over relatively pristine regions
- Northern Hemisphere maritime Equatorial (NHmE), characterised as having passed over relatively unpolluted regions
- Northern Hemisphere continental Tropical (NHcT), the air flow passing over India
- Northern Hemisphere continental extratropical (NHcX), the air flows passing over the Arabian Peninsula.

The cruise tracks and the daily position are presented in Figure 18. The prevailing airflow patterns during the three legs of INDOEX are shown in Figure 19. These overall patterns of air movement represent the average situation but there is significant local, spatial, and temporal variability.

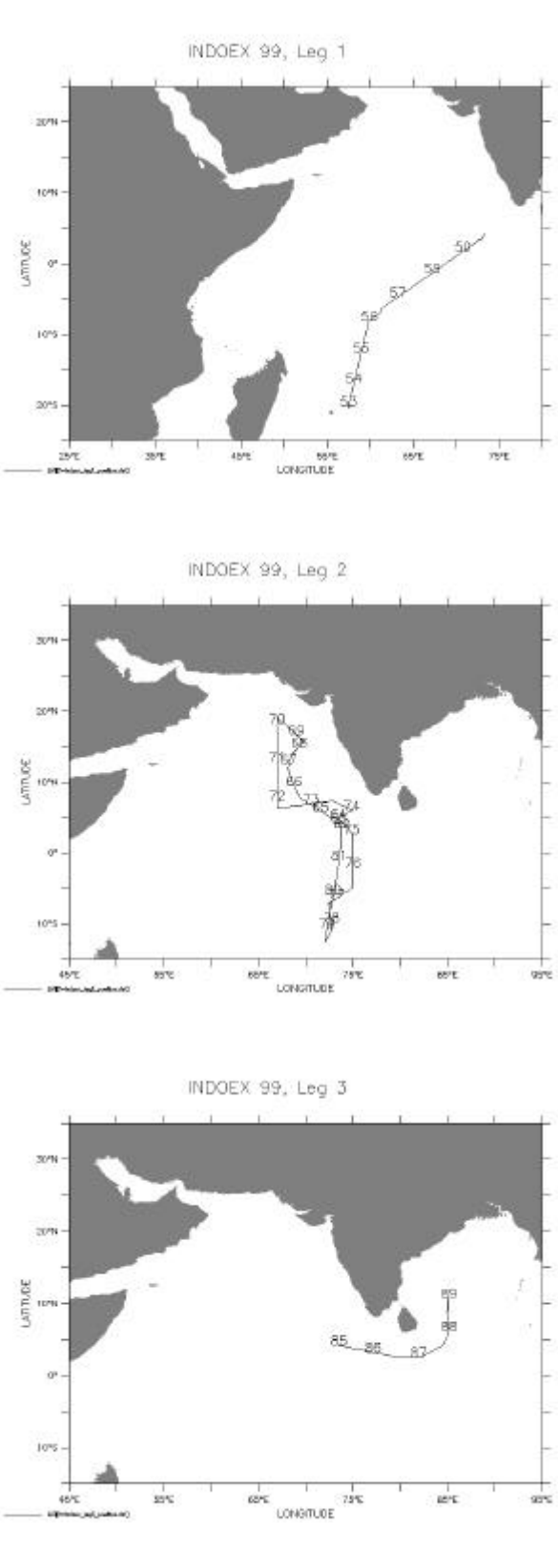

Figure 18: INDOEX cruise tracks for leg 1-3, numbers along the track indicate day of the year (DOY).

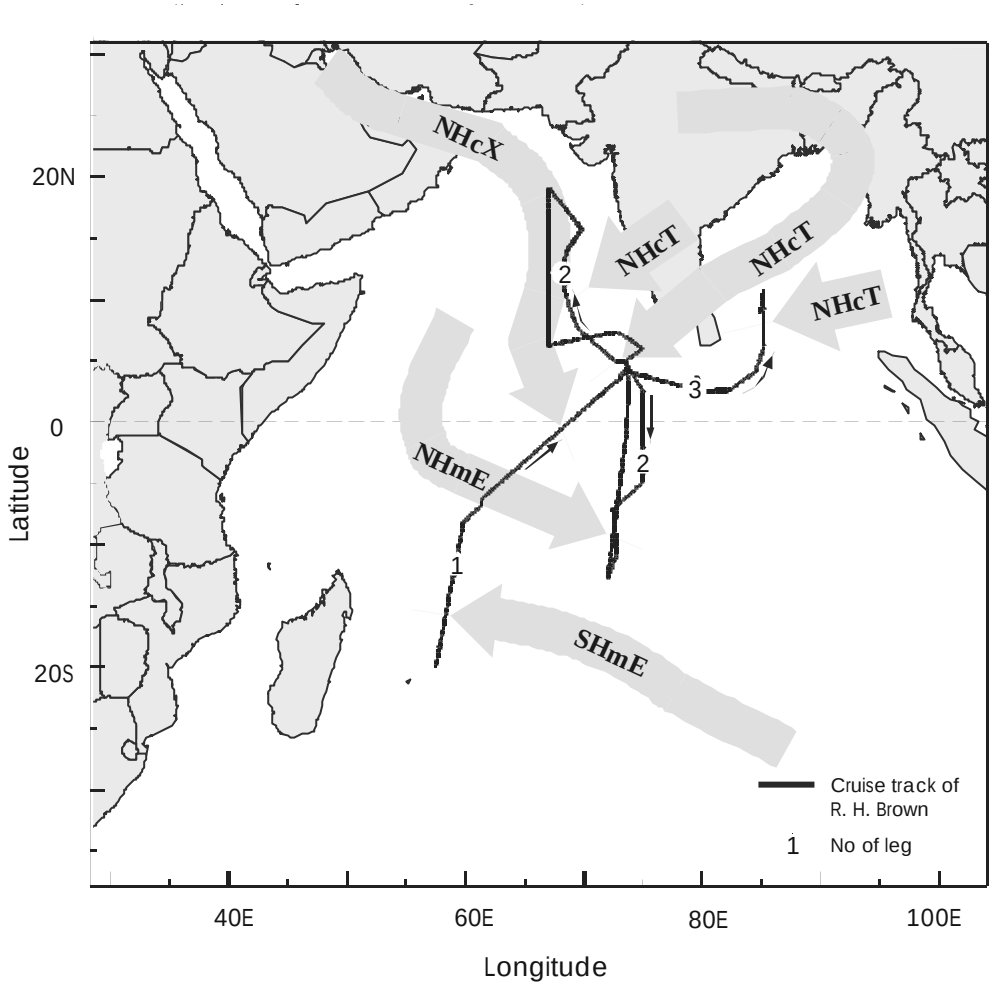

Figure 19: Cruise track of the RV Ronald H. Brown during the 1999 INDOEX campaign and the cluster trajectories (950 hPa) showing the origin of the air masses encountered during the different segments of the cruise. The flow regimes are labelled SHmE, Southern Hemisphere marine equatorial; NHmE, Northern Hemisphere marine equatorial; NHcT, Northern Hemisphere continental tropical (subdivided in the sub-regimes Bengal and West); and NHcX, Northern Hemisphere continental extra-tropical.

4.2 Trace gas and radical behaviour

4.2.1 Introduction

The accurate measurement of trace gases over the ocean provides a particularly useful approach to assess the accuracy of atmospheric chemical models, because the simple dynamics and the lack of anthropogenic emissions, reduce the number of physico-chemical processes required to describe and interpret the results. This study describes trace gas and free radical measurements made in the remote marine boundary layer (MBL), during INDOEX an international research initiative, proposed to study chemistry of remote regions of the Indian Ocean and the influence of outflow from the Indian subcontinent on these regions [see Crutzen and Ramanathan, 2001, Ramanathan et al., 2001, Lelieveld et al., 2001, Ball et al., 2003, http://www-indoex.ucsd.edu].

One result of the Pre-INDOEX studies was the clear observation of strong diurnal cycling of O_3 having a minimum during the day [Rhoads et al., 1997]. Similar but generally weaker cycling has been occasionally observed in the most remote regions of the Atlantic ocean from the German research vessels Polarstern and Meteor in a series of cruises from 1987 to 1996 [Burkert et al., 2001b]. In addition to the loss of O_3 by the reaction with HO_2, evidence for a significant role of reactive halogens in the chemistry of the pristine MBL was inferred from an analysis of the Pre-INDOEX observations [Dickerson et al., 1999].

This study describes the measurements of RO_2^*, NO, NMHC, $j(NO_2)$, $j(O(^1D))$ and O_3 made from the National Oceanic and Atmospheric Administration (NOAA) research vessel RV Ronald H. Brown in the MBL. These observations continued those made within AEROSOL campaign, which made measurements from Norfolk Virginia via the North and South Atlantic into the Indian Ocean [Andrés-Hernández et al., 2001].

The cruise track of the RV Ronald H. Brown during INDOEX was similar to the track of the Pre-INDOEX cruise, which took place during the fall of 1995 [Rhoads et al., 1997]. One overarching goal of the AEROSOL and INDOEX campaign is to improve our knowledge of the fast photochemistry of the MBL. Specific objectives of this study are to assess the impact of aerosols on photolysis rates, the role of continental emissions on pollution levels in the remote marine atmosphere, and the link between levels of O_3 and RO_2^*. To achieve this objective the measured concentrations and

diurnal variation of RO_2^* and HCHO [Wagner et al., 2001], predicted by a zero dimensional chemical model of the MBL have been compared with those measured to assess the possible role of multiphase and halogen chemistry in the budget of this species. The different behaviour of the observed amounts of RO_2^* above the Atlantic and the Indian Ocean is also discussed in this study.

The following scientific issues and questions are raised and discussed in this paper: How do aerosols influence the photolysis frequency at ground level? Are the current parameterisations for the radiative properties suitable and appropriate? Are the measured amounts of RO_2^* in agreement with that predicted by box model simulations? Are the observations of RO_2^* and HCHO consistent and do they reflect the close chemical linkage between these constituents? Is the difference between HCHO measurements and model results observed during INDOEX different to the observations above the Atlantic Ocean [Weller et al., 2000]? Does the presence of $1x10^4$-$1x10^5$ molec cm^{-3} amounts of reactive halogens provide a reasonable and plausible explanation of the unexpected behaviour of RO_2^* and HCHO? What are the potential sources of reactive chlorine and bromine in the remote MBL? Do geographical or regional effects help to explain the difference between model results and measurements?

4.2.2 Results

4.2.2.1 Characteristics of the different air masses observed

The four different air masses exhibited the following characteristics:

SHmE (observed during DOY 54-58, 78.25-79.5)

The SHmE regime showed the lowest mixing ratios for all trace species and in this sense was the least polluted air encountered. The maximum RO_2^* mixing ratio during DOY 54 – 58 decreased with decreasing latitude from 35 to 25 pptv. The O_3 mixing ratio revealed the same behaviour, decreasing from 15 to 8 ppbv. The loss of O_3 per latitude decreased with decreasing latitude. The mean CO mixing ratio was 56 ppbv, the daytime average NO mixing ratio was below the detection limit of around 3 pptv. The NMHC mixing ratios were the lowest observed during the whole campaign. The mean values were: ethane 194 pptv, propane 7 pptv, and acetylene 21 pptv [Mühle et al., 2002]. The vertical profiles of O_3 mixing ratio showed a weak positive gradient with

increasing altitude up to 12 km between 12°S and the ITCZ, where the O_3 reached levels about 40 ppbv [Hermann Smit, personal communication, 2001].

NHmE (observed during DOY 76-78.25, 79.5-81)

In the NHmE regime the CO and O_3 mixing ratios were around 90 ppbv and approximately 10 ppbv, respectively. The maximum RO_2^* mixing ratio varied between 55 – 60 pptv. The back-trajectories indicate a long travel time of the air parcel along the west coast of India. The NO mixing ratio was below the detection limit. Most of the NMHC doubled their mean mixing ratios compared to the SHmE air mass: ethane 332 pptv, propane 10 pptv, and acetylene 44 pptv. The vertical profiles of O_3 in this regime indicate an even weaker positive gradient in altitude compared to the SHmE regime, reaching levels of about 30 ppbv at 12 km.

NHcT (observed during DOY 63-66, 74-76, 85-89)

The NHcT regime was characterised by the highest observed maximum mixing ratios in RO_2^* and CO during the whole campaign. Maximum levels of up to 90 pptv RO_2^* and 200 ppbv CO were observed. NO measurements were higher than in the SHmE, but still close to the detection limit, around 6 pptv. The O_3 mixing ratios showed strong diurnal variations, with O_3 losses during the day being as large as 50%. The latitudinal gradient in O_3 was ~ 1.25 ppbv/°latitude heading North. The NMHC main mixing ratios increased for ethane up to 403 pptv, propane to 20 pptv, and acetylene to 133 pptv. The vertical O_3 profiles revealed an enriched layer between 1 and 3 km having mixing ratios larger than 70 ppbv. The upper level O_3 values were different depending on the periods of observation. Back-trajectory analysis indicated that the air masses originated over India and the Bay of Bengal. The NHcT regime also appears to contain high concentrations of ash, soot, and other organic matter [Dickerson et al., 2002, Neusüß et al., 2002, Quinn, et al., 2002]. In addition the regime is heavily contaminated by fossil fuel combustion (indicated by sulphate), biomass burning (indicated by nss-potassium), and wind-blown mineral dust (indicated by ash and nss-calcium) [Ball et al., 2003, Quinn et al., 2002, Stehr et al., 2002]. The black carbon from India is currently considered to result mainly from internal combustion engines, biomass burning, and small-scale coal combustion. However, bottom-up estimates of black carbon emissions from India yield much smaller values than in situ observations do. This suggests an additional source not yet considered or unusually high emissions

factors [Dickerson et al., 2002]. Therefore a large uncertainty in the sources and/or emissions remains.

NHcX (observed during DOY 66-74):

The NHcX regime was characterised by the highest observed concentration of O_3 and NMHC at the most northerly point of the whole campaign. O_3 mixing ratios reached levels up to 53 ppbv and the NMHC averaged mixing ratios were: ethane 927 pptv, propane 133 pptv, and acetylene 169.3 pptv. The latitudinal gradient in O_3 remained ~ 1.25 ppbv/°latitude heading North. RO_2^* and CO varied weakly around 55 pptv and 122 ppbv respectively. NO mixing ratios reached their highest values of the campaign being approximately 9 pptv. The vertical profile in O_3 showed the same behaviour as in the NHcT regime with an O_3 enriched layer above the MBL. The back-trajectories indicate that the air masses originated over the Arabian Peninsula.

4.2.2.2 Measurements trace constituents and parameters

4.2.2.2.1 RO_2^*, O_3, and CO measurements

RO_2^*, O_3 and CO were continuously measured from DOY 54 to DOY 89. The observed RO_2^*, O_3, and CO diurnal cycles for the three legs are presented in Figure 20. The RO_2^* mixing ratios showed the typical diurnal variation with the maximum occurring between midday and early afternoon. The RO_2^* daytime maximum values varied from 25 to 90 pptv. CO concentrations did not show any significant diurnal variation, they only changed with different air masses. The CO values varied in the NH between 100 and 200 ppbv and in the SH between 40 and 70 ppbv.

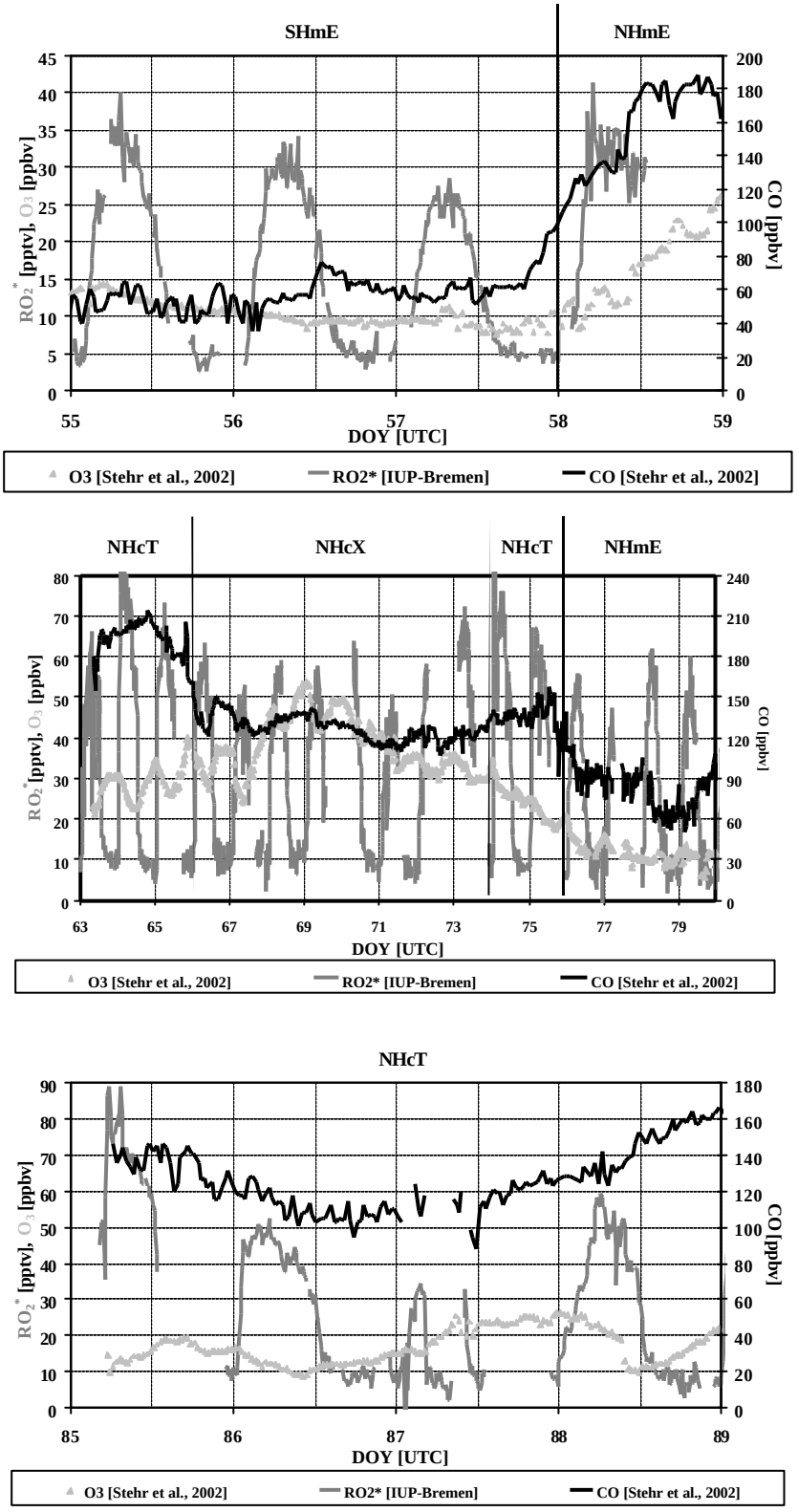

Figure 20: Plots of the individual diurnal variation of RO_2^*, O_3, and CO observed on legs 1 to 3 of INDOEX. The classification of the air masses encountered are written above, the days and vertical lines separate the different types of air masses.

The O_3 mixing ratio typically decreases during daytime with a minimum close to sunset and a recovery during the night. In contrast to this behaviour the O_3 in leg 1 does not show any recovery at night and each day the average O_3 mixing ratio is smaller. This implies that the net photochemical losses during the day are equal to the latitudinal variation of O_3. The maximum values of O_3 varied in the SH between 8 and 15 ppbv and in the NH between 10 and 55 ppbv.

4.2.2.2.2 NO measurements

The NO data collection for INDOEX began on DOY 53. The average mixing ratio of NO in the SHmE air mass was 3 pptv, being comparable to the 4.8 pptv reported for the SHmE regime [Rhoads et al., 1997]. The average mixing ratio for NO within NHcT was 6 pptv, compared to 4.7 pptv found in the earlier cruise.

A summary of the measurements of NO associated with the different air mass type is given in Table 4.

airmass design.	NO mixing ratio mean [pptv]	stdev.	Number of measurements (24 hour avg.)
SHmE	3	5	6
NHcT	6	11	7
NHcX	9	8	6
NHmE	below detection limit	-	2

Table 4: Averaged NO mixing ratios observed in four different air masses. Mixing ratios were computed as day-night differences.

The largest mixing ratios of NO were found within the NHcX air mass, where input from the Indian continental regions is expected to be low and the travel time over the ocean relatively long compared with that for the other air mass types, being about 3-5 days. Therefore, the NO was most likely transported in the upper layers of the troposphere, where the lifetime of NO is much longer compared to the MBL.

4.2.2.2.3 j($O(^1D)$) and j(NO_2) photolysis frequency measurements

In Figure 4, the measured j($O(^1D)$) and j(NO_2) photolysis frequencies for leg 2 of INDOEX and two selected days in the NH and SH, respectively, are shown. The variation in the maximum j($O(^1D)$) values indicates the large influence of the aerosols on the photolysis frequencies. The reduction is about 40% for j($O(^1D)$) and about 22% for j(NO_2).

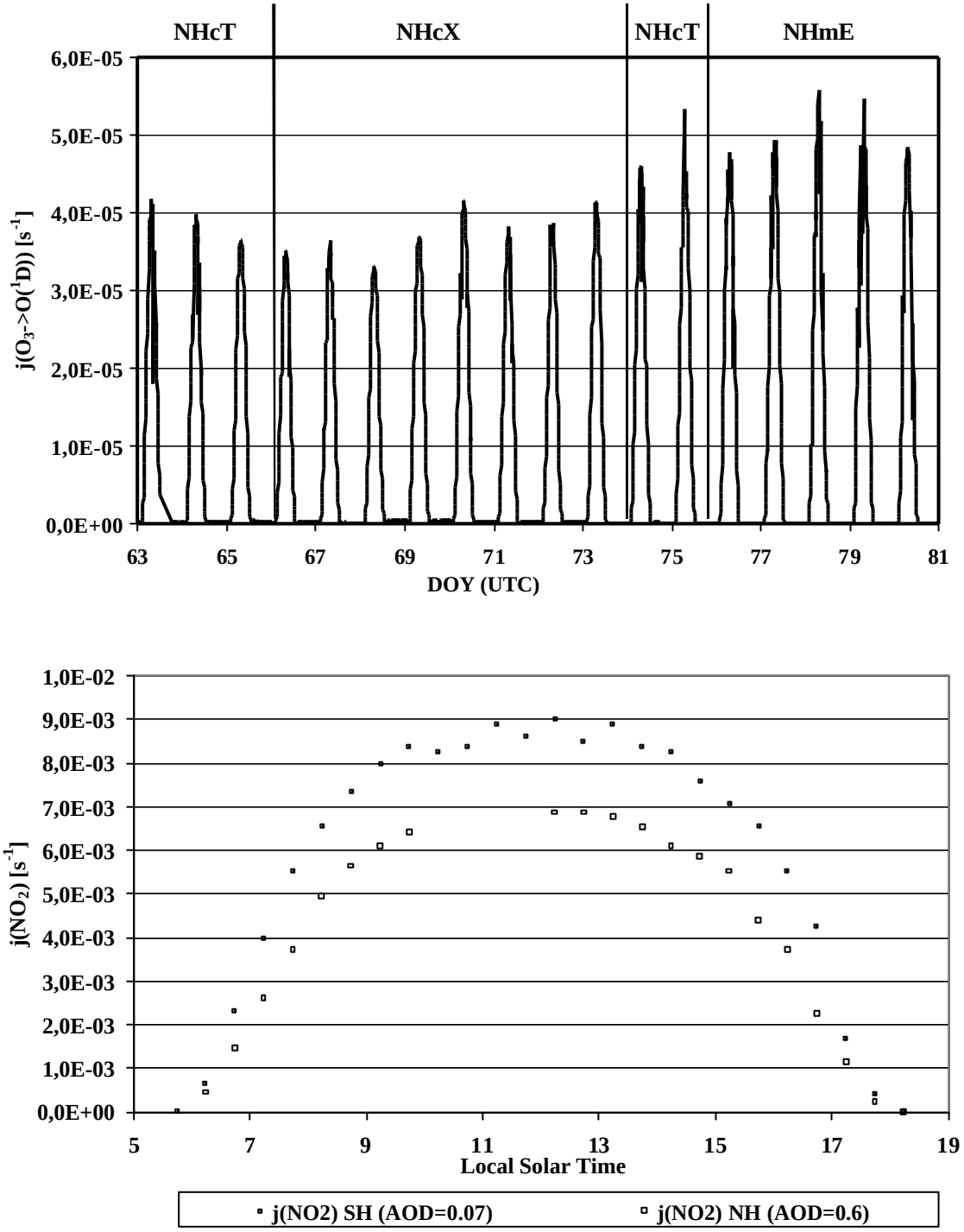

Figure 21: a) Measured j($O(^1D)$) photolysis rates for leg 2 (DOY 63 – 80) during INDOEX. b) Diurnal variation in the photolysis rate coefficient for NO_2; only cloud-free data are shown. Filled squares represent data from the clean, marine atmosphere on DOY 57 at 4°S with an AOD of about 0.07 at 500 nm. Open squares represent data from a polluted atmosphere over the northern Indian Ocean on DOY 65 at 6°N with an AOD of 0.4 at 500 nm.

Taking into account that more than half of the light driving the photolysis of O_3 to $O(^1D)$ is scattered "skylight" rather than direct sunlight, the sometimes observed small cumulus clouds have little impact and the assumption of clear sky conditions for the model used later on is therefore reasonable.

4.2.2.2.4 NMHC measurements

The NMHC measurements have been separated into the amounts of smaller (C<5) and larger (C>4) alkanes and are presented in Figure 22. Some of the data have already been presented by Mühle et al. [2002]. The highest amount of all alkane was observed in the NHcX regime, moderate levels being present in the NHcT regime and the lowest values were encountered in the NHmE: the latter being around half of that in the NHcT regime. The transition between NHcT and NHmE was gradual, and not as sharp as the transition between other air masses. Air masses, influenced by the Arabian Peninsula, contain the highest amounts of NMHC: the daily peak being up to twice as high as the average concentration.

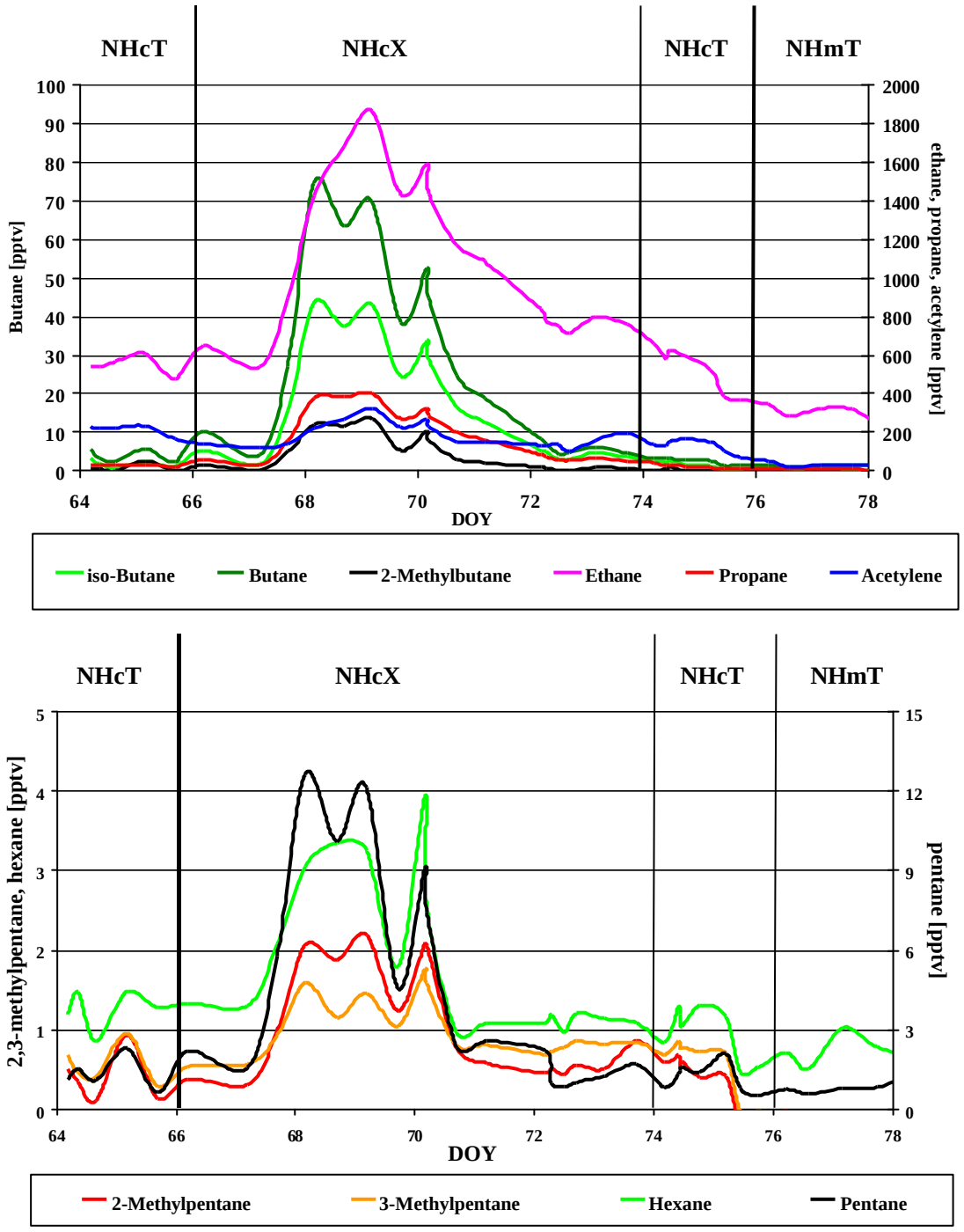

Figure 22: NMHC, i.e. alkane and acetylene measurements in the NH during INDOEX (DOY 64 – 78) a) the lighter alkanes and acetylene, b) the heavier alkanes measured.

The observed decrease in the measured concentrations of the NMHC on DOY 66, 67, 72, and 73 cannot be explained by chemical destruction but rather by transport effects. The 800 mbar back trajectories, which originated over India, indicate an increasing downward mixing of NHcT air masses into the NHcX air masses in the MBL.

4.2.3 Discussion and Interpretation

In this section the measurements of trace constituents and parameters are analysed. Initially the photolysis frequencies, which were determined by calculation in the model, are compared with the ground based measurements. The role of aerosol on the photolytic radiation in the MBL is then discussed. Accurate knowledge of the photolysis frequencies is required as input for the chemistry of the box model.

4.2.3.1 Simulation of photolysis frequencies

Photolysis frequencies for the photolytic active trace gases were calculated in this study using PHOTOST, an improved version of the model PHOTOGT [Blindauer et al., 1996], which has been upgraded to use the radiative transfer model (RTM) SCIATRAN [Buchwitz, 2000] in place of its predecessor GOMETRAN [Rozanov et al., 1998]. To initialise the RTM, the in situ measurements of the aerosol optical depth (AOD) made during INDOEX were used [Welton et al., 2002]. These agreed with the observed sun photometer measurements [Meywerk and Ramanathan, 1999, Welton et al., 2002]. The photolytic radiation, encountered in the MBL during the INDOEX campaign, was determined in the model taking explicitly into account the following:

- Rayleigh single and multiple scattering by air molecules,
- O_3 absorption of ultraviolet radiation, the values of total O_3 column being those measured by GOME on board the ERS-2 satellite [Burrows et al., 1999 and references therein], all other trace gases were taken from a climatology database [Brühl and Crutzen, 1993].
- the effective surface spectral reflection at the ocean surface, albedo (α=0.05). The underestimation of the actinic flux on account of neglecting the SZA dependence of the albedo is below 1% (SZA = 60°), 2.5% (SZA = 70°), 6% (SZA = 80°), and 8% (SZA = 90°) [Cox and Munk, 1954, Jin et al., 2002]

- single and multiple scattering and absorption by aerosol, the aerosol parameters being defined in the model such that the aerosol composition and the aerosol optical depth (AOD) were compatible with the in situ and sun photometer measurements.

During INDOEX the aerosol composition of the MBL was continuously measured at the island station of Kaashidoo [Lelieveld et al., 2001]. The average of the entire dataset is shown in Table 5 a) and is used to describe the aerosol composition in the model. The atmosphere above the MBL contains only the Kaashidoo compositions, whereas the MBL contains a mixture between the a) Kaashidoo aerosol compositon and b) sea salt aerosol composition, as described in Table 5 c).

a) non sea salt composition (nss)

Kaashidoo aerosol composition:	
Type	Dry mass %
Sulfate	31
Organics	25
Black carbon	15
Mineral dust	11
Ammonia	9
Fly ash	6
Minor components	3

b) sea salt composition (ss)

Sea Salt aerosol composition:	
Type	Dry mass %
Water soluble	7.1
Sea salt (acc. mode)	90.8
Sea salt (coarse mode)	2.1

c) mixing in the model

DOY	Composition
55-57; 78	87 % ss; 13 % nss
58-60; 63-67; 85-88	18 % ss; 82 % nss
68-70	40 % ss; 60 % nss
71-76	33 % ss; 67 % nss
77; 79-82	65 % ss; 35 % nss

Table 5: a) Averaged aerosol composition measured at Kaashidoo during the INDOEX campaign [Lelieveld, et al., 2001] and b) typical sea salt aerosol composition [Shettle and Fenn, 1976]. c) describes the MBL mixing between a) and b) assumed in the model.

The average daily measurements of the AOD [Welton et al., 2002] were used. The diurnal variation in aerosol composition was not taken into account. Analysis using the LOWTRAN-7 parameterisation for several different types of aerosols indicates that changes in the aerosol composition within the range of that observed in INDOEX, have only a negligible effect on the photolytic radiation field in the MBL. This assumption is supported by comparing the measured single scattering albedo of 0.874 ± 0.028 at 500 nm for the INDOEX period at Kaashidoo island [Bush and Valero, 2002] and our calculated value of 0.882 for this region. For the whole campaign the single scattering albedo values varied between 0.882 for the most polluted case and 0.932 for the SH region encountered during the campaign.

The profile of the aerosol extinction, $\alpha(\lambda, z)$ [km^{-1}] was obtained by using the LOWTRAN-7 aerosol profiles [Shettle and Fenn, 1976] for different scenarios, but modifying them in the lowest 5 km of the troposphere in order to fit the measured AOD (Figure 23).

$$AOD(\lambda) = \int_{z_1}^{z_2} a(\lambda, z)dz \tag{141}$$

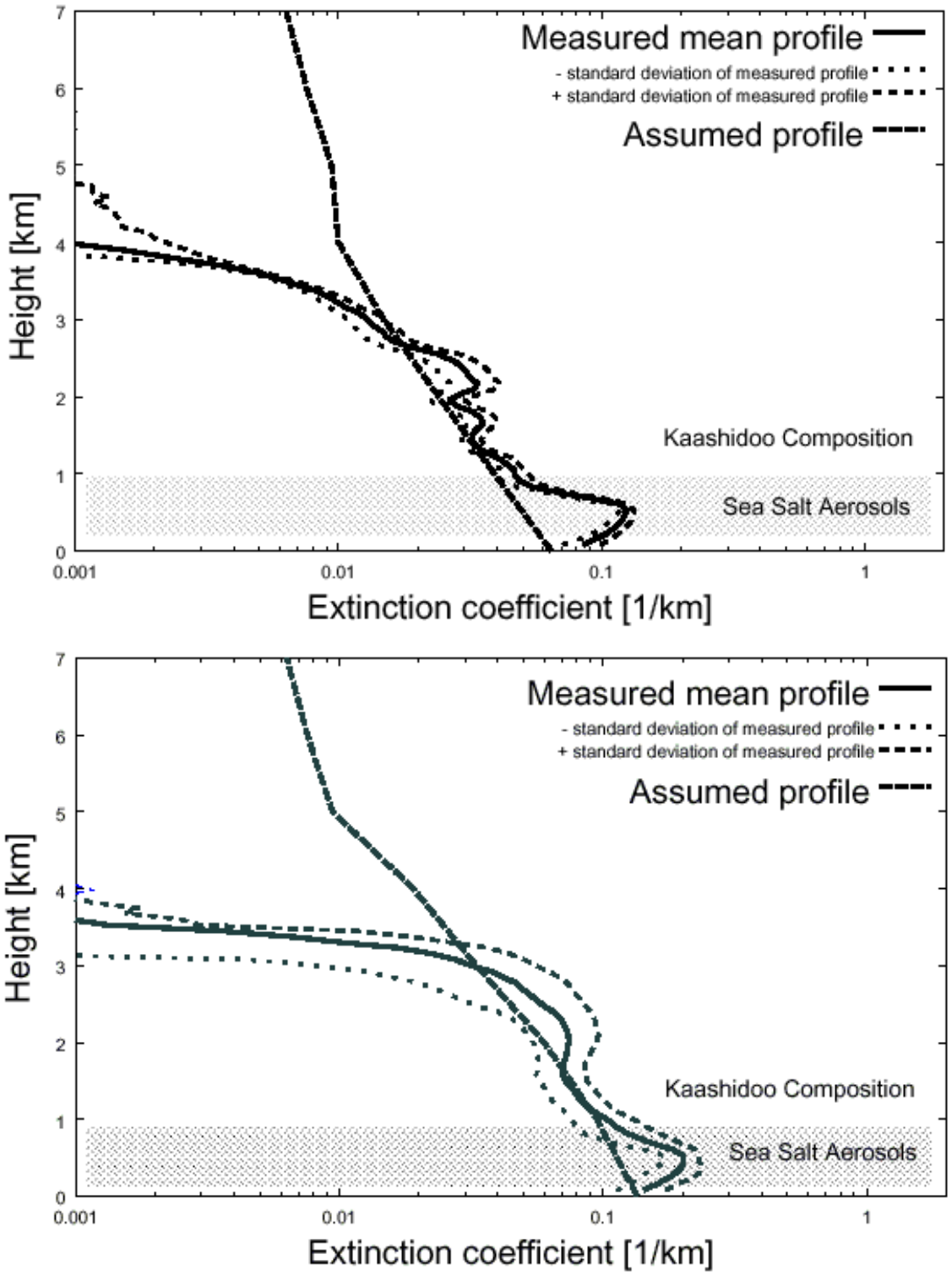

Figure 23: Micropulse Lidar (MPL) average profiles for AOD=0.15, 0.30, 0.45, 0.6. All extinction coefficient profiles are a mixture between the measured and the smooth Lowtran-profile [Welton, et al., 2002].

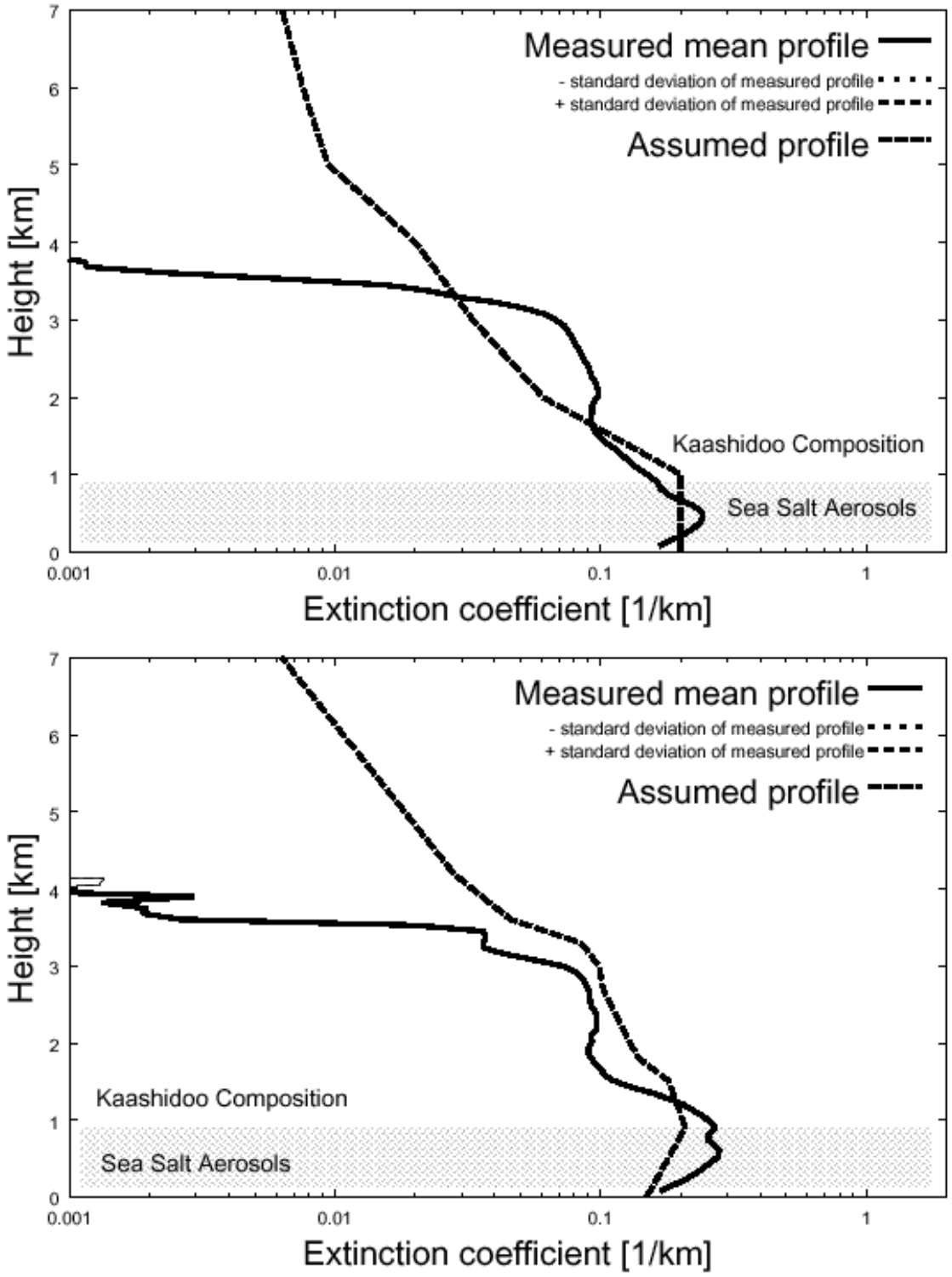

Figure 23: Micropulse Lidar (MPL) average profiles for AOD=0.15, 0.30, 0.45, 0.6. All extinction coefficient profiles are a mixture between the measured and the smooth Lowtran-profile [Welton, et al., 2002].

In situ measurements of the aerosol extinction coefficient with respect to height have been performed on board the RV Ronald H. Brown [Welton et al., 2002].

The measured photolysis frequencies shown in Figure 24, Figure 25, Figure 26, and Figure 27 are based on 2π sr, whereas the model results are for 4π sr. Therefore all measured photolysis frequencies for 4π sr should be approximately 5-7% higher to account for the upwelling flux caused by the reflection at the ocean surface.

Figure 24 shows the modelled photolysis frequencies $j(O(^1D))$ and $j(NO_2)$ for AOD varying between 0.0 and 0.6, versus sec(SZA). The results show that the influence of aerosols varies with the SZA. The $j(O^1D)$ rate for AOD = 0.0 decreases up to 23% for AOD = 0.6 for sec(SZA) = 1, the relative effect decreases up to 39% for sec(SZA) = 2. The same behaviour is observed for $j(NO_2)$, for sec(SZA) = 1 the relative decrease is 17% and for sec(SZA) = 2 the relative decrease is 37%.

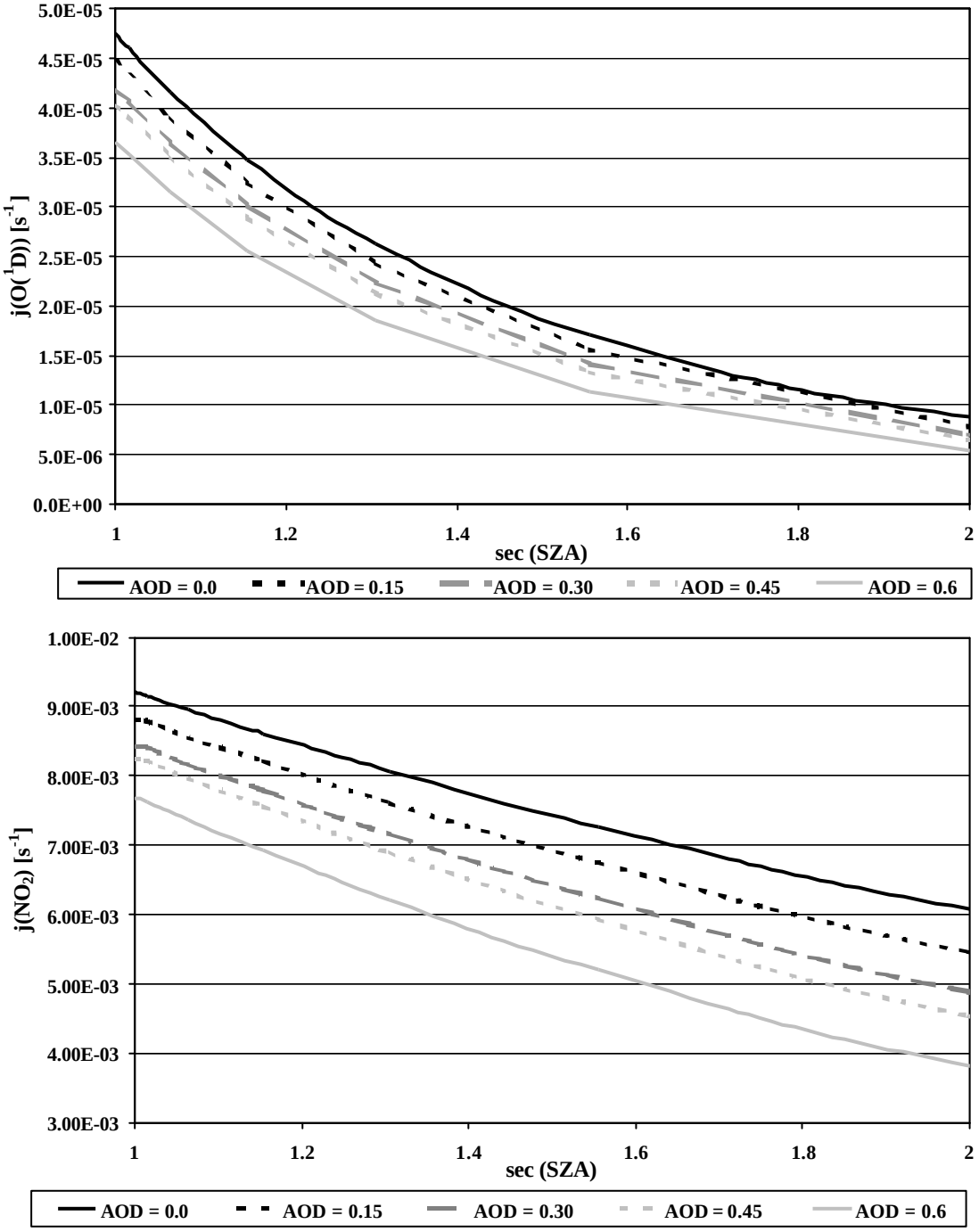

Figure 24: Modelled photolysis frequencies of $j(O(^1D))$ and $j(NO_2)$ for different AOD vs. sec(SZA).

The calculated j values depend upon Rayleigh scattering (α_{ray}), trace gas absorption (α_{trace}), and Mie scattering (α_{Mie}, i.e. aerosol scattering). The influences of these three effects are wavelength dependent. In general the α_{ray} and α_{trace} (e.g. O_3 and NO_2) are more important in the short wavelength region and α_{Mie} becomes more

significant in the longer wavelength region. Therefore, the relative influence of aerosols on the photolysis frequencies, as measured by the ratio j(AOD=0.0)/j(AOD=0.6), which varies with sec(SZA), is higher at longer wavelengths. Thus $j(NO_2)$, which is weighted towards 400 nm is expected to be more influenced by the presence of significant amounts of aerosol than $j(O(^1D)$, which is weighted towards 300 nm.

In Figure 25, the correlation of simulated and measured $j(O(^1D))$ is plotted separated into different AOD regimes. Overall the agreement is reasonable, but in general the calculated j values underestimate the measured photolysis frequencies when lower AODs are present. This leads to differences of up to 11% for the lowest aerosol loading observed during the campaign. This effect is most probably caused by the assumed climatology profile of the trace gases, which is not representing the encountered situation correctly. However, even if we use a profile in the model that represents the low aerosol cases, we cannot reproduce the decreasing effect of the aerosols on the photolysis frequencies. The model accounts only for a decrease in $j(O(^1D))$ by aerosols of 10% (AOD 0.1 to 0.4, SZA 20°, see Figure 24), whereas the measurements show a decrease of 33% for DOY 57 (SZA 20°, AOD 0.1) compared to DOY 68 (SZA 20°, AOD 0.4).

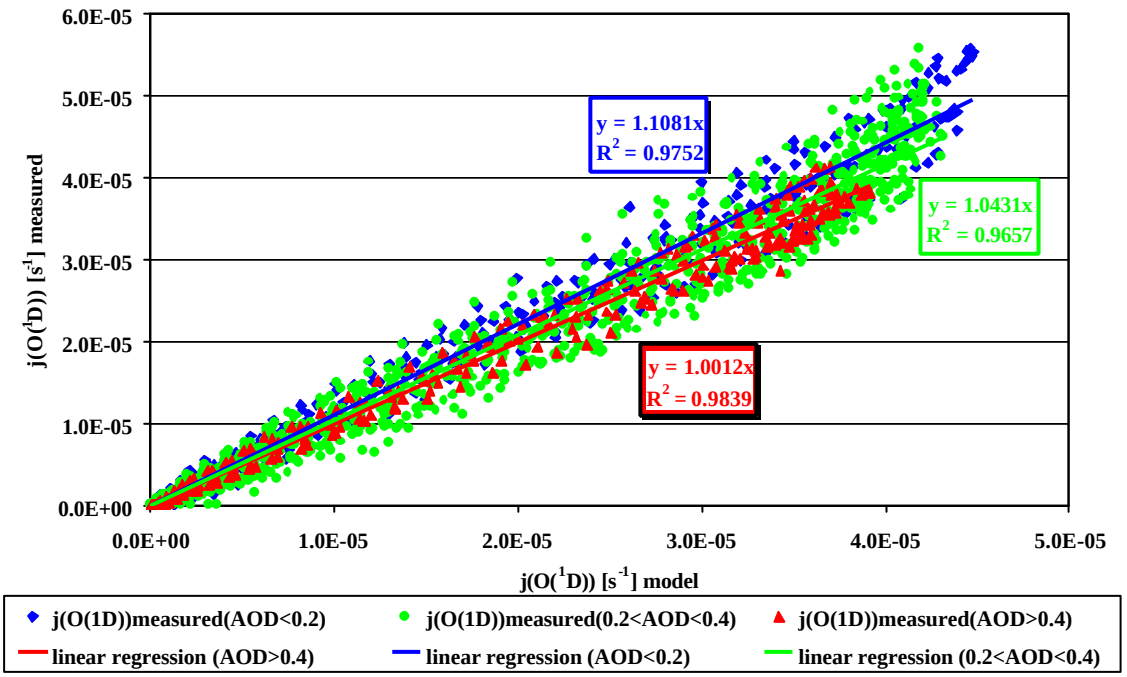

Figure 25: Correlation between measured and modelled $j(O(^1D)$ photolysis rates during INDOEX, separated into different AOD ranges.

Figure 26 shows $j(NO_2)$ versus local solar time for different conditions: clean maritime air above the Indian Ocean, polluted air above the Indian Ocean and polluted air over the eastern US for comparison. Figure 27 is similar to Figure 26 but plotted versus sec(SZA). The comparison between measured and modelled $j(NO_2)$ show a good agreement for the low aerosol case (DOY 57), but the high aerosol case (AOD = 0.4) is overestimated by the model, even for AOD 0.6. Again the model cannot account for the influence of the aerosol on the photolysis rate. It appears that the absorption of aerosols in the UV is not well parameterised in the LOWTRAN-7 algorithm [Burkert et al., 2003c]. Within this context, Jacobson [1999] hypothesized the absorption of nitrated and aromatic aerosol components and nitrated aromatic gases can play a significant role in the attenuation of the ultraviolet irradiances. In contrast to Figure 25, Figure 26 and Figure 27 show, that $j(NO_2)$ for the low aerosol case is well described in the model, whereas the high aerosol case is overestimated by ~ 15%. This different behaviour indicates an inaccurate model parameterisation in the wavelength behaviour of the absorption and/or scattering of the aerosols and/or absorption of nitrated aromatic gases [Jacobson, 1999].

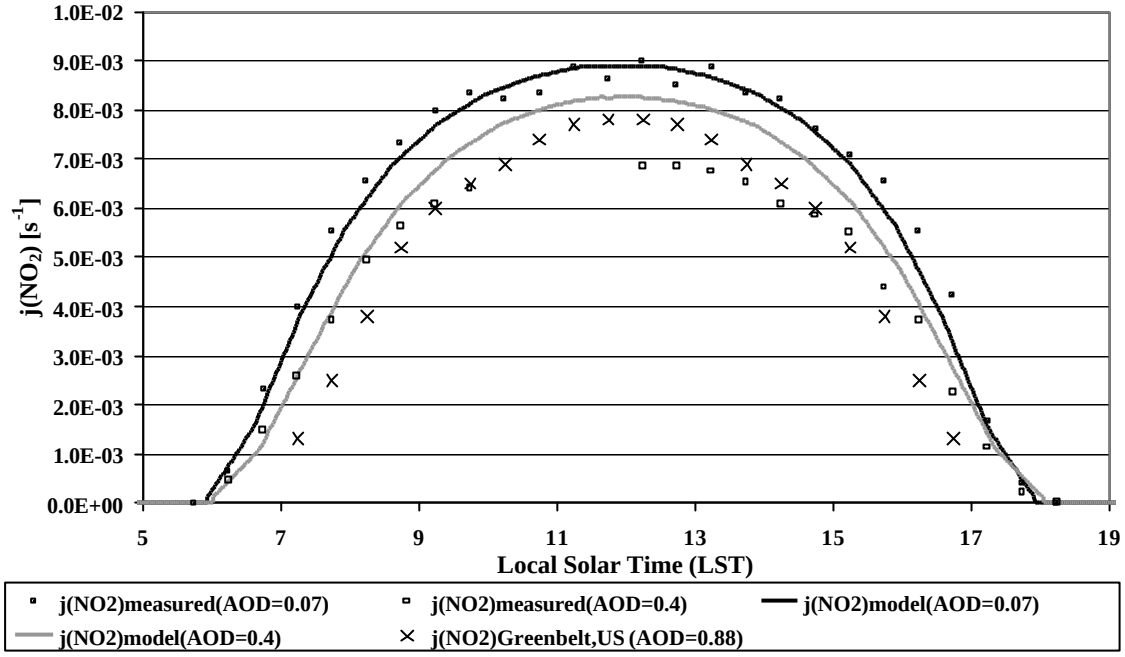

Figure 26: Diurnal variation in the photolysis rate coefficient for NO_2; only cloud-free data are shown. Filled squares (measurements) and the black curve (model) represent data from the clean, marine atmosphere on DOY 57 at 4°S with an AOD of about 0.07 at 500 nm. Open squares (measurements) and grey curve (model) represent data from a polluted atmosphere over the northern Indian Ocean on DOY 65 at 6°N with an AOD of 0.4 at 500 nm. Crosses represent data from the polluted atmosphere over the Eastern US (Greenbelt, Maryland, 39°N) on July 15, 1995 with an AOD of 0.88 at 520 nm and 1.4 at 380 nm.

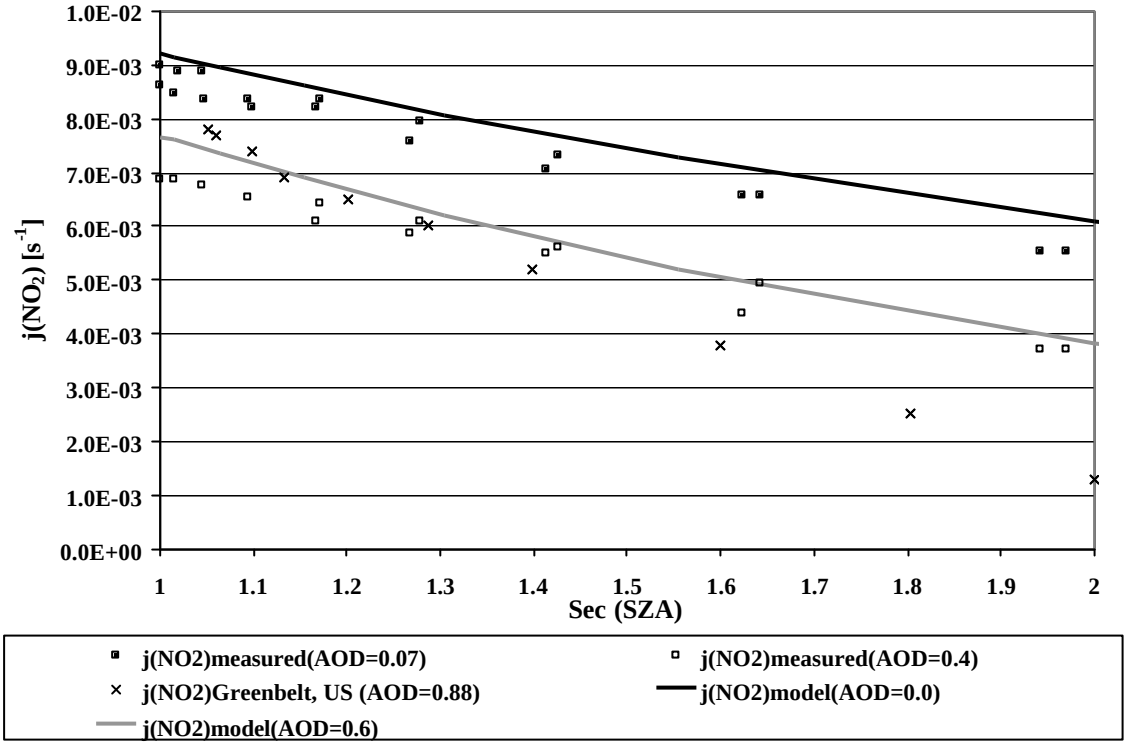

Figure 27: The same data as Figure 26, but with the photolysis rate coefficients plotted as a function of the secant of the solar zenith angle. Filled squares (measurements) and black curve (model) represent data from the clean marine environment; Crosses represent data from a polluted environment over North America, and open squares (measurements) and grey curve (model) represent data from a polluted environment in the Northern Indian Ocean.

Clearly the polluted Indian Ocean air appears to be the most severely impacted by the presence of aerosols. Particles with a low single scattering albedo (ω), as were encountered downwind of India, are more effective at reducing the rate of NO_2 photolysis (and the rate of O_3 production) than are particles having a single scattering albedo near unity, which is the normal situation, encountered over the eastern US. This is especially true for small solar zenith angles (near solar noon) when enhanced scattered radiation from particles with a high ω compensates for losses in the direct beam. Comparing the j(NO_2) model results with the measurements in Figure 27 shows that the weaker variation with the sec(SZA) for the INDOEX data is well reproduced in the model. Therefore the assumed aerosol composition seems reasonable, only the total amount of absorption by the aerosols is not in agreement with the measured results.

4.2.3.2 Interpretation of the MBL chemistry

The chemistry of the MBL during INDOEX was simulated constraining the model to the measurements of trace gases and conditions described above. In more detail, the species, DMS [Wisthaler et al., 2002], H_2 (500 pptv), O_2 (21 %), N_2 (78 %), CH_4 (1.8 ppmv NH, 1.7 ppmv SH), CO_2 (350 ppmv), NMHC (i.e. C_2H_6, C_3H_8, C_2H_2, C_2H_4, C_3H_6) were held constant in the model. The trace gases, C_2H_2, C_2H_4, and C_3H_6 were fixed to the values measured by [Jens Mühle, personal communication, 2002] and are shown in Table 6.

	C_2H_4	C_3H_6	C_2H_2
SHmT	48	15	20
NHcT	62	22	200
NHcX	60	23	250
NHmT	66	22	25

Table 6: Assumed mixing ratios for C_2H_4, C_3H_6, and C_2H_2 seperated into different air mass regions [according to Jens Mühle, personal communication, 2002]

These values can only be treated as rough estimates as the probes were partly contaminated by the building up of alkenes due to the long storage time of the canisters [for details Mühle et al., 2002]. The concentrations can be assumed as upper limits compared with literature values [Singh and Salas, 1982, Duce et al., 1983, Heikes et al., 1996]. However, sensitivity studies have shown that the concentration of these species have a negligible influence on the RO_2^* and HCHO model results. The mixing ratios of H_2O, CO, O_3, HCHO [Wagner et al., 2002], and CH_3OH [Wisthaler et al., 2002] were initialised each day with the measured values at 0 UTC. For the trace gases not measured during the cruise, the following values were used for initiation of the photochemistry: H_2O_2 (1000 pptv), and CH_3O_2H (400 pptv). The photolysis frequencies were initialised every 10 min with the values calculated by the PHOTOST model. The model results were scaled to the measured $j(NO_2)$ and $j(O(^1D))$, including the correction for the reflected radiance. No dynamic processes were considered in the box model. Reasonable agreement between simulated and measured trace gases was achieved on most of the days. The analysis of the results highlights the following interesting features:

4.2.3.2.1 RO_2^* diurnal variation

Figure 28 shows the averaged diurnal behaviour for the measured and modelled RO_2^* mixing ratios for the NH and SH. A clear early morning and late afternoon bulge of RO_2^* is observed: The maximum of RO_2^* being around local noon (~UTC +4 hrs).

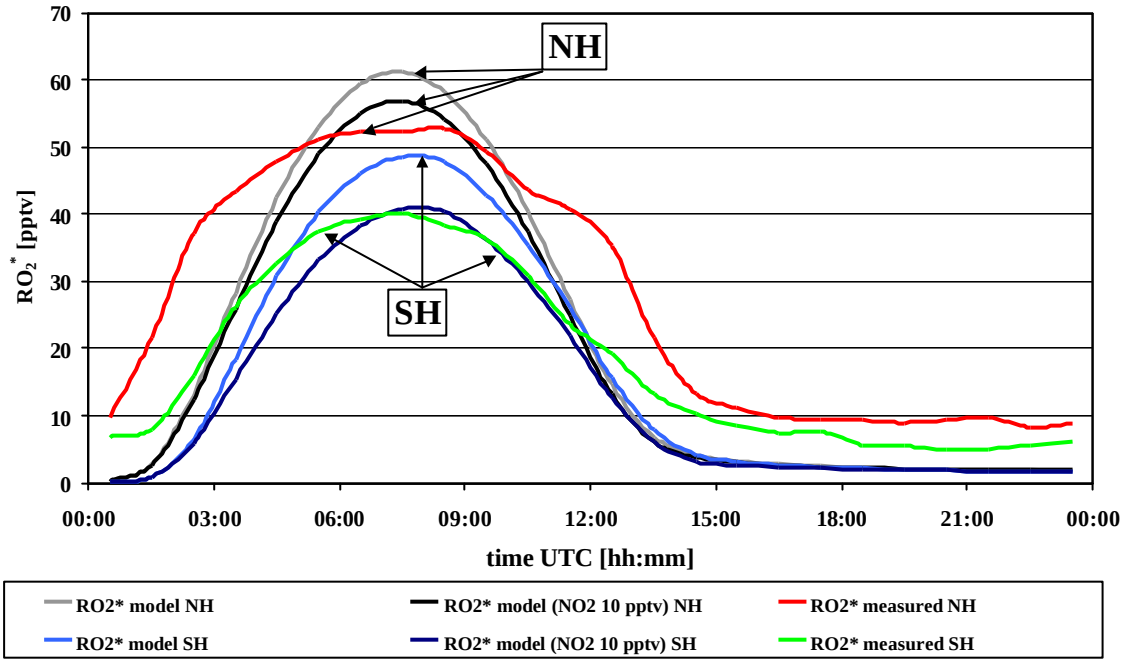

Figure 28: Average diurnal variation of measured and modelled RO_2^* mixing ratios for the NH and SH during INDOEX. Local time is given by UTC + ~4 hrs.

The chemical simulations were performed with two different input values comprising the reported NO for the NH and the SH. In order to achieve reasonable NO behaviour, the NO_2 mixing ratio was fixed to either 0 or 10 pptv. In the 10 pptv case, the photodissociation of NO_2 and the reactions between NO, O_3, and NO_2 lead to a diurnal variation of NO with maximum mixing ratios around noon, varying between ~5-8 pptv. Any variation of NO_2 can be neglected, because its reactions are of minor importance for RO_2^* under the investigated conditions.

The averaged maximum RO_2^* mixing ratio, occurring within two hours of local noon, is reasonably well simulated in both hemispheres within the experimental error. Maximum mixing ratios are reached at solar noon. In the SH air masses, the CO mixing ratios are lower than those in the NH air masses, while the amount of CH_4, the dominant hydrocarbon is about the same (SH ~ 1.7 ppmv, NH ~ 1.8 ppmv). As a result, the rate of

conversion of OH to HO_2 is reduced and relative to the amount of HO_2 more RO_2, i.e., only organic peroxy radicals without HO_2 are produced. These effect result in the ratio of RO_2 to HO_2 being higher in the SH than in the NH. When small amounts of NO are added to clean NH or SH air in the model, the relative effect in the RO_2^* mixing ratio is larger in the SH, because the ratio of RO_2 to HO_2 is larger in the SH than in the NH. A variation of the fixed input NO_2 mixing ratios in the model between 0 and 10 pptv leads to differences in the maximum RO_2^* mixing ratios at noontime up to 20% in the SH and up to 10% in the NH.

The modelled local noontime averaged ratio of RO_2/HO_2 without NO_x chemistry is about 2 for the NH and 3 for the SH. In the model run with 10 pptv NO_2 the ratio decreases to ~1.6 for the NH and ~1.8 for the SH.

A non negligible nocturnal signal of RO_2^* varying between 5 and 10 pptv is observed on most of the days. In contrast the RO_2^* signal decreases to values below the detection limit and close to zero during the occasional rain periods observed during INDOEX. Similar nocturnal signals have been observed previously in the MBL [Burkert et al., 2001b, Andrés-Hernández et al., 2001] and their potential origin has been discussed. According to model investigations, a nocturnal RO_2^* signal of no more than ~ 3 pptv can be explained. The expected amounts of NO_3 in such remote regions are too low to lead to significant production of RO_2^* through the reactions of NO_3 with VOC during the night. Significant production of radicals by the ozonolysis of alkenes or biogenic species seems also unlikely. The isoprene mixing ratio observed by Yokouchi et al. [1999] was generally below 10 pptv above the northern Indian Ocean. This low amount cannot significantly contribute to the production of OH during the night. The ozonolysis of alkenes is also assumed to be negligible due to the low concentrations of light NMHC observed in remote marine regions [Koppmann et al., 1992]. A long lived RO_2 may explain the observed behaviour but its presence is questionable. Such radicals left over from daytime would anyway give decreasing concentrations during nighttime, contrary to the plateau-like signal that is observed.

A likely explanation for the nighttime maritime residual signal of RO_2^* lies in the sensitivity of the PERCA towards ClO_x (Cl+ClO+OClO), reported by Perner et al. [1999]. The chain length measured in a PERCA of identical construction to that used during INDOEX has been estimated to be ~300 for dry conditions. As a result the PERCA is about 10 times more sensitive to OClO/ClO than to RO_2^* under the high humidity conditions encountered during the INDOEX campaign, provided that this

chain reaction is independent of H_2O. Assuming that this is the origin of the nighttime signal an upper limit of the nighttime ClO/OClO mixing ratio of between 0.3 and 1 pptv is estimated.

There is an ongoing discussion about the presence of halogens in the troposphere. Several mechanisms have been proposed which yield Br_2, BrCl and possibly Cl_2 from inorganic reactions of acidic aerosols [Sander and Crutzen, 1996]. Br_2, BrCl and Cl_2 are photolysed during daytime and the resulting Br and Cl atoms react with O_3 to form ClO and BrO. ClO reacts with BrO to form OClO. During the day OClO is photolysed but at night it is long lived. Thus the daytime production of relatively small amounts of BrO and ClO might lead to small but significant amounts of OClO at night. No ClO_x measurements were performed during INDOEX. The presence, however, of photochemically produced halogen oxides, in particular iodine oxide in the MBL has been indicated recently by measurements at Mace Head, Ireland [Carpenter et al., 1999].

In early morning and late afternoon the modelled and observed RO_2^* are significantly different. Figure 28 shows that the measured curves of RO_2^* are clearly broader than the simulated diurnal cycles. This effect is less pronounced for the SH. Previous campaigns in the MBL above the Atlantic Ocean have not revealed so clearly such behaviour [Burkert et al., 2001b, Andrés-Hernández et al., 2001].

The production of RO_2^* appears to start earlier in the morning and continues longer in the later afternoon than in the model. The broad shape of the RO_2^* diurnal evolution is most pronounced in air parcels originating from India and the Bay of Bengal (see Figure 29). This effect is not correlated with the appearance of higher amounts of NMHC (see Figure 22), but rather with higher amounts of CO, acetone, and HCHO.

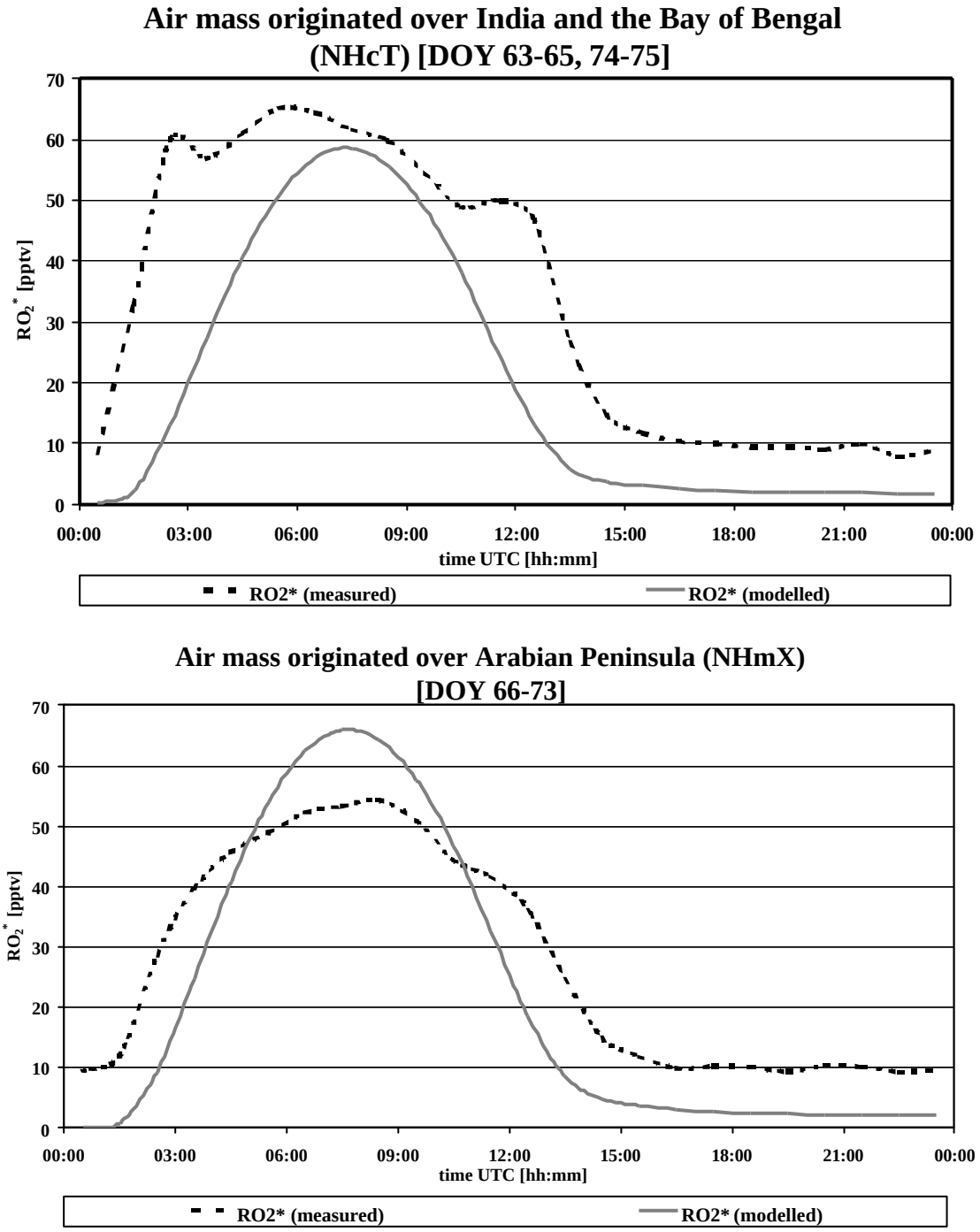

Figure 29: Modelled and measured average diurnal behaviour of RO_2^* mixing ratios for different air mass regions during INDOEX. Note: absolute concentrations of measurements and model are in good agreement, but the observations are broader.

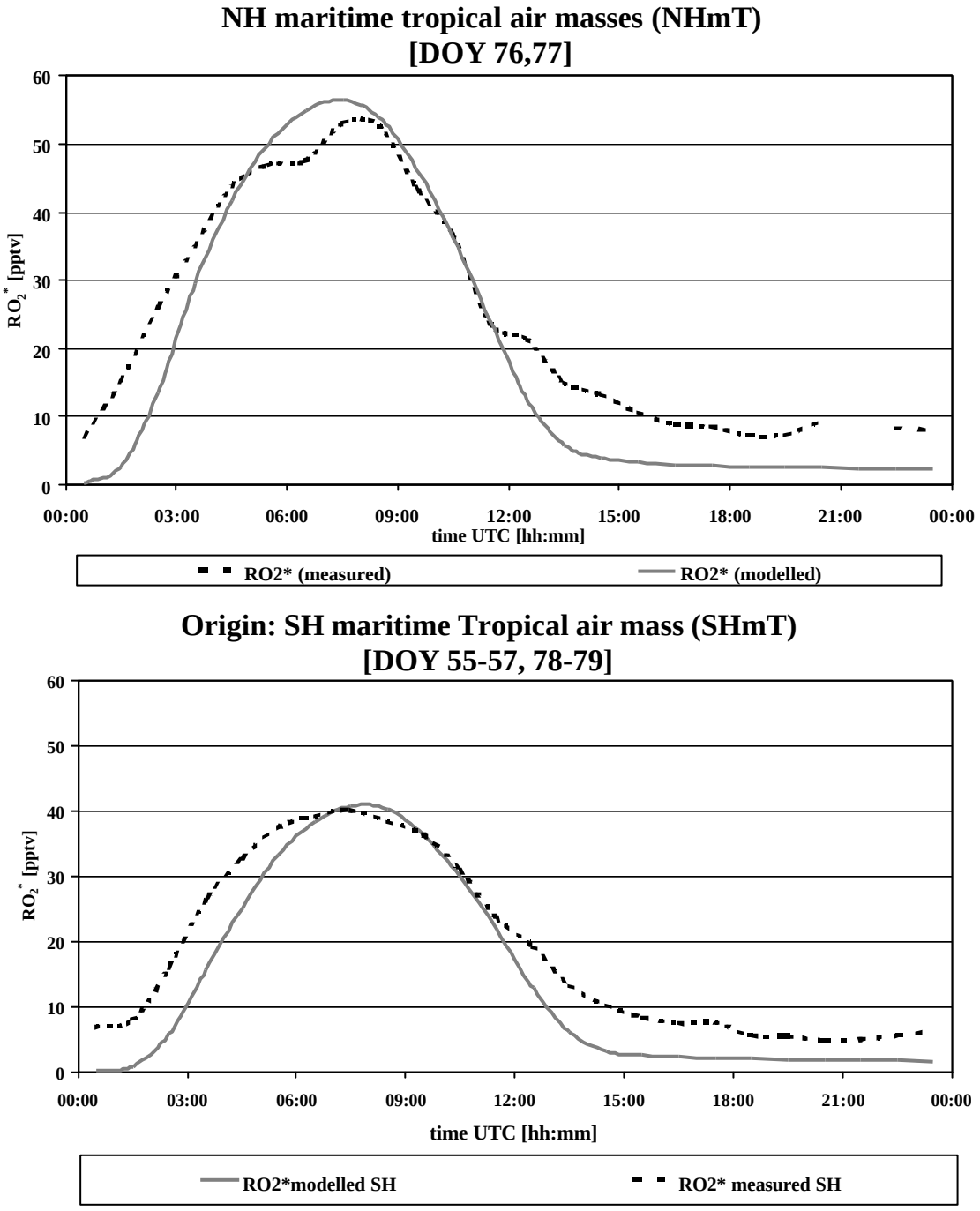

Figure 29: Modelled and measured average diurnal behaviour of RO_2^* mixing ratios for different air mass regions during INDOEX. Note: absolute concentrations of measurements and model are in good agreement, but the observations are broader.

Possible explanations for the broad shape behaviour or bulge in the morning and evening of the RO_2^* are as follows:

1) Unidentified VOC: The presence of an "as yet" unidentified VOC having faster reactions rates with OH than either CH_4 and CO, leading to RO_2^* radicals other than HO_2 and CH_3O_2. The RO_2 additional radical loss reactions also need to be slow compared to the RO_2 reactions considered in the model. This combination of effects would explain the shape of the curve in the early morning and in the evening, but not the flatter plateau at midday.

   This further requires that the diurnal variation of this as yet unknown NMHC has a minimum around noon. This implies a short photochemical lifetime, which would prevent such compounds from reaching the open ocean, if emitted by continental sources.

   Should such a NMHC be emitted from the ocean, the observed NH/SH difference in the RO_2^* diurnal behaviour could not readily be explained. Similarly the requirement of having a large source of NMHC is somewhat in conflict with such a compound having a short photochemical lifetime.

2) Radical Reservoir: The presence of a radical reservoir substance, which photolysis in the early morning, produces higher amounts of RO_2^*. This is most likely to be a reservoir for HO_2 radicals i.e. XHO_2.

$$X + HO_2 \rightarrow HOOX$$

.

.

.

$$HOOX + h\nu \rightarrow X + HO_2$$

   The additional reaction of HO_2 with X would lead to smaller amounts of RO_2^* radicals around midday and explain the plateau observed. The consequent reduction of the HO_2/CH_3O_2 ratio implies an increasing lifetime for CH_3O_2 in the evening, which could partly account for the measured nighttime signal. This effect would be more pronounced in the NH due to the higher HO_2/CH_3O_2 ratio, which is a consequence of the higher CO/CH_4 ratio in the NH as compared to the SH.

3) Bromine and Iodine: The presence of the halogen oxides BrO or IO would mean that Br and I atoms are present. These react rapidly with alkenes, alkynes, and aldehydes but not with alkanes. This is, however, an unlikely source of sufficient early morning or late afternoon RO_2^* to explain the bulge. These halogen oxides do

react rapidly with both HO_2 and RO_2 and form HOBr and HOI respectively. In the gas phase it is unlikely that sufficient HOBr or HOI is present to explain the bulge in RO_2^*, because this would require relatively large amounts of BrO or IO which would remove O_3.

The presence of halogenoxides like BrO, which react with HO_2 as described in the reactions ((48),(49), and (50)), leads to a loss of RO_2^*. However, the amounts of halogens needed for the reservoir would unrealistically influence other species, e.g. BrO mixing ratios in the range of a few ppbv would destroy all O_3 present in the MBL.

$$Br + O_3 \rightarrow BrO + O_2 \quad (48)$$

$$BrO + HO_2 \rightarrow BrOH + O_2 \quad (49)$$

$$BrOH + hn \rightarrow Br + OH \quad (50)$$

4) Chlorine. The presence of only small amounts of Cl leads to the oxidation of all VOC, alkanes, alkenes alkynes and thus to an increase of RO_2 radicals. This possible explanation of the bulge in RO_2^* is consistent with the observations of relatively large amounts of HCHO during INDOEX [Wagner et al., 2001, 2002]. The nighttime signal of the PERCA additionally provides indirect evidence for the presence of OClO/ClO/Cl in the MBL [Burkert et al., 2001b]. The largest nighttime signals are in regions where the bulge in the diurnal evolution of RO_2^* is most pronounced.

The presence of both chlorine and bromine is predicted to come from sea salt aerosols by the MOCCA model [Sander and Crutzen, 1996, Dickerson et al., 1999, Vogt et al., 1996]. Interestingly the diurnal behaviour of Cl is different from that of Br: Cl having a maximum in the early morning and late afternoon as required to explain the RO_2^* bulge.

The diurnal evolution of Cl, inferred from the RO_2^* observations required to explain the missing source of RO_2^*, is described in Figure 30. This is similar to and in agreement with the diurnal behaviour simulated and predicted by the MOCCA model [Sander and Crutzen 1996, R.R. Dickerson et al. 2000, personal communication, 2002].

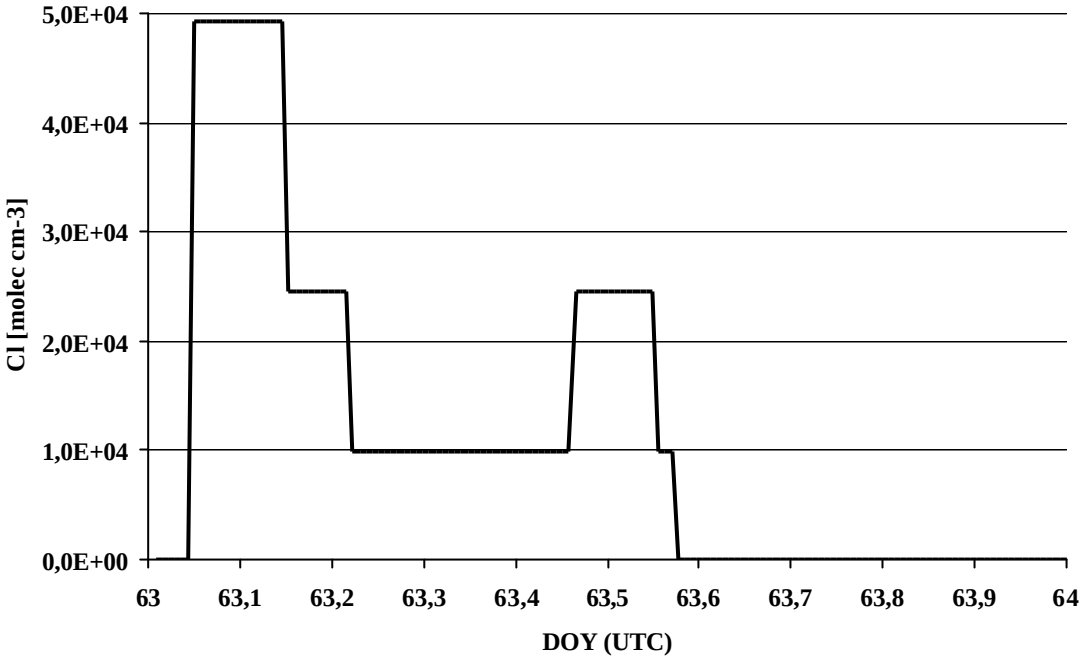

Figure 30: The required diurnal behaviour of Cl to describe the observed broad shape in the measured RO_2^* diurnal behaviour.

In recent years there has been discussion about the possible presence of a source of Cl in the planetary boundary layer [Singh et al., 1983, Cicerone, 1981, Finlayson-Pitts, 1993, Graedel and Keene, 1995, Vogt et al., 1996, Moore et al., 1996, Spicer et al., 1998, Yokouchi et al., 2000, Rhew et al., 2000, Keppler et al., 2000]. The largest bulge in the diurnal behaviour of RO_2^* was observed in the air masses from India and the surrounding areas of the Bay of Bengal (NHcT). These air masses were characterised by moderate levels of acidity in the aerosols and a moderate nitrate to sulphate ratio [Ball et al., 2003]. The presence of small amounts of NO in these air masses compared to the pristine MBL, would convert ClO to Cl via the reaction:

$$NO + ClO \rightarrow Cl + NO_2 \qquad (142)$$

Thereby leading to the regeneration of O_3 via the photolysis of NO_2, but enhancing the concentration of Cl. However, concerning the measurements of NO, again the NHcX air masses indicate slightly higher amounts compared to the NHcT air masses (see Figure 29).

The measurements of Cl_2 [Spicer et al., 1998] in a coastal region of the eastern USA showed high amounts of Cl_2 during the night, reaching levels up to 150

pptv. Photolysis in the early morning, therefore, produces Cl concentrations of the order of 1.3 x 10^5 atoms cm^{-3} at maximum. The source of the inorganic Cl_2 is presumably multi-phase reactions involving aerosols.

An alternative potential explanation for the presence of higher amounts of Cl in the NHcT regime is the enhanced emissions of halogenated carbon compounds such as CH_3Cl in coastal regions. The oxidation, proceeds as described in chapter 2.2.1.8.

Several studies [Khalil and Rasmussen, 1999, Moore et al., 1996] have shown that the ocean is not a significant source. However Yokouchi et al. [2000] observed up to 2100 pptv of CH_3Cl on islands in the tropics. It is not clear, whether these high mixing ratios are related to emissions from the forested land.

An upper limit of Cl mixing ratio generated from 2100 pptv of CH_3Cl can be calculated by a simple steady state assumption for Cl and the hypothesis that every CH_3Cl oxidised by OH leads to a Cl.

$$[Cl] = \frac{k_{CH_3Cl+OH}[CH_3Cl][OH]}{k_{CH_4+Cl}[CH_4]} \tag{143}$$

This yields [Cl] = 5.9×10^3 [atoms cm^{-3}], for an [OH] = 1×10^7 [molecule cm^{-3}] and mixing ratio of CH_4 = 1.8 ppmv, i.e. apparently too small to explain the observed effect. In addition, the measurements of CH_3Cl onboard the citation plane during INDOEX only indicated amounts in the NHcT air masses of up to 750 pptv [Scheeren et al., 2002].

Overall, the nighttime RO_2^* signals and the bulge in RO_2^* appears to provide evidence for a source of Cl in the MBL, which maximises in the early morning. This source is most likely to comprise inorganic multiphase reactions on sea salt aerosol, but the oxidation of organic halides cannot be excluded.

Contribution of Cl to the tropospheric oxidising capacity (OC) of CH_4

The OC with respect to oxidation and consequent removal of a species from the marine boundary layer can be defined as the sum of the effective first-order reactive removal processes.

$$OC_{CH_4} = \int_{day} \left(k_{OH+CH_4}[OH][CH_4] + k_{Cl+CH_4}[Cl][CH_4] \right) dt$$

Assuming that the bulge in RO_2^* results from Cl, and this indicates that above the Indian Ocean Cl accounts for up to ~8% of the average oxidising capacity of CH_4. A

daily integral was chosen to compare the OC of OH and Cl. The Cl diurnal profile was the same as presented in Figure 30.

Comparison of the remote MBL above the Atlantic and Indian Ocean

The average RO_2^* behaviour from the measurements made in the NH and SH in the Atlantic Ocean are shown in Figure 31 and Figure 32. These measurements were made during the ALBATROSS campaign in 1996 [Burkert et al., 2001b] and AEROSOL in 1999, immediately prior to INDOEX with the same instrument [Andres-Hernandez et al., 2001]. The ALBATROSS cruise went aboard the Polarstern from Bremerhaven, Germany (54°N, 9°E) to Punta Quilla, Argentina (50°S, 67°W). Much of the voyage was around 30°W with the Polarstern travelling from North to South. In contrast the AEROSOL cruise went from Norfolk, Virginia (37°N, 76°W) to Cape Town, South Africa (34°S, 22°E), cutting across the North and South Atlantic Oceans.

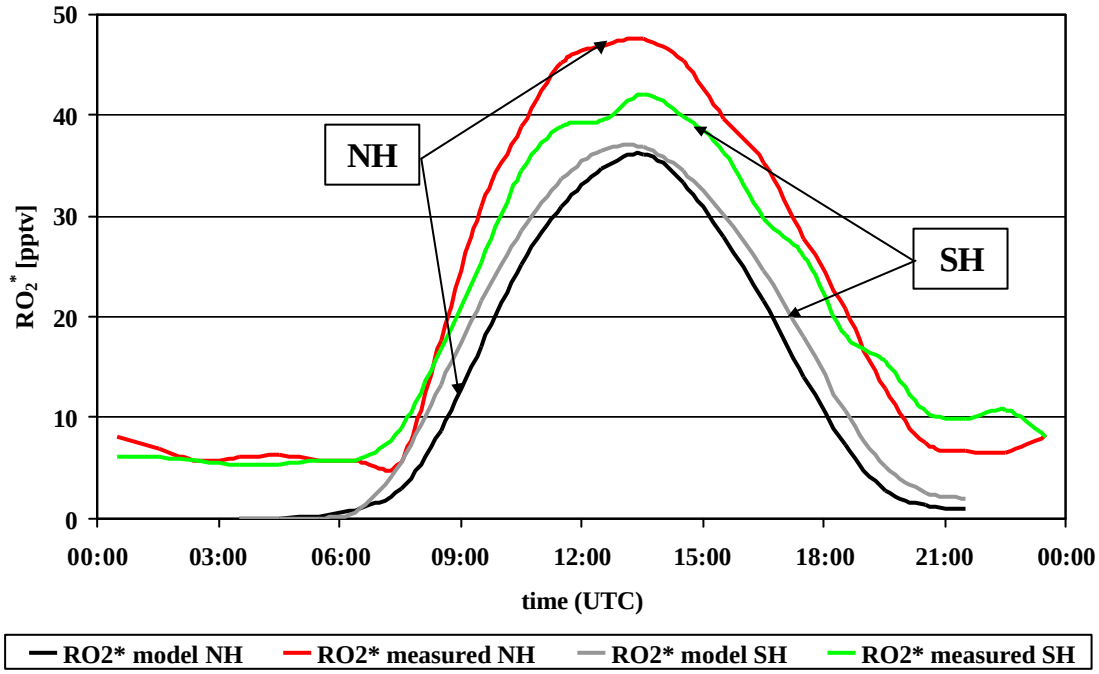

Figure 31: Average diurnal variation of measured and modelled RO_2^* mixing ratios for the NH and SH during ALBATROSS (1996) above the Atlantic Ocean. Local time is given by UTC + ~2 hrs.

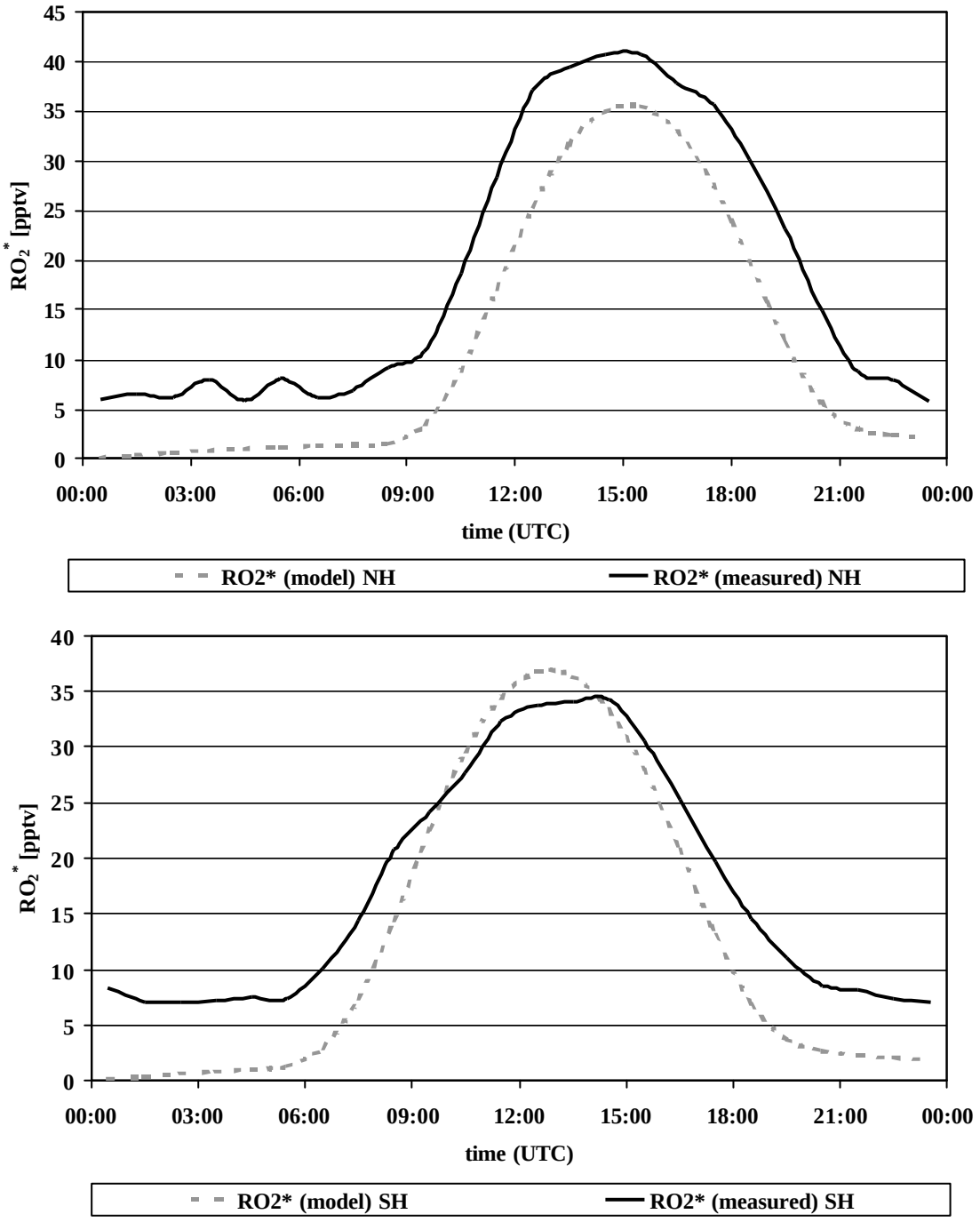

Figure 32: Average diurnal variation of measured and modelled RO_2^* mixing ratios for the a) NH and b) SH during AEROSOL (1999) above the Atlantic Ocean. Local time approximately UTC a) +4 hrs and b) +2 hrs.

Using the measured amounts of O_3 and related trace gases and neglecting any halogen chemistry, the model predicts similar concentrations of RO_2^* in both the NH and the SH in both 1996 and 1999: the noontime maximum mixing ratio of RO_2^* being around 36 pptv. In contrast the estimated amounts of RO_2^* in the northern and southern part so the Indian Ocean are significantly different.

The measurements from the Atlantic Ocean show for both the ALBATROSS and the AEROSOL campaign the following:

1) The broader shape behaviour is more pronounced in the NH than in the SH.
2) The noontime maximum of RO_2^* is small but significantly higher in the NH than in the SH.
3) The early morning increase of RO_2^* is not as fast as in the results from the Indian Ocean.
4) The broader shape in the Atlantic Ocean results appears similar to an offset throughout the day.
5) The nighttime unexplained signal is not considered to be an artefact of the PERCA, because during periods of rain the signal was observed to go zero both during the day and during the night.

The differences between the Atlantic and the Indian Ocean are most probably caused by the presence of higher amounts of NO_x, CO, NMHC, and different meteorological conditions (i.e. higher MBL height in the Atlantic compared to the Indian Ocean). The diurnal behaviour of the O_3 mixing ratio above the Atlantic Ocean does not often show significant loss of O_3. This is another indication for production of O_3 from the higher amounts of NO_x although the measurements above the Atlantic Ocean were performed far away from coastal regions. In addition, the difference in the O_3 mixing ratio between NH and SH was small above the Atlantic Ocean during the ALBATROSS and AEROSOL campaign.

The MBL of the remote Indian Ocean generally seems to be cleaner than the remote parts of the Atlantic Ocean visited on the research voyages and exhibits the cleanest air observed thus far in the SH. This may explain why the behaviour of the small amounts of halogens has a more pronounced effect on the RO_2*.

4.2.3.2.2 HCHO chemistry

The RO_2^* and HCHO chemistry is closely related in the MBL. The production of alkoxy, RO, radicals from peroxy radicals leads to the production of aldehydes and ketones via the reactions of RO with O_2: the reaction of CH_3O with O_2 is expected to be the main source of HCHO in the remote MBL. The photolysis of HCHO is an additional significant source of HO_2 radicals in the MBL as compared with the reaction of OH with CO in the presence of O_2.

It has been reported in the past that measured HCHO concentrations in the MBL of the Atlantic Ocean are in disagreement with model results [Burkert et al., 2001b, Weller et al., 2000, and references therein]. This has been attributed to additional sources of non methane hydrocarbons e.g. from ship exhaust and biomass burning plumes crossing the ocean [Burkert et al., 2001b].

The HCHO expected in the MBL above the Indian Ocean was simulated using the chemical model and compared with the measurements performed during INDOEX. As for RO_2^* simulations, the NO_2 was constrained to fixed amounts of either 0 or 10 pptv, which represent the minimum and maximum in the range of observations.

In regions exhibiting low CO values, the effect of NO_x on the amount of HCHO is more pronounced due to the higher rate of conversion of RO_2 radicals to HO_2. As a result, the NO_2 values used in the model determine to a large extent the calculated HCHO mixing ratio. In Figure 33 the daily averages of measured and calculated HCHO mixing ratios are plotted. In spite of the uncertainty in the NO measurements mentioned above, the agreement is fair between measured and simulated HCHO, taking the experimental error into account. This is similar to the results obtained by Wagner et al. [2001].

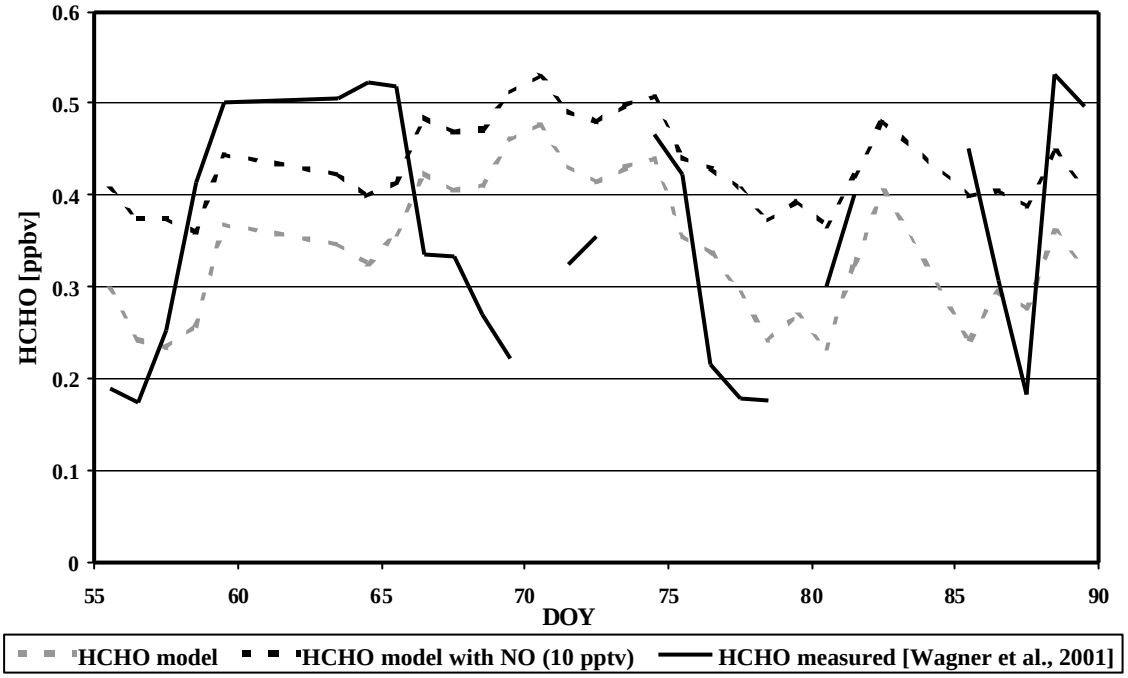

Figure 33: Measured and modelled HCHO mixing ratios during INDOEX.

In the period DOY 68-70 the simulated HCHO values are significantly larger than the measured amounts. This is similar to previous results [Liu et al., 1992, Jacob et al., 1996]. Some investigators have proposed that the heterogeneous chemistry in clouds or aerosols as being responsible for the fast loss of HCHO. On those days, where this behaviour is observed however, the AOD measured is lower than on previous days.

An alternative explanation of the low HCHO mixing ratios has recently been reported by Wagner et al. [2001]. For this explanation, the lower HCHO mixing ratios are interpreted to be an indication of the prevailing free tropospheric character of the subsiding air measured. The back trajectories of the air masses in this case, however, indicate that the air sampled on the days in question remained for at least two days in the MBL which is sufficient time for HCHO to achieve a stationary state.

The observed relationship between the daily maximum measured mixing ratios of CO, HCHO, and RO_2^* confirm the close chemical link between these species. The model results cannot explain the extremely high concentrations of RO_2^* observed during the DOY 64 and 65. Surprisingly during days with enhanced levels of NMHC (DOY 68-72) no enhanced RO_2^* or HCHO mixing ratios are observed.

For enhanced CO levels (DOY 63-65) and maximum noontime RO_2^* mixing ratios, the model does not reproduce the observed HCHO values. In the model higher

CO concentrations lead to higher HO_2 and less OH. This results in a lower production rate of CH_3O_2 via the oxidation of methane and also a higher loss rate as a result of the HO_2 reaction with CH_3O_2. The CH_3O_2 loss reactions are the main source for HCHO. Under the assumption that all other radical sources do not significantly increase, then for higher CO concentrations it is difficult to explain the CO and HCHO correlation observed, because the opposite effect is predicted from the expected chemistry.

Possible explanations of the HCHO behaviour:

- A reaction of CO and OH in the presence of water producing HCHO via a complex mechanism e.g. .

$$CO + OH \rightarrow COOH$$
$$COOH + H_2O \rightarrow HCHO + HO_2$$

  However, this reaction is expected to be slow and is endoergic.

- A reaction of CO and HO_2 catalysed by the presence of water, which produces OH and CO_2. Some studies in the past have indicated that their reaction may occur but other have obtained a very low upper limit for this reaction rate coefficient [DeMore et al., 1997, and references therein]. However, an extended investigation concerning the influence of water on the reaction rate coefficient has not yet been done. A reaction of the described type would change the ratio between HO_2 and OH and would also increase the amount of RO_2 due to the higher amount of OH present. Such a reaction would lead via enhanced OH concentrations to an enhanced oxidation of hydrocarbons and rate of production of RO_2 and consequently to a larger production of HCHO in the atmosphere.
- The presence of a NMHC, which has not yet been identified and included in the model having similar sources to CO. Its rate of oxidation needs to be in the same order of magnitude to that of CH_4.
- The presence of another oxidising agent like OH for example Cl, which leads to additional amounts of RO_2^* and therefore higher concentrations of HCHO. This requires amounts of Cl to be in the order of $1x10^4$ to $1x10^5$ molec cm^{-3}.

  It is very interesting to note that recent measurements of the isotopic fractionation of CH_4 above the Pacific Ocean have recently provided evidence for the enrichment of the CH_4 fractions, which cannot be explained by OH chemistry alone. An additional oxidant is required [Allan et al., 2001].

In summary it is probably far from surprising that the broad shape behaviour of RO_2^* is coincidental with increased amounts of HCHO in the INDOEX measurements. The oxidation of CH_4 and for that matter any other NMHC, initiated by Cl would in pristine regions of the atmosphere yield additional HCHO, compared to that predicted from the OH initiated CH_4 and NMHC oxidation in the remote pristine atmosphere.

Finally assuming that the bulge in RO_2^* results from Cl, and this indicates that in the remotes and pristine Cl accounts for up to ~8% of the average oxidising capacity of CH_4 of the atmosphere.

4.2.4 Summary

A set of trace gases and photolysis frequencies has been successfully measured in the MBL above the Indian Ocean during the INDOEX campaign in February and March 1999. Air masses with different trace gas mixing ratios and origins have been encountered and analysed.

The photolysis frequencies at the ground level were calculated using an RTM and compared with measured values. The model was initialised with the measured AOD profiles and aerosol composition. The $j(O(^1D))$ and $j(NO_2)$ calculated photolysis frequencies at 30° SZA for AOD of 0 and 0.6 differ by about 30% and 24% respectively.

A box homogenous gas phase chemistry model has been used to simulate the chemistry of the MBL and its results compared with the trace gas and radical measurements. The diurnal behaviour of the measured RO_2^* is observed to be significantly broader than that estimated using an OH oxidation scheme suitable for the pristine and remote MBL. This broad RO_2^* or bulge behaviour indicates that more RO_2^* is present in the early morning and late afternoon than OH chemistry predicts.

The presence of the broader RO_2^* behaviour is not correlated with the amount of NMHC but can be related to the origin of the air masses. Overall this behaviour indicates the presence of missing chemistry in the model in the early morning and late afternoon. One reasonable explanation of the observed behaviour is the presence of small amounts of chlorine in the MBL. The sources of Cl are most likely to be the release from aerosols and also possibly the oxidation of organic halides.

The agreement between the modelled and measured HCHO is reasonable taking the experimental error and the uncertainty of NO measurements into account. The observed relationship between the daily measured maximum mixing ratios of CO, HCHO, and RO_2^* indicates a close chemical link between these species, which cannot be well explained by the known OH oxidation chemistry used in the box model. The most likely explanation of this behaviour is the presence of Cl in the MBL, as proposed above.

Overall the measurements of trace gases and radicals, obtained aboard the R.V. Ronald H. Brown during INDOEX have provided the first detailed observations of the chemistry of the remote marine boundary layer above the Indian Ocean. The observed RO_2^* is not that expected for OH initiated hydrocarbon oxidation. Evidence is presented which indicates that Cl contributes significantly to the oxidative capacity of the tropical MBL. To gain confidence about the proposed explanation of the RO_2^* behaviour, research campaigns focusing on the identification of halogen oxide radicals in the MBL are required.

4.3 Photochemistry and radiative effects of aerosols

4.3.1 Introduction

For this study measurements of in situ and vertical profiles of O_3 were taken above the Indian Ocean. These measurements were enlarged by satellite observations of excess O_3, total NO_2, total HCHO, and lightning produced NO_2. These measurements were part of INDOEX [Lelieveld et al., 2001a, 2001b, Ball et al., 2003, http://www-indoex.ucsd.edu].

The main objective of this study is to understand the fast photochemistry of O_3 in the MBL, in particular the production and loss mechanisms responsible for the diurnal behaviour of O_3, together with a qualitative estimate of the influence of transport on these mechanisms. Special attention was given to the advective and convective processes [de Laat et al., 2000, 2001a, 2001b] and the MBL behaviour. The MBL behaviour is discussed in context with the presence of aerosols and their effect on stabilising the atmosphere by absorbing the direct sunlight [Kinne and Pueschel, 2001, Jacobson, 1998b, Gamazayachikov et al., 1998, Kiehl et al., 1999]. Aerosols also have an impact on the UV actinic flux and therefore on O_3 [Burkert et al., 2002, Dickerson et al., 1997, Liao et al., 1999, Kondragunta, 1997].

Measurements in the southern Indian Ocean are used to analyse the different contributions of sources responsible for O_3 in remote areas.

4.3.2 Results

4.3.2.1 Characteristics of the different air masses observed

The four different air masses exhibited the following characteristics:

SHmE (observed during DOY 54-58, 78.25-79.5)

The SHmE regime showed the lowest mixing ratios for most trace species and in this sense was the least polluted air encountered. The maximum RO_2^* mixing ratio during DOY 54-58 decreased with decreasing latitude from 35 to 25 pptv. The O_3

mixing ratio revealed the same behaviour, decreasing from 15 to 8 ppbv. The loss of O_3 per latitude decreases with decreasing latitude. The mean CO mixing ratio was 56 ppbv, the daytime average NO mixing ratio was below the detection limit of around 3 pptv. The NMHC mixing ratios were the lowest observed during the whole campaign. The mean values were: ethane 194 pptv, propane 7 pptv, and acetylene 21 pptv [Muehle et al., 2002]. The vertical profiles of O_3 mixing ratio showed a weak positive gradient with increasing altitude up to 12 km between 12°S and the ITCZ, where the O_3 reached levels about 40 ppbv [Hermann Smit, personal communication, 2001].

NHmE (observed during DOY 76-78.25, 79.5-81)

In the NHmE regime the CO and O_3 mixing ratios were around 90 ppbv and approximately 10 ppbv, respectively. The maximum RO_2^* mixing ratio varied between 55-60 pptv. The back-trajectories indicate a long travel time of the air parcel along the west-coast of India but staying over the ocean. The NO mixing ratio was below the detection limit (<5 pptv). Most of the NMHC doubled their mean mixing ratios compared to the SHmE air mass: ethane 332 pptv, propane 10 pptv, and acetylene 44 pptv. The vertical profiles of O_3 in this regime indicate an even weaker positive gradient in altitude compared to the SHmE regime, reaching levels of about 30 ppbv at 12 km.

NHcT (observed during DOY 63-66, 74-76, 85-89):

The NHcT regime was characterised by the highest observed maximum mixing ratios in RO_2^* and CO during the whole campaign. Maximum levels of up to 90 pptv RO_2^* and 200 ppbv CO were observed. NO measurements were higher than in the SHmE, but still close to the detection limit, around 6 pptv. The O_3 mixing ratios showed strong diurnal variations, with O_3 losses during the day being as large as 50%. The latitudinal gradient in O_3 was ~ 1.25 ppbv/°latitude heading North. The NMHC main mixing ratios increase for ethane up to 403 pptv, propane to 20 pptv, and acetylene to 133 pptv. The vertical O_3 profiles revealed an enriched layer between 1-3 km having mixing ratios larger than 70 ppbv. The upper level O_3 values were different depending on the periods of observation. Back-trajectory analysis indicate that the air masses originated over India and the Bay of Bengal. The NHcT regime also appeared to contain high concentrations of ash, soot, and other organic matter [Dickerson et al., 2002, Neusüß et al., 2002, Quinn et al., 2002]. This is evidence for heavy contamination by fossil fuel combustion, biomass burning, and wind-blown dust [Ball et al., 2003, Quinn

et al., 2002, Stehr et al., 2002]. The black carbon from India is currently considered to result mainly from internal combustion engines, biomass burning, and small-scale coal combustion. However, estimates of black carbon emissions from India yield much smaller values than do in situ observations. This suggests an additional source not yet considered, or, unusually high emissions factors [Dickerson et al., 2002]. Therefore considerable uncertainty remains about the sources and/or emissions.

NHcX (observed during DOY 66-74)

The NHcX regime was characterised by the highest observed concentration of O_3 and NMHC at the most northerly point of the whole campaign. O_3 mixing ratios reached levels up to 53 ppbv and the NMHC averaged mixing ratios were: ethane 927 pptv, propane 133 pptv, and acetylene 169.3 pptv. The latitudinal gradient in O_3 remained ~ 1.25 ppbv/°latitude heading North. RO_2^* and CO varied weakly around 55 pptv and 122 ppbv respectively. NO mixing ratios reached their highest values of the campaign being approximately 9 pptv. The vertical profile in O_3 showed the same behaviour as in the NHcT regime with an O_3 enriched layer above the MBL. Back-trajectories indicate that the air masses originated over the Arabian Peninsula.

4.3.2.2 Measurements of trace constituents and parameters

4.3.2.2.1 O_3 in situ measurements

The O_3 mixing ratio was measured successfully between DOY 54 and DOY 89. The three legs are presented in Figure 34 and the air masses encountered are labelled in the header. During the first leg the daily averaged O_3 concentration decreased while heading North to the ITCZ. In the course of the second and third leg the daily averaged O_3 concentrations varied strongly depending on the distance from the sources and the latitude. In the clean MBL, however, similar O_3 levels (24 hrs average) seem to correspond to the same latitudinal position.

In order to calculate the O_3 gradient per latitude, the O_3 gradient was calculated for the positions more at the South and the North of leg 2, i.e. DOY 65 (6°N, 35 ppbv)/ 73 (7°N, 35 ppbv) which have similar O_3 concentrations and DOY 70 (18°N, 50 ppbv). The difference is calculated considering the O_3 maximum of DOY 65, 70, and 73. The resultant gradient is ~1.25 ppbv/°latitude in O_3 heading North.

Similarly in the SH a comparison is possible between DOY 75 (3°N, 25 ppbv) and 78 (10°S, 10 ppbv) and between 78 with 82 (4°N, 30 ppbv), i.e. there is a decrease of 15 ppbv going to the South and an increase of 20 ppbv going to the North. This average leads to a gradient of ~1.25 ppbv/°latitude in O_3 heading North.

The gradient in the SH between DOY 55 (12°S, 14 ppbv) and 57 (5°S, 9 ppbv) is about 0.7 ppbv/°latitude in O_3 heading South. The latitudinal gradient in O_3 in the SH seems to be decreasing while heading towards the ITCZ as expected because the loss reactions of O_3 are dependent on the amount of O_3 itself. However, in the NH the gradient appears to be constant, which is in disagreement with the theory.

The O_3 diurnal variation within the MBL during INDOEX is characterised by a daytime depletion (around 10-50%) [Stehr et al., 2002], and a clear nocturnal recovery. The short term variations of O_3 seem to be superimposed on the latitudinal gradient described above.

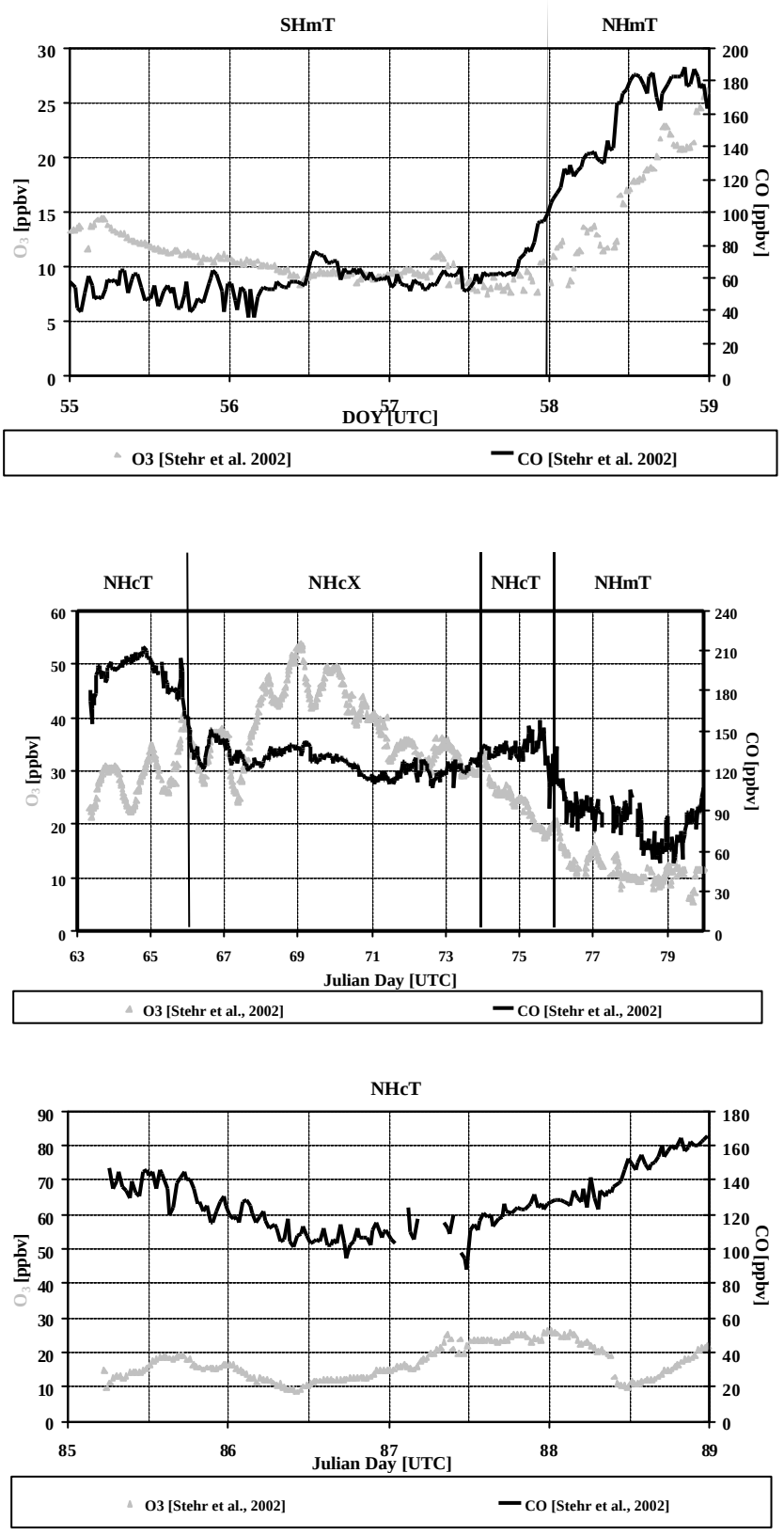

Figure 34: Plots of the individual diurnal variation of O_3 and CO observed on legs 1 to 3 of INDOEX. The classification of the air masses encountered are written above the days, and vertical lines separate the different types of air masses.

4.3.2.2.2 O_3 soundings

In this section the cross sections for all O_3 soundings performed during the ship cruise are presented. They are grouped to represent more clearly the latitudinal behaviour of the vertical profiles. In Figure 35 the O_3 soundings are plotted from 0 to 5 km to more clearly illustrate the boundary layer structure. Figure 36 shows the complete series of cross sections (0 to 20 km).

In the NH a clear structure in the O_3 vertical distribution is observed. The lowest first kilometre also has the lowest O_3 mixing ratios (see Figure 35, leg 2 a-c, and leg 3). Directly above the MBL between 1 and 3 km there is a highly enriched O_3 layer, which is linked with high amounts of aerosols. In addition this layer is in most cases extremely dry. This is especially true during leg 3 within the 1 to 3 km layer O_3 mixing ratios reaching levels up to 80 ppbv, whereas the maximum O_3 mixing ratio in the MBL (0-1km) remained around 20 ppbv. During leg 1 and leg 2 d-e the vertical O_3 gradient was weaker and the O_3 mixing ratios increased evenly in relation to increasing height.

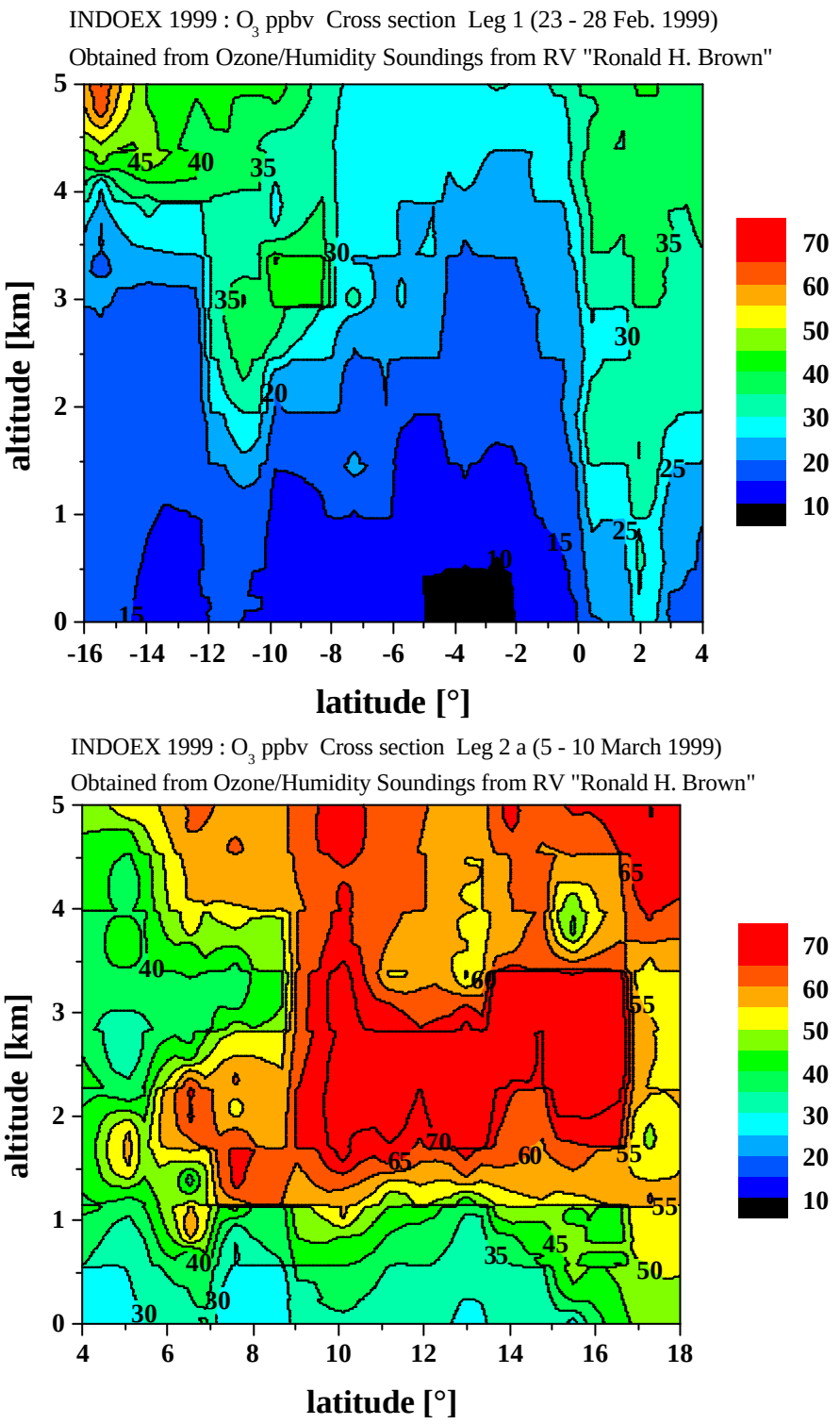

Figure 35: O3 soundings (0 to 5 km) grouped into a) leg 1 (23-28 Feb.), b) leg 2 (5-10 March), c) NH leg 2 (11-13 March), d) leg 2 (13-14 March) days with same latitude, e) leg 2 (14-19 March), f) leg 2 (19-22 March), g) leg 3 (26-30 March) [H.G.J. Smit, Research Centre Jülich (ICG 2), Germany].

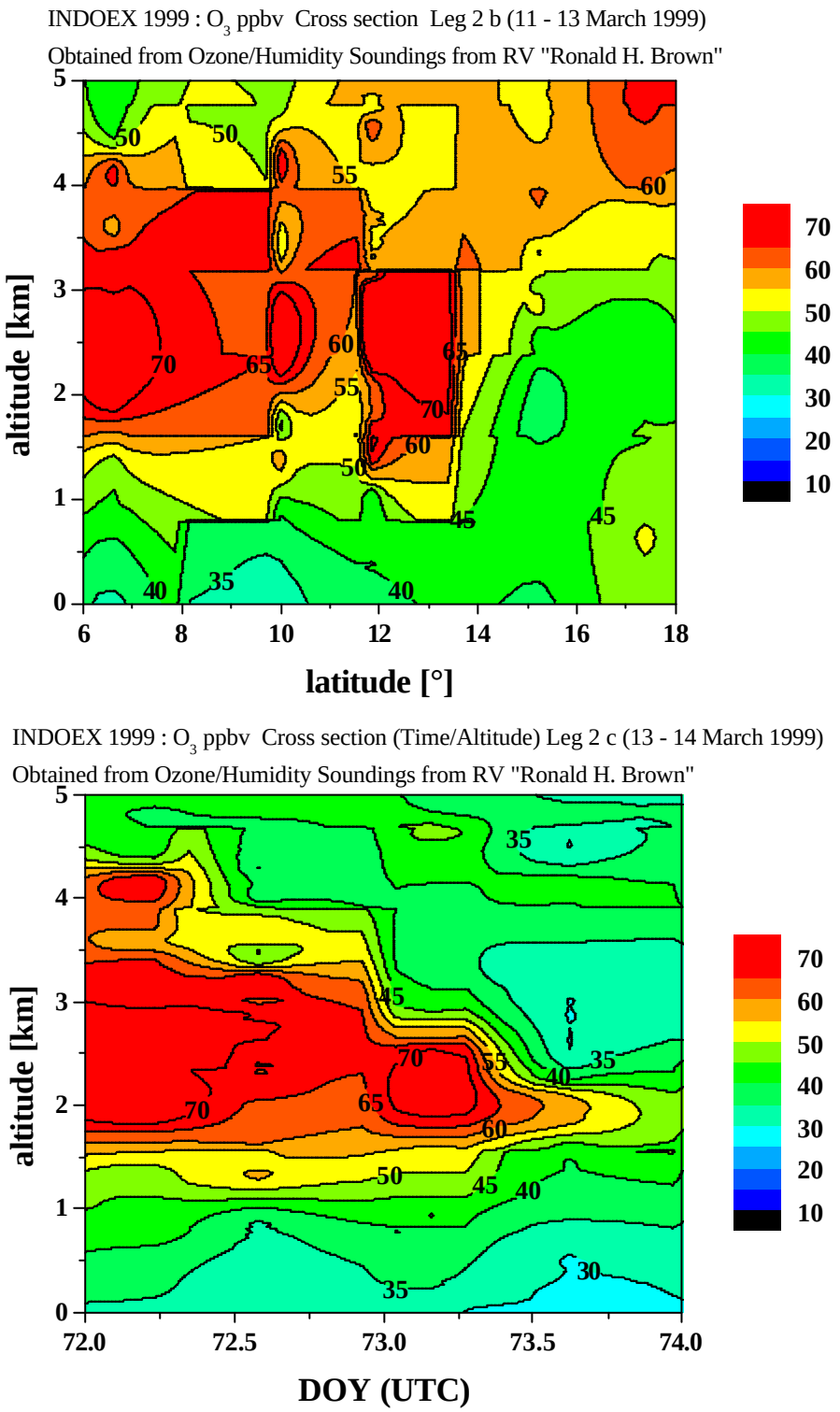

Figure 35: O3 soundings (0 to 5 km) grouped into a) leg 1 (23-28 Feb.), b) leg 2 (5-10 March), c) NH leg 2 (11-13 March), d) leg 2 (13-14 March) days with same latitude, e) leg 2 (14-19 March), f) leg 2 (19-22 March), g) leg 3 (26-30 March) [H.G.J. Smit, Research Centre Jülich (ICG 2), Germany].

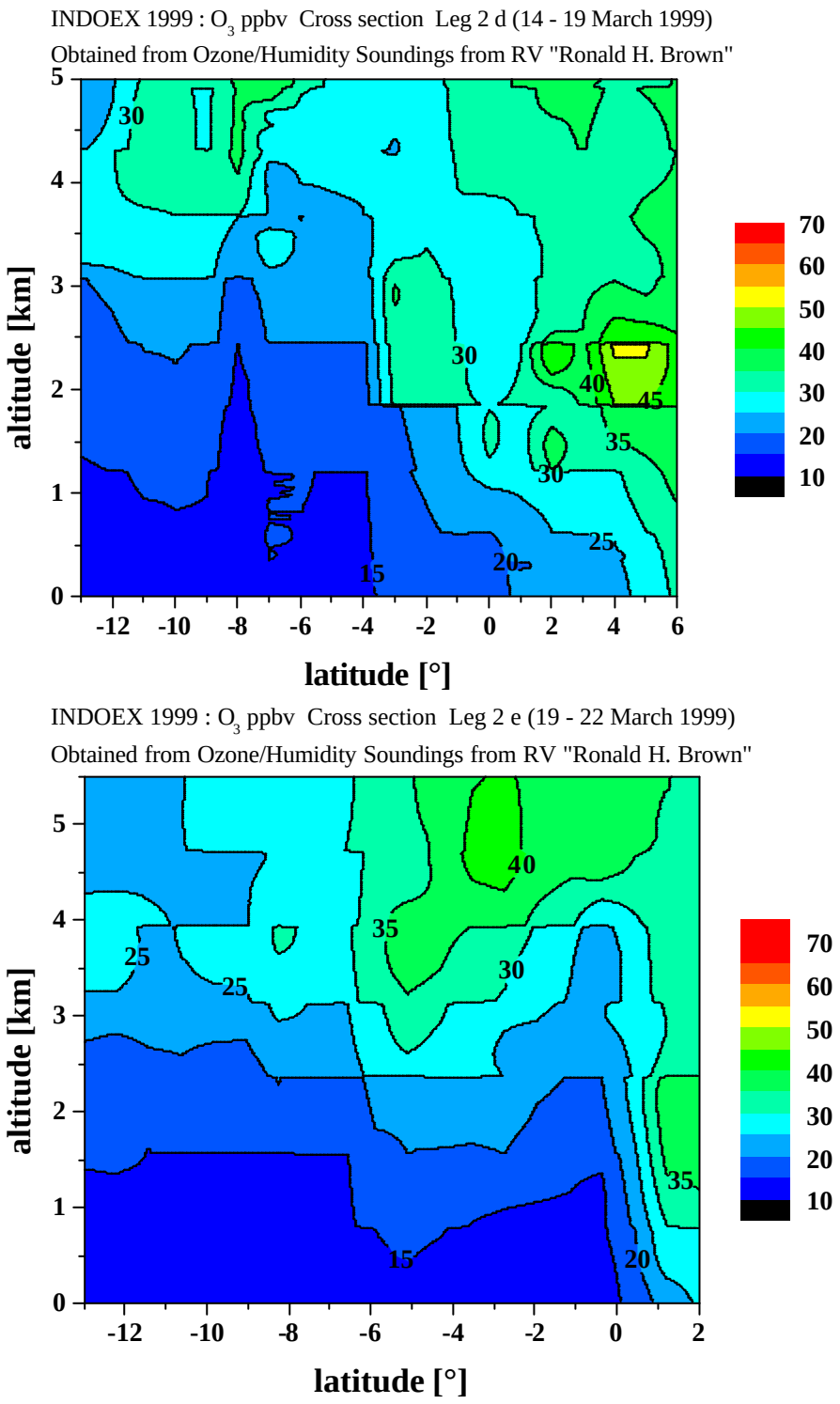

Figure 35: O3 soundings (0 to 5 km) grouped into a) leg 1 (23-28 Feb.), b) leg 2 (5-10 March), c) NH leg 2 (11-13 March), d) leg 2 (13-14 March) days with same latitude, e) leg 2 (14-19 March), f) leg 2 (19-22 March), g) leg 3 (26-30 March) [H.G.J. Smit, Research Centre Jülich (ICG 2), Germany].

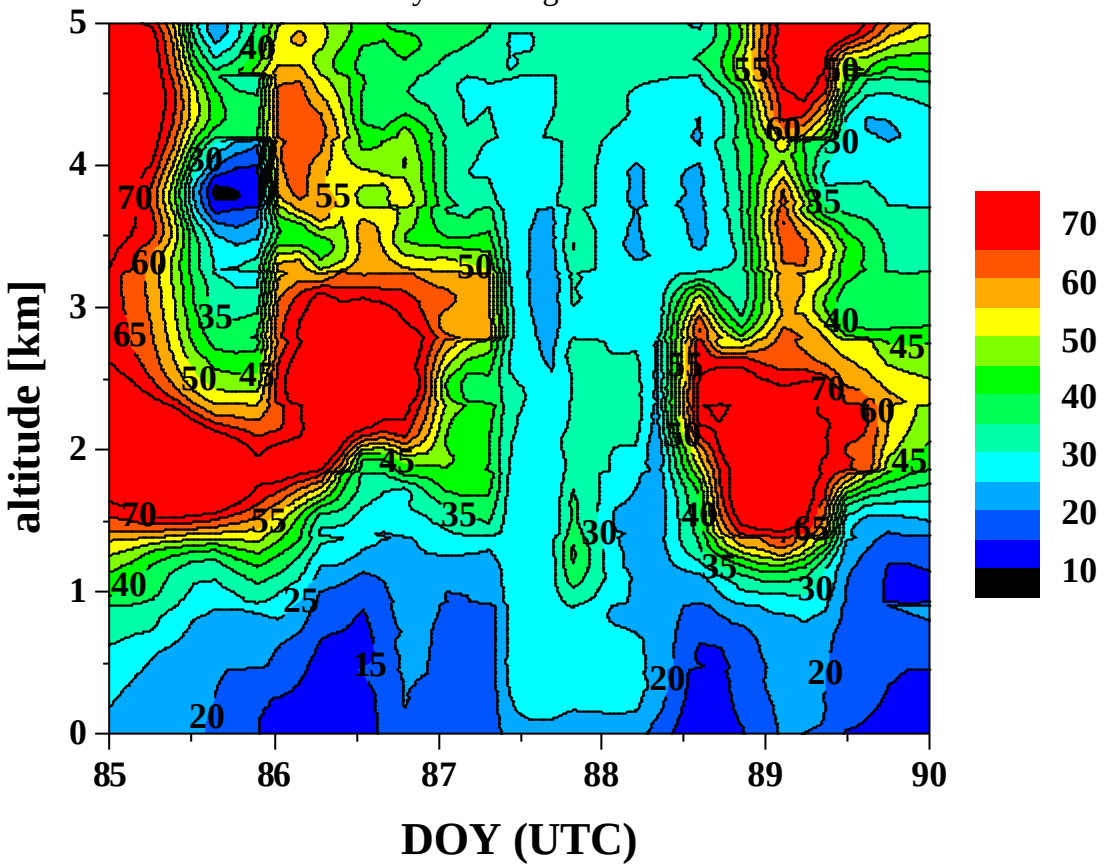

Figure 35: O_3 soundings (0 to 5 km) grouped into a) leg 1 (23-28 Feb.), b) leg 2 (5-10 March), c) NH leg 2 (11-13 March), d) leg 2 (13-14 March) days with same latitude, e) leg 2 (14-19 March), f) leg 2 (19-22 March), g) leg 3 (26-30 March) [H.G.J. Smit, Research Centre Jülich (ICG 2), Germany].

In Figure 36 some macro-scale phenomena can be seen. During leg 1 the ITCZ can be identified at around 3°S, with low levels of O_3 being pumped upwards toward the tropopause. At the most southern soundings (~15 S) higher amounts of O_3 are observed in the mid-troposphere. The back trajectories for the 500 hPa niveau (Figure 37) show that air masses travelled for at least six days over the open ocean far away from any source region. There was also no evidence for lightning induced O_3 production (Figure 40, Figure 41). Back trajectories indicate that the air masses were originated at approximately 200 mbar. Therefore, it seems most likely that this air mass has stratospheric origin. This assumption is further supported by relative humidity data [http://saga.pmel.noaa.gov/indoex/rsonds/index.html] which show extremely low values (below 10 %) between 3 and 8 km altitude.

In the past, stratospheric layers just below the tropopause have been repeatedly observed all over the Indian Ocean. Zachariasse et al. [2000] suggest that the extra tropical stratosphere feeds O_3 to the tropical troposphere from the NH and SH. The typical tropical and extra tropical O_3 vertical profiles indicate that decreasing tropopause height and the presence of the Subtropical Jetstreams at the transition zone between tropical and extra tropical hemispheres can lead to the intrusion of stratospheric O_3 into the troposphere [Zachariasse et al., 2000]. This assumption is supported by the potential vorticity maps for this region. On the way downward the stratospheric O_3 is diluted into the whole troposphere.

The presence of a strictly layered mid-tropospheric O_3 maximum in the NH and its correspondence with high amounts of absorbing aerosols leads to the conclusion that O_3 does not originate in the stratosphere [Zachariasse et al., 2000, Welton et al., 2002]. Under the assumption that the STE in the NH and SH is similar, and the observed SH vertical O_3 profiles are not influenced by anthropogenic sources, the differential profile between NH and SH must be equal to the anthropogenic influence in the tropics of the NH.

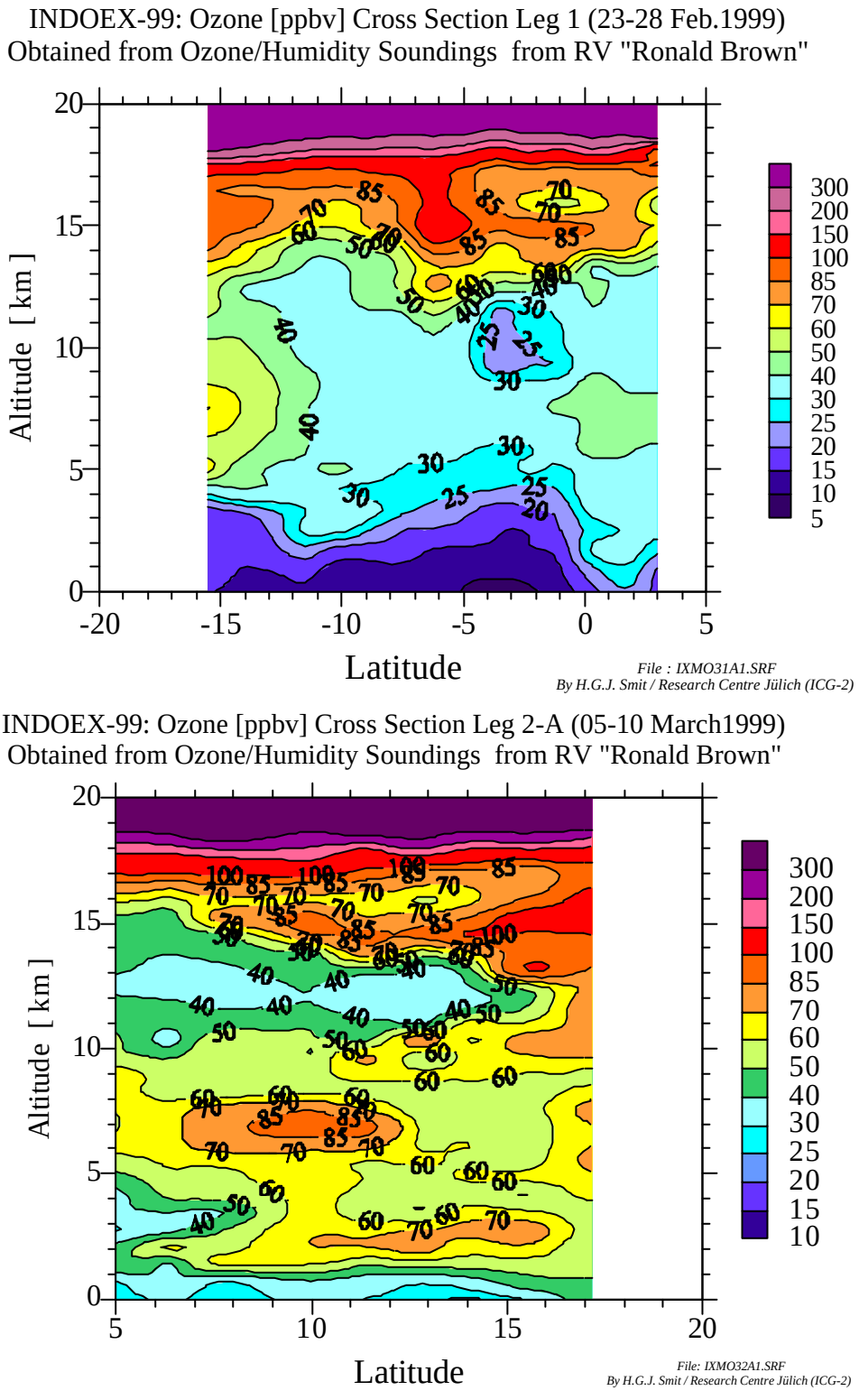

Figure 36: O_3 soundings (0 to 20 km) grouped into a) leg 1 (23-28 Feb.), b) leg 2 (5-10 March), c) NH leg 2 (11-13 March), d) leg 2 (13-14 March) days with same latitude, e) leg 2 (14-19 March), f) leg 2 (19-22 March), g) leg 3 (26-30 March) [H.G.J. Smit, Research Centre Jülich (ICG 2), Germany].

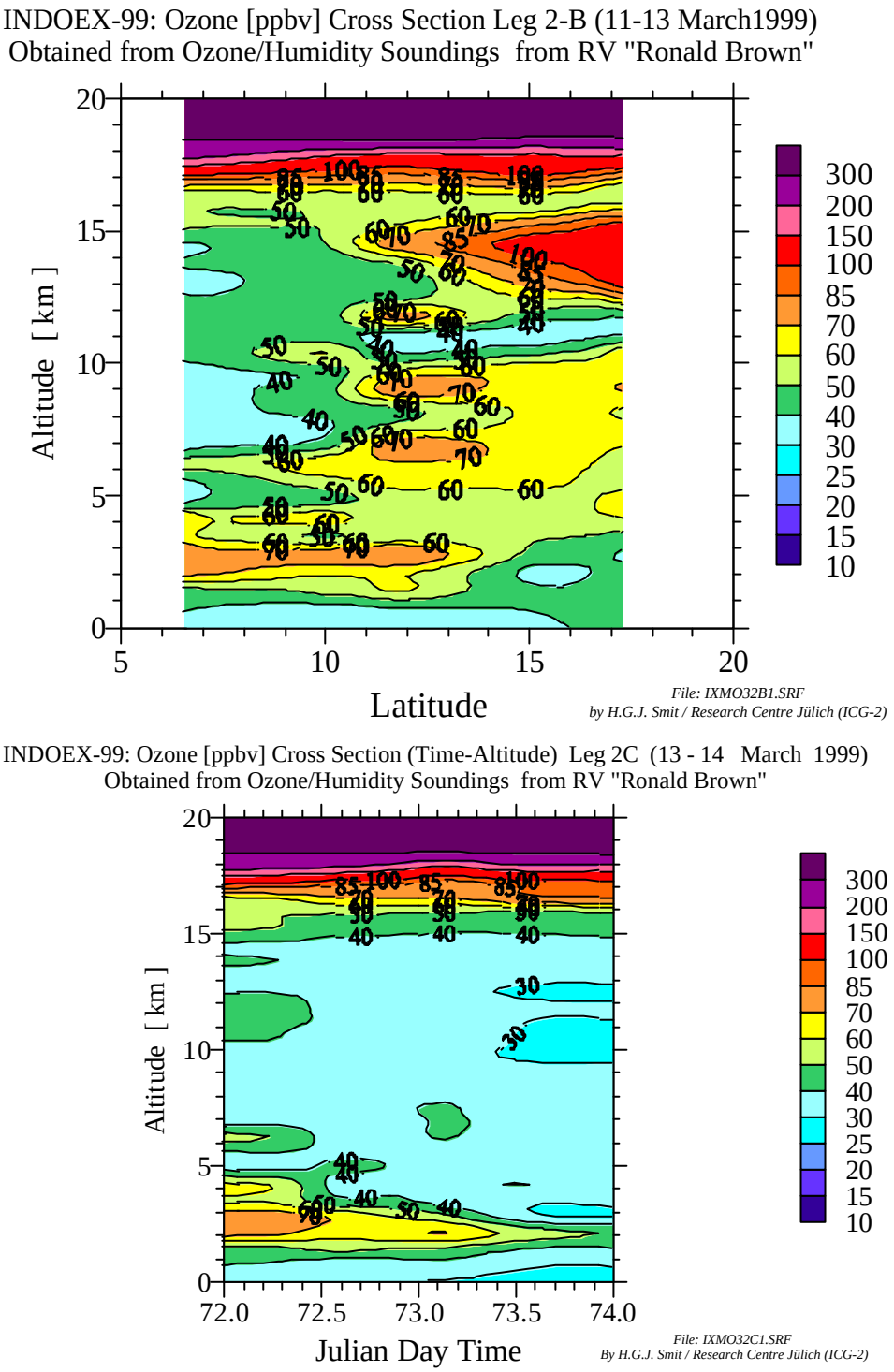

Figure 36: O_3 soundings (0 to 20 km) grouped into a) leg 1 (23-28 Feb.), b) leg 2 (5-10 March), c) NH leg 2 (11-13 March), d) leg 2 (13-14 March) days with same latitude, e) leg 2 (14-19 March), f) leg 2 (19-22 March), g) leg 3 (26-30 March) [H.G.J. Smit, Research Centre Jülich (ICG 2), Germany].

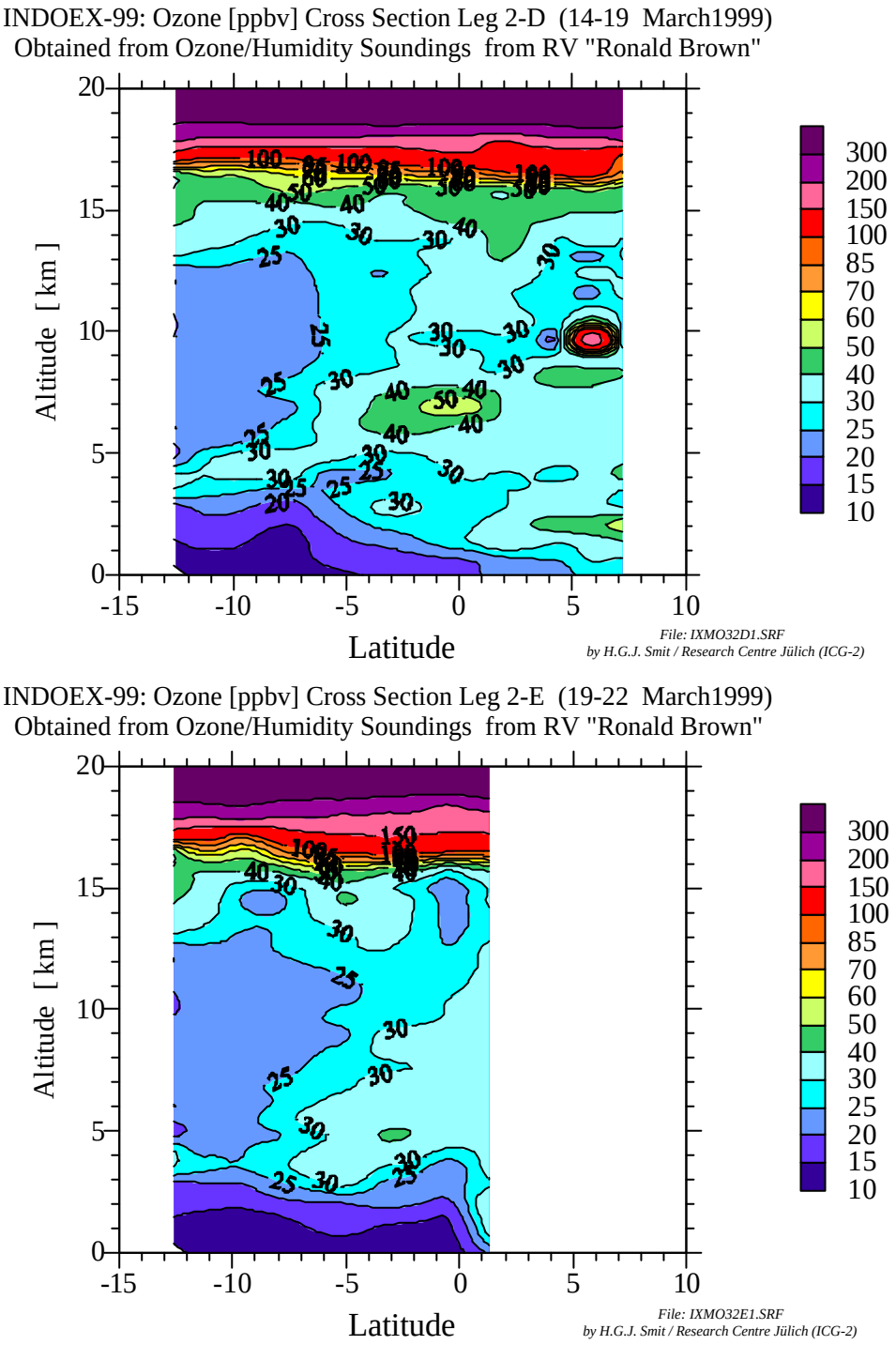

Figure 36: O_3 soundings (0 to 20 km) grouped into a) leg 1 (23-28 Feb.), b) leg 2 (5-10 March), c) NH leg 2 (11-13 March), d) leg 2 (13-14 March) days with same latitude, e) leg 2 (14-19 March), f) leg 2 (19-22 March), g) leg 3 (26-30 March) [H.G.J. Smit, Research Centre Jülich (ICG 2), Germany].

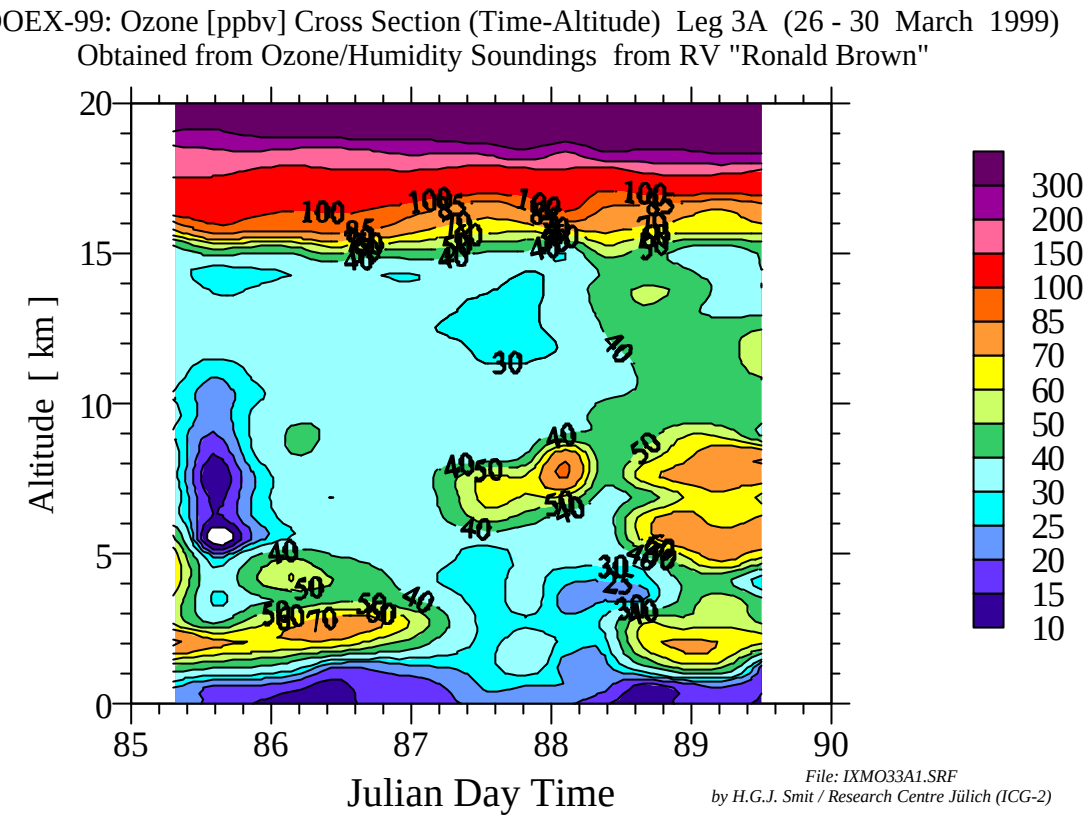

Figure 36: O_3 soundings (0 to 20 km) grouped into a) leg 1 (23-28 Feb.), b) leg 2 (5-10 March), c) NH leg 2 (11-13 March), d) leg 2 (13-14 March) days with same latitude, e) leg 2 (14-19 March), f) leg 2 (19-22 March), g) leg 3 (26-30 March) [H.G.J. Smit, Research Centre Jülich (ICG 2), Germany].

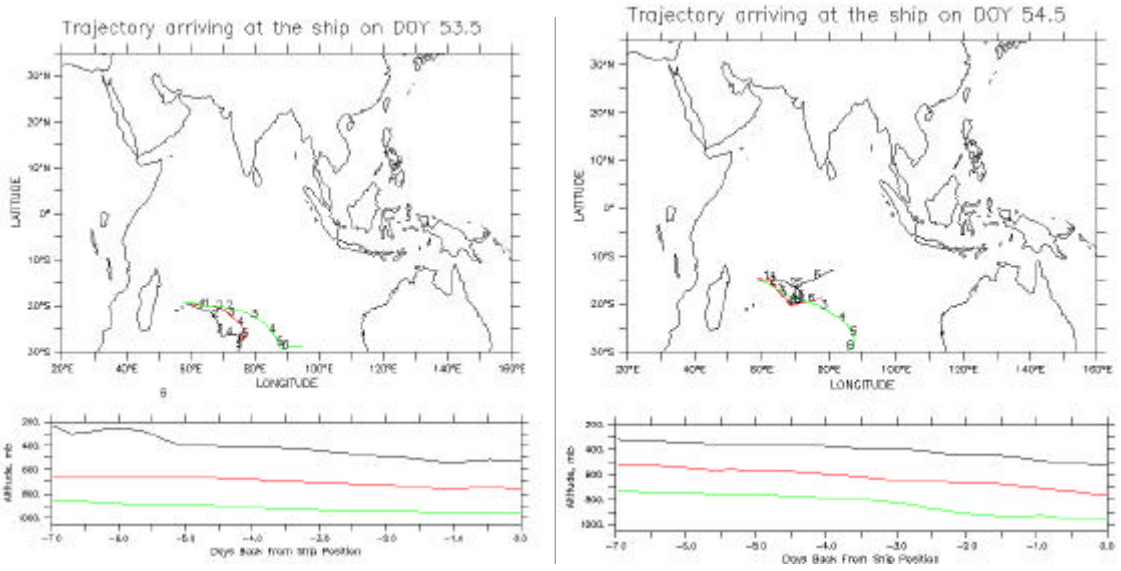

Figure 37: 6 day back trajectories arriving at the ship at 950, 750, and 500 mbar (12Z) for DOY 53 and 54 during leg 1 (INDOEX) [http://saga.pmel.noaa.gov/indoex/traject/].

4.3.2.2.3 Satellite data

Figure 38 shows the vertical O_3 column of the troposphere derived by using the "excess method". The values indicate that there is negligible transport from southern Africa into the Indian Ocean. It has to be mentioned, however, that the excess method is only reliable between 10°N and 10°S, therefore Figure 38 gives only a qualitative impression. The qualitative impression is, however, suitable to determine whether biomass burning and/or other large anthropogenic sources are present and to what extent they influence the investigated region.

Figure 39 shows the number of fires around the Indian Ocean and as expected only relatively low numbers of biomass burning activities occur during this time of the year. Figure 40 shows the lightning activities during February and March 1999. There is no indication of enhanced O_3 levels through local NO_x production (Figure 41). Therefore, the O_3 present in the SH Hadley cell has been most dominantly intruded by the stratosphere, since there are no sources of O_3 precursors in the vicinity and the interhemispheric transport of O_3 remains unlikely.

In the Figure 42 and Figure 43 the vertical columns of tropospheric NO_2 and HCHO are presented respectively. These two trace gases reveal no new sources for O_3 precursors and support the observed excess tropospheric columns in Figure 38. The results by Randriambelo et al. [2000] give further evidence that during February and March there is little influence of biomass burning or other anthropogenic sources on the observed area.

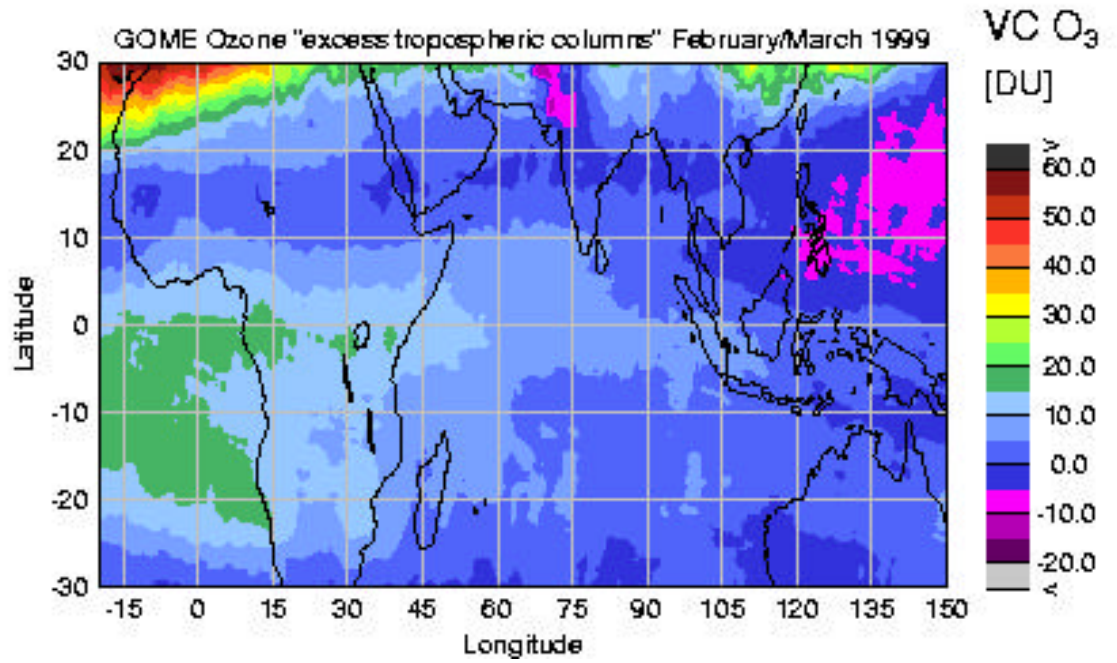

Figure 38: Tropospheric O_3 vertical column [DU] measured by GOME (Feb./March 1999).

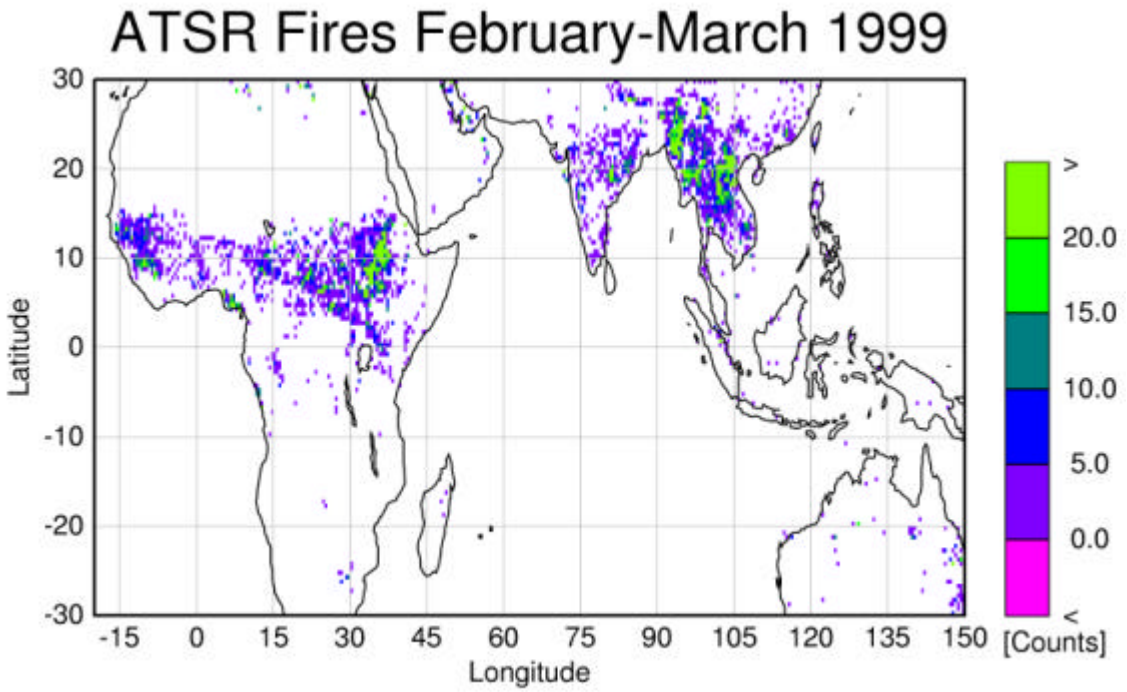

Figure 39: Number of fires according to Along Track Scanning Radiometer (ATSR) for Feb. and March 1999.

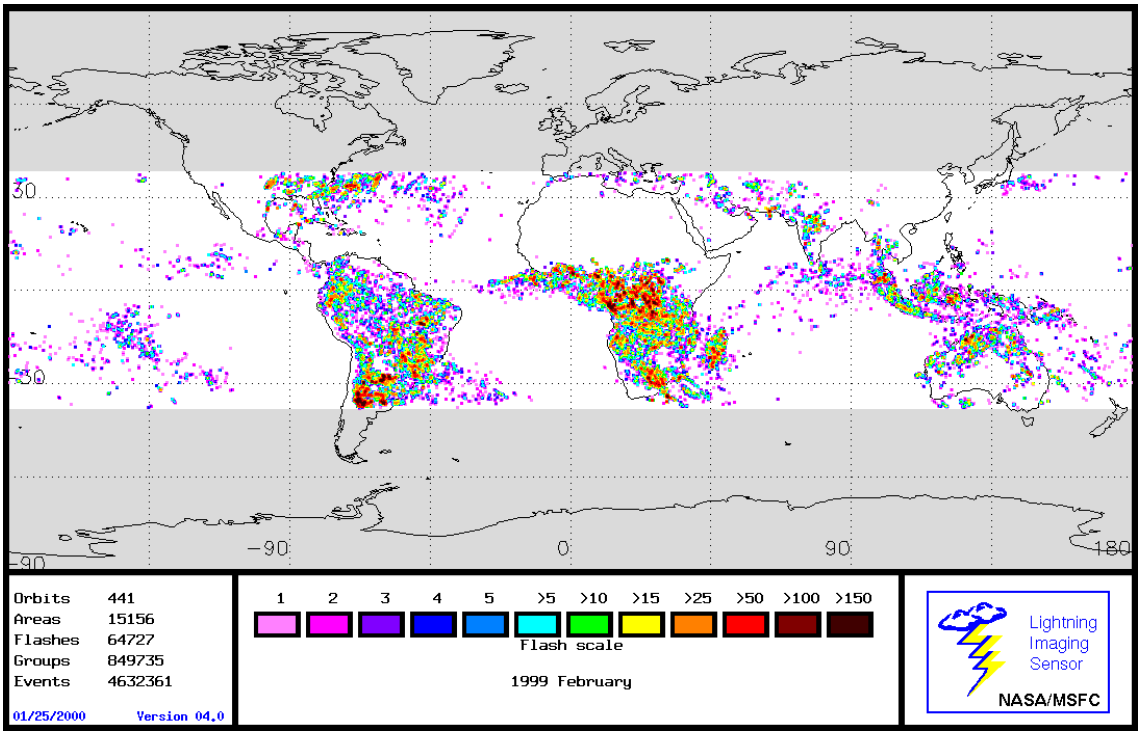

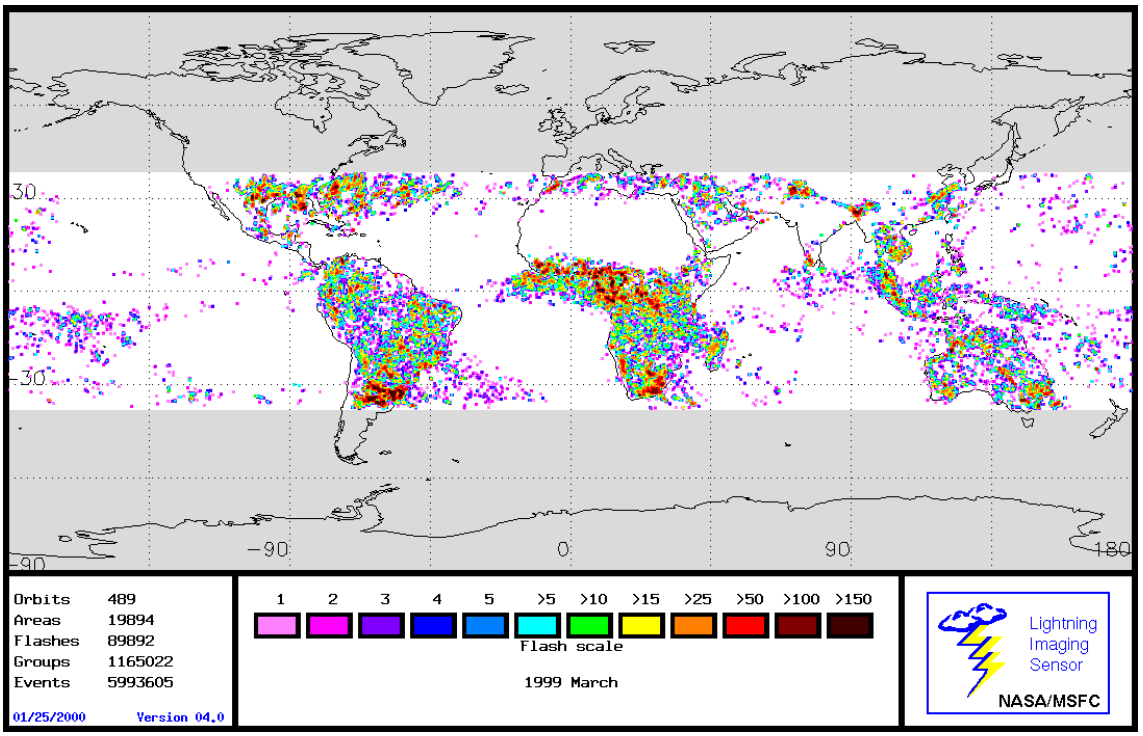

Figure 40: Lightning activity during Feb. and March 1999 [NASA/MSFC].

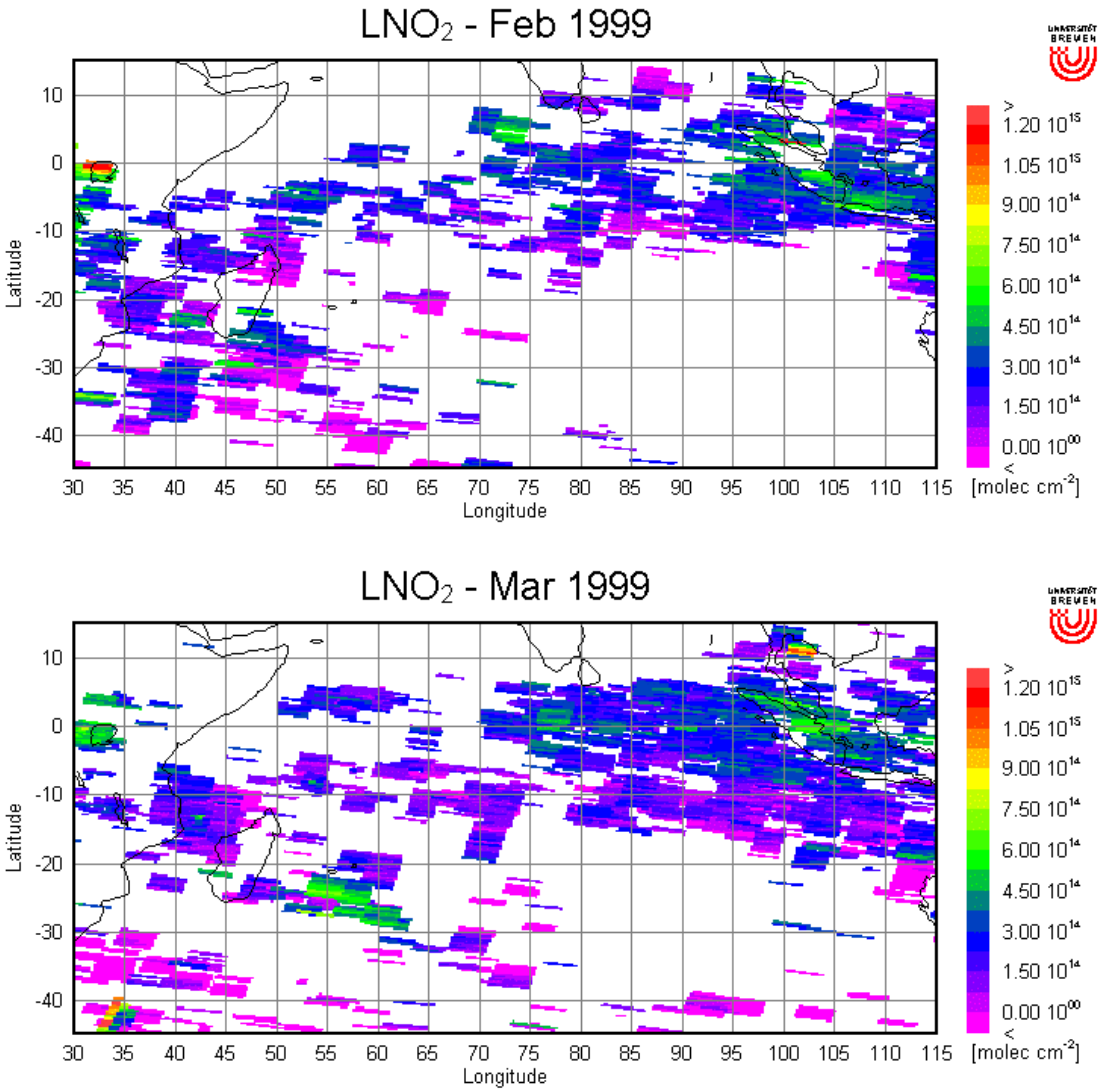

Figure 41: Lightning produced tropospheric NO_2 vertical columns Feb. and March 1999.

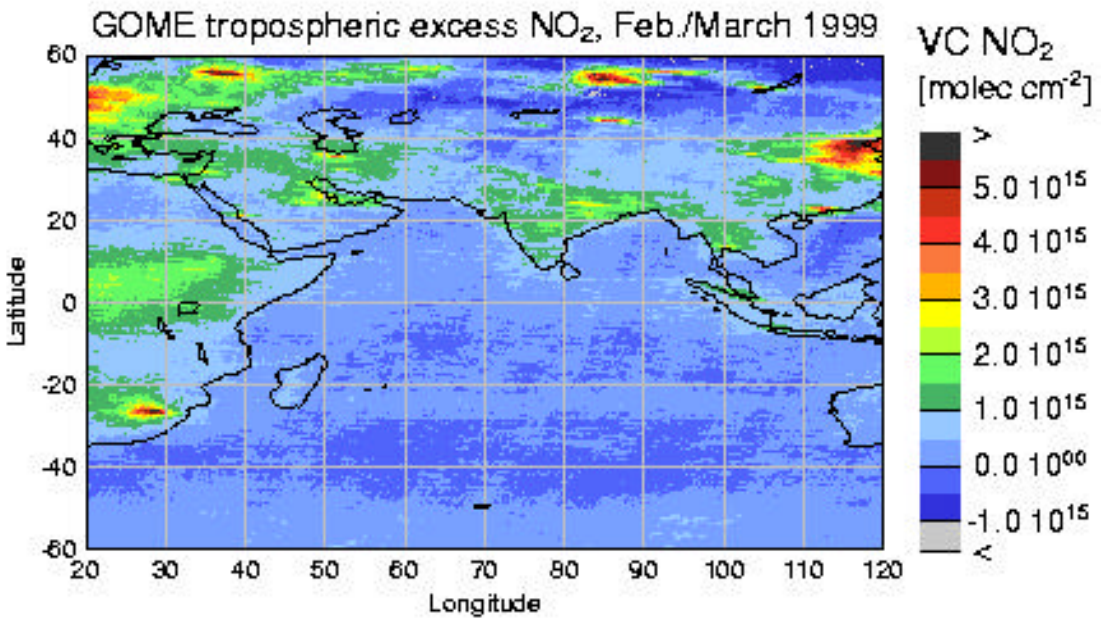

Figure 42: Tropospheric NO_2 vertical column measured by GOME (Feb./March 1999).

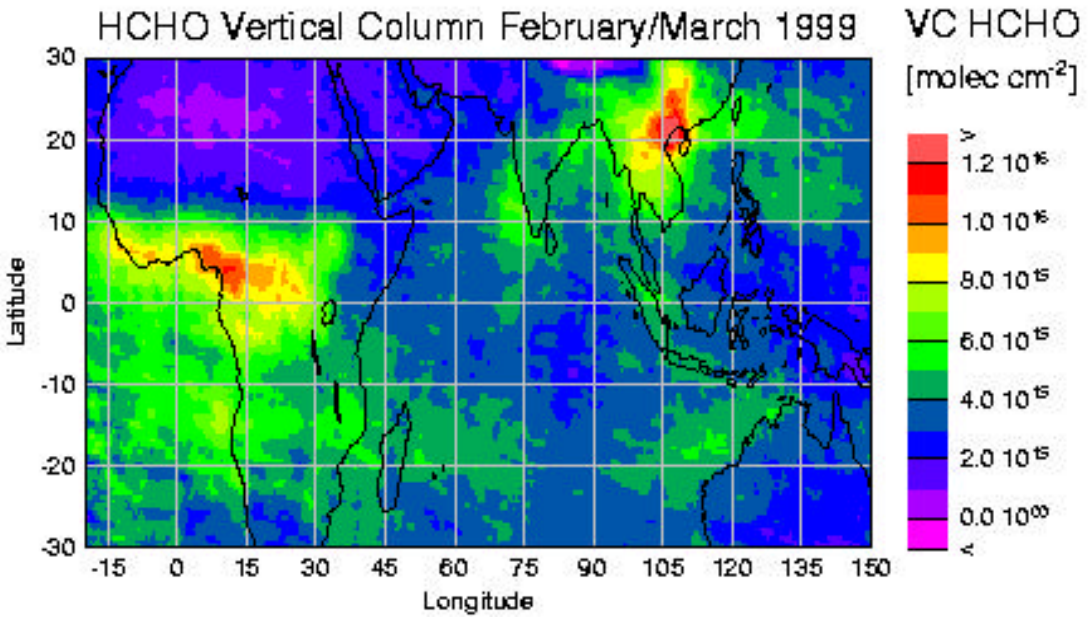

Figure 43: Tropospheric HCHO vertical column measured by GOME (Feb./March 1999).

It can be concluded that the SH O_3 levels measured during the INDOEX campaign have mainly stratospheric origin. However, the influence of long range transport of O_3 cannot be excluded because of the long lifetime of O_3 in the middle and upper troposphere. However, the evidence for the stratospheric origin is clear. The divergence of high O_3 mixing ratios in the transition zone between tropics and extra-tropics seems to indicate the stratospheric tropospheric exchange.

4.3.3 Discussion

The chemistry of the MBL over the period of the INDOEX campaign was simulated using the trace gas measurements, meteorological data, and modelling conditions described above. There is a reasonable agreement between simulated and measured trace gases on most of the days [Burkert et al., 2003a]. Analysis of the results highlights the following features.

4.3.3.1 O_3 depletion

The diurnal behaviour of the O_3 mixing ratio within the MBL during INDOEX typically showed a daytime depletion followed by a clearly visible nocturnal recovery. The short-term variations of O_3 seem to be superimposed on a latitudinal gradient, likely determined by the distance to the precursor sources.

The measured daytime O_3 diurnal variations are reasonably well simulated. Note that O_3 changes associated with both the latitudinal gradient and the change of air parcels (in a 24 hours period) are not considered in this simulation.

In order to rule out any interference associated to the latitudinal effect the days 72 and 73 corresponding to a horizontal transect were more closely analysed. In Figure 44 both the measured and the simulated O_3 diurnal variations are plotted.

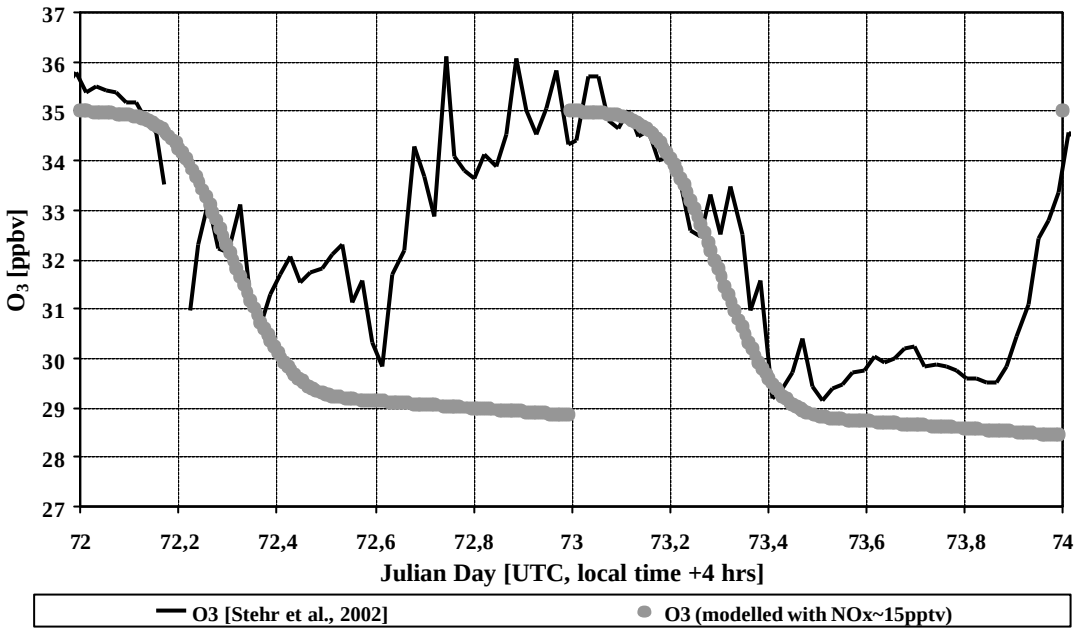

Figure 44: Diurnal variation of measured and modelled O_3 mixing ratios for DOY 72-73 (horizontal transect, no change in the latitude).

The considered photochemistry adequately reproduces the daytime concentrations observed. Since only daily NO averages are available, it is difficult to calculate accurately the daytime O_3 production term. In the case of NO being higher than the mixing ratio considered (NO_x ~ 15 pptv) in the simulation, an additional loss mechanism (i.e. reactions (48), (49), and (50)) involving halogens (as suggested by Dickerson et al., [1999] and Vogt et al., [1996]) would be necessary to explain the measurements.

$$Br + O_3 \rightarrow BrO + O_2 \quad (48)$$

$$BrO + HO_2 \rightarrow BrOH + O_2 \quad (49)$$

$$BrOH + hn \rightarrow Br + OH \quad (50)$$

Figure 45 exemplifies the relative importance of the main daytime photochemical loss reactions involved in the O_3 cycle of remote areas (under clear sky conditions) for both the NH (DOY 64) and SH (DOY 55).

O_3 photolysis is the most important contributor to O_3 losses and represents approximately 40% for the NH and 65% for the SH of the total. The corresponding

percentages for HO_2 are 20% and 10% respectively. Deposition over the surface accounts only for 5% in both hemispheres.

Figure 45 is an overview for the influence of halogens showing the possible loss of O_3 through reactions (48), (49), and (50) for 10 pptv BrO. According to the literature, this value can be consideredas a BrO upper limit in the troposphere [e.g. Keene et al., 1990, Fan and Jacob, 1992, Finnlayson-Pitts, 1993b, Parrish et al., 1993, McKeen and Liu, 1993, Graedel and Keene, 1995, Ariya et al., 1998, Richter et al., 1998, Wagner and Platt, 1998, Vogt et al., 1996, Sander and Crutzen, 1996, Sander et al., 1997]. Under these conditions, Br contributes 25% to the total loss of O_3 in the NH and less than 20% in the SH.

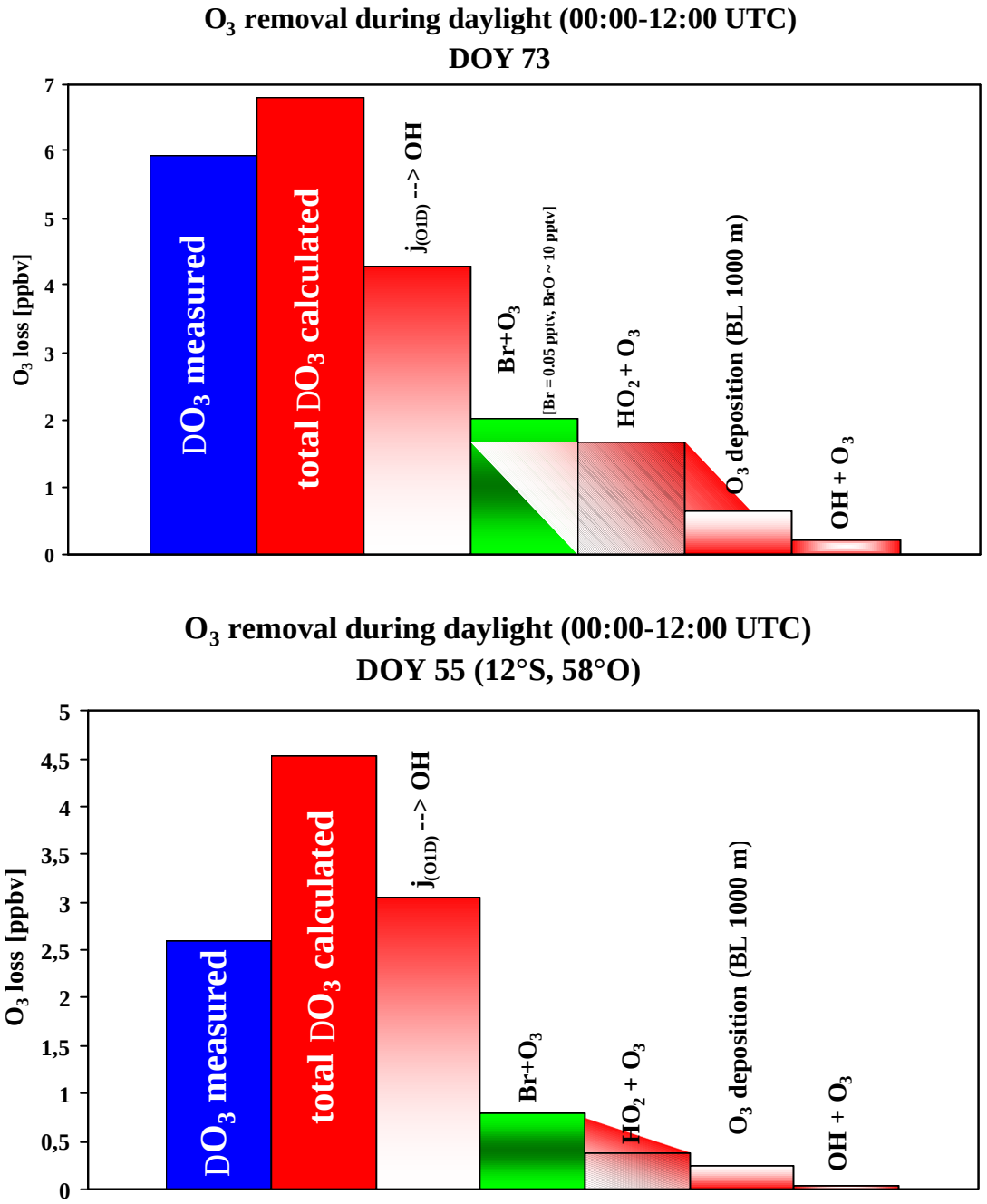

Figure 45: Relative importance of the main first order reactions defining O_3 losses over remote areas of the MBL in the NH (a) and SH (b). The calculations have been made considering the measured amounts of $j(O^1D)$, H_2O, OH and O_3 for DOY 73 (a) and 55 (b) respectively. The following assumptions have been made: HO_2 = ½ RO_2^* (i.e. RO_2+HO_2), Boundary layer height = 1000 m, deposition velocity = 0.045 cm s^{-1} and Br = 0.05 pptv.

4.3.3.2 O_3 recovery

This section discusses the results of measuring nocturnal O_3 variation the data showing a clear recovery most days. This recovery might be the result of horizontal or vertical mixing, or a combination of both. Since the model is not accounting for any dynamic processes, recovery is not calculated by the model.

The different time of appearance of the recovery (DOY 72 at ~ 1500 hrs (UTC) and DOY 73 at ~ 2100 hrs (UTC)) suggests a time dependent effect. Two processes will be discussed explicitly, the advective process transporting O_3 horizontally to the observed measurement site, and the convective processes leading to an entrainment from the layer above the MBL.

4.3.3.2.1 Advective processes

It has recently been shown by de Laat [2000, 2001a, 2001b] that horizontal transport and photochemical processes can explain the typical diurnal O_3 cycle in the MBL close to the source region. This mechanism proposes that the daytime decrease and nighttime increase are closely related.

Daytime O_3 destruction, combined with horizontal advection and diffusion, creates the latitudinal gradient in O_3 from the source regions. This gradient causes the nighttime increase because air with higher O_3 concentrations is advected to regions with lower O_3 concentrations. Using this approach the daytime decrease will always be counteracted by the nighttime increase. The daytime depletion rate is therefore equal to the amplitude of the diurnal O_3 cycle. Although the horizontal advection of air masses with higher O_3 concentrations continues during daytime, net photochemical O_3 destruction dominates daytime O_3 behaviour.

Differences in wind speed are required in order to explain the different start-up times for O_3 recovery on DOY 72 and 73 by horizontal transport and the associated latitudinal gradient. This has not been observed. However, it could be argued that different air masses have been observed, but according to data of other trace gases this was not the case.

During the first leg of INDOEX SHmT air masses were observed coming from the East and with no sources available, the diurnal behaviour of O_3 was exactly the same. A latitudinal gradient was also observed. As the source for SH tropospheric O_3 during leg 1 is expected to come from the stratosphere by downward transport at the end

of the Hadley cell, the advective process would still be an excellent explanation. Also the decrease in the latitudinal gradient in O_3 in the SH is in agreement with the theory. The NH latitudinal gradient does not reveal a decrease with decreasing amount of O_3. This is in disagreement with the expected behaviour.

4.3.3.2.2 Convective processes

The convective processes caused by the strong variation in the Earth's temperature (and the resultant vertical temperature profile) are a main source for O_3 transport at the surface over land [Brasseur et al., 1999, and references therein]. Over the ocean there is only a slight T-variation.

The vertical distribution of temperature over the ocean obtained from meteorological radiosondes, does not clearly indicate the stability of the air parcels. According to the potential temperature the air is in almost all cases conditional unstable. The observed lapse rate is smaller than the dry adiabatic lapse rate (on average the gradient over ocean is between 0.6 and 0.7 °K/100 m). The virtual potential temperature behaves similarly due to the negligible difference of the heat capacities between dry and moisturised air. However, the effect leads only to a more stabilised atmosphere, since the amount of water in the atmosphere has its maximum in the MBL.

For calculating the stability of an air parcel the equivalent potential temperature (EPT) can be used as an indicator. The observed EPT indicates that the layer above the MBL was conditionally unstable, because in the NH during INDOEX the MBL (R.H. between 70 and 95%) was mostly covered with a dry layer (R.H. between 30 and 50%) (Figure 46). In areas where vertical mixing is expected (i.e. ITCZ), which implies a homogenous vertical distribution of relative humidity, the EPT indicates a conditionally stable atmosphere. This leads to the conclusion that, either the stability of the atmosphere is driven by other processes, or the adiabatic approach is inappropriate.

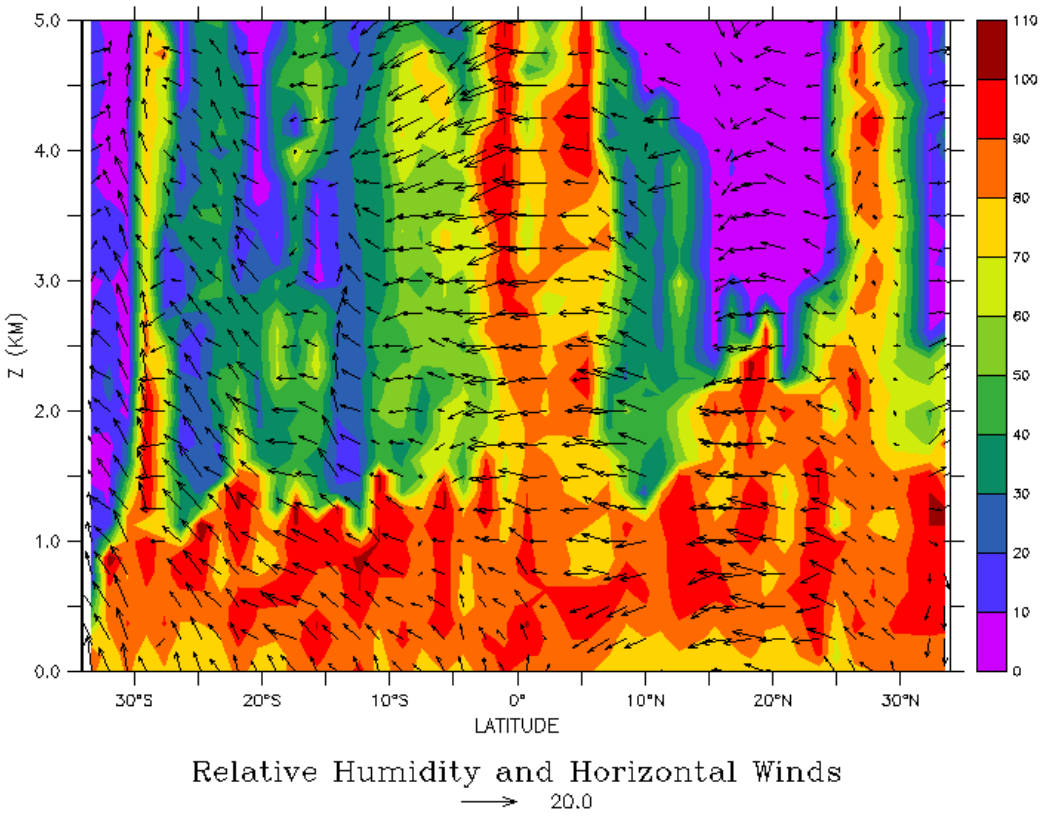

Figure 46: Cross section of relative humidity and horizontal winds observed during INDOEX [http://saga.pmel.noaa.gov/indoex/rsonds/hw_a1_lat_5_c.gif].

Apart from the thermodynamical view of stability two possibilities of vertical mixing have been discussed in the past, a constant entrainment [e.g. Dickerson et al., 1999], and a diurnal variable entrainment [e.g. Bremaud et al., 1998].

Constant entrainment

The assumption of constant entrainment can describe the nighttime recovery of ozone. However, this process seems to be unlikely because of the different recovery times for O_3 (Figure 44) and the time over which O_3 is recovered. Furthermore, this mechanism produces an additional amount of O_3 during daytime which requires another loss process to be compensated, in order to reproduce the measurements. Even halogens could not account for such an additional loss [Dickerson et al., 1999].

Diurnal variable entrainment

This section discusses the possibility of a diurnal variation of the entrainment strength. This assumption can be supported by the fact that the presence of absorbing aerosols lead to a warming of the layer where they are present.

Figure 47 shows the model results of the warming rate (K h^{-1}) due to the absorption of direct solar radiation by aerosols derived from PHOTOST for an AOD of 0.47 and a vertical distribution as measured by Welton et al. [2002]. According to the observed air masses in the NH especially the NHcT and NHcX regimes, there was always a highly polluted aerosol layer above the MBL [Welton et al., 2002]. The described effect leads to an entrainment velocity which is dependent on the solar radiation and the amount of absorbing aerosols. The warming over a day is about 1°K in the aerosol layer (~1 to 3 km) which is significant compared to a dry adiabatic lapse rate. However, there was no systematic difference in the extension of the temperature inversions observed [radiosonde data, http://saga.pmel.noaa.gov/indoex/index.html], that would indicate a change in the entrainment strength between day and night. The only evidence for the warming effect of aerosols can be seen in Figure 49, where the temperature profiles from sondes have been averaged according to the air mass characterisation by Welton et al. [2002] shown in Figure 48.

These averaged vertical temperature profiles show an increasing slight inversion layer (i.e. the vertical temperature gradient decreases to ~0°K/m) as the air masses change the cleaner (C1-C3) to the more polluted regions (C4-C6). The change from the cleaner region to the more polluted region coincidences with an enhancement in the amount of absorbing aerosols [Dickerson et al., 2002].

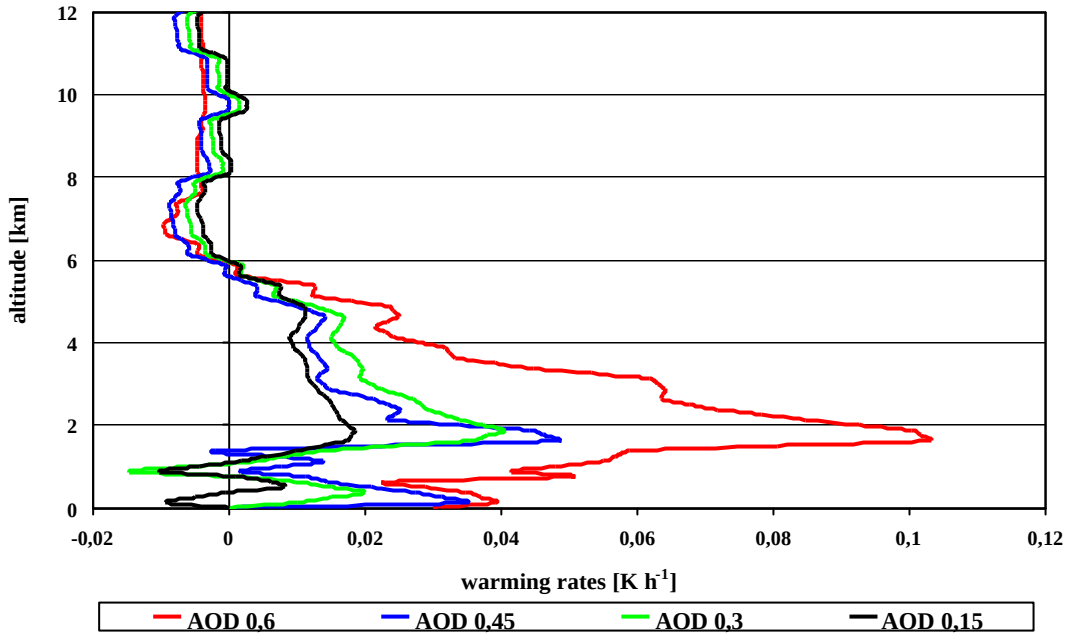

Figure 47: Modelled warming rates caused by aerosols for different AOD at a SZA of 30°. Composition and vertical distribution are described in Table 5 and Figure 23 respectively.

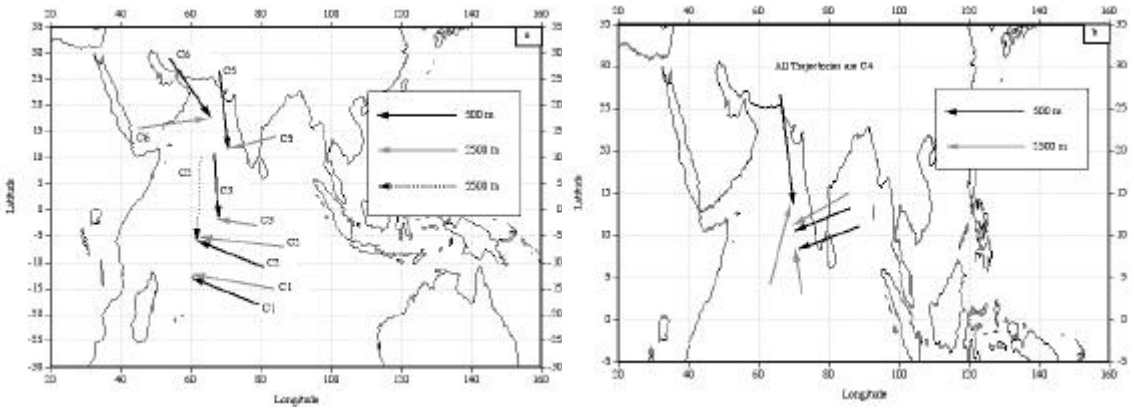

Figure 48: Air mass trajectories at 0.5, 2.5, and 5.5 km are shown for each category defined in the text. The C1, C2, C3, C5, and C6 trajectory patterns are shown in (a), and C4 trajectory patterns are shown in (b) [Welton et al., 2002].

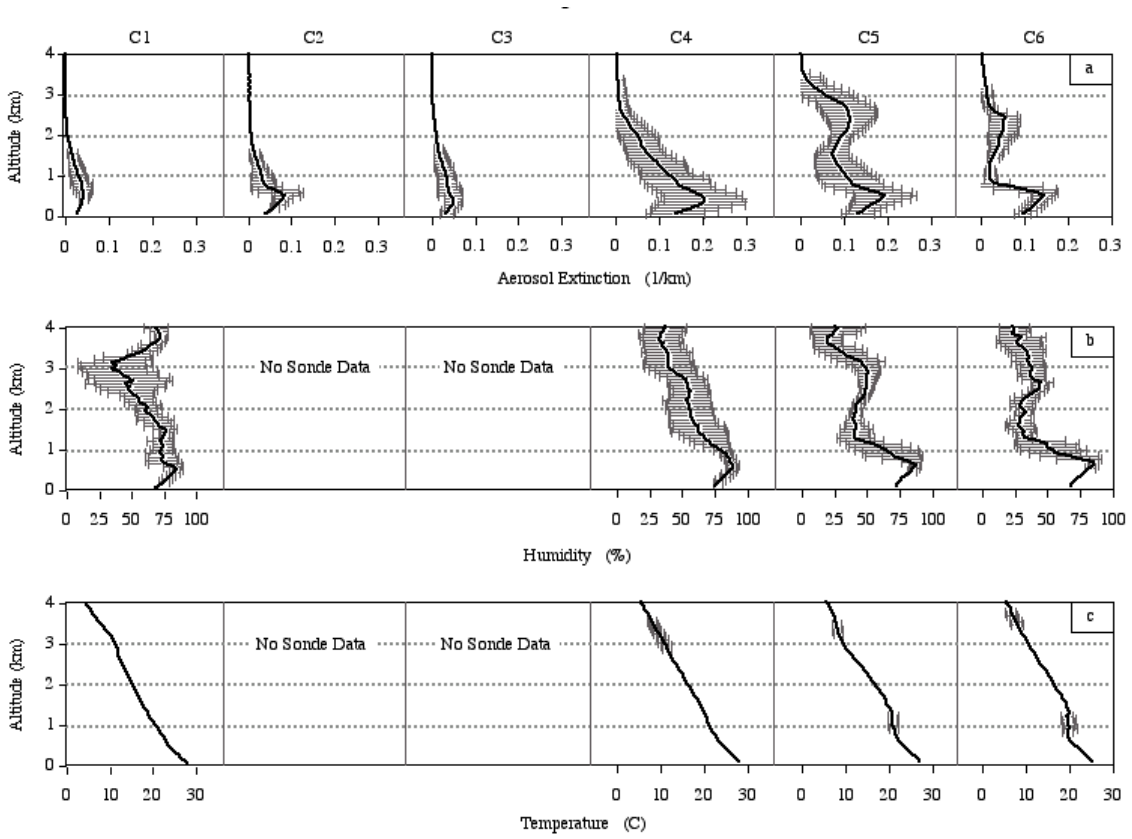

Figure 49: The average extinction profile for each air mass category (see Figure 48) is shown in (a), the humidity profile is shown in (b), and the temperature profile is shown in (c). Horizontal bars represent the standard deviation in each average profile [Welton et al., 2002].

The O_3 (2km)/O_3 (0km) ratio gives some information about the entrainment strength from the layer above into the MBL. Table 3 presents the daily averaged O_3 mixing ratios in the MBL [Stehr et al., 2002] and at 2km height [Figure 9] measured on board the RV Ron Brown. On most of the days the ratio is about 1.6 +/- 0.5, which indicates that the possible variability in the entrainment strength is not high. The correlation between AOD and the ratio is well pronounced (Figure 22) and supports the effect of aerosols and radiation on the vertical temperature structure.

Despite this, on DOY 85 and 86 the O_3 (at 2 km)/ O_3 (at 0 km) ratio was above 5 while the diurnal cycle of O_3 showed a decreasing O_3 mixing ratio during the day and a recovery after sunset to the same level as before sunrise. Taking into account that the O_3 mixing ratio in the MBL was ~15 ppbv and the mixing ratio at 2 km height was ~71 ppbv, the two layers seem to be isolated from each other. The AOD during these two

days was around 0.4, which is comparable to the AOD measured in the NHcT and NHcX regimes.

DOY	O_3 (2km) [ppbv]	O_3 (0 km) [ppbv]	O_3(2km)/O_3(0km)
55	22	11	2
56	17	10	1.7
57	15	9	1.7
58	35	18	1.9
64	45	28	1.6
65	55	32	1.7
66	68	35	1.9
67	72	35	2.1
68	66	47	1.4
69	62	49	1.3
70	45	44	1.0
71	60	36	1.7
72	65	33	2.0
73	53	33	1.6
74	45	28	1.6
75	35	22	1.6
76	27	15	1.8
77	16	12	1.3
78	17	10	1.7
79	16	10	1.6
80	20	18	1.1
81	30	27	1.1
85	77	15	5.1
86	65	12	5.4
87	27	21	1.3
88	25	20	1.3

Table 3: Daily O_3 mixing ratio at ground level and at 2 km and the resultant ratio.

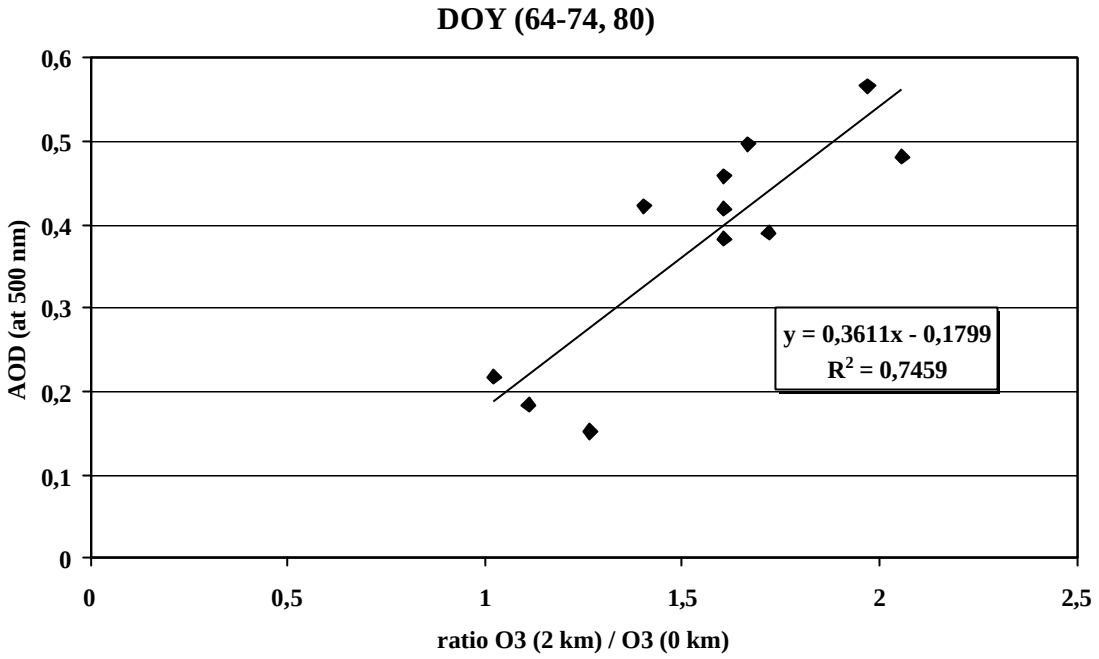

Figure 22: Correlation between the ratio of O_3 (at 2 km) / O_3 (at 0 km) and measured AOD (at 500 nm). DOY 64-74 and 80 were selected according to the availability of the AOD measurements, except for DOY 85 which is discussed in the text.

Overall, it seems to be impossible with the information presented here to rule out any of the above mentioned processes. The possibility of a diurnal variation in the entrainment strength seems to be most likely, although accepting this process still includes the presence of other possible loss processes (such as halogens) for explaining the diurnal behaviour of O_3.

In addition, diurnal variation in the entrainment strength still includes entrainment during the day, however it only gives evidence for less daytime entrainment than nighttime entrainment.

4.3.4 Interpretation

The measurements of vertical O_3 profiles in the SH, together with satellite pictures of a variety of trace gases have shown in a qualitative way the strong influence of stratospheric O_3 within the troposphere. The satellite pictures show that the influence of biomass burning or lightning produced NO_x in the area of observation was minimal.

Other possible sources of O_3 and its precursors are far away, but due to the long lifetime of O_3 in the middle and upper troposphere this influence cannot be neglected.

However, taking all the data into account it appears that the amount of STE of O_3 was the major source in the SH Indian Ocean during February and March.

Overall, the collected data give the excellent opportunity to analyse the reliability of global models in this area. Therefore, a comparison of the data with model results should be performed in the future.

A zero dimensional model was used to investigate the diurnal evolution of O_3 concentrations. The known chemistry without any entrainment or horizontal transport and without halogens can describe the daytime decrease of O_3. The role of halogens, however, must be reconsidered when transport processes are leading to an additional source in the model. The expected bromine concentrations can account for about 20% of the total O_3 loss [Dickerson et al., 1999].

The qualitative analysis of the two dynamical processes most likely responsible for the nocturnal recovery of O_3 revealed that neither of them alone can explain the observed behaviour. As a result of this work, convective processes will have to be reconsidered in all models concerning the influence of aerosols. For example, the encountered aerosols during INDOEX can lead to warming rates in the free troposphere of about 1°K a day (AOD of 0.6 and an aerosol composition as described above) which is sufficient to stabilise the atmosphere.

The analysis has shown that neither the convective nor the advective processes on their own can explain the observed diurnal behaviour of O_3. A combination of both processes appears reasonable, but a more detailed analysis of the micro and macro meteorological parameters is required.

It can be summarized that the daytime destruction of O_3 is well reproduced by the known chemistry, but the presence of for example halogens cannot be ruled out and absorbing aerosol can be responsible for a diurnal variation in the entrainment strength. In future studies of this type it is suggested that this information should be collected so that it can improve chemical knowledge in the MBL.

5 PRIME campaign

5.1 Introduction

The Institute of Environmental Physics of the University of Bremen (IUP-UB) and the University of Leeds (Uni-Leeds) participated on a EU project called PRIME (Peroxy Radical Initiative for Measurements in the Environment). It consisted of a field campaign to measure tropospheric trace gases near London during the period July-August 1999.

One of the objectives of the field work was to investigate the role of oxy-, hydroxy-, and peroxy radicals in urban environments, and to characterise sources and sinks of these radicals in the troposphere. Therefore an extensive suite of ancillary measurements necessary for photochemical modelling, including measuring levels of trace gases, photodissociaton rates and meteorological parameters, also formed part of the study (see http://www.huxley.ic.ac.uk/research/emma/prime/).

In the present study, measurements of RO_2^*, NO, NO_2, PAN, and CO performed by the IUP-UB and H_2O_2 and ROOH made by the Uni-Leeds are presented and compared with the results from a zero dimensional model. The discussion focuses on the measured daytime amounts of RO_2^* in relation to HO_2 using the FAGE technique (Fluorescence Assay with Gas Expansion) [Creasey et al., 1997, Carslaw et al., 1999], and to the peroxide measurements of the Uni-Leeds. In addition, one issue of special interest is the coexistence of high amounts of NO and RO_2^*, especially in the early morning hours.

5.2 Results and discussion

5.2.1 Air mass classification and measurement site description

According to the back trajectories [British Atmospheric Data Centre – Trajectory service, http://www.badc.rl.ac.uk/], three different types of air masses (hereafter referred to as North West, East and South-West) were identified during the course of this study at the measuring site.

Figure 50 represents typical back trajectories for the different air masses. In the case of North-West trajectories the air parcels originated from south of Iceland and passed the northern part of the UK before reaching London. The eastern air mass initially came from the north and north east. The air passes the European Continent before heading towards London. Locally these air parcels reached the measurement site from the East and South East. The south-west air masses originated over the Atlantic Ocean, passing over the north western part of Spain and the north western part of France reaching London from the South-West.

Three classes have been identified as being significantly different in terms of air mass origin and composition, whereas the latter is superimposed by local emissions. The types of air masses (North-West, East, and South-West) comprise the following periods:

- North-West: 23.7 – 27.7; 10.8 –12.8
- East: 28.7 – 3.8; 9.8
- South-West: 4.8 – 8.8

As the local wind direction is independent of the air mass origin, the origin of the air mass is only relevant for long lived species not emitted by local sources.

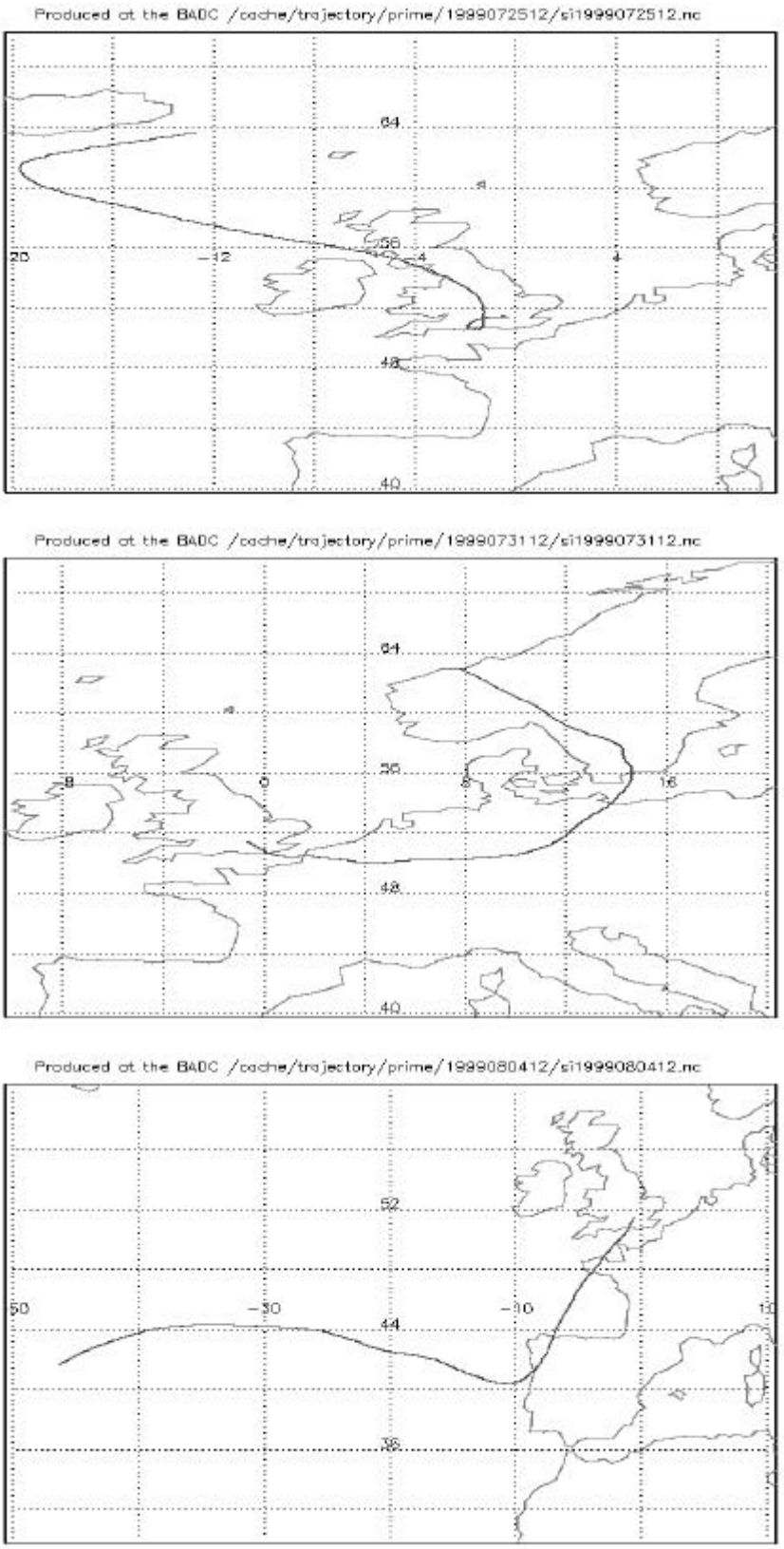

Figure 50: Typical 5-day back trajectories for a) North-West (23.7 – 27.7; 10.8 – 12.8), b) East (28.7 – 3.8; 9.8), c) South-West (4.8 – 8.8) [British Atmospheric Data Centre – Trajectory service, http://www.badc.rl.ac.uk/].

The measurement site, although located in a park, is surrounded by roads with significant traffic. In general, the diurnal behaviour of the trace gases in the area of study is expected to be mainly determined by the local/regional emissions. During the period field measurements were taken local winds were of variable intensity, indicating an unsteady influence of local emissions in the air composition measured. Therefore, and as a consequence of the rough resolution of the trajectories, no clear correlations between trace gases and general air flows are expected.

Two episodes of elevated concentrations of trace gases were observed, from the 23rd to the 25th July, by North-West conditions and from the 29th July to the 3rd August, characterised by East trajectories. Jenkin et al. [2000b] have recently reported that the most intense photochemical ozone episodes are associated with trajectories over mainland Europe where they are enriched with VOC and NO_x for several days before arriving in the UK from a broadly eastern or south-eastern direction.

5.2.2 Trace gas measurements

In the following the complete dataset recorded during the PRIME campaign by the IUP-UB and the Uni-Leeds is presented. The NO, NO_2, CO, RO_2^*, and PAN mixing ratios measured by the IUP-UB are shown in Figure 51. The O_3 mixing ratios measured by Imperial College are also included for clarification. The different air masses are labelled on top of the figures.

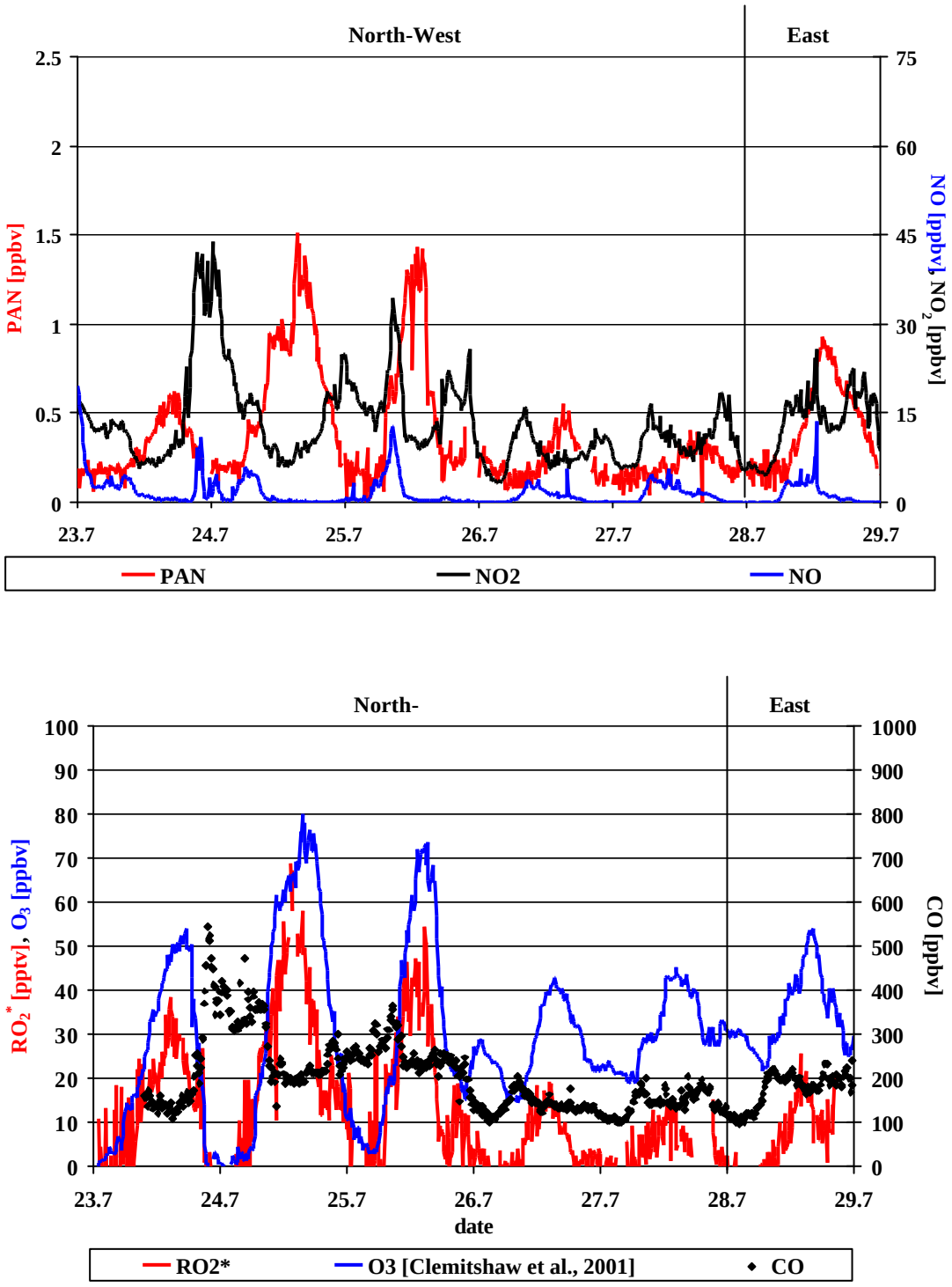

Figure 51: RO2*, CO, O3, NO, NO2, and PAN mixing ratios measured during the PRIME 1999 field campaign.

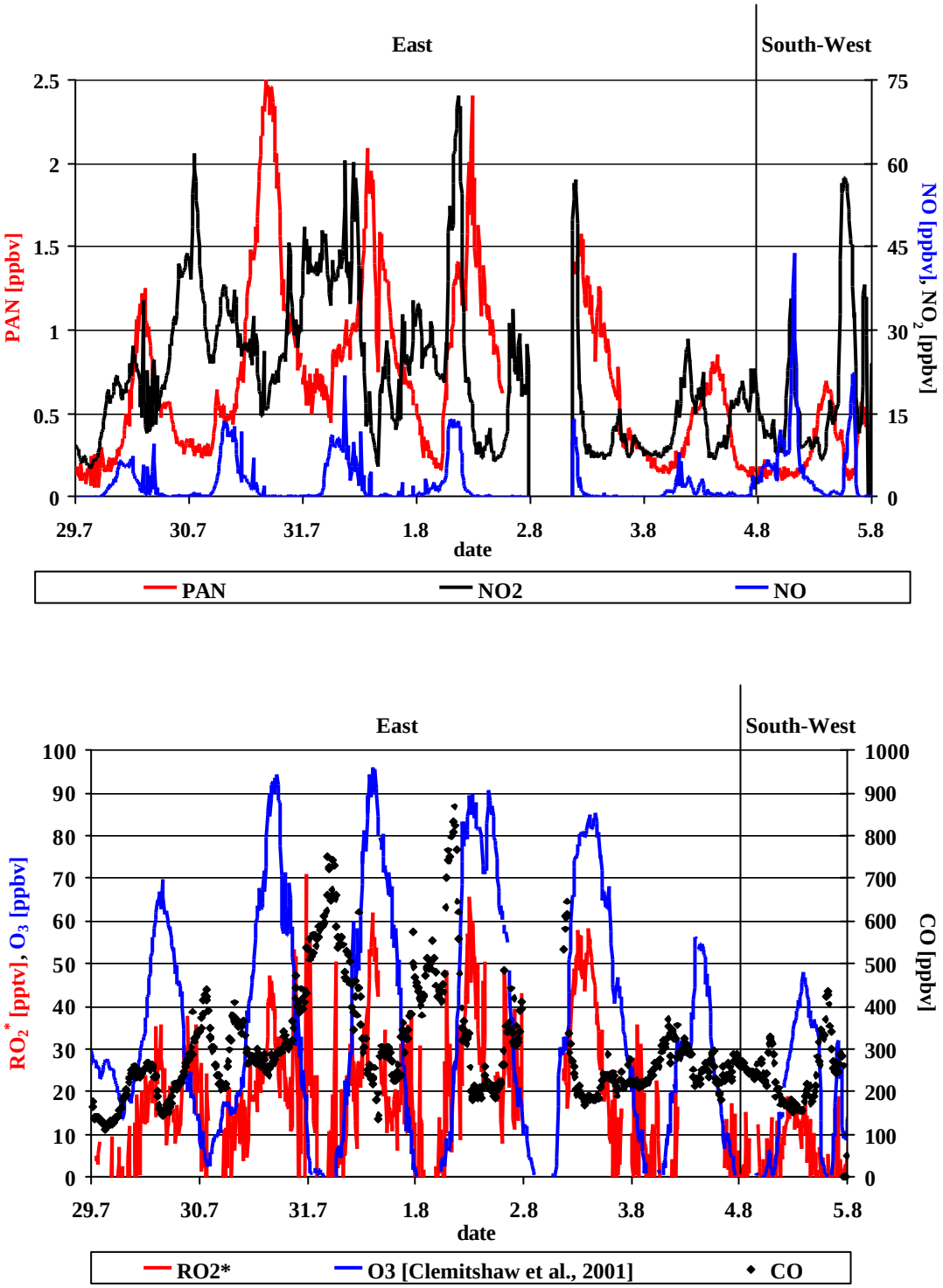

Figure 51: RO_2*, CO, O_3, NO, NO_2, and PAN mixing ratios measured during the PRIME 1999 field campaign.

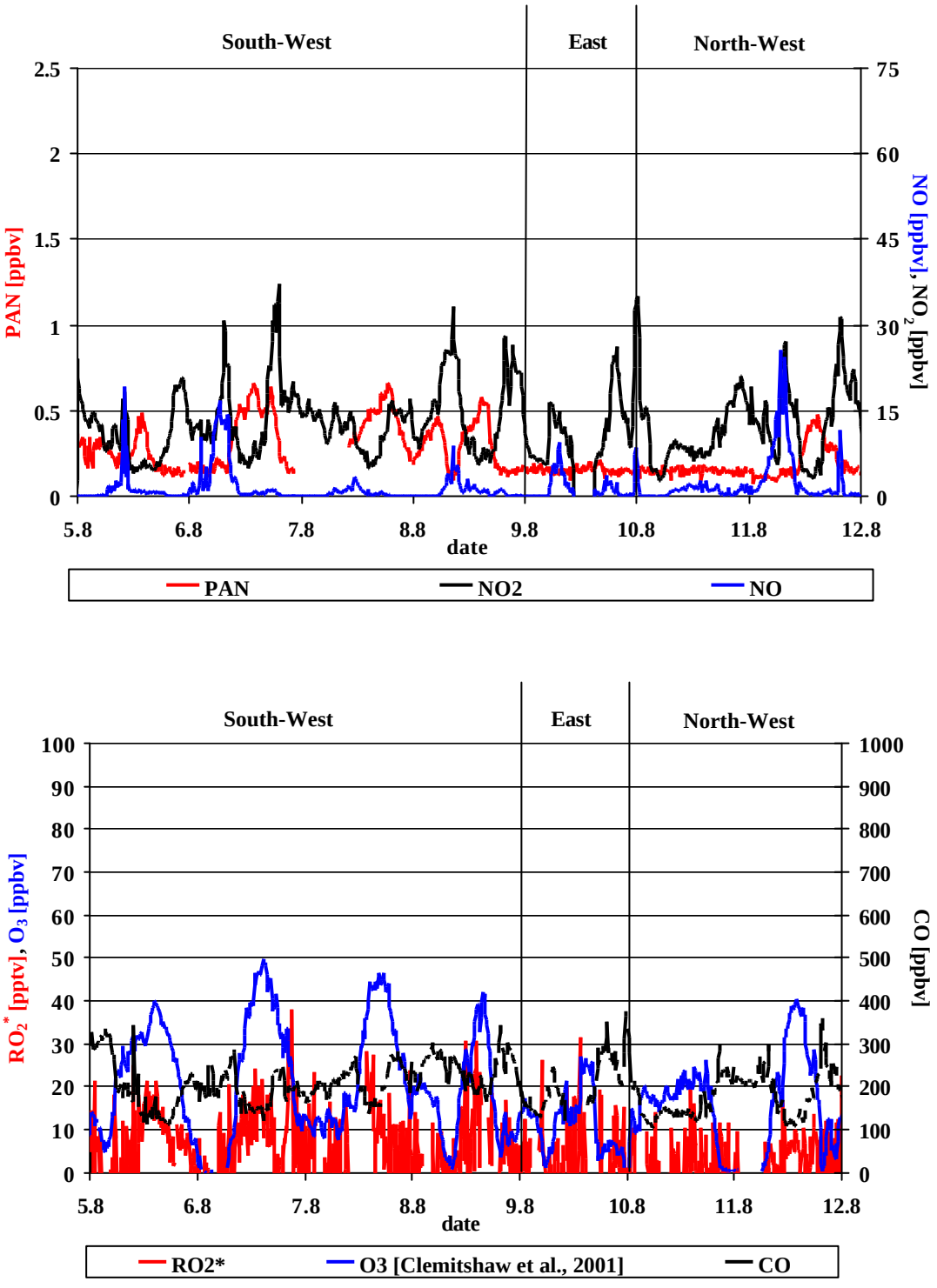

Figure 51: RO_2*, CO, O_3, NO, NO_2, and PAN mixing ratios measured during the PRIME 1999 field campaign.

Two periods have been identified as being highly photochemical active: 23rd-26th July and 29th-3rd August. The other periods are characterised by lesser amounts of all reactive trace species. Figure 52 shows the measured amounts of HO_2, H_2O_2, and CH_3OOH by the Uni-Leeds.

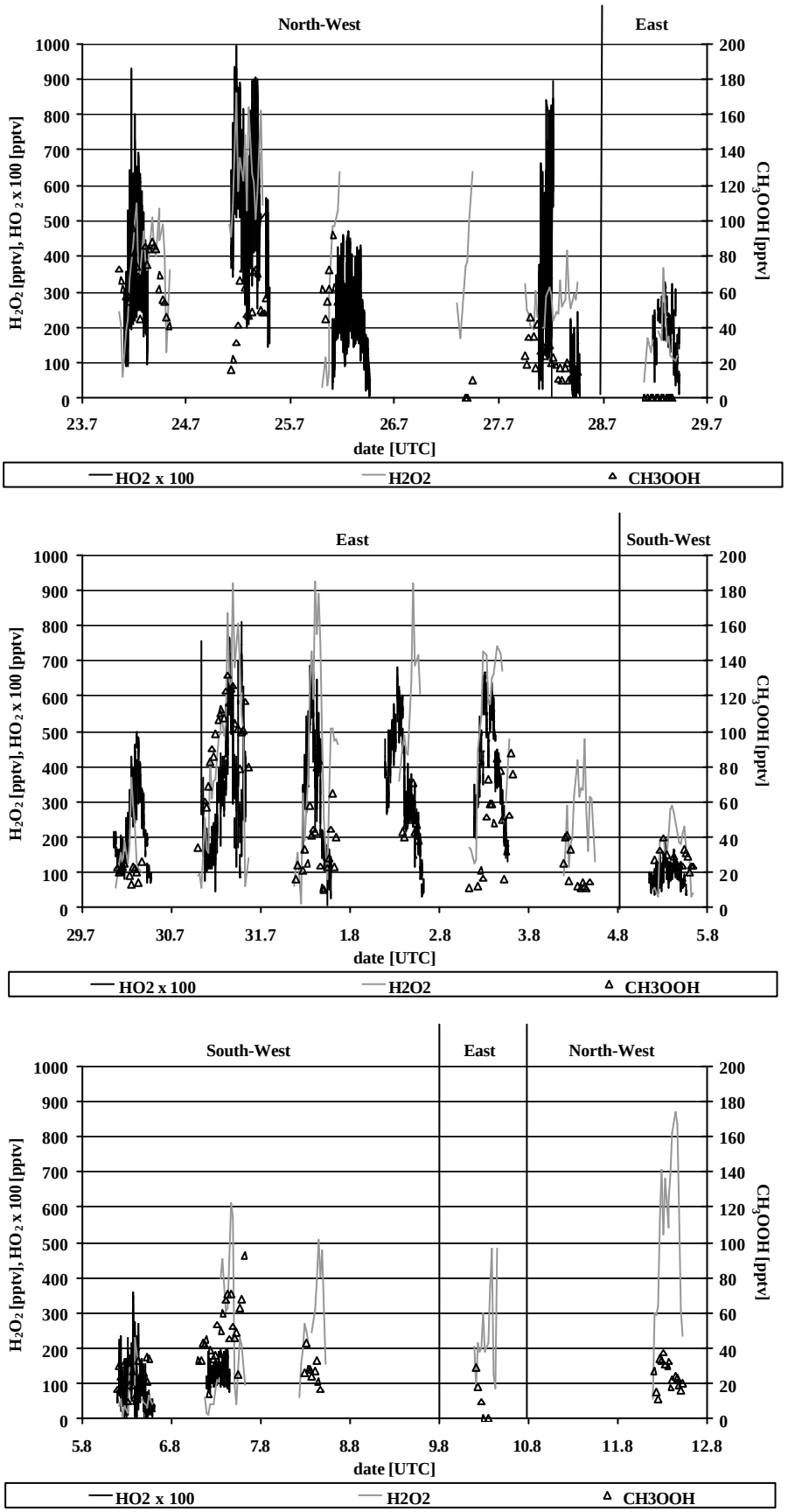

Figure 52: HO_2 (x 100), H_2O_2, and CH_3OOH mixing ratios measured during the PRIME 1999 field campaign.

5.2.2.1 General diurnal behaviour of trace gases

Over the general long term evolution of the air composition, some diurnal features are observed at the measurement site.

NO_2 mixing ratios increase typically at dawn as a result of the NO_x local emissions (i.e. for example rush hour) followed by the subsequent titration of O_3 with NO and the low radiation (i.e. low photolytical decompositon of NO_2). This effect is enhanced by the build up of the nocturnal planetary boundary layer (PBL) during the night, which captures the emission within a much smaller volume compared to the daytime PBL. This is corroborated by the CO nocturnal increase which mostly correlates temporally with the NO_2 variation.

The NO_2 maximum is reached before sunrise. Afterwards, high amounts of NO_2 are produced as it becomes photodissociated to form NO and O_3. This effect, together with the morning rush hour vehicle traffic leads to a maximum in the NO mixing ratio and a maximum in the O_3 production ($d[O_3]/dt$).

With increasing solar radiation the nocturnal PBL vanishes favouring entrainment from above and mixing. Therefore, the direct emissions are diluted, which prevents a further increase in the NO_x mixing ratio. The well mixed PBL around noon is characterised by production of O_3 via the reaction of RO_2^* with NO and the subsequent photodissociation of NO_2. As expected, PAN and O_3 present a very similar diurnal evolution reaching maximum mixing ratios in the late afternoon. However the O_3 plateau generally persists longer than in the case of PAN.

The diurnal behaviour of the RO_2^* concentration is explained in more detail in the next section. It is typically characterised by an increase after the NO maximum, reaching a maximum around noon and staying at a constant level till afternoon. During sunset the RO_2^* concentration decreases and remains on a nocturnal value which likely depends on the amount of NO_3 and O_3 available.

The HO_2 mixing ratios seem to support the presence of non negligible amounts of radicals in the evening. During the day the behaviour is comparable to the behaviour of the RO_2^*, with a stronger decrease in the afternoon due to the faster loss reactions of HO_2 compared to RO_2.

The CH_3OOH diurnal profile is variable, the data shown here does not reveal a clear daily cycle. By contrast, the mixing ratios of H_2O_2 increase at sunrise reaching their maximum during midday, remaining at that level until late afternoon (Figure 52).

Taking into account that H_2O_2 is exclusively produced via the HO_2 self reaction and that production dominates over losses during the day, a correlation of the daily maxima of HO_2 and H_2O_2 is expected, but is not observed.

5.2.2.2 Peroxy radical diurnal variation

The measured RO_2^* diurnal behaviour reflects the photochemical nature of these radicals. The increase in the mixing ratios with increasing solar radiation in the morning is retarded by the presence of NO. The maximum level was generally reached around noon and varied between 15 and 70 pptv during the campaign. After 3-4 hours at an almost constant level of concentration, the RO_2^* mixing ratios decreased to a minimum.

The most striking feature of the PRIME radical dataset is the detection of significant amounts of RO_2^* in the presence of high NO concentrations (Figure 2). This situation is observed repeatedly in the period of high mixing related to the increase of the PBL height at around 9-10 am. The observed coexistence of NO and RO_2^* cannot be explained easily if the time scale of mixing and chemistry are of similar magnitude. The chemistry is expected to be dominated by the reactions of NO with RO_2^* ((86)-(87)), leading to a RO_2^* lifetime of about 1-2 seconds for 3-5 ppb NO.

First of all it is important to rule out a measurement error as an explanation for this RO_2^* in the presence of high NO concentrations anomaly. The complexity and variability of the trace gas composition complicates the measurement of radicals in polluted areas. Very fast variations (within the minute range of the measurements) in the O_3 and NO_2 ambient levels which constitute the background signal of the PERCA can result in an artificial signal, which if not adequately corrected can lead to a wrong interpretation. The IUP-UB considers this effect by switching every 30 seconds between background and signal mode and averaging the background signal before and behind the signal mode. Therefore, the expected error is small and should be negligible while averaging the 1 minute values over longer time intervals.

The 31st of July (Figure 53) is selected as representative of days with active photochemistry at the measurement site. This is one of the days measured during the second episode of elevated concentrations during the PRIME campaign. The analysis concentrates on the variations produced by the model as a function of the assumed amounts of hydrocarbons and CO. The model results represent a sensitivity study focused on the chemistry of HO_2, RO_2, OH, and the peroxides. Both the ratio between

HO_2 and RO_2 and the total amount of radicals present will be discussed, especially in the case of high NO concentrations in the morning hours (see shaded area in Figure 53).

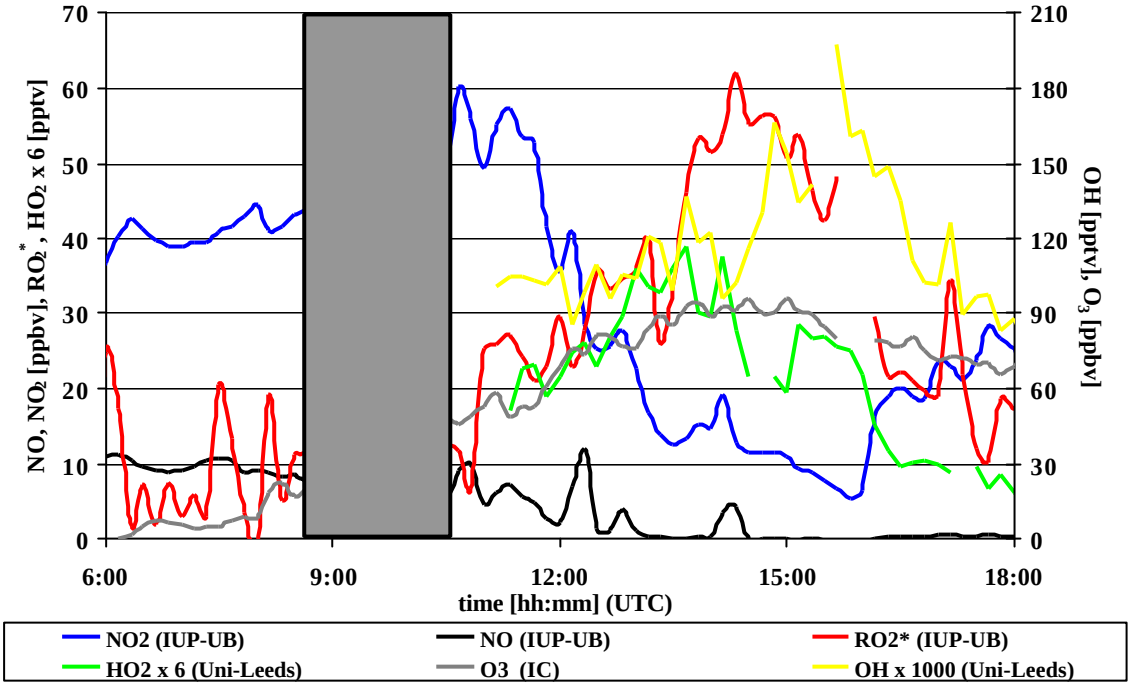

Figure 53: NO, NO_2, RO_2^*, HO_2 x 6, O_3, and OH x 1000 mixing ratios on the 31st of July between 600 and 1800 (UTC) during the PRIME campaign.

5.2.2.3 Nocturnal radical mixing ratios

The model used here does not consider heterogeneous chemistry, a factor which has a significant impact, particularly on the amount of NO_3 present. Therefore this section should be treated as an outlook for further modelling perspectives and measurement campaigns.

On several days the nocturnal RO_2^* mixing ratio showed significant amounts above the detection limit. Nocturnal RO_2^* mixing ratios have been measured before [Cantrell et al., 1992, Hu and Stedman, 1995, Mihelcic et al., 1993, Burkert et al., 2001a, 2001b, 2003a and 2003c]. Bey et al. [2001a, and 2001b] have studied the radical nighttime tropospheric chemistry of different scenarios and found that the peroxy radical concentrations peak at night at 40 pptv in the urban case with OH concentrations ranging from 1 to $6x10^6$ molecules cm^{-3}.

The production of OH is attributed to ozonolysis of alkenes or to the conversion of peroxy radicals initially formed by VOC+NO_3 or VOC+O_3 reactions. In an urban scenario under nocturnal NO mixing ratios on the range of our measurements (100-200 pptv), the NO_3 radical seems to play only a secondary role both in the formation of RO_2, which are produced directly by ozonolysis of alkenes or indirectly from the reactions of the OH produced and other VOC, and in the production of HO_2 ,which mainly occurs via conversion RO_2 to HO_2 by RO_2 + NO reactions.

Increasing the content of biogenic VOC, like isoprene and terpenes, can however increase notably the importance of the contribution of the NO_3 reaction path to the primary production of RO_2 radicals. However the participation of NO_3 to the recycling of radicals remains negligible relative to NO [Bey et al., 2001b].

During the PRIME campaign the average isoprene mixing ratios were usually between 100 and 300 pptv. Interestingly the higher isoprene mixing ratios were coincided with pollution episodes because of the sunny conditions and higher temperatures associated to the smog episodes observed during PRIME.

Significant nocturnal RO_2^* mixing ratios were observed on the 24th, 29th, 30th and 31st of July and on August the 1st. The discussion of the nocturnal behaviour of RO_2 and HO_2 will be subject of a paper published separately [Burkert et al., 2003d].

5.2.3 Model results

This section compares model results and measurements, starting with a base case. In this base case the simulations were performed while constraining the model to the actual measurements of CH_4, CO, NO, NO_2, and propene and ethane equivalent calculated according to reactions (144) and (145) on July 31st. The propene and ethane equivalent considers the C_3-C_6 NMHC measurements by University of Leeds.

$$[\text{propene equivalent}] = \sum_{\text{alkene}_i} [\text{alkene}_i] \left(\frac{n^o C_{\text{alkene}_i}}{3} \right) \left(\frac{k_{OH+\text{alkene}_i}}{k_{OH+C_3H_6}} \right) \quad (144)$$

$$[\text{ethane equivalent}] = \sum_{\text{alkane}_i} [\text{alkane}_i] \left(\frac{n^o C_{\text{alkane}_i}}{2} \right) \left(\frac{k_{OH+\text{alkane}_i}}{k_{OH+C_3H_6}} \right) \quad (145)$$

The assumed amounts for the NMHC in the model are expected to be a lower limit, because the propene equivalent is calculated only for the measured species, and

according to Lewis et al., [2000] the measured amounts of the C_3-C_6 NMHC represent only approximately 30% of the total. Therefore, all unmeasured species, if present, should increase the values used. However, in order to account for this effect each of the NMHC was varied over a large range of mixing ratios (Figure 54). This should be sufficient to cover the unmeasured real case for the interpretation of the possible amounts and ratios of RO_2 and HO_2 in urban environments.

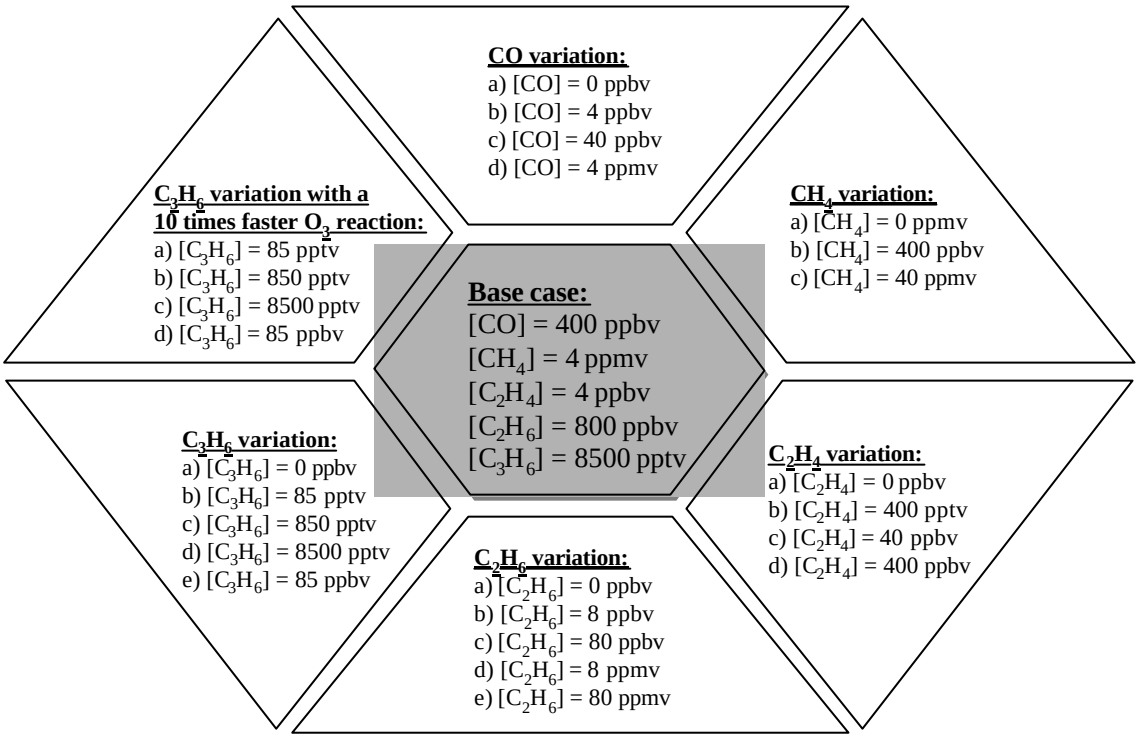

Figure 54: Overview of the different cases considered in the sensitivity study.

5.2.3.1 Base case

In the base case the following trace gas mixing ratios have been assumed: [CO]=400 ppbv, [CH_4]=4 ppmv, [C_2H_4]=4 ppbv, [C_2H_6]=800 ppbv, [C_3H_6]=8500 pptv. The modelled and measured amounts of HO_2, RO_2^*, NO and O_3 are shown in Figure 55.

There is a good agreement between RO_2^* measured and modelled values whereas the amounts of HO_2 differ quite substantially. However, in the early morning hours both the measured HO_2 and RO_2^* amounts are significantly higher than the resulting amounts from the model. This is most likely caused by the presence of high amounts of NO especially in the early morning hours (Figure 53 and Figure 55).

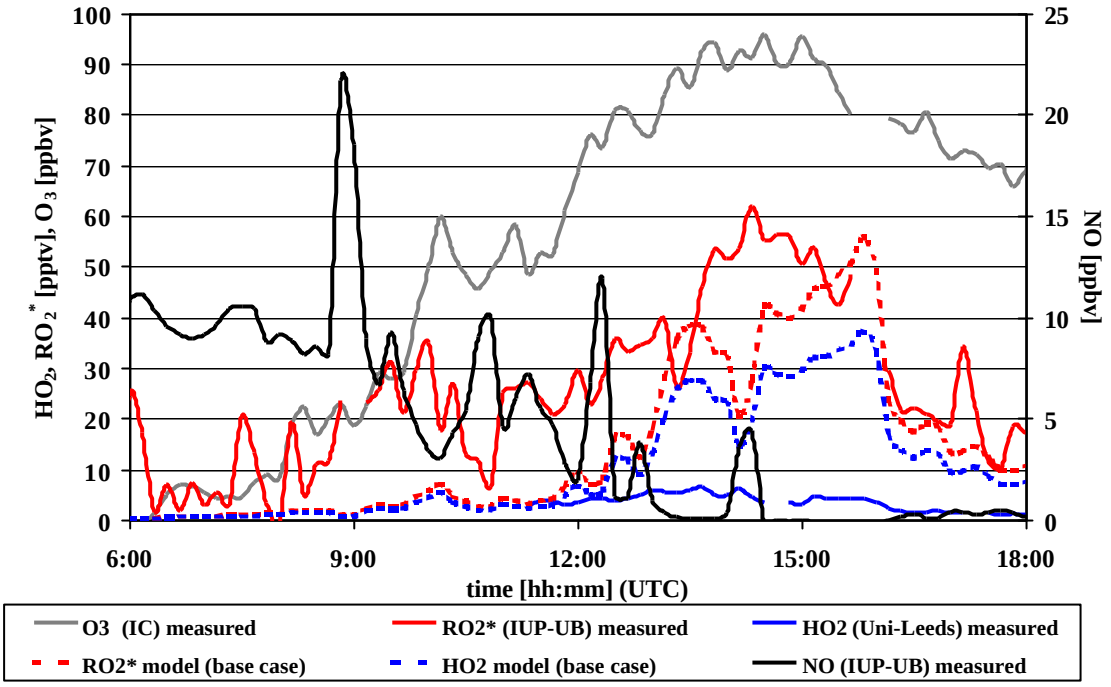

Figure 55: Modelled (dotted lines) and measured (solid line) HO_2 and RO_2^* mixing ratios for the 31st of July 1999 during the PRIME campaign.

The NO reactions involved in the radical interconversion dominate over the other reactions. Assuming the steady state the following equations result.

$$\frac{d[RO_2]}{dt} = -k_{NO+RO_2}[NO][RO_2] + k_{OH+HC}[OH][RH] + k_{Cl+Alkanes}[Cl][Alkanes] + k_{NO_3+RH}[NO_3][RH] - k_{RO_2+HO_2}[RO_2][HO_2] \pm \ldots \quad (146)$$

$$\frac{d[HO_2]}{dt} = -k_{NO+HO_2}[NO][HO_2] + k_{OH+CO}[OH][CO] + k_{CH_3O+O_2}[CH_3O][O_2] \pm \ldots \quad (147)$$

$$\frac{d[OH]}{dt} = k_{NO+HO_2}[NO][HO_2] - k_{OH+RH}[OH][RH] - k_{OH+CO}[OH][CO] + k_{O(^1D)+H_2O}\left[O\left(^1D\right)\right][H_2O] + 2 \cdot j_{H_2O_2}[H_2O_2] \pm \ldots \quad (148)$$

$$[OH] = \frac{k_{NO+HO_2}[NO][HO_2] + k_{O(^1D)+H_2O}\left[O\left(^1D\right)\right][H_2O] + 2 \cdot j_{H_2O_2}[H_2O_2] + \ldots}{k_{OH+RH}[RH] + k_{OH+CO}[CO] + \ldots} \quad (149)$$

$$[RO_2] = \frac{k_{OH+RH}[OH][RH] + k_{Cl+Alkanes}[Cl][Alkanes] + k_{NO_3+RH}[NO_3][RH] + \ldots}{k_{NO+RO_2}[NO] + k_{RO_2+HO_2}[RO_2] + \ldots} \quad (150)$$

These strongly simplified steady state approaches (equations (146)-(148)) illustrate the close interdependence between RO_2, HO_2, and OH caused by their chain reaction involving NO, CO, and HC. The equations (149) and (150) show that the OH and RO_2^* quantities respond non linear to the variation of hydrocarbons. Nevertheless, this interdependence can be clarified by considering only the dominant reactions of (149) and (150) (in black). For example, doubling the hydrocarbon mixing ratio leads to a doubling and a halving of the RO_2^* and OH mixing ratio, respectively.

The mixing ratio of neither of these species does therefore effectively change because OH and hydrocarbons are involved in both equations (149) and (150). The dominance of the NO reactions over the reactions marked in grey leads to the conclusion that in the presence of sufficient high NO mixing ratios, the OH, RO_2, and HO_2 amounts are mainly controlled by NO.

As can be seen in Figure 55, while the RO_2^* diurnal evolution is reasonably well reproduced, the HO_2 mixing ratios are clearly overestimated by the model. Therefore, the ratio between RO_2^* and HO_2 is highly underestimated. The possible variability of this ratio will be investigated in sections 5.2.3.2 - 5.2.3.7.

5.2.3.2 CO variation

Figure 56 shows the base(case) and four additional cases corresponding to 0 ppbv, 4 ppbv, 40 ppbv, and 4 ppmv CO.

a)

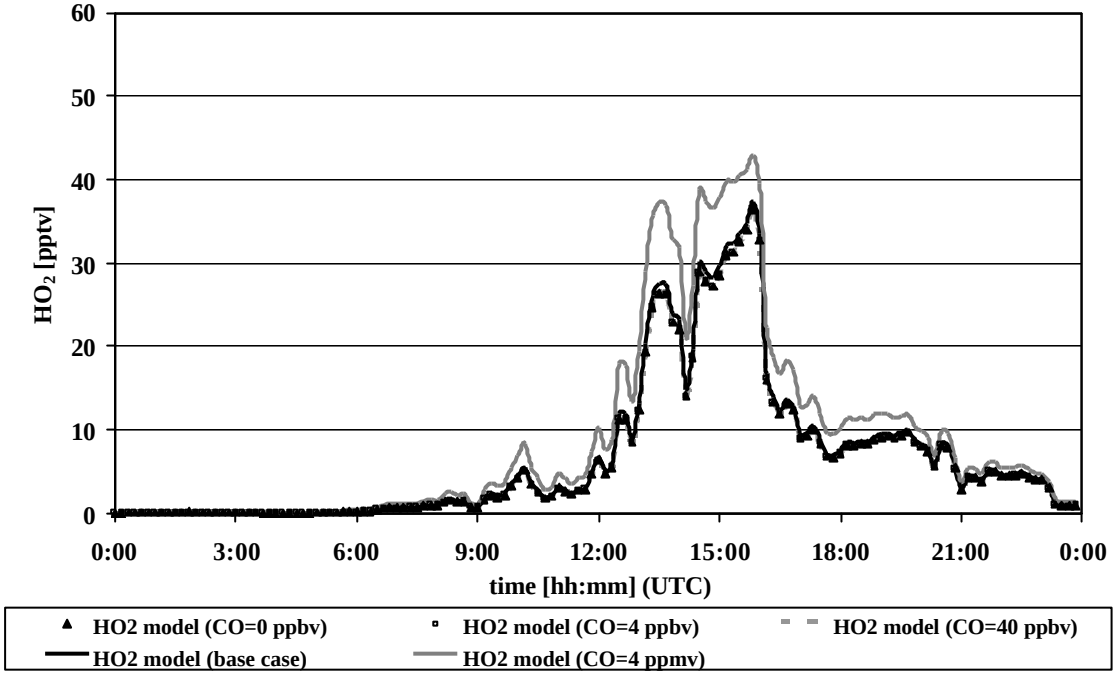

b)

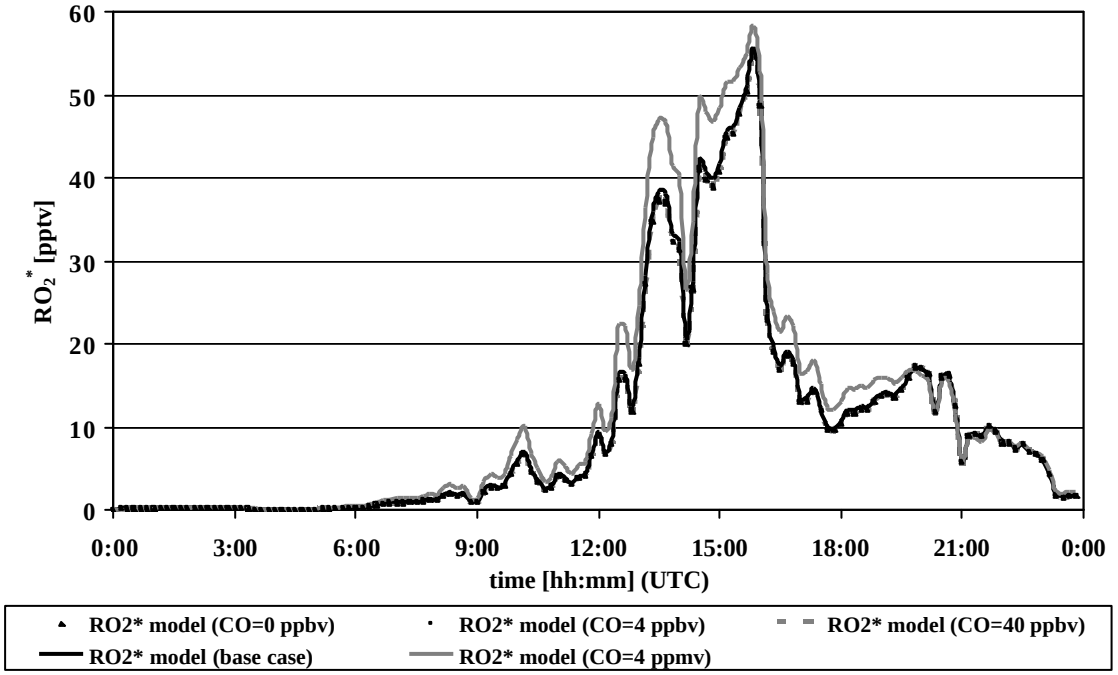

Figure 56: Diurnal variation of modelled HO_2 and RO_2^* mixing ratio for CO 0 ppbv, 4 ppbv, 40 ppbv, base case (400 ppbv), and 4 ppmv.

Even a variation of the CO mixing ratio (Figure 56) up to 4 ppmv leads to an increase in the amount of peroxy radicals of less than 20%. Therefore, the amount of peroxy radicals in the area of observation seems to be determined by the amount of hydrocarbons present. The difference between the corresponding ratios of RO_2^* and HO_2 is small and close to constant as a consequence of the high amounts of NO present. The NO converts very rapidly the RO_2 into HO_2 and a change in the amount of CO has little impact on the amounts of HO_2.

5.2.3.3 CH_4 variation

Figure 57 shows the diurnal variations of HO_2 and RO_2^* for different CH_4 (0 ppbv, 400 ppbv, 4 ppmv, 40 ppmv) mixing ratios. As in the case of the CO variation, the HO_2 concentration remains invariable except for the "unrealistic" 40 ppmv case. The same is true for the RO_2^* mixing ratios.

a)

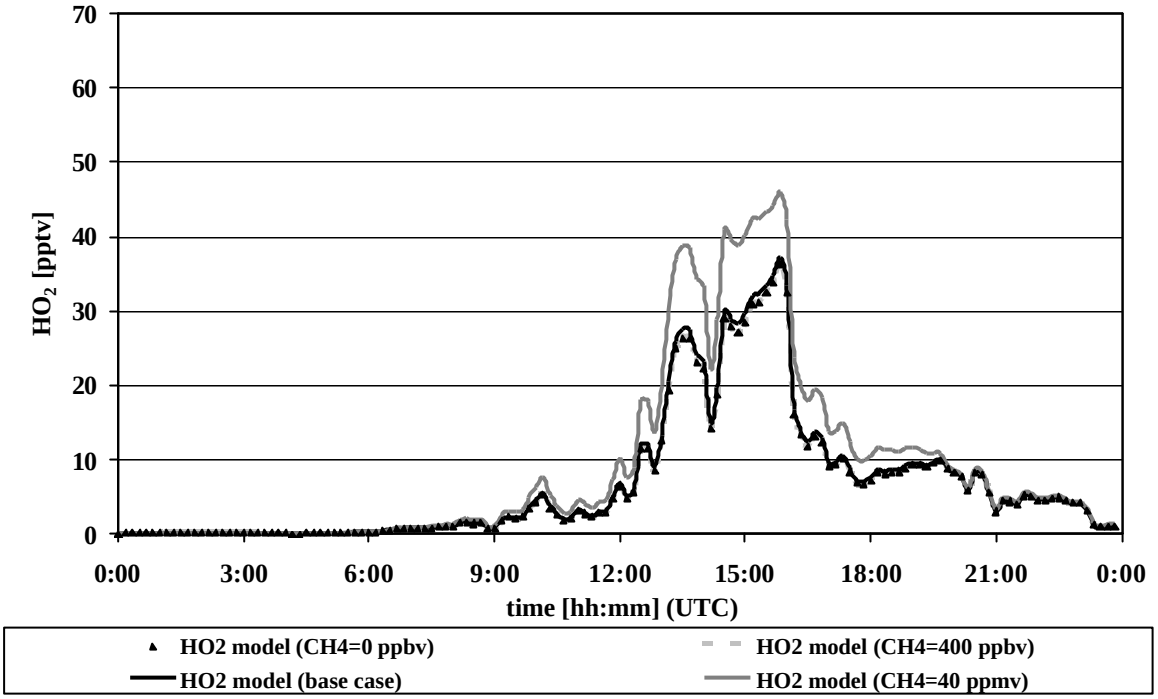

b)

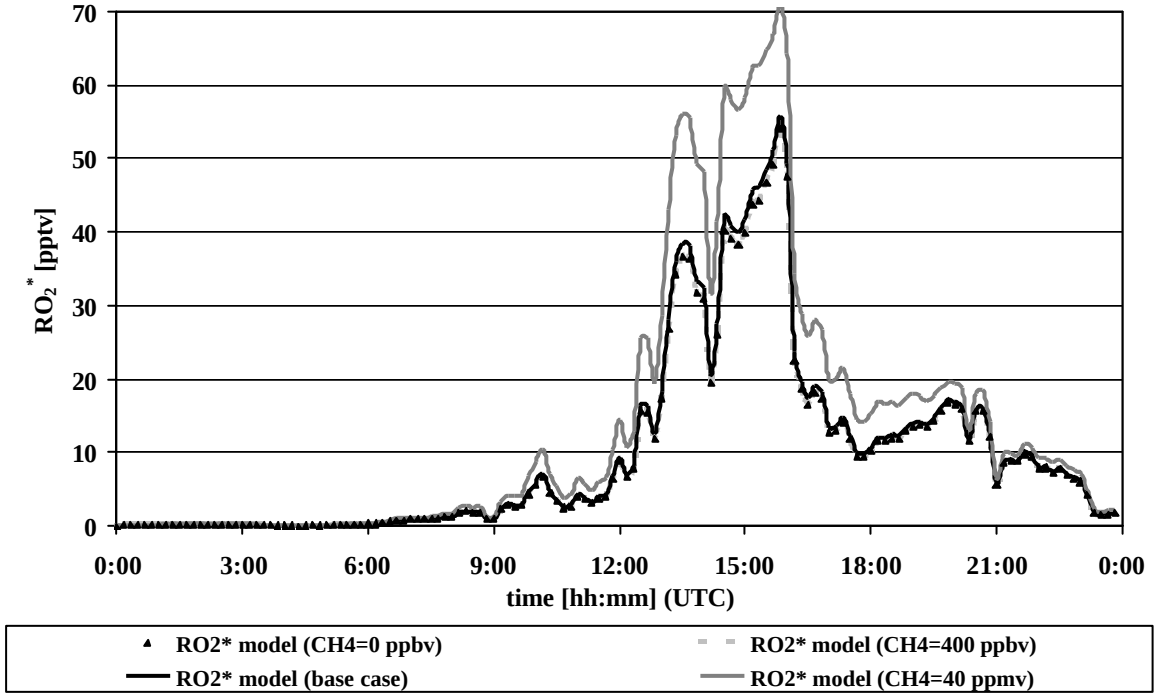

Figure 57: Diurnal variation of modelled HO_2 and RO_2^* mixing ratios for CH_4 0 ppbv, 400 ppbv, base case (4 ppmv), and 40 ppmv.

5.2.3.4 C_2H_4 variation

Figure 58 shows the diurnal variation of HO_2 and RO_2^* for C_2H_4 0 pptv, 400 pptv, 4 ppbv (base case), 40 ppbv, and 400 ppbv. As in the former cases HO_2 does not vary except for the 40 ppbv and 400 ppbv case. The same is observed for the RO_2^* mixing ratios.

The influence of the C_2H_4 concentrations on the amount of peroxy radicals up to 4 ppbv C_2H_4 is negligible. The shape of the diurnal profile of both the HO_2 and RO_2^* mixing ratio seems not to change significantly up to C_2H_4 levels of 40 ppbv. The 400 ppbv C_2H_4 case, however, has a different shape. The shape seems to follow the solar radiance, as expected.

At these high levels of C_2H_4 the early morning production of OH is predominantly defined by the amounts of C_2H_4 present. Therefore, in agreement with the model results, the OH diurnal profile adopts the form shown in Figure 58 for HO_2 and RO_2^*. The influence of NO seems to have become negligible.

Although these high values are unrealistic, they illustrate the behaviour of atmospheric trace gases by turning from a regime dominated by the NO_x present to a regime dominated by the C_2H_4.

a)

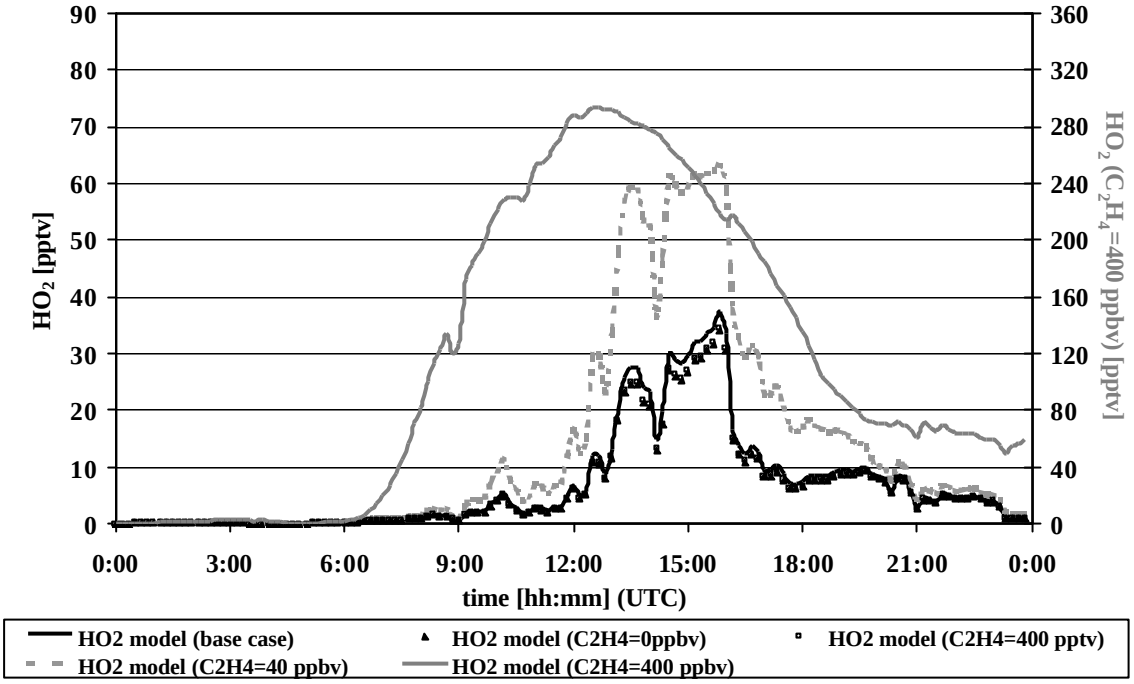

b)

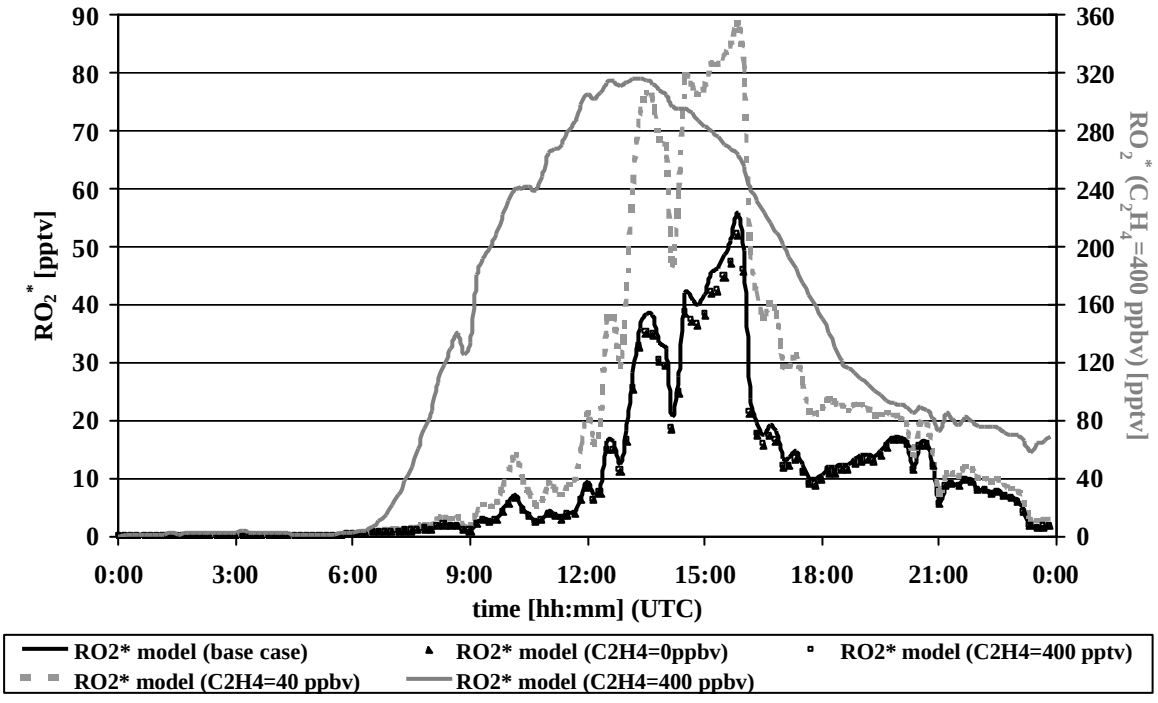

Figure 58: Diurnal variation of modelled HO_2 and RO_2^* mixing ratio for C_2H_4 0 pptv, 400 pptv, 4 ppbv (base case), 40 ppbv, and 400 ppbv.

5.2.3.5 C_2H_6 variation

Figure 59 shows the diurnal variation of HO_2 and RO_2^* for different C_2H_6 (0 ppbv, 8 ppbv, 80 ppbv, 800 ppbv (base case), 8 ppmv, 80 ppmv) mixing ratios. The amounts of HO_2 show no significant increase up to 8 ppmv of C_2H_6.

In Figure 59 b) the RO_2^* mixing ratios seem not to be influenced by the variation of C_2H_6, up to 800 ppbv.

Overall it can be summarised that the impact of C_2H_6 on the amount of peroxy radicals is small and comparable to the influence of CH_4 and CO. In addition, increasing amounts of C_2H_6 change the ratio between RO_2 and HO_2 towards more RO_2.

a)

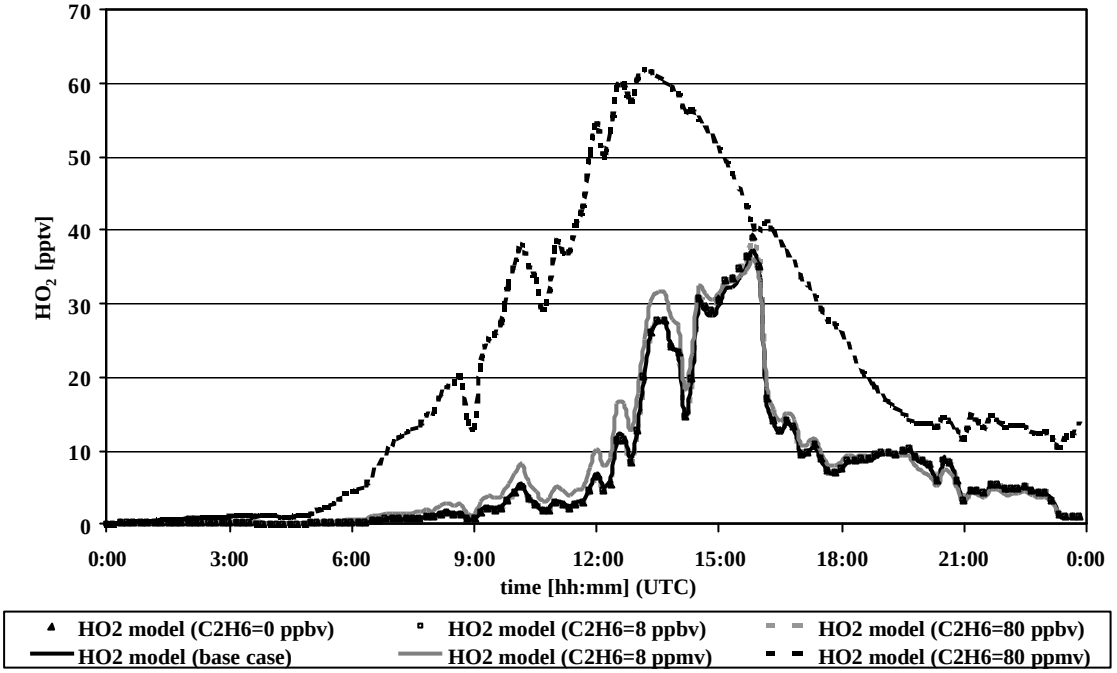

b)

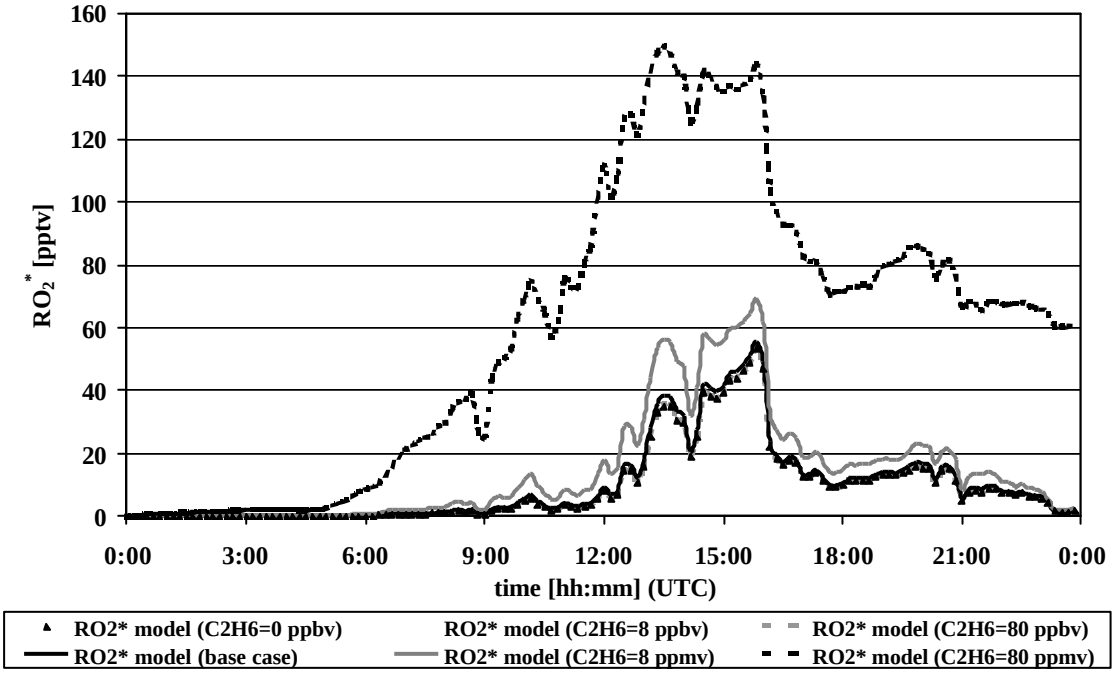

Figure 59: Diurnal variation of modelled HO_2 and RO_2^* mixing ratio for C_2H_6 0 ppbv, 8 ppbv, 80 ppbv, 800 ppbv (base case), 8 ppmv, and 80 ppmv.

5.2.3.6 C_3H_6 variation

Figure 60 shows the diurnal variation of HO_2 and RO_2^* for different C_3H_6 (0 pptv, 85 pptv, 850 pptv, 8500 pptv (base case), and 85 ppbv) mixing ratios. The variation of C_3H_6 mixing ratios have a much higher influence on the amounts of RO_2^* and HO_2 than all previous cases, due to the higher amounts of radicals produced through each step of oxidation. Again a transition is observed in the diurnal shape, starting from a highly structured diurnal profile (the result of the variation of NO) and moving into a more smooth profile correlated with solar radiation.

a)

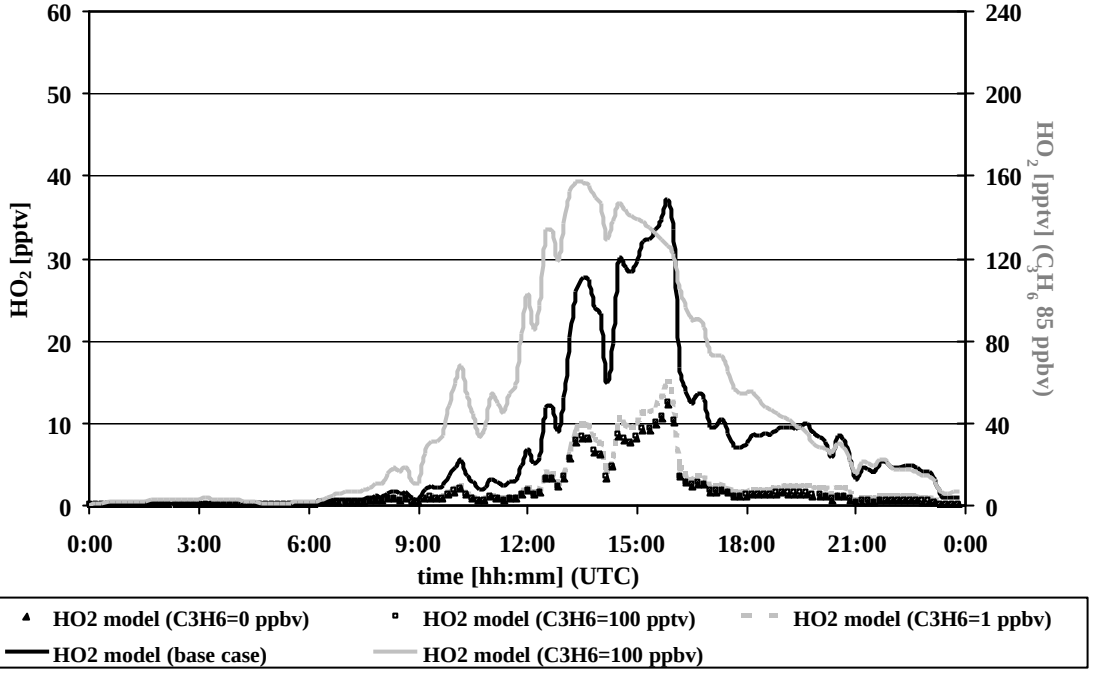

b)

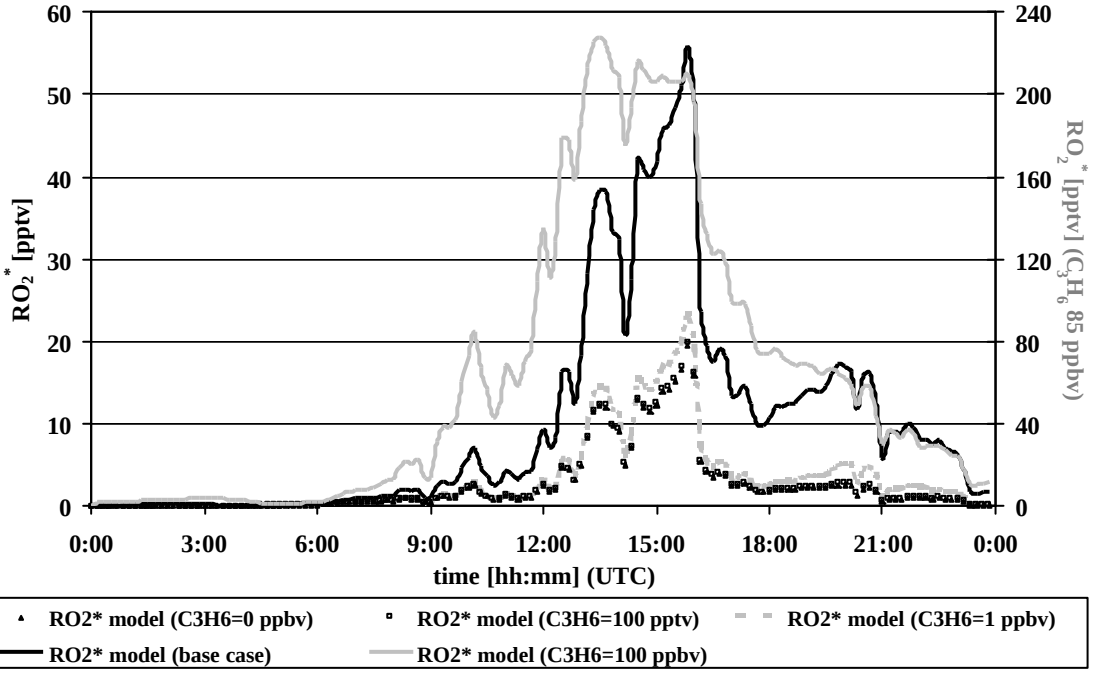

Figure 60: Diurnal variation of modelled HO_2 and RO_2^* mixing ratio for C_3H_6 0 pptv, 15 pptv, 150 pptv, 1500 pptv, 15 ppbv (base case), 150 ppbv, and 1500 ppbv.

5.2.3.7 C_3H_6 variation with 10 times higher reactivity with O_3

Figure 61 shows the diurnal variation of HO_2 and RO_2^* for different amounts of C_3H_6 (0 pptv, 85 pptv, 850 pptv, 8500 pptv (base case), and 85 ppbv). In this case study the reaction of O_3 with C_3H_6 was enhanced by a factor of 10. We also enhanced the reaction rate coefficient to estimate how the behaviour of peroxy radicals change if species like diene (especially: terpene) are present.

To a good approximation the dienes react on average ten times faster than the mono-alkenes. In comparison with Figure 60 the mixing ratio of the peroxy radicals in Figure 61 are slightly higher. Focussing on the maximum daytime mixing ratios the increase between case 5.2.3.6 and 5.2.3.7 is below 20% for C_3H_6 mixing ratios below 850 pptv and increase to differences of more than 50% for maximum RO_2^* for the base case (8500 pptv). Interestingly, the ratio between RO_2^* and HO_2 is not changing within the simulated range of C_3H_6 mixing ratios. Therefore, we conclude that the amount of NO present defines the ratio between HO_2 and RO_2^*.

The enhancement in the O_3 and C_3H_6 reactions leads to a strong increase in the amount of all radicals (i.e. OH + RO_2^*) present, but this increase is not caused by the direct production of peroxy radicals, but it is rather caused by an increase in the total amount of all radicals.

a)

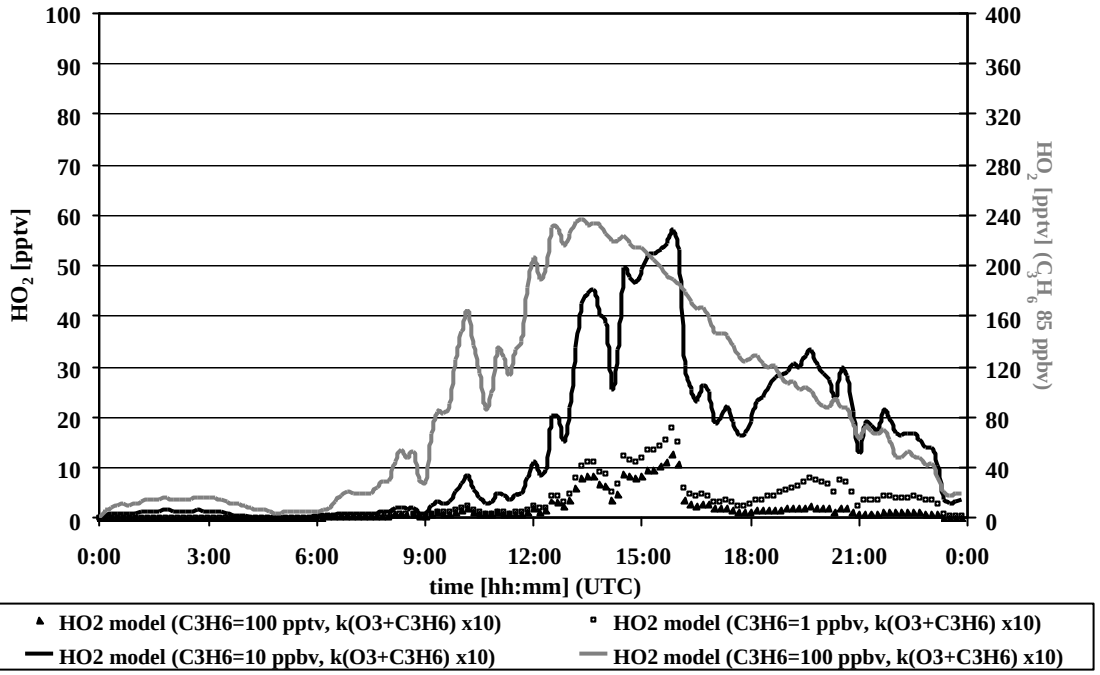

b)

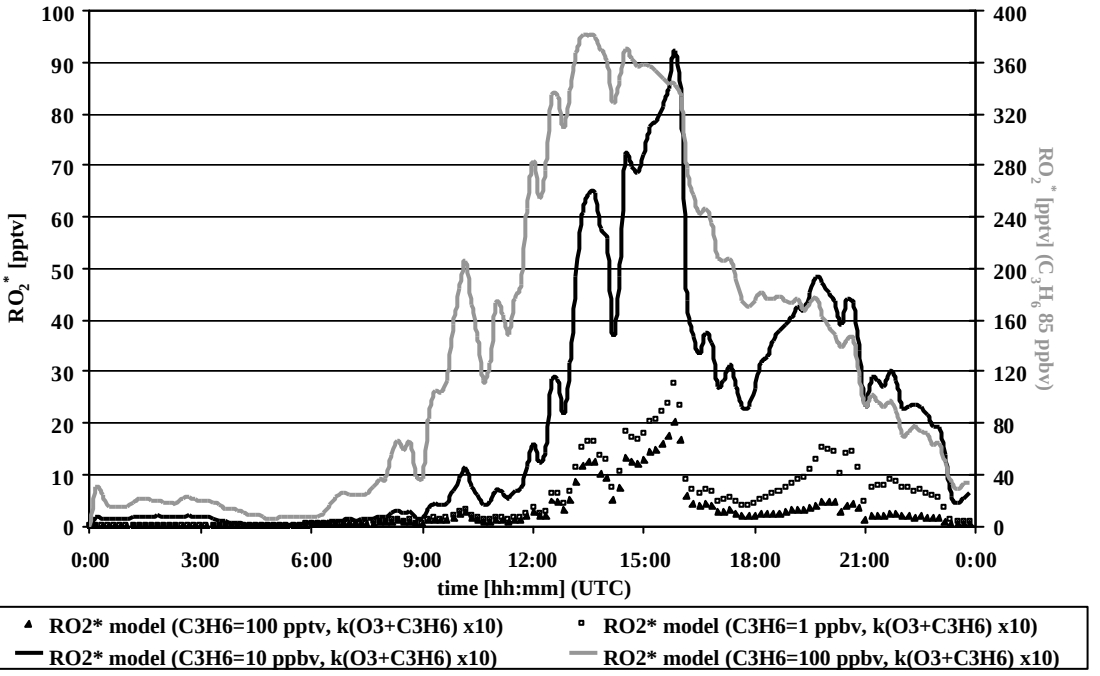

Figure 61: Diurnal variation of modelled HO_2 and RO_2^* mixing ratio for C_3H_6 0 pptv, 15 pptv, 150 pptv, 1500 pptv, 15 ppbv (base case), 150 ppbv, and 1500 ppbv (the O_3 with C_3H_6 reaction rate coefficient is enhanced by a factor of 10).

5.2.3.8 RO_2^* to HO_2 ratio

Sections 5.2.3.1 to 5.2.3.7 have shown that the maximum RO_2^* and HO_2 mixing ratios vary only slightly. Therefore, the ratio between max RO_2^* and max HO_2 under heavily polluted conditions is expected to be constant. The steady ratio seems to be caused by the fast reactions with NO dominating the loss and/or interconversion of peroxy radicals leading to lifetimes of a few seconds (see section 5.2.3.1).

Consequently, the ratio between max RO_2^* and max HO_2 is insensitive to the amount of precursors present. The ratio of the maximum daytime RO_2^* and HO_2 mixing ratios varies in all studied cases between 1.1 and 2.3. Neglecting the cases in which the base case concentrations have been enhanced or reduced by two orders of magnitude or more the resultant ratios vary only between 1.4 and 1.7.

5.2.4 Comparison between model and measurements

This chapter will focus on the comparison between the modelled and measured RO_2^* to HO_2 ratio and the amounts of H_2O_2 and OH.

5.2.4.1 RO_2^* to HO_2 ratio

The measured ratio between maximum RO_2^* and HO_2 is significantly higher than that expected based on the results of the sensitivity study presented in chapter 5.2.3 (Table 7). In general the ratio was between 7 and 10, the deviating values corresponding to cloudy days, when the radiation reaching the ground was substantially reduced.

Date	avg. OH [pptv]	max. OH [pptv]	avg. HO_2 [pptv]	max. HO_2 [pptv]	avg. RO_2^* [pptv]	max. RO_2^* [pptv]	max. RO_2^* / max. HO_2
23. Jul	0.069	0.155	3.6	9.3	12	38	4
24. Jul	0.091	0.199	5.5	10.0	26	69	7
25. Jul	0.072	0.187	2.2	4.7	17	54	12
26. Jul	0.095	0.214			5	19	
27. Jul	0.063	0.157	2.8	8.9	4	15	2
28. Jul	0.205	0.396	1.9	3.2	6	26	8
29. Jul	0.066	0.136	2.3	5.0	12	38	8
30. Jul	0.066	0.196	3.2	8.1	18	71	9
31. Jul	0.112	0.214	3.4	7.0	21	62	9
1. Aug	0.108	0.190	3.5	6.8	24	65	10
2. Aug	0.079	0.138	4.1	6.7	32	58	9
3. Aug					6	36	
4. Aug	0.051	0.177	0.9	1.8	5	19	10
5. Aug	0.159	0.348	1.0	3.6	6	25	7
6. Aug	0.061	0.126	1.3	2.0	7	38	19
7. Aug					5	28	
8. Aug					4	31	
9. Aug					3	32	
10. Aug					1	21	
11. Aug	0.045	0.128			2	17	

Table 7: Measured daily average and maximum mixing ratios for OH, HO_2, and RO_2^* during the PRIME campaign 1999.

Comparing the measured RO_2^* to HO_2 ratios (7-10) with the modelled ratios (1.3-2) it becomes obvious that there is a large gap between the actual observations and theory. As will be discussed later the RO_2^* levels measured within PRIME are in agreement with other studies in similar areas, when the measurements are corrected for the water interference of the PERCA [Burkert et al., 2001b, Reichert et al., 2003].

5.2.4.2 H_2O_2 mixing ratio

It is important to note that at these observed low levels of HO_2 the modelled H_2O_2 clearly underestimates the measurements. As H_2O_2 is expected to be formed exclusively from the HO_2 self reaction this underestimation indicates an inconsistency in the chemistry or in the measurements considered, and/or discrepancies among the species involved in the interconversion of OH and peroxy radicals.

One possible explanation is that H_2O_2 is not exclusively produced via the HO_2 self reaction. Several studies in the literature [Horie et al., 1994, Gäb et al., 1995, Neeb et al., 1997, Wolff et al., 1997, Sauer et al., 1999] discuss the possibility of the production of H_2O_2 through the ozonolysis of alkenes and the subsequent reaction.

$$CH_2 = CHR + O_3 \rightarrow primary - ozonide \quad (117)$$

$$primary - ozonide \rightarrow CH_2OO^* + RCHO \quad (118)$$

$$CH_2OO^* + M \rightarrow CH_2OO + M \quad (119)$$

$$CH_2OO + H_2O \rightarrow CH_2O + H_2O_2 \quad (120)$$

R represents the organic group and corresponds to H in the case of ethene. These reactions (117) to (120) are not the dominant pathways, however, they can contribute significantly to the total amount of H_2O_2.

Figure 62 shows the contribution of reaction (120) to the total amount of H_2O_2 present, simulated for the base case. This simulation used a rate constant of $k=6x10^{-18}$ (molec cm^{-3}) as assumed in the MCM2 model [http://chmlin9.leeds.ac.uk /MCMframe.html].

Recent literature contains controversial discussion, about whether the production of H_2O_2 via this reaction path takes place at all [Geert Moortgat, personal communication, 2002]. Neeb et al. [1997] observed no significant production of H_2O_2 and found that formation of HCHO was linearly coupled to the consumption of alkenes, indicating that HCHO is formed only as a primary product from the primary ozonide [Hatakeyama and Akimoto, 1994] (see section 2.2.2.4).

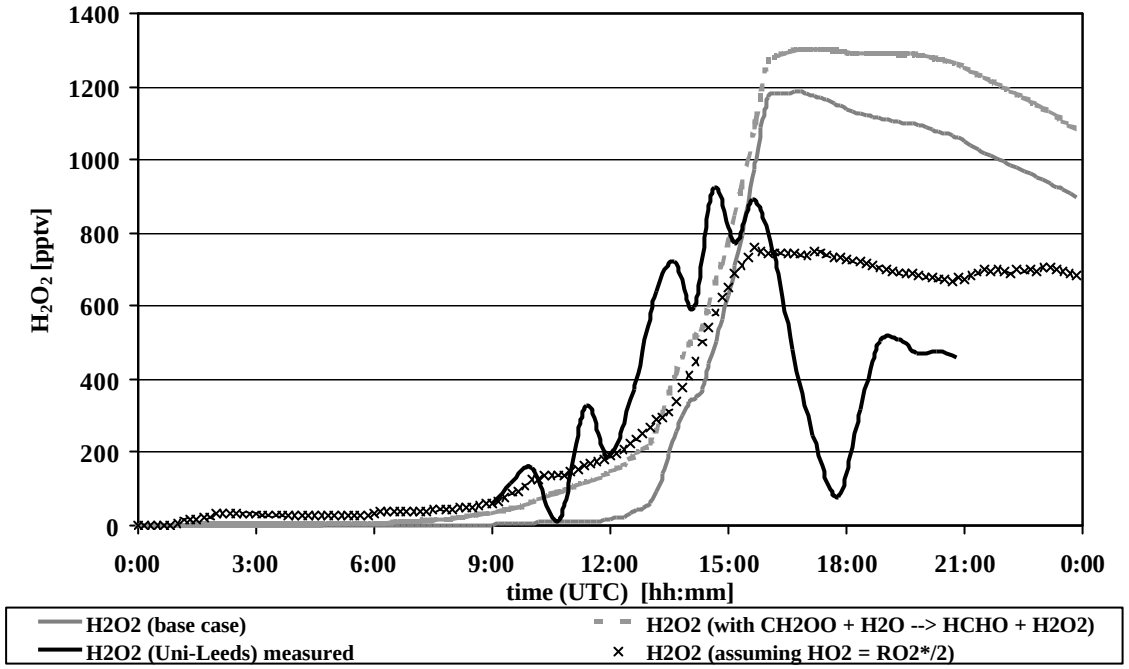

Figure 62: Diurnal variation of H_2O_2 mixing ratios of the base case, the observations, and the base case with additional production of H_2O_2 via reaction (120).

Interesting to note is the earlier production of H_2O_2 in Figure 62 for the case of "additional production via reaction (120)".

However, as the model cannot describe the early morning radical behaviour, the beginning of the modelled H_2O_2 production is delayed. If the amount of radicals in the early morning were adequately simulated another production process for H_2O_2 besides the HO_2 self reaction would not be necessary. Figure 62 shows the corresponding H_2O_2 amount modelled assuming that half of the RO_2^* measured is HO_2.

In

Figure 63 the H_2O_2 mixing ratios which correspond with the maximum amounts of HO_2 are shown to reveal the inconsistency between the measured HO_2 (up to 10 pptv) and the measured H_2O_2 (up to 1000 pptv). A simulated HO_2 diurnal profile reaching a maximum of 10 pptv corresponds with a H_2O_2 diurnal maximum of no more than 50 pptv.

In addition, as can be seen in Figure 55, the base case simulation can reproduce the measured RO_2^* mixing ratios. The corresponding maximum daytime mixing ratios of HO_2 and H_2O_2 are approximately 38 pptv and 1200 pptv, respectively, therefore the amount of H_2O_2 in the base case is in the range of the observations.

Finally, it can be concluded that either a reaction which produces high amounts of H_2O_2 is missing or there is an artefact in the measurements of either HO_2 or H_2O_2.

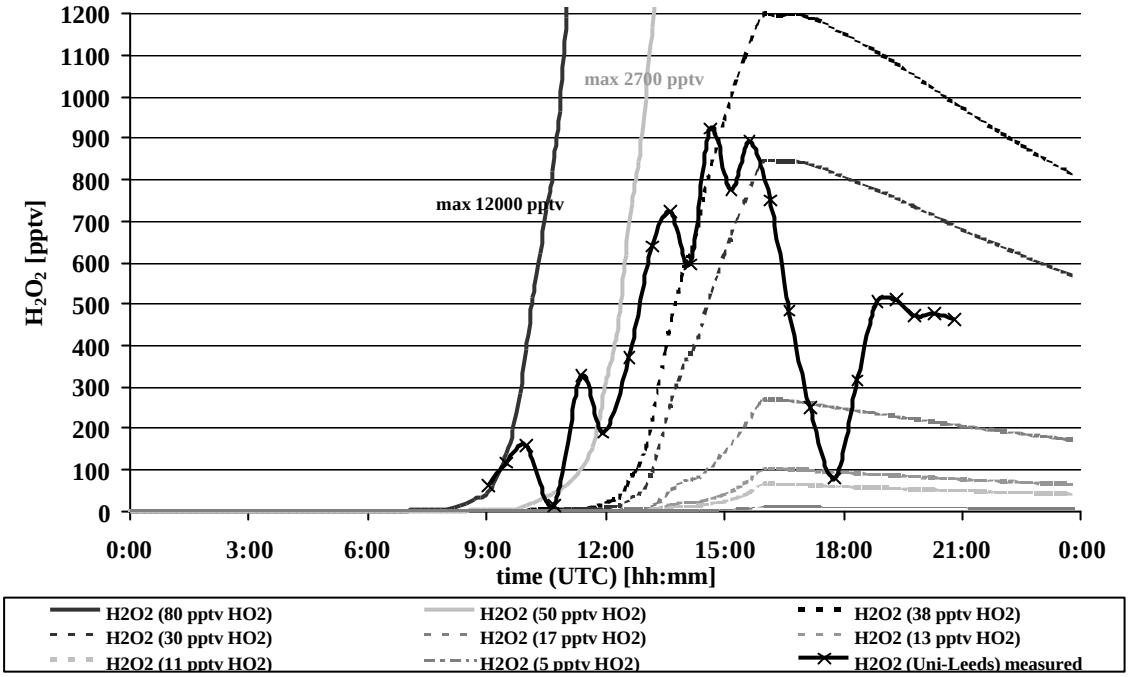

Figure 63: Diurnal profiles of measured and simulated amounts of H_2O_2 for different HO_2 mixing ratios.

5.2.4.3 OH mixing ratio

The increase in the total amount of available radicals and therefore in the amount of available OH radicals leads to the highest amounts of peroxy radicals, as can be seen in the diurnal profile of the radicals.

Figure 64 shows that the model can reproduce the measured OH mixing ratios. However, the OH diurnal profile shows a late afternoon peak which cannot be described by the model. Even the assumption that all present C_3H_6 are reacting 10 times faster with O_3 than described in the literature (i.e. we assume that all alkenes are dienes (especially terpenes)) does not lead to such a high OH peak in the late afternoon. Suggesting a mechanism responsible for this behaviour in OH, which is not included in our model.

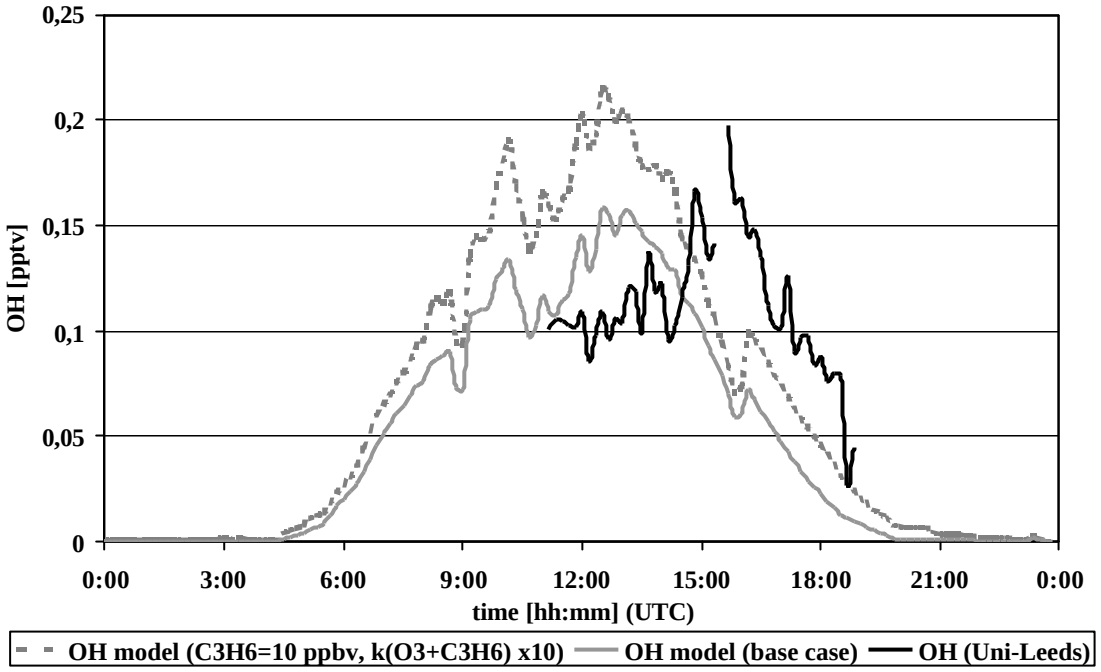

Figure 64: Diurnal variation of measured and simulated (base case (C_3H_6 = 8500 pptv) and base case with a 10 times faster O_3 reaction rate) OH mixing ratios.

5.2.5 Comparison with other datasets

To get a deeper insight on the problem of the ratio of RO_2^* and HO_2 the same simulation as described above was repeated for air masses measured over the remote Atlantic Ocean with NO_x mixing ratios <20 pptv [Burkert et al., 2001b]. The simulated mixing ratios of HO_2 and RO_2^* agree well with the measurements [Andreas Hofzumahaus et al., personal communication, 2002]. The measured H_2O_2 concentrations were also well simulated (Figure 65). The ratio between RO_2^* and HO_2 varied around two, whereas, during the PRIME campaign the ratio reached levels up to 10. Even high amounts of NMHC (sections 5.2.3.2 - 5.2.3.7) cannot lead to such high ratios in the model.

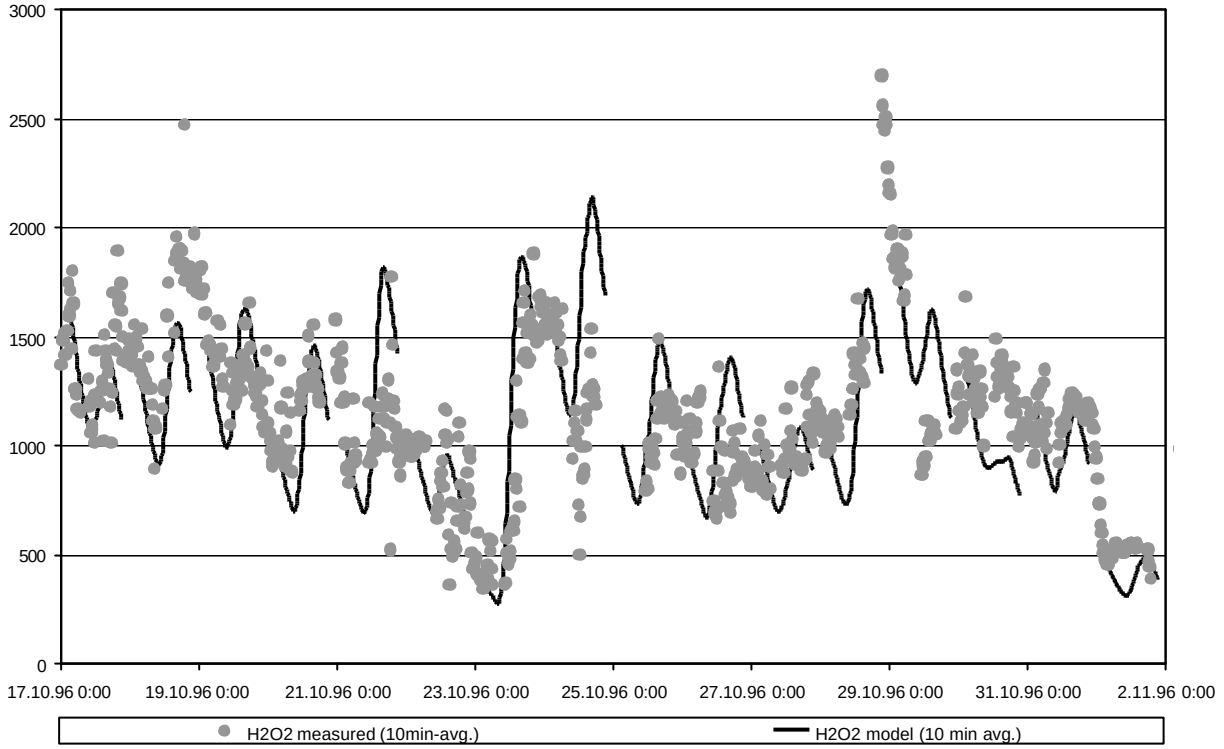

Figure 65: Comparison between measured and simulated H_2O_2 mixing ratios for the ALBATROSS campaign [Burkert et al., 2001b]. H_2O_2 data were measured by Weller et al. [2000].

Overview of available HO_2 datasets:

- BERLIOZ: HO_2 measurements with the laser induced fluorescence (LIF) technique performed by the Forschungszentrum Jülich [Hofzumahaus et al., 1998] up to 20 pptv on July 20th 1998 in Berlin [Platt et al., 2002]. RO_2^* measurements using the PERCA technique reached levels up to 53 pptv Mihelcic et al. [2003]. The MIESR measurements of HO_2 and RO_2^* of Mihelcic et al. [2003] are in agreement with the LIF and PERCA observations.

- ORION99: HO_2 measurements (LIF) by Kanaya et al., [2000, 2001] show mixing ratios between 10 and 25 pptv. The measurements were made at a remote island of Okinawa. Different air masses were encountered, clean marine (O_3 10 ppbv, CO 90 ppbv), polluted from Japan (O_3 35 ppbv, CO 100 ppbv), south-eastern

clean (O_3 20 ppbv, CO 100 ppbv), polluted from China east coast (O_3 30 ppbv, CO 150 ppbv), south-western (O_3 20 ppbv, 110 ppbv).

- PROPHET98: The HO_2 measurements by Tan et al., [2001] used the LIF technique reached levels up to 25 pptv. The site in the northernmost part of Michigan, was located in a hardwood forest.

- Tropospheric OH Photochemistry Experiment: HO_2 mixing ratios were measured by LIF [Stevens et al., 1997, Mather, 1997, Mount et al., 1997] up to 3 pptv, the RO_2^* (PERCA) measurements of Cantrell et al. [1997], which do not consider any water interference [Burkert et al., 2001b, Reichert et al., 2003], reached levels up to 40 pptv. The Idaho Hill site was located in remote mountains near Caribou, Colorado, elevation 3091 m. The measurements were taken during August and September of 1993.

- Los Angeles free radical experiment (LAFRE): The experiment was situated in Claremont, California, 55 km downwind from downtown Los Angeles during September 1993 [George et al., 1999]. The HO_2 mixing ratios reached up to 10 pptv (FAGE).

- EASE96, EASE97: Measurement site, Mace Head, a remote island at the west coast of Ireland. The HO_2 mixing ratios performed by Creasey et al. [1997, 2002, Carslaw et al., 1999, 2001] using the FAGE technique, reached levels up to 10 pptv. The PERCA measurements [Carslaw et al., 1999, 2001, and 2003] of RO_2^* observed mixing ratios up to 12 pptv which are not corrected for the water interference and 38 pptv for the corrected mixing ratios in 1997.

- ALBATROSS: Measurements of HO_2 (LIF) and RO_2^* (PERCA) mixing ratios reached levels up to 25 pptv and 80 pptv respectively [Andreas Hofzumahaus, personal communication, 1997, Burkert et al., 2001b]. The ALBATROSS campaign took place over the Atlantic Ocean (50°N to 40° S) in November 1996 on board the German research vessel Polarstern.

	PRIME	BERLIOZ	LAFRE	ORION99	PROPHET98	Trop. OH Photochem. Exp.	EASE97, EASE98	ALBATROSS
Pollution level	urban	urban	urban	Urban/rural	Rural (forested)	Rural (elev.3091 m)	remote	remote
Measurement technique	FAGE, PERCA	LIF, MIESR, PERCA	FAGE	LIF	LIF	LIF, PERCA	FAGE, PERCA	LIF, PERCA
max HO_2 [pptv]	10	20	10	10 - 25	25	3	10	25
max RO_2^* [pptv]	70	53				40	38	80

Table 8: Overview of different campaigns where HO_2 and/or RO_2^* mixing ratios have been determined.

The measurements of HO_2 and RO_2^* performed in the studies listed (Table 8) show large variabilities. Even under comparable meteorological and pollution levels the variability remains.

There are several campaigns described in the literature which also mention an overestimation of both measured RO_2^* and HO_2 concentrations by models. These measurements of RO_2^* were partly not corrected for the water interference or using an old unreliable system for the measurement of HO_2 with an interference of water cluster [Mount and Williams, 1997, Tanner et al., 1997, Hard et al., 1992, Stevens et al., 1994, McKeen et al., 1997, Cantrell et al., 1997].

During the PROPHET summer 1998 campaign Tan et al. [2001] observed OH, which was a factor of 2.7 underestimated by the model on average. The measured HO_2 concentration, however, was in good agreement with the simulations.

During the BERLIOZ campaign which took place near Berlin, Germany, in an area comparable to the region investigated during PRIME, the measured HO_2 mixing ratios were on average about a factor of two to four higher than the HO_2 mixing ratios observed during PRIME. The observed ratio between RO_2^* and HO_2 varied between 2 and 2.5 around noon. The maximum mixing ratios of RO_2^* reached up to 53 pptv at noon.

The discrepancy in the results of both campaigns is large, but to explain this by an artefact in either of the measurement techniques for HO_2 is inappropriate. There are still many unknowns in the composition of both encountered air masses.

5.2.6 Interpretation

The large discrepancies between the model results and the measurements of HO_2 and RO_2^* might be explained as follows:

- There is a process which leads to a reduction of HO_2 and a large increase of RO_2. This process could be the reaction of CO with HO_2 in the presence of H_2O. The reaction rate coefficient of CO and HO_2 is expected to be higher in the presence of H_2O [Reichert et al., 2003]. The disagreement between the measured HO_2 and H_2O_2 mixing ratios, however, can be explained if one of the pathways of this reaction leads to H_2O_2 (see reaction (151)).

$$\begin{aligned} CO + HO_2 + H_2O &\rightarrow CO_2 + OH + H_2O \\ &\rightarrow CO_2 + H + H_2O_2 \end{aligned} \qquad (151)$$

Some studies in the past have indicated that this reaction may occur but only a very low upper limit for this reaction rate coefficient was obtained [NIST Standard Reference Database 17 and references therein, 1998]. However, an extended investigation concerning the influence of water on the reaction rate coefficient has not yet been done.

A reaction of the type just described would change the ratio between HO_2 and OH and would consequently lead to an enhanced oxidation of hydrocarbons due to enhanced amounts of OH, and therefore would increase the rate of production of RO_2.

However, the CO and H_2O mixing ratios measured during the BERLIOZ campaign were similar to the PRIME conditions. In addition, the fast interconversion of the RO_2 radicals into HO_2 via their reaction with NO is still dominant.

- There is another oxidising agent present like OH, for example Cl, which could lead to additional amounts of RO_2 and therefore to a higher ratio of RO_2^* to HO_2. In contrast to OH, Cl does not react with CO and therefore increases the ratio between RO_2 and HO_2. The required levels of Cl to oxidise the same amounts of alkanes can be two orders of magnitude lower than OH due to the higher reactivity especially with alkanes.

It is very interesting to note that measurements of the isotopic fractionation of CH_4 above the Pacific Ocean have recently provided evidence for the enrichment of the CH_4 fractions, which cannot be explained by OH chemistry alone, therefore Allan et al. [2001] concluded an additional oxidant is required. The expected source could either be the ocean or halogenated organics. If the ocean is the dominant source, the differences in the measured mixing ratios of HO_2 between PRIME and BERLIOZ might be explained.

As in the previous point the importance of this reaction in polluted regions should be almost negligible, unless unexpectedly high amounts of Cl are present.

- The reaction rate frequencies of NO with RO_2 are substantially lower for larger RO_2 than reported, i.e. the RO_2 radicals produced by the oxidation of larger alkanes, alkenes, and alkynes react slower with NO than HO_2 or CH_3O_2. This would imply a longer lifetime of RO_2. In the model used here this effect has not been taken into account due to the assumption of a propene and ethene equivalent. There has been a disagreement about the corresponding reaction rate coefficients [Eberhard and Howard, 1997, Jenkin and Hayman, 1995, Peeters et al., 1992]. However, the expected variability is too small to have an important impact on the ratio of RO_2^* to HO_2.

- The FAGE system has an artefact which leads to an underestimation of the HO_2 concentration by a factor of two to four. Taking this into account, the measurements of RO_2^* and HO_2 are in good agreement, particularly concerning the ratio. An artefact in a measurement technique is always possible, however there is no indication for this assumption.

Overall, there is still a large disagreement between the total amounts of RO_2^* measured and simulated in the early morning hours, which cannot be solved with the current understanding of the atmospheric chemistry. The major problem is associated with the high amounts of NO present during this period of the day, together with non-negligible amounts of RO_2^* radicals. Possible explanations are:

- There are high amounts of hydrocarbons present, which are produced locally and trapped in the nocturnal boundary layer. The hydrocarbons do not belong to the measured species, because the observations do not reveal any big increases in the early morning hours. These hydrocarbons have to be strongly diluted after the break up of the nocturnal boundary layer, otherwise this species would increase the RO_2^* mixing ratio during the day. Such a species seems to be unlikely, but it cannot be ruled out. It has to be mentioned that enhanced amounts of 1,3 butadiene have been observed during PRIME which seems to be locally produced. However the time resolution of the hydrocarbon measurements is inappropriate to analyse the diurnal behaviour.

- There is a reservoir species which builds up during the night and can easily be photolysed during the day, producing radicals. This would lead to an enhanced production of peroxy radicals in the early morning. During the day this species had no impact due to its low concentration. But during the evening the production of this species would lead to a higher loss of radicals. However, it is too speculative to name a species or describe reaction mechanisms.

In summary, there is still not a definite explanation for the observed behaviour, but the extention of the assumptions in either of the above mentioned directions is inappropriate without first having access to a more detailed set of trace gas species and some sort of characterisation of emissions from local sources.

5.3 Conclusions

During the PRIME campaign an extensive set of ambient trace gas mixing ratios (RO_2^*, OH, HO_2, H_2O_2, CH_3OOH, CO, PAN, NO, NO_2) was successfully measured. The daytime HO_2 and RO_2^* measured maximum mixing ratios show levels up to 10 and 70 pptv, respectively. Maximum values were generally observed after solar noon, with HO_2 and RO_2^* often persisting in significant amounts overnight.

Supporting carbonyl and hydrocarbon data are suggestive of HO_2/RO_2 production via carbonyl photolysis and/or O_3-alkene chemistry, in addition to VOC and CO oxidation initiated by OH.

The comparison between simulations and observations showed, in particular in the early morning hours, large discrepancies in the amounts of HO_2 and RO_2^*. The model is not able to reproduce the peroxy radicals observed in the presence of the measured high amounts of NO_x (up to 80 ppbv) during this period of the day. Also there is no clear explanation for this phenomena, because all peroxy radicals measured by the PERCA or FAGE system are reacting with NO prior to their detection as NO_2 or OH, respectively, having a lifetime of seconds.

On the other hand, if there were an additional production term not yet considered in the model, the production would have to take place exclusively in the early morning hours, otherwise the additional production term would lead to much higher peroxy radical mixing ratios later during the day. Therefore, a reservoir substance present in high amounts, is required which photolyses easily leading to additional production during the morning but then disappears later during the day. This explanation seems to be unlikely.

According to box model simulations and sensitivity studies of the radical diurnal evolution, the RO_2^*/HO_2 ratios during pollution episodes vary between 1.1 and 2.3. Excluding the cases with enhanced or reduced initial NMHC concentrations of two or more orders of magnitude, the ratio varies only between 1.4 and 1.7, depending on the NMHC content of the air mass. In contrast, the measured ratios for RO_2^* and HO_2, were typically in the range of 7 to 10.

The large discrepancy between measured and simulated ratios cannot be explained by the known chemistry or the presence of higher amounts of larger NMHC, according to the sensitivity study. Even 100 ppbv of a propene equivalent with a 10

times higher reaction rate with O_3 leads to a ratio between RO_2^* and HO_2 of 1.5. Therefore the presence of an additional oxidising agent to the known OH, O_3, and NO_3 cannot be excluded.

A possible species is Cl which reacts only with VOC predominantly producing RO_2 radicals. According to the sensitivity study even a reaction pathway which predominantly produces RO_2 radicals cannot result in a significant change in the ratio of RO_2^* to HO_2, due to the presence of high amounts of NO. These high amounts of NO lead to a non linear response of the ratio of RO_2^* to HO_2 to the ratio of VOC to CO.

Large discrepancies have also been observed between the closely linked amounts of H_2O_2 and HO_2. Assuming that H_2O_2 is exclusively formed by the HO_2 self reaction the measured HO_2 cannot explain the measured amounts of H_2O_2. Even assuming an additional production of H_2O_2 via the ozonolysis of VOC and the subsequent reaction of the Criegee intermediates with water vapour cannot explain this discrepancy.

A comparison of radical measurements during the BERLIOZ and PRIME campaigns shows large differences in the measured amounts of HO_2 in these similarly polluted regions being the HO_2 measured by Andreas Hofzumahaus [personal communication, 2002] a factor between 2 and 3 higher than by Dwayne Heard [personal communication, 2002].

The maximum concentrations of RO_2^* in different regions and levels of pollution seem not to be strongly dependent on the origin of the air mass. However, this cannot be generalized, because observations in forested regions in Portugal showed RO_2^* mixing ratios up to 260 pptv [Burkert et al., 2001a].

6 Epitome

6.1 Summary

6.1.1 Trace gas and radical behaviour [Burkert et al., 2003a]

Selected trace gas mixing ratios (i.e. peroxy radicals ($RO_2^* = HO_2 + \Sigma RO_2$), non methane hydro carbons (NMHC), O_3, CO, HCHO, and NO) and photolysis rate coefficients of $j(NO_2)$ and $j(O(^1D))$ were measured in the marine boundary layer (MBL) over the Indian Ocean. The measurements were performed during February, March, and April 1999 as a part of the Indian Ocean Experiment (INDOEX) on board the research vessel Ronald H. Brown. During the campaign air parcels having different origins and consequently variable compositions were encountered, but all air masses, including those heavily polluted with NMHC's and aerosols, were in the regime of rapid photochemical ozone destruction. The influence of aerosols on the photolysis frequencies was investigated by comparison of measurements and results from the radiative transfer model PHOTOST; the high optical depth (up to 0.6) and low single scattering albedo of the aerosol reduces the UV flux at the surface substantially downwind of India and Arabia, causing for instance a reduction in $j(O(^1D))$ by up to 40%. The diurnal behaviour of the trace gases and parameters in the MBL has been investigated by using a time dependant 0-D chemical model. Significant differences between the diurnal behaviour of RO_2^* derived from the model and observed in measurements were identified. The measured HCHO concentrations differed from the model results and are best explained by some missing chemistry involving low amounts of Cl. Other possible processes, describing these two effects are presented and discussed.

6.1.2 Photochemistry and radiative effects of aerosols [Burkert et al., 2003b]

During the intensive field phase of the Indian Ocean Experiment (INDOEX) measurements of a large set of trace gases were performed on board the RV Ronald H.

Brown. The campaign took place in February-April 1999 over the Indian Ocean. Measurements of all relevant trace gases have been used within a 0-D model to simulate and analyse the observed O_3 diurnal behaviour. For most of the days, the daytime losses are very well reproduced by the model. Additionally, the possible influence of halogens on the O_3 losses is discussed.

The amount of O_3 transported to the area of observation has been analysed in more detail. Particularly, the possibility of diurnal variability in the entrainment strength of trace gases from the free troposphere into the MBL has been investigated. Also in this context, the influence of aerosols on the stability of the lower troposphere is discussed and evaluated by results from the radiative transfer model (RTM) SCIATRAN.

The results of the RTM calculations of the warming rates caused by the aerosols' absorption of solar radiation during the INDOEX campaign showed temperature increases up to 1 K. The temperature increase particularly above the MBL stabilises the atmosphere significantly. Therefore, the presence of aerosols in the layer above the MBL leads to enhanced stability during the day and less stability during the night.

The role of macro and mesoscale processes in the photochemistry of the MBL was also investigated using O_3 soundings, tropospheric columns of O_3, NO_2, and HCHO from satellite based measurements and back trajectory analysis. During the Indian Ocean field work air masses of very different origin, and pollutant content, were encountered, for example, air masses of Southern Hemispheric pristine origin through to air masses of continental Northern Hemispheric (extra tropical) origin.

Vertical profiles of O_3 soundings show the different situations in the Northern and Southern Hemispheres. By combination of vertical profiles, satellite pictures of tropospheric columns of O_3, NO_2, HCHO, and meterological data, it was possible to analyse the strength of strato-tropospheric exchange within the Headly cell and the anthropogenic influences in the mid troposphere of the Northern Hemisphere (NH).

6.1.3 Peroxy radicals and peroxides in the urban troposphere [Burkert et al., 2003c]

Ambient measurements of trace gases were carried out during the Peroxy Radical Initiative for Measurements in the Environment (PRIME) campaign. The data include measurements of following trace gases: hydrogen peroxy radicals (HO_2), peroxy

radicals (RO_2^*=HO_2+RO_2), hydroxyl radicals (OH), hydrogen peroxide (H_2O_2), methyl peroxide (CH_3OOH), carbon monoxide (CO), peroxy acetyl nitrate (PAN), nitrogen oxide (NO), and nitrogen dioxide (NO_2). The measurement site was located near to London, UK, the air coming from the city centre. The campaign took place in July-August 1999.

During daylight, the maximum RO_2^* mixing ratios varied between 15 and 70 pptv during "polluted episodes". At night non negligible amounts of RO_2^* were observed, varying between 5 to 20 pptv. Daytime measurements were compared with results from a box model simulation to identify differences between theory and the actual observations. Some of the model parameters were constrained to measured concentrations of trace gases to minimize the influence of transport processes.

The comparison between simulated and measured daytime trace gas concentrations showed good agreement for RO_2^*, H_2O_2, OH and large discrepancies for HO_2. In addition, a sensitivity analysis was run to look at variability in the amount of peroxy radicals and the influence of the ozonolysis of alkenes. The measured RO_2^* to HO_2 ratio varied between 5 to 10, which is in total disagreement with the model results where this ratio varied between 1.1 and 2.3 even when the model was run with unrealistically high amounts of volatile organic compounds (VOC). The measured H_2O_2 mixing ratios are also in disagreement with the observed HO_2 amounts under the assumption that H_2O_2 is exclusively produced via the HO_2 self reaction.

The actual measurements of RO_2^*, HO_2, and NO taken during the early morning hours showed that these three species coexisted in high amounts. This cannot be explained by the known chemistry. A sensitivity study of the model run assuming extremely high amounts of NMHC also failed to explain this coexistence.

6.2 Conclusion

The photochemistry and the dynamics of the Earth's atmosphere are highly complex and interlinked. Therefore it is unrealistic in this discussion to separate out either of these aspects. Even the best computers cannot solve this complex system as a whole.

The main focus of this study is to investigate processes responsible for the amounts of radicals and ozone in the atmospheric boundary layer. Analysis of short lived radicals has the advantage that dynamic processes occurring in the atmosphere have only a minor impact on their behaviour. On the other hand these short lived radicals are involved in almost all of the photochemical reaction taking place in the atmosphere. Therefore, in order to maintain the necessary photochemical complexity an essential part of this work was to develop a 0-D homogeneous gas phase chemistry model.

In addition the processes responsible for the amount of O_3 present in the atmosphere were analysed. O_3 has a moderately long lifetime and therefore neither the dynamical processes nor the photochemical processes can be neglected. To simplify the complexity of the analysis, the marine boundary layer above the Indian Ocean was selected. The study of the radical and ozone chemistry was complemented by using sonde and satellite observations to identify possible transport processes

The present investigation is based on two field studies, one in the "clean" and the other in "polluted" atmospheres. A set of trace gases, meteorological parameters, and photolysis frequencies were successfully measured within these two types of environment.

The 0-D model developed in this study was then used to test our conventional knowledge of the atmosphere. In addition, a radiative transfer model was used and adapted to calculate the photolysis frequencies.

This study highlights several features of relevance for improving current knowledge about the Earth's atmosphere. These are described in more detail in the following sections.

6.2.1 Evidence for Cl in the atmosphere

In recent years, some evidence for the presence of Cl in the atmosphere has been reported in the literature. Several scientists have estimated Cl concentrations in the order of 10^3 to 10^6 molecules cm^{-3}.

Within this present study, some evidence for the presence of Cl has also been found. This knowledge has been extended by combining it with further interpretation of other supporting data found in the literature. The main evidence for Cl in the atmosphere can be summarized as follows:

1. The measured diurnal behaviour of RO_2^* over the Indian Ocean is observed to be significantly broader than that estimated using an OH oxidation scheme suitable for the pristine and remote MBL. This broad RO_2^* or bulge shape indicates that more RO_2^* is present in the early morning and late afternoon than the known OH chemistry predicts.

   The appearance of a broader RO_2^* shape is not correlated with the measured amount of NMHC but can be related to the origin of the air masses. Overall this indicates the presence of missing chemistry in the model in the early morning and late afternoon. One reasonable explanation for the observed behaviour is the presence of small amounts chlorine in the MBL producing additional RO_2^* by hydrocarbon oxidation (chapter 2.2.2.4). The sources of Cl are most likely to be release from sea salt aerosols and also possibly the oxidation of organic halides.

   The proposed mechanism of Cl release from aerosols have been described in detail in chapter 2.2.1.8. However, the measurements of aerosols during INDOEX indicated no correlation between the appearance of the bulge in the RO_2^* behaviour with the appearance of maxima in either the total number of aerosols or levels of acidity [Ball et al., 2003]. The Cl release of aerosols is predicted to be catalysed by higher levels of acidity.

2. The high HCHO mixing ratios measured by Wagner et al., [2001] during the INDOEX campaign suggested the presence of another oxidising agent like OH. If present, Cl would lead to additional amounts of RO_2^* and therefore to higher

concentrations of HCHO. The required level of Cl was estimated in this work to be in the order of $1x10^4$ to $1x10^5$ molec cm^{-3} (section 4.2.3.2).

3. The observed relationship between the daily measured maximum mixing ratios of CO, HCHO, and RO_2^* during INDOEX indicates a close chemical link between these species. This link cannot be well explained by the known OH oxidation chemistry used in the 0-D model. The most likely explanation of this behaviour is the presence of Cl in the MBL (section 4.2.3.2.2).

4. Recent measurements of the isotopic fractionation of CH_4 above the Pacific Ocean by Allan et al. [2001] have provided evidence for the enrichment of CH_4 fractions, which cannot be explained by OH chemistry alone. An additional oxidant such as Cl is required.

5. The measurements of Cl_2 [Spicer et al., 1998] in a coastal region of the eastern USA showed high amounts of Cl_2 during the night (up to 150 pptv). Photolysis in the early morning therefore has to produce Cl concentrations of up to 1.3×10^5 atoms cm^{-3}. The source of the inorganic Cl_2 is presumably multi-phase reactions involving aerosols.

6. Lagrangian experiments (i.e. measurement at two sides upwind and downwind, or in a plume with aircrafts and mobile laboratories) including measurements of hydrocarbons have been used to estimate the concentrations of OH.
   These estimated OH amounts differ depending on the hydrocarbon group used for the calculation (i.e. alkanes, alkenes, or aromates).

   Using Lagrangian experiments, Kramp et al., [1994] calculated OH concentrations between 5.5 and $8.5x10^6$ molecules cm^{-3}. Their study investigated the transport processes between Kappel (upwind) and Schauinsland (TOR-station, downwind). For the OH calculations some alkenes (isoprene and 1-hexene) were excluded, because the corresponding calculated OH was much lower than the average obtained from the other hydrocarbon measurements.

The same behaviour was observed by Klemp et al., [1993] calculating OH concentration of $2x10^6$ molecules cm^{-3} from long-term measurements of C3-C5 alkanes. The measurement stations were at Lyon and Schauinsland with an average transport time of about 28 hrs. As a consequence, the estimated OH concentrations have a much higher uncertainty than the values by Kramp et al., [1994] (transport time ~ 3 hrs). However, the calculations considering the measured alkene concentrations (ethane, propene, 1-butene) lead likewise to much lower OH concentrations.

Blake et al. [1993] estimated OH concentrations from airborne VOC measurements in the London plume (London Photochemical Plume Experiment). They estimated twice the concentration of OH from their [$aromate_i$]/[acetylene] measurements (day 1 OH = (3.0 +/- 0.3) x 10^6 molec cm^{-3} and day 2 (9.4 +/- 1.4) x 10^6 molec cm^{-3}) as they did from their [$alkene_i$]/[acetylene] measurements (day 1 (1.7 +/- 0.4) x 10^6 molec cm^{-3} and day 2 (4.1 +/- 1.0) x 10^6 molecules cm^{-3}). They proposed an additional loss process for the aromates, not involving OH in the destruction cycle. In addition, they found that their measured alkanes showed the same behaviour as the aromates.

In the studies presented so far, the ozonolisis of alkenes has been neglected in the calculations of OH because it accounts only for approximately 5% of the total destruction of alkenes and therefore would lead to an overestimation of the OH concentration.

None of the above mentioned authors reported any obvious explanation for these discrepancies in the calculated amount of OH.

However, taking into account the knowledge recently gained and reported on this thesis, discrepancies in the calculated amount of OH can be explained, if Cl is present in sufficient amounts. In general, k_{Cl}/k_{OH} ratio vary between 60 and 230 for the alkanes and between 4 and 14 for the alkenes (Table 9). Thus being predicated on the assumtion that approximately 50% of the alkanes are oxidised by Cl and that $k_{Cl} \sim 10^2 \times k_{OH}$, (i.e. [OH] = $2x10^6$ molecules cm^{-3} (50%) and [Cl] ~ $1\text{-}2x10^4$ molecules cm^{-3} (50%)) the total losses of the alkanes would be the same as calculated with the double amount of OH, and in agreement with the observations given by Kramp et al. [1994].

Additionaly the corresponding theoretical total losses of the alkenes would be approximately 40% lower , i.e. the total calculated loss of alkenes consists of 50% by OH and 10% by Cl (as the reaction of Cl with alkenes proceeds more slowly).

In this manner, i.e. assuming that the Cl concentration is two orders of magnitude lower than OH, and taking into account the different reactivity of alkanes and alkenes with Cl, both alkane and alkene measurements would lead to the same estimated concentration of OH.

	Cl	**OH**	**NO_3**	**O_3**	**k_{Cl}/k_{OH}**
Alkanes	k^{298K} ($10^{-11}cm^3$ $molec^{-1}$ s^{-1})	k^{298K} ($10^{-11}cm^3$ $molec^{-1}$ s^{-1})	k^{298K} ($10^{-17}cm^3$ $molec^{-1}$ s^{-1})	k^{298K} ($10^{-18}cm^3$ $molec^{-1}$ s^{-1})	
Methane	0.01	0.000618	<0.1		16
Ethane	5.9	0.0254	0.14		232
Propane	13.7	0.112	1.7		122
n-Butane	21.8	0.244	4.59		89
n-Pentane	28	0.4	8.7		70
n-Hexane	34	0.545	11		62
Alkenes					
Ethene	12	0.852	21	1.6	14
Propene	25	2.63	950	10.1	10
1-Butene	22	3.14	1400	9.64	7
1,3-butadiene	49	6.66	10000	6.3	7
Isoprene	45	10.1	68000	12.8	4
Aldehydes					
HCHO	7.3	0.92	58		7
CH_3CHO	7.2	1.6	270		5
CH_3CH_2CHO	12	2			6
Ketones					
CH_3COCH_3	0.35	0.022	<3		16
Alcohols					
CH_3OH	5.5	0.093	24		59
C_2H_5OH	9.4	0.32	200		29
n-C_3H_7OH	15	0.55			27

Table 9: Reaction rate coefficients for Cl, OH, NO_3, and O_3 with VOC [Finnlayson-Pitts and Pitts, 2000].

7. The analysis of long term measurements at the Schauinsland site in Germany, showed higher alkene/i-butane ratios during summer than in winter. Due to the more intense photochemistry during summer the opposite effect would be expected. Klemp et al., [1993] proposed additional biogenic sources for smaller alkenes (C2-C4) which they assumed overcompensates for the higher losses during summer relative to the alkanes. Isidorov et al. [1985] and Sawada and Totsuka [1986] reported biogenic emissions of smaller olefins.

   As already stated, Cl is more reactive with alkanes than with alkenes relative to their reaction with OH, therefore this different alkene/i-butane ratios can also be explained by the presence of Cl in the following way. Provided that Cl is produced by the photodissociation of a reservoir substance XCl (e.g. CHOCl) and the photodissociation energy is higher than for O_3, HONO, and HCHO, then the ratio (Cl production / OH production) would be higher in summer than in winter. As a consequence the ratio Cl/OH is higher in summer and the alkanes are removed more efficiently than the alkenes in the summer scenario i.e., more i-butane is removed relative to the alkenes in the summer than in the winter scenario.

8. There is ongoing discussion about "missing HO_x" in the free troposphere (i.e. measured HO_x 2-4 times larger than predicted from primary OH production).

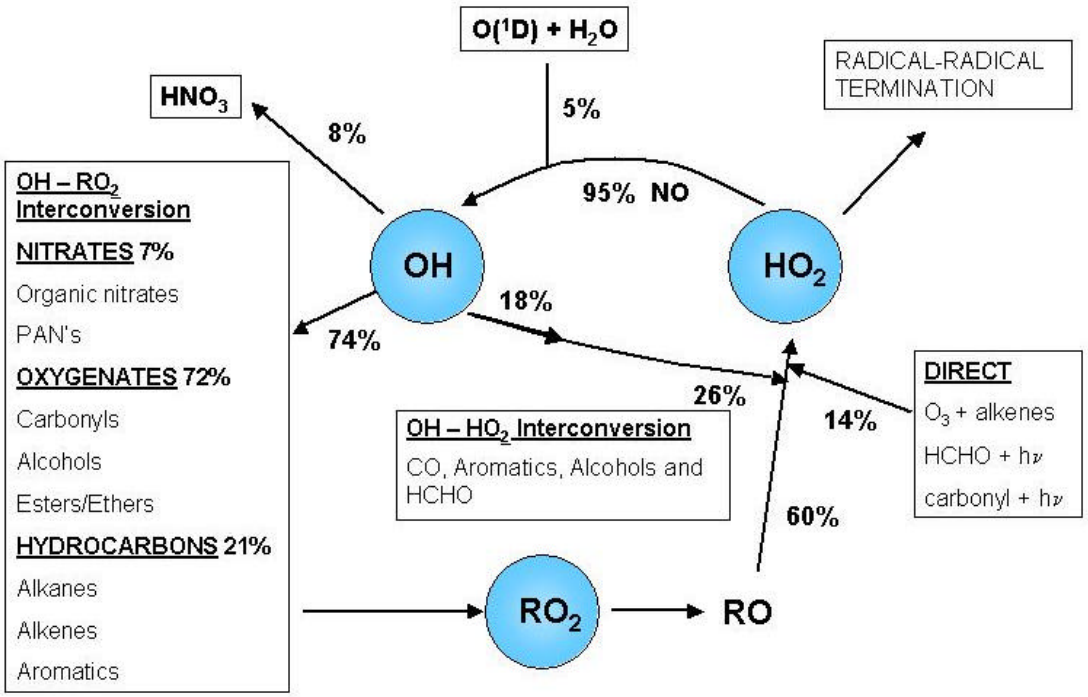

Figure 66: Relative fluxes in the free troposphere calculated by Nic Carslaw – U. York., UK using the Master Chemical Mechanism (MCM, Uni-Leeds)

One possible role for Cl has however not yet been considered in the analysis. Provided that 60% of HO_2 in the free troposphere is produced via RO as illustrated by Figure 66, then Cl might explain the difference of simulated and measured HO_x mixing ratios. Assuming the long-lived alkanes are homogenously vertically distributed throughout the middle and lower troposphere, in contrast to the shorter lived alkenes. Then the presence of sufficient levels of Cl could lead to an additional production of RO by oxidation of hydrocarbons and subsequently to HO_2.

The above mentioned arguments support the presence of Cl, however the possible origins still remain as an open question. As described below, there are several **sources of Cl** already mentioned or excluded in the literature. In addition, the mentioned evidences for the presence of Cl characterise the possible sources of Cl.

Several studies [Khalil and Rasmussen, 1999, Moore et al., 1996] have shown that the ocean is not a significant source of CH_3Cl. Yokouchi et al. [2000] observed up to 2100 pptv of CH_3Cl on islands in the tropics, but these high mixing ratios might be related to emissions from forested land.

Spicer et al. [1998] suggested multi-phase reactions involving aerosols as a possible source of Cl_2, which is easily photodissociated producing Cl.

Calculating the production of Cl via the oxidation of halogenated hydrocarbons (see section 2.2.2.4.3) yield to an upper limit of [Cl] = $5.9x10^3$ [atoms cm^{-3}], for an [OH] = $1x10^7$ [molecule cm^{-3}] and mixing ratio of CH_4 = 1.8 ppmv, i.e. apparently too small to produce significant amounts of Cl. However, the total oxidation of all present halogenated hydrocarbons might increase the calculated upper limit.

In conclusion, the possible source(s) of Cl remain unclear, but the variety of regions, where indications for the presence of Cl was found gives evidence for the ubiquity of Cl. Heterogeneous production mechanisms seem therefore to be unlikely. Taking into account their long lifetime and homogeneous distribution throughout the atmosphere, halogenated hydrocarbons might be the most likely source of Cl.

To summarise this discussion I conclude, perhaps provocatively given the potential consequence of this finding on the chemistry of the Earth's atmosphere, that:

"*Cl is present in the whole atmosphere in levels between $1x10^4$ and $1x10^5$ molecule cm^{-3}. The sources of Cl are ubiquitous and most likely halogenated hydrocarbons. This results in a oxidising capacity of Cl comparable to that of OH in particular in reactions with the alkanes. This would imply that the "cleansing efficiency of the atmosphere" is significantly higher than expected from conventional models. The OH radical would no longer be the "detergent" of the atmosphere. Lifetimes of hydrocarbons would be significantly reduced and strategies to increase air qualitiy would have to be rethought.*"

6.2.2 Influence of aerosol absorption in the dynamics of the atmosphere

In the present study the results of the RTM calculation of warming rates (i.e. caused by the aerosols' absorption of solar radiation during the INDOEX campaign) showed temperature increases up to 1 K within the aerosol layer (1-3km). This has a significant effect in the stability of the atmosphere. The presence of aerosols in the layer above the MBL leads to enhanced stability during the day and less stability during the night and therefore to a diurnal variation in the entrainment strength.

This work has shown the necessity reconsidering the parameterisation of convective processes in all models to account for the impact of ærosols in atmospheric dynamics.

6.2.3 Importance of the STE as a source of O_3 over the Indian Ocean

The interpretation of vertical O_3 profiles in the SH and satellite data of a variety of trace gases above the Indian Ocean has shown that stratospheric O_3 can be the major source of tropospheric O_3. Satellite data indicated no influence of biomass burning or lightning produced NO_x in the area of observation. In spite of the distant location of other possible sources (due to the long lifetime of O_3 in the middle and upper troposphere) their influence cannot completely ruled out. However, back trajectory analysis showed that transport processes from polluted regions was unlikely.

Taking all the data into account it appears that the amount O_3 resulting from the STE is the major source for tropospheric O_3 in the SH Indian Ocean during February and March. Therefore these data provide adequate information for the quantification of the stratospheric contribution.

Additionally this dataset also gives an excellent opportunity to analyse the reliability of global models in the SH Indian Ocean region. Further comparisons of the data collected with model results are recommended.

6.2.4 Open questions in the radical chemistry of the "polluted" atmosphere

Coexistence of NO_x and RO_2^*

In this study comparison between the results of model simulations and actual observations showed, especially in the early morning hours, large discrepancies in the amounts of HO_2 and RO_2^*. The model is not able to reproduce the peroxy radicals observed in the presence of the measured high amounts of NO_x (up to 80 ppbv) during this period of the day.

There is no easy explanation for this phenomena, due to the short lifetime of the peroxy radicals (~seconds). On the other hand, if there were an additional production term not yet considered in the model, this should be activated only in the early morning hours, in order to prevent the additional production of peroxy radicals later during the day. Therefore, high amounts of a reservoir substance which photolyses easily, and which leads to additional radical production during the morning but disappears later during the day is required. The existence of such a substance seems to be unlikely.

Unexplainable RO_2^*/HO_2 ratios

According to box model simulations and sensitivity studies of the radical diurnal evolution, RO_2^*/HO_2 ratios during pollution episodes are expected to vary between 1.1 and 2.3. Excluding cases with enhanced or reduced initial NMHC concentrations of two or more orders of magnitude, the ratio varies only between 1.4 and 1.7, depending on the NMHC content of the air mass. By contrast, the actual RO_2^*/HO_2 ratios measured in this study were typically in the range of 7 to 10.

This large discrepancy between measured and simulated ratios cannot be explained by any known chemistry.

Sensetivity studies have shown that the maximum RO_2^* and HO_2 mixing ratios vary only slightly. Therefore, the ratio between max RO_2^* and max HO_2 under heavily polluted conditions is expected to be constant. This steady ratio seems to be caused by fast reactions with NO which dominate the loss and/or interconversion of peroxy radicals, which leads to peroxy radical lifetimes of a few seconds. The presence of an additional oxidising agent to the known OH, O_3, and NO_3 cannot be excluded, but seems unlikely.

Inconsistency between HO_2 and H_2O_2 measurements

Large discrepancies have been observed in this study between the closely linked amounts of H_2O_2 and HO_2. Assuming that H_2O_2 is formed exclusively by the HO_2 self reaction, then the actual levels of HO_2 measured cannot explain the measured amounts of H_2O_2. Even some additional production of H_2O_2 via the ozonolysis of VOC and the subsequent reaction of the Criegee intermediates with water vapour cannot explain this discrepancy.

6.3 Outlook

The results of this study have shown some deficits in the current physicochemical description of the processes occurring in the Earth's atmosphere.

The results obtained with the developed 0-D model for the "clean" and "polluted" atmospheric boundary layer have indicated that the radical and O_3 chemistry is insufficiently understood. Limitations of available computing time require simplifications which are inadequate to identify new processes with a high accuracy. In addition, measurement techniques need to be improved to get both a higher confidence and a more detailed dataset.

Direct detection of Cl is desirable to quantify to what extent Cl oxidises hydrogen-containing gases, however the requirements to improve the current measurement techniques to detect Cl with sufficient accuracy seem to present insurmountable difficulties, at least with current technologies. A possible alternative would be to measure a directly linked species like ClO or Cl_2 to achieve on short term scale the required information.

The absorption of solar radiation by aerosols and the possible large impacts on the local dynamics is poorly understood. Further research is required for a better physical description of the optical behaviour of the aerosols.

The results of the investigation of a polluted part of the Earth's atmosphere poses the question of how reliable are predictions from existing large scale models, when the chemical processes are relatively poorly understood. In particular the lack of clear understanding of "fast photochemistry", (i.e. photochemical reactionswhere it is appropiate to neglect transport processes), where I have found dramatic discrepancies between my simulations and actual measurements.

References

AEA Technology, FACSIMILE V 3.0 Users Guide, 1994.

Abram, J.P., D.J. Creasey, D.E. Heard, J.D. Lee, and M.J. Pilling, Hydroxyl radical and ozone measurements in England during the solar eclipse of 11 August 1999, Geophys. Res. Lett., 27, 3437, 2000.

Allan, W., D.C. Lowe, and J.M. Cainey, Active chloride in the remote marine boundary layer: Modeling anomalous measurements of $\delta^{13}C$ in methane, Geophys. Res. Lett., 28, 17, 3239-3242, 2001.

Allen, M., and M. Delitsky, A test of odd-oxygen photochemistry using Spacelab 3 Atmospheric Trace Molecule Spectroscopy Observations, J. Geophys. Res., 96, 12,883-12,891, 1991.

Aloisio, S., and J.S. Francisco, J. Phys. Chem., A, 102, 1899-1902, 1998.

Andrés Hernández, M.D., J. Burkert, L. Reichert, D. Stöbener, J. Meyer-Arnek, R.R. Dickerson, B.G. Doddridge, and J.P. Burrows, Marine boundary layer peroxy radical chemistry during the AEROSOLS99 campaign: Measurements and analysis, J. Geophys. Res., 106, D18, 20,833-20,846, 2001.

Antikainen, V., and Paukkunen, A., Studies on improving humidity measurements in radiosondes. In: Instruments and observing methods, Report No. 57, WMO-TD-No 588, 137-141, 1994.

Ariya, P.A., B.T. Jobson, R. Sander, H. Niki, G.W. Harris, and J.F. Hopper, Measurements of C2-C7 hydrocarbons during the polar sunrise experiment 1994: Further evidence for halogen chemistry in the troposphere, J. Geophys. Res., 103 (11), 13,169-13,180, 1998.

Armerding, W., M. Spiekermann, and F. J. Comes, OH multipass absorption: Absolute and in situ method for local monitoring of tropospheric hydroxyl radicals, J. Geophys. Res., 99, D1, 1225-1239, 1994.

Aschmutat, U., Photolyse von Wasserdampf-/Luft-Gemischen bei 185 nm in einem Strömungsrohr zur Kalibration troposphärischer OH-/HO_2-Meßverfahren, Dissertation, Universität Köln, 1994.

Atherton, C.S., and J.E. Penner, The effects of biogenic hydrocarbons on the transformation of nitrogen oxides in the troposphere, J. Geophys. Res., 95, 14,027-14,038, 1990.

Atkinson, R., and S.M. Aschmann, OH radical production from the gas-phase reactions of O_3 with a series of alkenes under atmospheric conditions. Environmental Science and Technology 27 (7), 1357-1363, 1993.

Atkinson R., D.L. Baulch, R.A. Cox, R.F. Hampson, J.A. Kerr, M.J. Rossi, and J. Troe, Evaluated kinetic and photochemical data for atmospheric chemistry: Supplement VIII - IUPAC subcommittee on gas kinetic data evaluation for atmospheric chemistry, J. of Phys. Chem. ref. Data, 29, 167-266, 2000.

Baardsen, E.L., and R.W. Terhune, Detection of OH in the atmosphere using a dye laser, Appl. Phys. Lett., Vol. 21, No 5, 209-211, 1972.

Bakwin, P.S., S.C. Wofsy, S.-M. Fan, M. Keller, S.E. Trumbore, and J.M. da Costa, Emissions of Nitric Oxide (NO) from Tropical Forest Soils and Exchange of NO between the Forest Canopy and Atmospheric Boundary Layers, J. Geophys. Res. 95/D10, 16,755-16,764, 1990.

Ball, W. P., R.R. Dickerson, B.G. Doddridge, J. Stehr, T. Miller, D. Savoie, and T.P. Carsey, Bulk and size-segregated aerosol composition observed during INDOEX 1999: Overview of meteorology and continental impacts, J. Geophys. Res., in press, 2003.

Batt, K, Sea breezes on the NSW coast, Offshore Yachting, Oct/Nov 1995, Jamieson Publishing, 1995.

Baumbach, G., K. Baumann and F. Dröscher, Luftverunreinigungen von Wäldern Baden-Würtenbergs, IVD-Bericht Nr. 16, Universität Stuttgart, 1990.

Becker, K.H. and K. Wirtz, Gas Phase Reactions of Alkyl Nitrates with Hydroxyl Radicals under Tropospheric Conditions in Comparison with Photolysis, J. Atmos. Chem., 1989.

Bey, I., B. Aumont, and G. Toupance, The nighttime production of OH radicals in the continental troposphere. Geophys. Res. Lett. 24 (9), 1067-1070, 1997.

Bey, I., B. Aumont, and G. Toupance, A modelling study of the nighttime radical chemistry in the lower continental troposphere, 1. Development of a detailed chemical mechanism including nighttime chemistry, J. Geophys. Res., 106, D9, 9959-9990, 2001a.

Bey, I., B. Aumont, and G. Toupance, A modelling study of the nighttime radical chemistry in the lower continental troposphere, 2. Origin and Evolution of HO_x, J. Geophys. Res., 106, D9, 9991-10,002, 2001b.

Blake, N.J., S.A. Penkett, K.C. Clemitshaw, P. Anwyl, P. Lightman, A.R.W. Marsh, and G. Butcher, Estimate of atmospheric hydroxyl radical concentrations from the observed decay of many reactive hydrocarbons in well defined urban plumes, J. Geophys. Res., 98, 2851-2864, 1993.

Blindauer, C., V. Rozanov, and J.P. Burrows, Actinic flux and photolysis frequency comparison computations using the model PHOTOGT, J. Atmos. Chem., 24, 1-21, 1996.

Bohren, C.F., and D.R. Huffman, Absorption and scattering of light by small particles, xiv + 530. Wiley, New York, 1983.

Bonsang B., N. Poisson, M. Kanakidou, T. Behmann, J. Burrows, H. Harder, A. Volz-Thomas, G.K. Moortgat, D. Trapp, F. Sauer, G. Schuster, R. Seuwen, T. Zenker, R. Zitzelberger, C. Goeltz, U. Platt, J. Senzig, A. Lewis, P. Seakins, T. Nunes, and C. Pio, Impact of natural non-methane hydrocarbon oxidation on free radical formation in an Eucalyptus forest. In: Larsen, B., Versino, B., Angeletti, G. (Eds.), Proceedings of the Seventh European Symposium on Physico-Chemical Behaviour of Atmospheric Pollutants, the Oxidising Capacity of the Troposphere, European Commission, Luxembourg, 35-46, 1997.

Brasseur, G.P., and S. Solomon, Aeronomy of the Middle Atmosphere, D. Reidel Publishing Company, Dordrecht, The Netherlands, 1984.

Brasseur, G.P., J.J. Orlando, and G.S. Tyndall, Atmospheric Chemistry and Global Change, edited by Oxford University Press, 688 pp., 23 plates, 323 line illustrations & halftones, ISBN 0-19-510521-4, 1999.

Brauers, T., M. Hausmann, A. Bister, A. Kraus, and H.P. Dorn, OH radicals in the boundary layer of the Atlantic ocean: First measurements by long-path laser absorption spectroscopy, J. Geophys. Res., 106, 7399ff., 1999.

Bremaud, P.J., F. Taupin, A.M. Thompson, and N. Chaumerliac, Ozone nighttime recovery in the marine boundary layer: Measurement and simulation of the ozone diurnal cycle at Reunion Island, J. Geophys. Res., 103, 3463-3473, 1998.

Brimblecombe, P., London air pollution, 1500-1900, Atmos. Environ., 11, 1157-1162, 1977.

Brimblecombe, P., Air-composition and chemistry, Cambridge University Press, 1986.

Brühl, C., and P.J. Crutzen, Scenarios of possible changes in atmospheric temperatures and ozone concentrations due to man's activities, estimated with a one-dimensional coupled photochemical climate model, Climate Dynamics, 2, 173-203, 1988.

Brühl, C., and P.J. Crutzen, MPIC Two-dimensional model. In: The atmospheric effects of stratospheric aircraft, NASA Ref. Publ. 1292, 103-104, 1993.

Buchwitz, M., A correlated-k distribution scheme for overlapping gases suitable for retrieval of atmospheric constituents from moderate resolution radiance measurements in the visible/near-infrared spectral region, J. Geophys. Res., 105, D12, 15,247-15,261, 2000.

Burkert, J., T. Behmann, M.D. Andrés Hernández, D. Stöbener, M. Weißenmeyer, D. Perner, and J.P. Burrows, Measurements of Peroxy Radicals in a forested area of Portugal, Chemosphere, Global change science, 3327-3338, 2001a.

Burkert, J., M.D. Andrés-Hernández, D. Stöbener, J.P. Burrows, M. Weißenmayer, and A. Kraus, Peroxy radical and related trace gas measurements in the boundary layer above the Atlantic Ocean, J. Geophys. Res., 106, 6, 5457-5477, 2001b.

Burkert, J. M.D. Andrés Hernández, L. Reichert, J. Meyer-Arnek, J. Mühle, A. Zahn, T. Carsey, R.R. Dickerson, B. Doddridge, and J.P. Burrows, Trace gas and radical behaviour in the marine boundary layer during INDOEX 1999, in press, J. Geophys. Res., 2003a.

Burkert, J., M.D. Andrés-Hernández, L. Reichert, J. Meyer-Arnek, R.R. Dickerson, J. Stehr, H. Smit, and J.P. Burrows, Photochemistry and radiative effects of

aerosols in the marine boundary layer during INDOEX 1999, submitted, J. Geophys. Res., 2003b.

Burkert, J., M.D. Andrés-Hernández, L. Reichert, D. Heard, J. Lee, R. Morgan, and J.P. Burrows, Peroxy Radicals in the Urban Troposphere (PRIME1999), submitted, J. Geophys. Res., 2003c.

Burkert, J., M.D. Andrés-Hernández, L. Reichert, D. Heard, J. Lee, R. Morgan, and J.P. Burrows, Nocturnal Chemistry of Peroxy Radicals in the Urban Troposphere (PRIME1999), in preparation, J. Geophys. Res., 2003d.

Burrows, J.P., M. Buchwitz, M. Eisinger, V. Rozanov, M. Weber, A. Richter, and A. Ladstätter-Weißenmayer, The Global Ozone Monitoring Experiment (GOME): Mission, instrument concept, and first scientific result, in Proc. 3rd ERS Symposium, Florence, 1997.

Burrows, J.P., M. Weber, M. Buchwitz, V. Rozanov, A. Ladstätter-Weißenmayer, A. Richter, R. DeBeek, R. Hoogen, K. Bramstedt, K.U. Eichmann, and M. Eisinger, The global ozone monitoring experiment (GOME): mission concept and first scientific results, J. Atmos. Sci., 56, 151-175, 1999.

Bush, B.C. and P.J. Valero, Spectral aerosol radiative forcing at the surface during the Indian Ocean Experiment (INDOEX), 107, D19, 2002.

Cadle, R.D., and H.S. Johnston, Chemical Reactions in Los Angeles Smog, Second National Air Pollution Symposium, Stanford Research Institute, Menlo Park, California 1952.

Cadle, S.H., and J.M. Dasch, Wintertime concentrations and sinks of atmospheric particulate carbon at a rural location in Northern Michigan. Atmos. Environ., 22 (7), 1373-1381, 1988.

Cantrell, C.A., and D.H. Stedman, A Possible Technique for the Measurement of Atmospheric Peroxy Radicals, Geophys. Res. Lett. 9/8, 846-849, 1982.

Cantrell, C.A., J.A. Lind, R.E. Shetter, J.G. Calvert, P.D. Goldan, W. Kuster, F.C. Fehsenfeld, S.A. Montzka, D.D. Parrish, E.J. Williams, M.P. Buhr, H.H Westberg, G. Allwine, and R. Martin Peroxy radicals in the ROSE experiment: measurement and theory, J. Geophys. Res., 97, D18, 20,671-20,686, 1992.

Cantrell, C.A., R.E. Shetter, J.G. Calvert, D.D. Parrish, F.C. Fehsenfeld, P.D. Goldan, W. Kuster, E.J. Williams, H.H. Westberg, G. Allwine, and R. Martin, Peroxy radicals as measured in ROSE and estimated from photostationary state deviations, J. Geophys. Res., 98, D10, 18,355-18,366, 1993.

Cantrell, C.A., R.E. Shetter, T.M. Gilpin, J.G. Calvert, F.L. Eisele, and D.J. Tanner, Peroxy radical concentrations measured and calculated from trace gas measurements in the Mauna Loa observatory photochemistry experiment 2, J. Geophys. Res., 101, D10, 14,653-14,664, 1996.

Cantrell, C.A., R.E. Shetter, J.G. Calvert, F.L. Eisele, E. Williams, K. Baumann, W.H. Brune, and P.S. Stevens, Peroxy radicals from photostationary state deviations and steady state calculations during the Tropospheric OH Photochemistry Experiment at Idaho Hill, Colorado, 1993, J. Geophys. Res., 102 , D5, 6369, 1997.

Carlier, P., P. Fresnet, S. Pashalidis, M. Tsetsi, A. Martinet, V. Lescoat, B. Dupont, A. Chebbi, and R. Girard, Study of the oxidation of acid precursors in marine atmosphere: Organosulphus compounds and aldehydes. In Air Pollution Research Report 35, 167-180, 1991.

Carpenter, L.J., W.T, Sturges, P.S. Liss, S.A Penkett, B. Alicke, K. Hebestreit, and U. Platt, Observations of alkyl iodides and bromides at Mace Head: Links to

macroalgal emissions an IO formation, Paper presented at EGS XXIII General Assembly, Nice, France 20-24, 1998, Annales Geophysicae Supplement II 16, C718, 1998.

Carpenter, L.J., W.T. Sturges, S.A. Penkett, P.S. Liss, B. Alicke, K. Hebestreit, and U. Platt, Short-lived alkyl iodides and bromides at Mace Head, Ireland: Links to biogenic sources and halogen oxide production, J. Geophys. Res., 104, D1, 1679-1690, 1999.

Carpenter, L.J., G. Malin, F. Kuepper, and P.S. Liss, Novel biogenic iodine-containing tri- trihalomethanes and other short-lived halocarbons in the coastal East Atlantic, Global Bio- halomethanes, Biogeochem. Cycles, 14, 1191-1204, 2000.

Carroll, M.A., M. McFarland, B.A. Ridley, and D.L. Albritton, Ground-based nitric oxide measurements at Wallops Island, Virginia, J. Geophys. Res., 90, 12,853-12,860, 1985.

Carsey, T.P., D.D. Churchill, M.L. Farmer, C.J. Fischer, A.A. Pszenny, V.B. Ross, E.S. Saltzman, M. Springer-Young, and B. Bonsang, Nitrogen oxides and ozone production in the North Atlantic marine boundary layer, J. Geophys. Res., 102, 10,653-10,665, 1997.

Carslaw, K.S., B. Luo, and T. Peter, An analytic expression for the composition of aqueous HNO_3-H_2SO_4 stratospheric aerosols including gas phase removal of HNO_3, Geophys. Res. Lett., 22, 1877-1880, 1995.

Carslaw, K.S., T. Peter, and S.L. Clegg, Modelling the composition of liquid stratospheric aerosols, Rev. of Geophys., 35 (2), 125-154, 1997.

Carslaw, N., D.J. Creasey, D.E. Heard, A.C. Lewis, J.B. McQuaid, M.J. Pilling, P.S. Monks, B.J. Bandy, and S.A. Penkett, Modelling OH, HO_2 and RO_2

radicals in the marine boundary layer: 1. Model construction and comparison with field measurements. J. Geophys. Res., 104, 30,241-30,255, 1999.

Carslaw, N., D.E. Heard, J. Hopkins, M.E. Jenkin, J.D. Lee, A.C. Lewis, and M.J. Pilling, Modelling radical chemistry in urban areas, European Geophysical Society Annual Meeting, Nice, March 2001.

Carslaw, N., D.J. Creasey, D.E. Heard, P.J. Jacobs, J.D. Lee, A.C. Lewis, J.B. McQuaid, M.J. Pilling, S. Bauguitte, S.A. Penkett, P.S. Monks, and G. Salisbury, The Eastern Atlantic Spring Experiment 1997 (EASE97): 2. Comparisons of model concentrations of OH, HO_2, and RO_2 with measurements, J. Geophys. Res., 2003.

Carver, G.D., P.D. Brown, and O. Wild, The ASAD atmospheric chemistry integration package and chemical reaction database, Computer Physics Communications, 105, 197-215, 1997.

Chameides, W.L., and D.D. Davis, Iodine - its possible role in tropospheric photochemistry, J. Geophys. Res., 85, 7383-7398, 1980.

Chance, K., W. Traub, D. Johnson, K. Jucks, P. Ciarpallini, R. Stachnik, R. Salawitch, and H. Michelsen, Simultaneous measurements of stratospheric HO_x, NO_x, and Cl_x: Comparison with photochemical model, J. Geophys. Res., 101, 9031-9043, 1996.

Chance, K., P.I. Palmer, R.J.D. Spurr, R.V. Martin, T.P. Kurosu, and D.J. Jacob, Satellite observations of formaldehyde over North America from GOME, Geophys. Res. Lett., 27, 3461-3464, 2001.

Charlson, R.J., J. Langner, H. Rodhe, C.B. Leovy, and S.G. Warren, Perturbation of the northern hemisphere radiative balance by backscattering from anthropogenic sulfate aerosols, Tellus, 43AB (4), 152-163, 1991.

Charlson, R.J., and J. Heintzenberg, Aerosol Forcing of Climate, John Wiley and Sons Limited, pp. 91-108, 1995a.

Charlson R.J., and J. Heintzenberg, Remote Sensing of the Direct and Indirect Aerosol Forcing, Review for the Dahlem Conference, Aerosol Forcing of Climate, Eds., pp. 298-332, Wiley, England, 1995b.

Chatfield, R.B., and P.J. Crutzen, Are there interactions of iodine and sulfur species in marine air photochemistry, J. Geophys. Res., 95, 22,319-22,341, 1990.

Chipperfield, M., E. Lutman, J. Kettleborough, J. Pyle, and A. Roche, Model studies of chlorine deactivation and formation of $ClONO_2$ collar in the Arctic polar vortex, J. Geophys. Res., 102, 1467-1478, 1997.

Chylek, P., and J.A. Coakley Jr., Aerosols and climate, Science, 183, 75-77, 1974.

Cicerone, R.J., Halogens in the atmosphere, Rev. Geophys. Space Phys. 19, 123-139. 1981.

Clarke, A.D., and K.J. Noone, Soot in the Arctic snowpack, A cause for perturbations in radiative transfer, Atmos. Environ., 19, 2045-2053, 1985.

Class, T., and K. Ballschmiter, Chemistry of organic traces in air, J. Atmos. Chem. 6, 35-46, 1988.

Clemitshaw, K.C., L.J. Carpenter, S.A. Penket, and M.E. Jenkin, A calibrated peroxy radical chemical amplifier (PERCA) instrument for ground-based tropospheric measurements, J. Geophys. Res., 102, 25,405-25,416, 1997.

Cowling, E.B., Acid precipitation in historical perspective, Environ. Sci. Technol., 16, 110A-123A, 1982.

Cox, C., and W. Munk, Measurement of the roughness of the sea surface from photographs of the sun's glitter, J. Opt. Soc. Am., 44, 838-850, 1954.

Creasey, D.J., P.A. Halford-Maw, D.E. Heard, M.J. Pilling, and B.J. Whitaker, Implementation and initial deployment of a field instrument for measurement of OH and HO_2 in the troposphere by laser-induced fluorescence, J. Chem. Soc. Faraday Trans., 93, 2907-2914, 1997.

Creasey, D.J., D.E. Heard, and J.D. Lee, Eastern Atlantic Spring Experiment 1997 (EASE97), 1, Measurements of OH and HO_2 concentrations at Mace Head, Ireland, J. Geophys. Res., 107, 2002.

Crutzen, P.J., A discussion of the chemistry of some minor constituents in the stratosphere and troposphere, Pure and applied Geophys. 106-108, 1385-1399, 1973.

Crutzen, P.J., and P.H. Zimmermann, The changing photochemistry of the troposphere, Tellus, 43AB, 136-151, 1991.

Crutzen, P., J.-U. Grooß, C. Brühl, and T. Peter, On the potential importance of the gas phase reaction $CH_3O_2+ClO \rightarrow ClOO+CH_3O$ and the heterogeneous reaction $HOCl+HCl \rightarrow H_2O+Cl_2$ in the "ozone hole" chemistry, Geophys. Res. Lett., 19, 1113-1116, 1992.

Crutzen, P.J., and V. Ramanathan, Foreword, J. Geophys. Res., 106, D22, 28,369-28,370, 2001.

Curtis, A.R., and W.P. Sweetenham, FACSIMILE Release H user´s manual, Computer Science and System Division, Harwell Laboratory, Oxfordshire, 1985.

Danilin, M., N.-D. Sze, M. Ko, J. Rodriguez, and M. Prather, Bromine-chlorine coupling in the Antarctic ozone hole, Geophys. Res. Lett., 23, 153-156, 1996.

DeHaan, D., I. Floisand, and F. Strodal, Modeling studies of the effects of the heterogeneous reaction ClOOCl+HCl→Cl_2+HOOCl on stratospheric chlorine activation and ozone depletion, J. Geophys. Res., 102, 1251-1258, 1997.

de Laat, A.T.J., INDOEX Chemistry of the Indian Ocean atmosphere, Ph.D. Dissertation, Institute for Marine and Atmospheric Research (IMAU), Utrecht University, 141 pp., 2000.

de Laat, A.T.J., J. Lelieveld, G.-J. Roelofs, R.R. Dickerson, and J.M. Lobert, Source analysis of carbon monoxide pollution during INDOEX 1999, J. Geophys. Res., 106 (D22), 28,481-28,495, 2001a.

de Laat, A.T.J., J.A. de Gouw, J. Lelieveld, A. Hansel, Model analysis of trace gas measurements and pollution impact during INDOEX, J. Geophys. Res., 106 (D22), 28,469-28,480, 2001b.

DeMajistre, R., D. Anderson, S. Lloyd, P. Swaminathan, and S. Zasadil, Effects of refraction on photochemical calculations, J. Geophys. Res., 100 (D9), 18,817-18,822, 1995.

DeMore, W.B., S.P. Sander, D.M. Golden, R.F. Hampson, M.J. Kurylo, C.J. Howard, A.R. Ravishankara, C.E. Kolb, and M.J. Molina, Chemical Kinetics and Photochemical Data for use in Stratospheric Modeling. JPL, Evaluation number 12, 1997.

Dickerson, R.R., Measurements of Reactive Nitrogen Compounds in the Free Troposphere, Atmos. Environ., 18 (12), 2585-2593, 1984.

Dickerson, R.R., and A.C. Delany, Modification of a commercial gas filter correlation CO detector for increased sensitivity, J. Atmos. Oceanic Technol., 5 (3), 424-431, 1988.

Dickerson, R.R., S. Kondragunta, G. Stenchikov, K.L. Civerolo, B.G. Doddridge, and B.N. Holbel, The impact of aerosols on solar ultraviolet radiation and photochemical smog, Science, 278, 827–830, 1997.

Dickerson, R.R., K.P. Rhoads, T.P. Carsey, S.J. Oltmans, J.P. Burrows, and P.J. Crutzen, Ozone in the remote marine boundary layer: A possible role for halogens, J. Geophys. Res., 104, 21,385-21,395, 1999.

Dickerson, R.R., M.O. Andreae, T. Campos, O.L. Mayol-Bracero, C. Neusüß, and D.G. Streets, Analysis of black carbon and carbon monoxide observed over the Indian Ocean: Implications for emissions and photochemistry, J. Geophys. Res., 107 (19), 2002.

Donahue, N.M., M.K. Dubey, R. Mohrschladt, K.L. Demerjian, and J.G. Anderson, High-pressure flow study of the reactions $OH+NO_x \rightarrow HONO_x$: Errors in the falloff region, J. Geophys. Res., 102 (D5), 6159-6168, 1997.

Donahue, N.M., J.H. Kroll, J.G. Anderson, and K.L. Demerjian, Direct observation of OH production from the ozonolysis of olefins. Geophys. Res. Lett. 25 (1), 59-62, 1998.

Dorn, H., U. Brandenburger, T. Brauers, M. Hausmann, and D.H. Ehhalt, In-situ detection of tropospheric OH radicals by folded long-path laser absorption. Results from the POPCORN field campaign in August 1994, Geophys. Res. Lett., 23, 18, 2537-2540, 1996.

Duce, R.A., V.A. Mohnen, P.R. Zimmermann, D. Grosjean, W. Cautreels, R. Chatfield, R. Jaenicke, J.A. Ogren, E.D. Pellizzari, and G.T. Wallace, Organic material in the global troposphere, Rev. Geophys. and Space Phys., 21, 4, 921-952, 1983.

Eberhard, J., and C.J. Howard, Rate Coefficients for the Reactions of Some C_3 to C_5 Hydrocarbon Peroxy Radicals with NO, JPC, 101, 3360-3366, 1997.

Eisinger, M., and J.P. Burrows, Tropospheric Sulfur Dioxide observed by the ERS-2 GOME instrument, Geophys. Res. Lett., 25, 4177-4180, 1998.

Emanuel, K.A., Atmospheric Convection, Oxford University Press, 580 pp., 1994.

Fan, S.–M., and D.J. Jacob, Surface ozone depletion in Arctic spring sustained by aerosol bromine reactions, Nature, 359, 522-524, 1992.

Farman, J., B. Gardiner, and J. Shanklin, Large losses of total ozone in Antarctica reveals seasonal ClO_x/NO_x interaction, Nature, 315, 207-210, 1985.

Finkbeiner, M., J. Crowley, O. Horie, R. Müller, G. Moortgat, and P. Crutzen, Reaction between HO_2 and ClO: Product formation between 210 K and 300 K, J. Phys. Chem., 99, 16,264-16,275, 1995.

Finlayson-Pitts, B.J., J. Pitts, and J.N. Pitts, Atmospheric chemistry: Fundamentals and experimental techniques, Wiley, New York, 1986.

Finlayson-Pitts, B.J., Comment on "Indications of photochemical histories of Pacific air masses from measurements of atmospheric trace species at Point Arena, California," J. Geophys. Res., 98 (8), 14,991-14,993, 1993a.

Finlayson-Pitts, B.J., Chlorine atoms as a potential tropospheric oxidant in the marine boundary layer. J. Res. Chem. Intermed., 19, 235-249, 1993b.

Finlayson-Pitts, B.J., C.J. Keoshian, B. Buehler, and A.A. Ezell, Kinetics of reaction of chlorine atoms with some biogenic organics, Int. J. Chem. Kinet., 31, 491-499, 1999.

Finlayson-Pitts, B.J., and J.N. Pitts, Chemistry of the Upper and Lower Atmosphere, Academic Press, p. 845, 2000.

Fish, D., R. Jones, and E. Strong, Mid-latitude observations of the diurnal variation of stratospheric BrO, J. Geophys. Res., 100, 18,863-18,871, 1995.

Froidevaux, L., M. Allen, and Y. Yung, A critical analysis of ClO and O_3 in the mid-latitude stratosphere, J. Geophys. Res., 90, 12,999-13,029, 1985.

Fuller, K.A., W.C. Malm, and S.M. Kreidenweis, Effects of mixing on extinction by carbonaceous particles, J. Geophys. Res., 15,941-15,954, 1999.

Gäb, S., W.V. Turner, S. Wolff, K.H. Becker, L. Ruppert, and K.J. Brockmann, Formation of alkyl and hydroxyalkyl hydroperoxides on ozonolysis in water and in air, Atmos. Environ., 29, 18, 2401-2407, 1995.

Galbally, I.E., The Emissions of Nitrogen to the Remote Atmosphere. In: Biogeochemical Cycling of Sulfur and Nitrogen in the Remote Atmosphere, D. Reidel, Norwell, Mass. 1985.

Gamazaychikov, M., G. Stenchikov, M. Fox-Rabinovitz, R. Dickerson, and K. Pickering, Aerosol radiative effects on dynamical mixing and chemical processes in the planetary boundary layer, Eos Trans. AGU, 79 (17), Spring Meet. Suppl., S34, 1998.

Ganzeveld, L,. J. and Lelieveld, Dry deposition parameterization in a chemistry general circulation model and its influence on the distribution of reactive trace gases, J. Geophys. Res., 100, D10, 20,999-21,012, 1995.

Gautrois, M., R. Koppmann, G. Leckebusch, A. Reiner, and P. Speth, The latitudinal distribution of hydrocarbons and halocarbons during the Albatross-campaign, Annales Geophys., Suppl. II to Vol. 16, C 805, 1998.

Gear, C., The automatic integration of ordinary differential equatins, Numer. Math., 14, 176-179, 1971.

George, L.A., T.M. Hard, and R.J. O'Brien, Measurement of free radicals OH and HO_2 in Los Angeles smog, J. Geophys. Res., 104, D9, 11,643-11,655, 1999.

Glossary of Meteorology, 2nd Edition. American Meteorological Society, Boston, 2000.

Graedel, T.E., and W.C. Keene, Tropospheric budget of reactive chlorine, Global Biogeochem. Cycles, 9 (1), 47-77, 1995.

Haagen-Smit, A.J., Chemistry and Physiology of Los Angeles Smog, Industrial and Engineering Chemistry 44/6, 1342-1346, 1952.

Hansen, A.D.A., and T. Novakov, Aerosol black carbon measurements over the western Atlantic Ocean, Global Biogeochem. Cycles, 2, 41-45, 1988.

Hansen, J., I. Fung, A. Lacis, D. Rind, S. Lebedeff, R. Ruedy, G. Russell, and P. Stone, Global climate changes as forecast by Goddard Institute for Space Studies 3-dimensional model, J. Geophys. Res., 93, 9341-9364, 1988.

Hanson, D., A. Ravishankara, and S. Solomon, Heterogeneous reactions in sulphuric acid aerosols: A framework for model calculations, J. Geophys. Res., 99, 3615-3629, 1994.

Hanson, P.J., and S.E. Lindberg, Dry Deposition of Reactive Nitrogen Compounds: A Review of Leaf, Canopy and non-foliar Measurements, Atmos. Environ. 25A/8, 1615-1634, 1991.

Hard, T.M., A.A. Mehrabzadeh, C.Y. Chan, and R.J. O'Brien, Fage measurements of tropospheric OH with measurements and model of interferences, J. Geophys. Res., 97, D9, 9795-9817, 1992.

Hastie, D.R., M. Weißenmayer, J.P. Burrows, and G.W. Harris, Calibrated chemical amplifier for atmospheric ROx measurements, Analytical Chemistry, 63, 2048-2057, 1991.

Hatakeyama, S., and H. Akimoto, Reactions of Criegee intermediates in the gas phase, Res. Chem. Intermed., 20, 503-524, 1994.

Hausmann, M., U. Brandenburger, T. Brauers, and H.-P. Dorn, Detection of tropospheric OH radicals by long-path differential-optical-absorption-spectroscopy: Experimental setup, accuracy and precision, 16,011-16,022, 1997.

Haywood, J.M., and K.P. Shine, The effect of anthropogenic sulfate and soot on the clear sky planetary radiation budget, Geophys. Res. Lett., 22, 603-606. 1995.

Haywood, J.M., and K.P. Shine, Multi-spectral calculations of the direct radiative forcing of tropospheric sulfate and soot aerosol using a column model. QJR, 123, 1907-1930, 1997.

Haywood, J.M., and V. Ramaswamy, Global sensitivity studies of the direct radiative forcing due to anthropogenic sulfate and black carbon aerosols, J. Geophys. Res., 103 (D6), 6043-6058, 1998.

Heikes, B., M. Lee, D. Jacob, R. Talbot, J. Bradshaw, H. Singh, D. Blake, B. Anderson, H. Fuelberg, and A.M. Thompson, Ozone, hydroperoxides, oxides of nitrogen, and hydrocarbon budgets in the marine boundary layer over the South Atlantic, J. Geophys. Res., 101, D19, 24,221-24,234, 1996.

Heintzenberg, J., Size-segregated measurements of particulate elemental carbon and aerosol light absorption at remote Arctic locations, Atmos. Environ., 16, 2461-2469, 1982.

Heintzenberg, J., and M. Wendisch, On the sensitivity of cloud albedo to the partitioning of particulate absorbers in cloudy air, Contr. Atmos. Phys., 69, 491-499, 1996.

Hess, M., P. Koepke, and I. Schult, Optical Properties of Aerosols and Clouds: The Software Package OPAC, Bulletin of the American Meteorological Society, Vol. 79, No 5, 1998.

Hild, L., A. Richter, V. Rozanov, and J. P. Burrows, Air Mass Factor Calculations for GOME Measurements of lightning-produced NO_2, ASR, 29 (11), 1685-1690, 2002.

Hirokawa, J., K. Onaka, Y. Kajii, and A. Akimoto, Heterogeneous processes involving sodium halide particles and ozone: Molecular bromine release in the marine boundary layer in the absence of nitrogen oxides, Geophys. Res. Lett., 25 (13), 2449-2452, 1998.

Hofzumahaus, A., U. Aschmutat, M. Heßling, F. Holland, and D. H. Ehhalt, The measurement of tropospheric OH radicals by laser-induced fluorescence spectroscopy during the POPCORN field campaign, Geophys. Res. Lett., 23, 18, 2541-2544, 1996.

Hofzumahaus, A., U. Aschmutat, U. Brandenburger, T. Brauers, H.-P. Dorn, M. Hausmann, M. Heßling, F. Holland, C. Plass-Dülmer, and D.H. Ehhalt, Intercomparison of tropospheric OH measurements by different laser techniques during the POPCORN campaign 1994, J. Atmos. Chem. 31, 227-246, 1998.

Hofzumahaus, A., A. Kraus, and M. Müller, Solar actinic flux spectroradiometry: a technique for measuring photolysis frequency in the atmosphere, Appl. Opt., 21, 4443-4460, 1999.

Holton, J.R., P.H. Haynes, M.E. McIntyre, A.R. Douglass, R.B. Rood, and L. Pfister, Stratosphere-troposphere exchange, Rev. Geophys., 33, 403-439, 1995.

Horie, O., P. Neeb, S. Limbach, and G.K. Moortgat, Formation of Formic acid and organic peroxides in the ozonolysis of ethane with added water vapour, Geophys. Res. Lett., 21, 14, 1523-1526, 1994.

Horvath, H., Comparison of the light absorption coefficient and carbon measures for remote aerosols, an independent analysis of data from the IMPROVE network I and II, Discussion, Atrmos. Environ., 31, 2885-2887, 1997.

Hoskins, B.J., M E. McIntyre, and A.W. Robertson, On the use and significance of isentropic potential vorticity maps, Quart. J. Roy. Meteorol. Soc., 111, 877-946, 1987.

Hu, J., and D. Stedman, Atmospheric RO_x Radicals at an urban site: Comparison to a Simple Theoretical Model, Environ. Sci. Technol., 29, 1655-1659, 1995.

Hübler, G., D. Perner, U. Platt, A. Tönnissen, and D.H. Ehhalt, Groundlevel OH radical concentration: New measurements by optical absorption, 1309-1319, 1984.

IPCC, The Supplementary Report to the IPCC Scientific Assessment, Cambridge University Press, 1992.

IPCC, Climate Change 1995: The Science of Climate Change. Contribution of Working Group I to the Second Assessment Report of the Intergovernmental Panel on Climate Change [J. T. Houghton., L.G. Meira Filho, B. A. Callander, N. Harris, A. Kattenberg, and K. Maskell (eds.)]. Cambridge University Press, Cambridge, United Kingdom and New York, NY, USA, 572 pp, 1996.

Isidorov, V.A., I.G. Zenkevich, and B.V. Ioffe, Volatile organic compounds in the atmosphere of forests, Atmos. Environ., 19, 1-8, 1985.

Jackman, C., R. Seals, Jr., and M. Prather, eds., Two-Dimensional Intercomparison of Stratospheric Models, vol. 3042 of NASA Conference Publication, 1988.

Jacob, D.J., B.G. Heikes, S.-M. Fan, J.A. Logan, D.L. Mauzerall, J.D. Bradshaw, H.B. Singh, G.L. Gregory, R.W. Talbot, D.R. Blake, and G.W. Sachse, Origin of ozone and NOx in the tropical troposphere: A photochemical analysis of aircraft observations over the South Atlantic basin, J. Geophys. Res., 101, 24,235-24,250, 1996.

Jacob, D.J., Introduction to Atmospheric Chemistry, Princeton University Press, ISBN: 0-691-00185-5, 1999.

Jacobson, M.Z., Fundamentals of Atmospheric Modeling, published by Cambridge University Press, New York, 1998a.

Jacobson, M.Z., Studying the effects of aerosols on vertical photolysis rate coefficient and temperature profiles over an urban airshed, J. Geophys. Res., 103, 10,593-10,604, 1998b.

Jacobson, M.Z., Isolating nitrated and aromatic aerosols and nitrated aromatic gases as sources of ultraviolet light absorption, J. Geophys. Res., 104, D3, 3527-3542, 1999.

Jacobson, M.Z., Atmospheric Pollution: History, Science and Regulation, published by Cambridge University Press, New York, 2002.

Jenkin M.E., The photochemistry of iodine-containing compounds in the marine boundary layer, Report AEA Harwell, AEA-EE-0405, 1992.

Jenkin, M.E.; and Hayman, G.D., Kinetics of reactions of primary, secondary and tertiary b-hydroxy peroxyl radicals. Application to isoprene degradation, J. Chem. Soc., Faraday Trans., 91, 1911, 1995.

Jenkin, M.E., and K.C. Clemitshaw, Ozone and other secondary photochemical pollutants: Chemical processes governing their formation in the planetary boundary layer. Atmos. Environ., 34 (16), 2499-2527, 2000a.

Jenkin, M.E., T.P. Murrells, and N.R. Passant, Temporal dependence of ozone precursor emissions: estimation and application. Report on the DETR contracts EPG 1/3/134 and EPG 1/3/143. Report AEAT/R/ENV/0355, 2000b.

Jin, Z., T. Charlock, and K. Rutledge, Analysis of broadband solar radiation and albedo over the ocean surface at COVE, J. of Atmospheric and Oceanic Technology, 19, No 10, 1585-1601, 2002.

Jobson, B.T., H.H. Niki, Y. Yokouchi, J. Bottenheim, F. Hopper, and R. Leaitch, Measurements of C_2-C_6 hydrocarbons during the polar sunrise experiment: Evidence for Cl and Br atom chemistry, J. Geophys. Res., 99 (12), 22.355-25.368, 1994.

Junge, C. E., Global ozone budget and exchange between stratosphere and troposphere. Tellus, 14, 363-377, 1962.

Junkermann, W., U. Platt, and A. Volz-Thomas, A photoelectric detector for the measurement of photolysis frequency of ozone and other atmospheric molecules, J. Atmos. Chem., 8, 203-227, 1989.

Kanaya, Y., Y. Sadanaga, J. Matsumoto, U.K. Sharma, J. Hirokawa, Y. Kajii, and H. Akimoto, Daytime HO_2 concentrations at Oki Island, Japan, in summer 1998: Comparison between measurement and theory, J. Geophys. Res., 105, D19, 24,205, 2000.

Kanaya, Y., Y. Sadanaga, K. Nakamura, and H. Akimoto, Behavior of OH and HO_2 radicals during the Observations at a Remote Island of Okinawa (ORION99) field campaign, 1, Observation using laser-induced fluorescence instrument, J. Geophys. Res., 106, D20, 24,197, 2001.

Kaplan, W.A., S.C. Wofsy, M. Keller, and J.M. da Costa, Emissions of NO and Deposition of O_3 in a Tropical Forest System, J. Geophys. Res., 93/D, 1389-1395, 1988.

Keene, W.C., A.A.P. Pszenny, D.J. Jacob, R.A. Duce, J.N. Galloway, J.J. Schultz-Tokos, H. Sievering, and J.F. Boatman, The geochemical cycling of reactive chlorine through the marine troposphere, Glob. Biogeochem. Cycles, 4 (4), 407-430, 1990.

Keene, W.C., D.J. Jacob, and S.M. Fan, Reactive chlorine: A potential sink for dimethylsulfide and hydrocarbons in the marine boundary layer, Atmos. Environ., 30 (6), 1-3, 1996.

Kelley, P., R.R. Dickerson, W.T. Luke, and G.L. Kok, Rate of NO2 photolysis from the surface to 7.6 km altitude in clear sky and clouds, Geophys. Res. Lett., 22 (19), 2621-2624, 1995.

Keppler, F., R. Eiden, V. Niedan, J. Pracht, and H.F. Schöler, Halocarbons produced by natural oxidation processes during degradation of organic matter, Nature, 403, 298, 2000.

Khalil, M.A.K., and R.A. Rasmussen, Atmospheric methyl chloride, Atmos. Environ., 33, 1305-1321, 1999.

Kiehl, J.T., and K.E. Trenberth, Earth's Annual Global Mean Energy Budget, Bull. Amer. Meteor. Soc., 78, 197-208, 1997.

Kiehl, J.T., V. Ramanathan, J.J. Hack, A. Huffman, and K. Swett, The role of aerosol absorption in determining the atmospheric ther-modynamic state during INDOEX, Eos Trans. AGU, 80 (46), Fall Meet. Suppl., F183, 1999.

Kinne S., and R. Pueschel, Aerosol radiative forcing for Asian continental outflow, Atmos. Environ., 35, 5019-5028, 2001.

Kirchner, F., F. Zabel, and K.H. Becker, Determination of the rate constant ratio for the reactions of acetylperoxy radical with NO and NO_2. Ber. Bunsenges. Phys. Chem., 94, 1379-1382, 1990.

Klemp, D., F. Flocke, F. Kramp, H.W. Pätz, A. Volz-Thomas, and D. Kley, Indications for biogenic sources in the vicinity of Schauinsland/Black Forest (TOR-station No. 11), Air Pollution Research Report 47 Editors: J. Slalina, G. Angeletti, and S. Beilke, Brüssel, 271-280, 1993.

Kley, D., H.G.J. Smit, H. Voemel, H. Grassl, V. Ramanathan, P.J. Crutzen, S. Williams, J. Meywerk, and S.J. Oltmans, Tropospheric Water Vapor and Ozone Cross Sections in a Zonal Plane Over the Central Equatorial Pacific. Quart. J. Roy. Met. Soc., 123, 2009-2040, 1997.

Koelemeijer, R.B.A., P. Stammes, J. W. Hovenier, and J. F. de Haan, A fast method for retrieval of cloud parameters using oxygen A-band measurements from the Global Ozone Monitoring Experiment, J. Geophys. Res., 106, 3475-3490, 2001.

Kondragunta, S., The impact of aerosols on urban photochemical ozone production, Ph.D. dissertation, Dept. of Chem., Univ. of Md., 230 pp., 1997.

Koppmann R., R. Brauers, F. J. Johen, C. Plass, and J. Rudolph, The distribution of light Non Methane Hydrocarbons over the Mid-Atlantic: Results of the Polarstern Cruise ANT VII/1, J. Atmos. Chem. 15, 215-234, 1992.

Kramp, F., D. Kley, and A. Volz-Thomas, Die Rolle reaktiver Kohlenwasserstoffe bei der Photooxidantienbildung in ländlichen Gebieten, Ein Beitrag zur Bilanzierung der photochemischen Ozonproduktion, Berichte des Forschungszentrums Jülich 3050, ISSN 0944-2952, FZ-Jülich GmbH, Zentralbibliothek, D-52425 Jülich, Germany, 1994.

Ladstätter-Weißenmayer, A., J.P. Burrows, P. Crutzen, and A. Richter, GOME: Biomass burning and its influence on the troposphere, in European Symposium on Atmospheric Measurements from Space, ESA WPP-161, Vol. 1, 369-374, 1999.

Lary, D., and J. Pyle, Diffuse radiation, twilight, and photochemistry – I, J. Atmos. Chem., 13, 373-392, 1991.

Le Bras, G., K.-H. Becker, R.A. Cox, R. Lesclaux, G. Moortgart, H.W. Sidebottom, and R. Zellner, LACTOZ: Laboratory Studies of Chemistry Related to Tropospheric Ozone, LACTOZ Annual Report 1993, EURUTRAC International Scientific Secreteriat, Garmisch-Patenkirchen, 1994.

Lefèvre, F., G. Brasseur, I. Folkins, and P. Simon, Chemistry of the 1991-1992 stratospheric winter: Three-dimensional model simulations, J. Geophys. Res., 99, 8153-8195, 1994.

Leighton, P.A., Photochemistry of Air Pollution, Academic Press, San Diego, Calif., 1961.

Lelieveld, J., P.J. Crutzen, V. Ramanathan, M.O. Andreae, C.A.M. Brenninkmeijer, T. Campos, G.R. Cass, R.R. Dickerson, H. Fischer, J.A. de Gouw, A. Hansel, A. Jefferson, D. Kley, A. T.J. de Laat, S. Lal, M.G. Lawrence, J.M. Lobert, O.L. Mayol-Bracero, A P. Mitra, T. Novakov, S.J. Oltmans, K.A. Prather, T. Reiner, H. Rodhe, H.A. Scheeren, D. Sikka, and J. Williams, The Indian Ocean Experiment: Widespread air pollution from South and Southeast Asia, Science, 291, 1031-1036, 2001.

Leue, C., M. Wenig, T. Wagner, O. Klimm, U. Platt, and B. Jahne, Quantitative analysis of NOx emissions from GOME satellite image sequences, J. Geophys. Res., 106, 5493-5505, 2001.

Levy, H., II, Normal atmosphere: large radical and formaldehyde concentrations predicted, Science, 173, 141-143, 1971.

Lewis, A.C., N. Carslaw, P.J. Marriott, R.M. Kinghorn, P. Morrison, A.L. Lee, K.D. Bartle, and M.J. Pilling, A larger pool of ozone-forming carbon compounds in urban atmospheres, Letters to Nature, Nature, 405, 778-781, 2000.

Liao, H., Y.L. Yung, and J.H. Seinfeld, Effects of aerosols on tropospheric photolysis rates in clear and cloudy atmospheres, J. Geophys. Res., 104, 23,697-23,707, 1999.

Lightfoot, P.D., R.A. Cox, J.N. Crowley, M. Destriau, G.D. Hayman, M.E. Jenkin, G.K. Moortgat, and F. Zabel, Organic peroxy radicals: Kinetics, spectroscopy and tropospheric chemistry, Atmos. Environ., 26A, 1805, 1992.

Liu, S.C., M. Trainer, M.A. Carroll, G. Hübler, D.D. Montzka, R.B. Norton, B.A. Ridley, J.G. Walega, E.L. Atlas, B.G. Heikes, B.J. Huebert, and W. Warren, A study of the photochemistry and ozone budget during the Mauna Loa Observatory Photochemistry Experiment, J. Geophys. Res., 97, 10,463-10,471, 1992.

Malm, W.C., J.F. Sisler, D. Huffman, R.A. Eldred, and T.A. Cahill, Spatial and seasonal trends in particle concentation and optical extinction in the United States, J. Geophys. Res., 99 (D1), 1347-1370, 1994.

Marston, G., C.D. McGill, and A.R. Rickard, Hydroxyl-radical formation in the gas-phase ozonolysis of 2-methylbut-2-ene, Geophys. Res. Lett., 25, 12, 2177-2180, 1998.

Mather, J.H., Peroxy radicals from photostationary state deviations and steady state calculations during the Tropospheric OH Photochemistry Experiment at Idaho Hill, Colorado, 1993, J. Geophys. Res., 102, D5, 6369, 1997.

Mather, J.H., P.S. Stevens, and W.H. Brune, OH and HO2 measurements using laser-induced fluorescence, J. Geophys. Res., 102, D5, 6427-6436, 1997.

McGill, C.D., A.R. Rickard, D. Johnson, and G. Marston, Product yields in the reactions of ozone with Z-but-2-ene, E- but-2-ene and 2-methylbut-2-ene. Chemosphere 38 (6), 1205-1212, 1999.

McKeen, S.A., and S.C. Liu, Hydrocarbon ratios and the photochemical history of air masses, Geophys. Res. Lett., 20, 2363-2366, 1993.

Meier, R., D. Anderson, and M. Nicolet, Radiation field in the troposphere and stratosphere from 240-1000 nm. General analysis, Planetary and Space Science, 30 (9), 923-933, 1982.

Meywerk, J., and V. Ramanathan, Observations of the spectral clear-sky aerosol forcing over the tropical Indian Ocean, J. Geophys. Res., 104, 24,359-24,370, 1999.

Meywerk, J., and V. Ramanathan, Influence of anthropogenic aerosols on the total and spectral irradiance at the sea surface during INDOEX 1999, J. Geophys. Res., revised, 2001.

Mihelcic, D., D. Klemp, P. Muesgen, H.W. Paetz, and A. Volz-Thomas, Simultaneous measurements of peroxy and nitrate radicals at Schauinsland, J. Atmos. Chem., 16, (4), 313-335, 1993.

Mihelcic, D., M Heitlinger, D. Kley, P. Musgen, and A. Volz-Thomas, Formation of hydroxyl and hydroperoxy radicals in the gas-phase ozonolysis of ethene, Chem. Phys. Lett., 301, (5-6), 559-564, 1999.

Mihelcic, D., K. Bächmann, A. Geyer, F. Holland, A. Hofzumahaus, P. Müsgen, H.W. Pätz, U. Platt, H.-J. Schäfer, S. Schlomski, T. Schmitz, S. Konrad, and A. Volz-Thomas, Peroxy radicals during BERLIOZ at Pabstthum: Measurements, radical budgets and ozone production, J. Geophys. Res., in press, 2003.

Mihele, C.M., and D.R. Hastie, The sensitivity of the radical amplifier to ambient water vapour, Geophys Res. Lett., 25, 1911-1913, 1998.

Mihele, C.M., M. Mozurkewich, and D.R. Hastie, Radical loss in a chain reaction of CO and NO in the presence of water: Implications for the radical amplifier and atmospheric chemistry, International J. Chem. Kin., 31, (2), 145-152, 1999.

Molina, M.J., and F.S. Rowland, Stratospheric sink for chlorofluoromethanes: Chlorine atom catalyzed destruction of ozone, Nature, 249, 810, 1974.

Moore, R. M., W. Groszko, and S.J. Niven, Ocean-atmosphere exchange of methyl chloride: results from NW Atlantic and Pacific Ocean studies, J. Geophys. Res., 101, 28,529-28,539, 1996.

Moortgart, G., B. Veyret, and R. Leslaux, Absorption Spectrum and Kinetics of Reactions of the Acetylperoxy Radical, J. Chem. Phys., 93, 2362-2368, 1989.

Mount, G.H., F.L. Eisele, D.J. Tanner, J.W. Brault, P.V. Johnston, J.W. Harder, E.J. Williams, A. Fried, and R. Shetter, An intercomparison of spectroscopic laser long-path and ion-assisted in situ measurements of hydroxyl concentrations during the Tropospheric OH Photochemistry Experiment, fall 1993, J. Geophys. Res., 102, D5, 6437, 1997.

Mühle, J., A. Zahn, C.A.M. Brenninkmeijer, V. Gros, and P.J. Crutzen, Air mass classification during the INDOEX R/V Ronald Brown cruise using measurements of non-methane hydrocarbons, CH_4, CO_2, CO, ^{14}CO, and $^{18}O(CO)$, J. Geophys. Res., 10, 2002.

Müller, J.F., Geographical Distribution and Seasonal Variation of Surface Emissions and Deposition Velocities of Atmospheric Trace Gases, J. Geophys. Res. 97, D4, 3787-3804, 1992.

Müller, R., T. Peter, P. Crutzen, H. Oelhaf, G. Adrian, T. v. Clarman, A. Wegner, U. Schmidt, and D. Lary, Chlorine chemistry and the potential for ozone depletion in the arctic stratosphere in the winter of 1991/92, Geophys. Res. Lett., 21, 1427-1430, 1994.

Müller, D., F. Wagner, U. Wandinger, A. Ansmann, M. Wendisch, D. Althausen, and W. v. Hoyningen-Huene, Microphysical particle parameters from extinction and backscatter lidar data by inversion with regularization: Experiment. Appl. Opt., 39, 1879-1892, 2000.

Neeb, P., F. Sauer, O. Horie, and G.K. Moortgat, Formation of hydroxymethyl hydroperoxide and formic acid in alkene ozonolysis in the presence of water vapour, Atmos. Environ., 31, 1417-1423, 1997.

Neusüß, C., T. Gnauk, A. Plewka, H. Herrmann, and P.K. Quinn, Carbonaceous aerosol over the Indian Ocean: OC/EC fractions and selected specifications from size-segregated samples taken onboard the R/V Ron Brown, J. Geophys. Res., 107 (D19), 2002.

NIST Chemical Kinetics Database, National Institute of Standards and Technology, U.S. Department of Commerce, Standard Reference Data, Gaithersburg, MD 20899, References therein, 1998.

Paluch, I., The entrainment mechanism in Colorado cumuli, J. Atmos. Sci., 36, 2467-2478, 1979.

Parrish, D.D., M. Trainer, E.J. Williams, D.W. Fahey, G. Hübler, C.S. Eubank, S.C. Liu, P.C. Murphy, D.L. Albritton, and F.C. Fehsenfeld, Measurements of the NO_x-O_3 photostationary state at Niwot Ridge, Colorado, J. Geophys. Res., 91, D5, 5361-5370, 1986.

Parrish, D.D., C.J. Hahn, E.J. Williams, R.B. Norton, F.C. Fehsenfeld, H.B. Singh, J.D. Shetter, B.W. Gandrud, and B.A. Ridley, Reply, J. Geophys. Res., 98, 8, 14,995-14,997, 1993.

Parsons, R.L., and R.R. Dickerson, NOAA Ship Ronald H. Brown: World global climate study, Sea Technology, 40, 39-45, 1999.

Paulson, S.E., and J.H. Seinfeld, Development and evaluation of a photooxidation mechanism for isoprene, J. Geophys. Res., 97, D18, 20,703-20,715, 1992.

Paulson, S.E., and J.J. Orlando, The reactions of ozone with alkenes: An important source of HO_x in the boundary layer. Geophys. Res. Lett., 23, 25, 3727-3730, 1996.

Paulson, S.E., A.D. Sen, P. Liu, J.D. Fenske, and M.J. Fox, Evidence for formation of OH radicals from the reaction of O_3 with alkenes in the gas phase, Geophys. Res. Lett. 24, (24), 3193-3196, 1997.

Peeters, J., J. Vertommen, and I. Langhans, Rate Constants of the Reactions of CF_3O_2, i-$C_3H_7O_2$ and t-$C_4H_9O_2$ with NO, Ber. Bunsenges. Phys. Chem., 96/3, 431-436, 1992.

Penndorf, R., Tables of the Refractive Index for Standard Air and the Rayleigh Scattering Coefficient for the Spectral Region Between 0.2 and 20.0, Microns

and their Application to Atmospheric Opt., J. Opt. Soc. Am., 47, 176-182, 1957.

Perner, D., T. Arnold, J. Crowley, T. Klüpfel, M. Martinez, and R. Seuwen, The measurement of active chlorine in the atmosphere by chemical amplification, J. Atmos. Chem., 34, 9-23, 1999.

Pfeiffer T., O. Forberich, and F.J. Comes, Tropospheric OH formation by ozonolysis of terpenes. Chem. Phys. Lett., 298, (4-6), 351-358, 1998.

Pierotti, D., S.C. Wolfsy, D. Jacob, and R.A. Rasmussen, Isoprene and its oxidation products: Methacrolein and methyl vinyl ketone, J. Geophys. Res., 95, 1871-1881, 1990.

Pio, C. T.V. Nunes, and A.R. Valente, Biogenic hydrocarbon emissions from vegetation in a Southern European environment, Proceedings of Eurotrac Symposium 96, pp.35-43 1996.

Platt, U., B. Alicke, R. Dubois, A. Geyer, A. Hofzumahaus, F. Holland, M. Martinez, D. Mihelcic, T. Klüpfel, B. Lohrmann, W. Pätz, D. Perner, F. Rohrer, J. Schäferm, and J. Stutz, Free Radicals and Fast Photochemistry during Berlioz, J. Atmos. Chem., 42, 359-394, 2002.

Poisson, N., M. Kanakidou, B. Bonsang, T. Behmann, J. Burrows, C. Gölz, H. Harder, A. Lewis, G.K. Moortgart, T. Nunes, C. Pio, U. Platt, F. Sauer, G. Schuster, P. Scakins, J. Senzig, R. Seuwen, D. Trapp, A. Voltz-Thomas, T. Zenker, and R. Zitzelberger, The impact of natural nonmethane hydrocarbon oxidation on the free radical and ozone budgets above a eucalyptus forest, Chemosphere-Global change science, 353-366, 2001.

Press, W.H., S.A. Teukolsky, W.T. Vetterling, and B.P. Flannery, Numerical Recipes in C: the art of scientific computing, Second Edition, Cambridge University Press, 1992.

Pszenny, A.A.P., W.C. Keene, D.J. Jacob, S. Fan, J.R. Maben, M.P. Zetwo, M. Springer-Young, and J.N. Galloway, Evidence of inorganic Cl gases other than hydrogen chloride in marine surface air, Geophys. Res. Lett., 20, 699-702, 1993.

Quinn, P.K., D.J. Coffman, T.S. Bates, T.L. Miller, J.E. Johnson, E.J. Welton, C. Neusüß, M. Miller, and P.J. Sheridan, Aerosol optical properties during INDOEX 1999: Means, variability, and controlling factors, J. Geophys. Res., 10.1029, 2000JD000037, 2002.

Ramanathan, V., P.J. Crutzen, J. Lelieveld, A.P. Mitra, D. Althausen, J. Anderson, M.O. Andreae, W. Cantrell, G.R. Cass, C.E. Chung, A.D. Clarke, J.A. Coakley, W.D. Collins, W.C. Conant, F. Dulac, J. Heintzenberg, A.J. Heymsfield, B. Holben, S. Howell, J. Hudson, A. Jayaraman, J.T. Kiehl, T.N. Krishnamurti, D. Lubin, G. McFarquhar, T. Novakov, J.A. Ogren, I.A. Podgorny, K. Prather, K. Priestley, J.M. Prospero, P.K. Quinn, K. Rajeev, P. Rasch, S. Rupert, R. Sadourny, S. K. Satheesh, G. E. Shaw, P. Sheridan, and F.P.J. Valero, Indian Ocean Experiment: An integrated analysis of the climate forcing and effects of the great Indo-Asian haze, J. Geophys. Res., 106, D22, 28,371-28,398, 2001.

Randriambelo, T., J.L. Baray, and S. Baldy, Effect of biomass burning, convective venting, and transport on tropospheric ozone over the Indian Ocean: Reunion Island field observations, J. Geophys. Res., 105, D9, 11,813-11,832, 2000.

Rasmussen, R.A., M.A. Khalil, R. Gunawarda, and S.D. Hoydt, Atmospheric methyl iodide (CH3I), J. Geophys. Res., 87, 3086–3090, 1982.

Ravishankara, A., Heterogeneous chemistry in the atmosphere: An assessment of current status, in: The Atmospheric Effects of Stratospheric Aircraft: A Fourth Program Report, NASA Reference Publication, 1359, 1995.

Ravishankara, A., Heterogeneous and multiphase chemistry in the troposphere, Science, 276, 1058-1065, 1997.

Reichert, L., Untersuchung des Wassereffektes eines Peroxyradikal-Detektors, M.S. thesis, University of Bremen, Germany, 2000.

Reichert, L., M.D. Andrés-Hernández, D. Stöbener, J. Burkert, and J.P. Burrows, Investigation of the effect of water complexes in the determination of peroxy radical ambient concentrations: implications for the atmosphere, J. Geophys. Res., 108, D1, 2003.

Reifenhäuser, W., and K.G. Heumann, Determination of methyl iodide in the Antarctic atmosphere and the south polar sea, Atmos. Environ., 26A, 2905-2912, 1992.

Renard, J.-B., M. Pirre, C. Robert, G. Moreau, D. Huguenin, and J. Russell III, Nocturnal vertical distribution of stratospheric O_3, NO_2, and NO_3 from balloon measurements, J. Geophys. Res., 101, 28,793-28,804, 1996.

Rhew, R. C., B.R. Miller, and R.F. Weiss, Natural methyl bromide and methyl chloride emissions from coastal salt marshes, Nature 403, 292, 2000.

Rhoads, K., P. Kelley, R.R. Dickerson, T.P. Carsey, M. Farmer, D. Savoie, and J. Prospero, The Composition of the Troposphere over the Indian Ocean during the Monsoonal Transition, J. Geophys. Res., 102, 18,981-18,995, 1997.

Richter, A., F. Wittrock, M. Eisinger, and J.P. Burrows, GOME Observations of Tropospheric BrO in Northern Hemispheric Spring and Summer 1997, Geophys. Res. Lett., 25, 2683-2686, 1998.

Ridley, B.A., S. Madronich, R.B. Chatfield, J.G. Walega, and R.E. Shetter, Measurements and model simulations of the photostationary state during the Mauna Loa observatory photochemistry experiment: implications for radical

concentrations and ozone production and loss rates, J. Geophys. Res., 97, D10, 10,375-10,388 1992.

Riehl, H., Tropical Meteorology, ch. II., ISBN: 163-234-832-624, 1954.

Roberts, J.M., The atmospheric chemistry of organic nitrates., Atmos. Environ., 24A/2, 243-287, 1990.

Rozanov, V., D. Diebel, R.J.D. Spurr, and J.P. Burrows, GOMETRAN: A radiative transfer model for the satellite project GOME - the plane parallel version, J. Geophys. Res., 102, 16,683, 1997.

Rozanov, V.V., T. Kurosu, and J.P. Burrows, Retrieval of atmospheric constituents in the UV-visible: A new quasi-analytical approach for the calculation of weighting functions, J. Quant. Spectrosc. Radiat. Transfer 60, 277-299, 1998.

Rudolph, J., and F.J. Johnen, Measurements of light atmospheric hydrocarbons over the Atlantic in regions of low biological activity, J. Geophys. Res. 95, 20,583ff, 1990.

Salisbury, G., P.S. Monks, S. Bauguitte, B.J. Bandy, and S.A. Penkett, A seasonal comparison of the ozone photochemistry in clean and polluted air masses at Mace Head, Ireland, J. Atmos. Chem., 41, 163-187, 2002.

Sander, R., and P.J. Crutzen, Model study indicating halogen activation and ozone destruction in polluted air masses transported to the sea, J. Geophys. Res., 101 (4), 9121-9138, 1996.

Sander, R., R. Vogt, G.W. Harris, and P.J. Crutzen, Modelling the chemistry of ozone, halogen compounds, and hydrocarbons in the arctic troposphere during spring, Tellus (b), 49 (5), 522-532, 1997.

Sauer, F., C. Schäfer, P. Neeb, O. Horie, and G.K. Moortgat, Formation of hydrogen peroxide in the ozonolysis of isoprene and simple alkenes under humid conditions, Atmos. Environ., 33, 229-241, 1999.

Sawada, S., and T. Totsuka, Natural and anthropogenic sources and fate of atmospheric ethylene, Atmos. Environ., 20, 821-832, 1986.

Schall, C., and Heumann, K. G., GC determination of volatile organoiodine and organobromine compounds in arctic seawater and air samples, Fres. J. Anal. Chem., 346, 717–722, 1993.

Scheeren, H.A., J. Lelieveld, J.A. de Gouw, C. van der Veen, and H. Fischer, Methyl chloride and other chlorocarbons in polluted air during INDOEX, accepted, J. Geophys. Res., 2002.

Schultz, M., M. Heitlinger, D. Mihelcic, and A. Volz-Thomas, A calibration source for peroxy radicals with built-in actinometry using H2O and O2 photolysis at 185nm, J. Geophys. Res., 100, D9, 18,811-18,816, 1995.

Schultz, M., D. Mihelcic, A. Volz-Thomas, and R. Schmitt, Die Bedeutung von Stickoxyden für die Ozonbilanz in Reinluftgebieten – Untersuchung der Photochemie in Reinluft anhand von Spurengasmessungen auf Teneriffa, Berichte des Forschungszentrum Jülich, Jül-3170, ISSN 0944-2952, 1996.

Sehested, J., and O.J. Nielsen, Absolute rate constants for the reaction of CF3O2 and CF3O radicals with NO at 295K, Chem. Phys. Lett., 206/1-4, 369, 1993.

Seinfeld, J.H., and S.N. Pandis, Atmospheric Chemistry and Physics: From Air Pollution to Climate Change, John Wiley & Sons, Inc., ISBN 0-471-17816-0, 1998.

Shah, J.J., J.G. Watson, J.A. Cooper, and J.J. Huntzicker, Aerosol chemical composition and light scattering in Portland, Oregon: the role of carbon, Atmos. Environ., 18, 235-240, 1984.

Shettle, E.P., and R.W. Fenn, Models of atmospheric aerosols and their optical properties, AGARD Conference Proceedings No. 183, ADA028-615, 1976.

Shi, J.C., and M.J. Bernhard, Kinetic studies of Cl-atom reactions with selected aromatic compounds using the photochemical reaction-FTIR spectroscopy technique, Int. J. Chem. Kinet., 29, 349-358, 1997.

Singh, H.B., and L.J. Salas, Measurement of selected light hydrocarbons over the Pacific Ocean: Latitudinal and seasonal variations, Geophys. Res. Lett., 9, 842-845, 1982.

Singh, H.B., L.J. Salas, and R.E. Stiles, Methyl halides in and over the eastern pacific (40°N–32°S), J. Geophys. Res., 88, 3684-3690, 1983.

Singh, H.B., D. Herlth, D. O´Hara, L. Salas, A.L. Torres, G.L. Gregory, G.W. Sachse, and J.F. Kasting, Atmospheric Peroxyacetyl Nitrate Measurements over the Brazilian Amazon Basin During the Wet Season: Relationships with Nitrogen Oxides and Ozone, J. Geophys. Res., 95, D10, 16,945-16954, 1990.

Singh, H.B., D. Herlth, D. O´Hara, K. Zahnle, J.D. Bradshaw, S.T. Sandholm, R. Talbot, P.J. Crutzen, and M. Kanakidou, Relationship of Peroxyacetyl Nitrate to Active and Total Odd Nitrogen at Northern High Latitudes: Influence of Reservoir Species on NO_x and O_3, J. Geophys. Res., 97, D15, 16,523-16,530, 1992.

Singh, H.B., D. Herlth, D. O´Hara, K. Zahnle, J.D. Bradshaw, S.T. Sandholm, and R. Talbot, Low ozone in the marine boundary layer of the tropical Pacific Ocean: Photochemical loss, chlorine atoms and entrainment, J. Geophys. Res., 101, (1), 1907-1917, 1996.

Smit, H.G.J., W. Sträter, D. Kley, and M.H. Profitt, The evaluation of ECC-ozone sondes under quasi flight conditions in the environmental simulation chamber at Jülich, in P.M. Borell et al. (eds.), Proceedings of Eurotrac symposium 1994, SPB Academic Publishing bv, The Hague, The Netherlands, 349-353, 1994.

Smit, H.G.J., and D. Kley, Jülich Ozone Sonde Intercomparison Experiment (JOSIE), WMO Global Atmosphere Watch report series, No. 130 (Technical Document No. 926), World Meteorological Organization, Geneva, 1998.

Smith, D.M., M.S. Akhter, J.A. Jassim, C.A. Sergides, W.F. Welch, and A.R. Chughtai, Studies of the structure and reactivity of soot, Aerosol Sci. Technol., 10, 311-325, 1989.

Sobolev, V., Light Scattering in Planetary Atmospheres, Pergamon Press Ltd., 1975.

Solomon, S., A. Schmeltekopf, and W. Sanders, On the interpretation of zenith sky absorption measurements, J. Geophys. Res., 92, 8311-8319, 1987.

Solomon, S., R.R. Garcia, and A.R. Ravishankara, On the role of iodine in ozone depletion, J. Geophys. Res., 99 D, 20,491-20,499, 1994.

Solomon, S., R. Portmann, R. Garcia, L. Thomason, L. Poole, and M. McCormick, The role of aerosol variations in anthropogenic ozone depletion at northern midlatitudes, J. Geophys. Res., 101, 6713-6727, 1996.

Spicer, C.W., E.G. Chapman, B.J. Finlayson-Pitts, R.A. Plastridge, J.M. Hubbe, J.D. Fast, and C.M. Berkowitz, First observations of Cl_2 and Br_2 in the marine troposphere, Nature, 394, 353, 1998.

Stamnes, K., S. Tsay, W. Wiscombe, and K. Jayaweera, Numerically stable algorithm for Discrete-Ordinate-Method: Radiative transfer in multiple

scattering and emitting layered media, Applied Optics, 27 (12), 2502-2509, 1988.

Stedman, D.H., J.G. Walega, C.A. Cantrell, J.P. Burrows, and G. Tyndall, Chemistry of multiphase atmospheric systems, NATO ASI Series G6, Springer Verlag, Berlin, 1986.

Stehr, J.W., W.P. Ball, R.R. Dickerson, B.G. Doddridge, C.A. Piety, and J.E. Johnson, Latitudinal gradients in O_3 and CO during INDOEX 1999, J. Geophys. Res., Atmosphere, 107 (D19), 8016, 2002.

Steil, B., M. Dameris, C. Brühl, P.J. Crutzen, V. Grewe, M. Ponater, and R. Sausen, Development of a chemistry module for GCMs: First results of a multiannual integration, Ann. Geophys., 16, 205-228, 1998.

Stevens, P.S., J.H. Mather, and W.H. Brune, Measurement of tropospheric OH and HO_2 by laser-induced fluorescence at low pressure, J. Geophys. Res., 99, D2, 3543-3557, 1994.

Stevens, P.S., J.H. Mather, W.H. Brune, F. Eisele, D. Tanner, A. Jefferson, C. Cantrell, R. Shetter, S. Sewall, A. Fried, B. Henry, E. Williams, K. Baumann, P. Goldan, and W. Kuster, HO_2/OH and RO_2/HO_2 ratios during the Tropospheric OH Photochemistry Experiment: Measurmement and theory, J. Geophys. Res., 102, D5, 6379, 1997.

Stöbener, D., Weiterentwicklung einer Peroxyradikalquelle für die Kallibration von RO_2-Messungen in Außenluft, Diplomarbeit, Universität Bremen, 1999.

Stull, R.B., An introduction to boundary layer meteorology, Kluwer Academic Publishers, ISBN 90-277-2769-4, 1988.

Tan, D., I. Faloona, J.B. Simpas, W. Brune, P.B. Shepson, T.L. Couch, A.L. Sumner, M.A. Carroll, T. Thornberry, E. Apel, D. Riemer, and W. Stockwell,

HO_x budgets in a deciduous forest: Results from the PROPHET summer 1998 campaign, J. Geophys. Res., 106, D20, 24,407, 2001.

Thomas, W., E. Hegels, S. Slijkhuis, R. Spurr, and K. Chance, Detection of biomass burning combustion products in Southeast Asia from backscatter data taken by the GOME spectrometer, Geophys. Res. Lett., 25, 1317-1320, 1998.

Thomson, A.M., and J.C. Witte, SHADOZ (Southern Hemisphere Additional Ozonesondes): A new ozonesonde dataset for the Earth Science Community, Earth Observer, 11 (4), 27-30, 1999.

Tie, X., G. Brasseur, X. Lin, P. Friedlingstein, C. Granier, and P. Rash, The impact of high altitude aircraft on the ozone layer in the stratosphere, J. Atmos. Chem., 18, 103-128, 1994.

Trainer, M., M.P. Buhr, C.M. Curran, F.C. Fehsenfeld, E.Y. Hsie, S.C. Liu, R.B. Norton, D.D. Parrish, E.J. Williams, B.W. Gandrud, B.A. Ridley, J.D. Shetter, E.J. Allwine, and H.H. Westberg, Observations and modeling of the reactive nitrogen photochemistry at a rural site, J. Geophys. Res., 96, D2, 3045-3063, 1991.

Trenberth, K.E., Climate System Modelling, Cambridge University Press, ISBN 0-521-43231-6, 1992.

Trentmann, J., Entwicklung eines photochemischen Atmosphärenmodells, Diplomarbeit, Universität Bremen, 1997.

Trijonis, J.C., Existing and natural background levels of visibility and fine particles in the rural East, Atmos. Environ., 16, 2431, 1982.

Troe, J., Specific rate constants k(E,J) for unimolecular bond fissions, J. Comput. Phys., 79, 6071 ff, 1983.

Velders, G.J.M., C. Granier, R.W. Portmann, K. Pfeilsticker, M. Wenig, T. Wagner, U. Platt, A. Richter, and J.P. Burrows, Global tropospheric NO_2 column distributions: Comparing 3-D model calculations with GOME measurements, J. Geophys. Res., 106, 12643-12660, 2001.

Vogt, R., P.J. Crutzen, and R. Sander, A mechanism for halogen release from sea salt aerosol in the remote marine boundary layer, Nature, 383 (6598), 327-330, 1996.

Vogt, R., R. Sander, R. von Gaslow, and P.J. Crutzen, Iodine Chemistry and its Role in Halogen Activation and Ozone Loss in the Marine Boundary Layer: A Model Study, J. Atmos. Chem., 32, 375-395, 1999.

Volz-Thomas, A., T. Behmann, P. Borrell, P.M. Borrell, J.P. Burrows, C.A. Cantrell, L.J. Carpenter, K.C. Clemitshaw, S. Gilge, M. Heitlinger, T. Kluepfel, D. Mihelcic, P. Muesgen, H.W. Paetz, S.A. Penkett, D. Perner, M. Schultz, R.E. Shetter, J. Slemr, and M. Weißenmayer, The PRICE (Peroxy Radical InterComparison Exercise), FA Jülich, Jül-3597, ISSN 0944-2952, 1998.

Wagner, T., and U. Platt, Satellite mapping of enhanced BrO concentrations in the troposphere. Nature, 395, 486-490, 1998.

Wagner, V., C. Schiller, and H. Fischer, Formaldehyde measurements in the marine boundary layer of the Indian Ocean during the 1999 INDOEX cruise of the RV Ronald H. Brown, submitted to J. Geophys. Res., 106, D22, 28,529-28,538, 2001.

Wagner, V., R. von Gaslow, H. Fischer, and P.J. Crutzen, Are CH_2O Measurements in the Marine Boundary Layer Suitable for Testing the Current Understanding of CH_4 Photooxidation?, 107 (3), 10.1029, 2001JD000722, 2002.

Wayne, R.P., I. Barnes, P. Biggs, J.P. Burrows, C.E. Canosa-Mas, J. Hjorth, G. Le Bras, G.K. Moortgat, D. Perner, G. Poulet, G. Restelli, and H. Sidebottom, The nitrate radical: Physics, chemistry and the Atmosphere, Air Pollution Research Report 31, Commission of the European Communities, 1990.

Wayne, R.P., Chemistry of Atmospheres, second edition, Oxford University Press, 1991a.

Wayne, R.P., I Barnes, P. Biggs, J.P. Burrows, C.E. Canosa-Mas, J. Hjorth, G. Le Bras, G.K. Moortgat, D. Perner, G. Poulet, G. Restelli, and H. Sidebottom, The nitrate radical: physics, chemistry and the atmosphere, Atmos. Environ., 25A, (1), 1-203, 1991b.

Weinstock, B., Carbon monoxide: Residence time in the atmosphere, Science 166, 224-225, 1969.

Weißenmayer, M., Peroxyradikalmessungen in der bodennahen Grenzschicht über dem Atlantik, Dissertation, Universität Mainz, 1994.

Weller, R., O. Schrems, A. Boddenberg, S. Gaeb, and M. Gautrois, Meridional distribution of hydroperoxides and formaldehyde in the boundary layer of the Atlantic (48°N-35°S) measured during the ALBATROSS campaign, J. Geophys. Res., 105, 14,401-14,412, 2000.

Welton, E.J., K.J. Voss, P.K. Quinn, P.J. Flatau, K. Markowicz, J.R. Campbell, J.D. Spinhirne, H.R. Gordon, and J.E. Johnson, Measurements of aerosol vertical profiles and optical properties during INDOEX 1999 using micro-pulse lidars, J. Geophys. Res., 10.1029, 2000JD000038, 2002.

Wendisch, M., T. Garrett, P.V. Hobbs, and J.W. Strapp, PVM-100A performance tests in the NASA and NRC wind tunnels, Preprints, 13th International Commission of Clouds and Precipitation, Reno, Nevada, 2000.

Williams, E.J., Hutchinson, G.L., Fehsenfeld, F.C., NO_x and N_2O emissions from soil, Global Biogeochem. Cycles 6/4, 351-388, 1992.

Winer, A. M., and H.W. Biermann, Long pathlength differential optical absorption spectroscopy (DOAS) Measurements of gaseous HONO, NO_2, and HCHO in the California South Coast Air Basin, Res. Chem. Intermed., 20, 423-445, 1994.

Wingenter, O.W., M.K. Kubo, N.J. Blake, T.W. Smith, D.R. Blake, and F.S. Rowland, Hydrocarbon and halocarbon measurements as photochemical and dynamical indicators of atmospheric hydroxyl, atomic chlorine and vertical mixing obtained during Lagrangian flights, J. Geophys. Res., 101 (2), 4331-4340, 1996.

Wisthaler, A., A. Hansel, R.R. Dickerson, and P.J. Crutzen, Organic trace gas measurements by PTR-MS during INDOEX 1999, J. Geophys. Res., 107 (D19), INX2 23-1 to INX2 23-11, 2001JD000576, 2002.

Wittrock, F., A. Richter, A. Ladstätter-Weißenmayer, and J.P. Burrows, Global Observations of Formaldehyde, in proceedings of the ERS-ENVISAT symposium, Gothenburg October 2000, ESA publication SP-461, 2000.

WMO, Scientific assessment of ozone depletion: 1994, Tech. Ber. Report No.37, World Meteorological Organization, Global Ozone Research an Monitoring Project, 1995.

Wolff, S., A. Boddenberg, J. Thamm, W. V. Turner, and S. Gäb, Gas-phase ozonolysis of ethane in the presence of carbonyl-oxide scavengers, Atmos. Environ., 31, 18, 2965-2969, 1997.

Yokouchi, Y., H.-J. Li, T. Machida, S. Aoki, and H. Akimoto, Isoprene in the marine boundary layer (Southeast Asian Sea, eastern Indian Ocean, Southern

Ocean): Comparison with dimethyl sulfide and bromoform, J. Geophys. Res., 104, D7, 8067-8076, 1999.

Yokouchi, Y., Y. Noijiri, L.A. Barrie, D. Toom-Sauntry, T. Machida, Y. Inuzuka, H. Akimoto, H.-J. Li, Y. Fujinuma, and S.A. Aoki, A strong source of methyl chloride to the atmosphere from tropical coastal land, Nature, 403, 295, 2000.

Zachariasse, M., P.F.J. van Velthoven, H.G.J. Smit, J. Lelieveld, T.K. Mandal, and H. Kelder, Influence of stratosphere-troposphere exchange on tropospheric ozone over the tropical Indian Ocean during the winter monsoon, J. Geophys. Res., 105, 15,403-15,416, 2000.

Acknowledgements

Foremost, I would like to thank my two advisors Prof. Dr. John Phillip Burrows and Prof. Dr. Russell R. Dickerson for their interest, support, and encouragement. Although, we rarely had the same opinion, but the numerous discussions with both John and Russ were of great benefit, hopefully not only for myself. The best thing I got to know was the fact that they always treated me with respect and never patronizing me. I am deeply indebted to Prof. John Phillip Burrows for giving me the opportunity from the beginning of my scientific career till now to be involved in so many national and international campaigns and to visit so many interesting international conferences. Many thanks to Prof. Dr. Russel R. Dickerson for inviting me to Maryland to discuss several issues and to get to know all the staff.

I also would like to thank Dr. Maria Dolores Andrés Hernández for many many fruitful discussions and for her encouragement. The most important thing I learned from her was bringing things to the end and being more disciplined.

I wish to thank Lars Reichert for helpful discussions and many experience which we made together during several campaigns.

I would like to thank my lovely girlfriend Birgit Behnke for her patience and her believing in me, giving me a big support.

Finally, I would like to thank my parents, Karla and Eckhard, and my grandparents Liselotte und Richard for their inexpressible love and support throughout my whole life. Everyone should have such a wonderful family, all my gratitude to you.

Ich liebe Euch.

Appendendix

Appendix 1

Derivation of $\frac{d[O_3]}{dt} = k_{\mathrm{NO+HO_2}}[\mathrm{NO}][\mathrm{HO_2}] + k_{\mathrm{NO+RO_2}}[\mathrm{NO}][\mathrm{RO_2}]$

In the lower troposphere the chemical reactions, which determine the amount of ozone are currently understood to be

$$NO + O_3 \rightarrow NO_2 + O_2, \mathrm{k_1}$$

$$\mathrm{NO_2} + \mathrm{h\nu}\left(\lambda < 420\ \mathrm{nm}\right) \rightarrow \mathrm{NO} + \mathrm{O}\left(^3\mathrm{P}\right), \mathrm{j_2}$$

$$\mathrm{O}\left(^3\mathrm{P}\right) + \mathrm{O_2} + \mathrm{M} \rightarrow \mathrm{O_3} + \mathrm{M}, \mathrm{k_3}$$

$$\mathrm{NO} + \mathrm{HO_2} \rightarrow \mathrm{NO_2} + \mathrm{OH}\ , \mathrm{k_4}$$

$$\mathrm{NO} + \mathrm{RO_2} \rightarrow \mathrm{NO_2} + \mathrm{RO}\ , \mathrm{k_5}$$

$$OH + O_3 \rightarrow HO_2 + O_2, \mathrm{k_6}$$

$$HO_2 + O_3 \rightarrow OH + 2 \cdot O_2, \mathrm{k_7}$$

$$O_3 + h\nu\left(l < 320nm\right) \rightarrow O\left(^1D\right) + O_2, \mathrm{j_8}$$

$$O\left(^1D\right) + H_2O \rightarrow OH + OH\ , \mathrm{k_9}$$

$$O\left(^1D\right) + N_2 \rightarrow O\left(^3P\right) + N_2, \mathrm{k_{10}}$$

$$O\left(^1D\right) + O_2 \rightarrow O\left(^3P\right) + O_2, \mathrm{k_{11}}$$

$$OH + NO_2 + M \rightarrow HNO_3 + M\ , \mathrm{k_{12}}$$

$$OH + CO \underset{M}{\rightleftharpoons} COOH\ , \mathrm{k_{13}}$$

$$COOH + O_2 \rightarrow HO_2 + CO_2, \mathrm{k_{14}}$$

$$OH + RH \rightarrow R + H_2O, \mathrm{k_{15}}$$

$$R + O_2 + M \rightarrow RO_2 + M\ , \mathrm{k_{16}}$$

$$RO + O_2 \rightarrow R_{-H}O + HO_2, \mathrm{k_{17}}$$

$$O\left(^3P\right) + NO_2 \rightarrow NO + O_2, \mathrm{k_{18}}$$

For simplicity reasons the reactions of O_3 with alkenes and other likely important reactions of VOC are negelcted.

Unlike in the troposphere the concentration of O atoms is sufficiently small that reaction 18 is of negligible importance in the troposphere. The time dependent variation of O_3, $O(^3P)$, and $O(^1D)$ is therefore given by

$$\frac{d[O_3]}{dt} = k_3\left[O\left(^3P\right)\right][O_2][M] - k_1[NO][O_3] - k_6[OH][O_3] - k_7[HO_2][O_3] - j_8[O_3], \text{ eq. 1}$$

$$\frac{d\left[O\left(^3P\right)\right]}{dt} = j_2[NO_2] + k_{10}\left[O\left(^1D\right)\right][N_2] + k_{11}\left[O\left(^1D\right)\right][O_2] - k_3\left[O\left(^3P\right)\right][O_2][M], \text{ eq. 2}$$

$$\frac{d\left[O\left(^1D\right)\right]}{dt} = j_8[O_3] - k_{10}\left[O\left(^1D\right)\right][N_2] - k_{11}\left[O\left(^1D\right)\right][O_2] - k_9\left[O\left(^1D\right)\right][H_2O], \text{ eq. 3.}$$

Assuming that the reactive oxygen atoms achieve a stationary state i.e. $\frac{d\left[O\left(^3P\right)\right]}{dt} = 0$, and $\frac{d\left[O\left(^1D\right)\right]}{dt} = 0$ yields,

$$k_3\left[O\left(^3P\right)\right][O_2][M] = j_2[NO_2] + k_{10}\left[O\left(^1D\right)\right][N_2] + k_{11}\left[O\left(^1D\right)\right][O_2], \text{ eq. 5}$$

$$k_{10}\left[O\left(^1D\right)\right][N_2] + k_{11}\left[O\left(^1D\right)\right][O_2] = j_8[O_3] - k_9\left[O\left(^1D\right)\right][H_2O], \text{ eq. 6}$$

Substituting eq 5 and 6 into the rate of formation of O_3 yields the following:

$$\frac{d[O_3]}{dt} = j_2[NO_2] + k_{10}\left[O\left(^1D\right)\right][N_2] + k_{11}\left[O\left(^1D\right)\right][O_2] - k_1[NO][O_3] - k_6[OH][O_3] - k_7[HO_2][O_3] - j_8[O_3], \text{ eq. 7}$$

$$\frac{d[O_3]}{dt} = j_2[NO_2] + j_8[O_3] - k_9\left[O\left(^1D\right)\right][H_2O] - k_1[NO][O_3] - k_6[OH][O_3] - k_7[HO_2][O_3] - j_8[O_3], \text{ eq. 8}$$

$$\frac{d[O_3]}{dt} = j_2[NO_2] - k_9\left[O\left(^1D\right)\right][H_2O] - k_1[NO][O_3] - k_6[OH][O_3] - k_7[HO_2][O_3], \text{ eq. 9}$$

where $k_9\left[\mathrm{O}\left(^1D\right)\right][\mathrm{H_2}O]$ is the amount of $\mathrm{O}\left(^1D\right)$ which produces OH radicals.

Assuming further, that NO_2 achieves a stationary state i.e. $\frac{d[NO_2]}{dt}=0$,

$$\frac{d[NO_2]}{dt}=k_1[\mathrm{NO}][\mathrm{O_3}]+k_4[\mathrm{NO}][\mathrm{HO_2}]+k_5[\mathrm{NO}][\mathrm{RO_2}] - j_2[NO_2]-k_{12}[OH][NO_2][M] \quad \text{, eq. 10}$$

then

$$j_2[NO_2]=k_1[\mathrm{NO}][\mathrm{O_3}]+k_4[\mathrm{NO}][\mathrm{HO_2}]+k_5[\mathrm{NO}][\mathrm{RO_2}]-k_{12}[OH][NO_2][M], \text{ eq. 11.}$$

Including equation eq. 11 into equation eq. 9 results in:

$$\frac{d[O_3]}{dt}=k_1[\mathrm{NO}][\mathrm{O_3}]+k_4[\mathrm{NO}][\mathrm{HO_2}]+k_5[\mathrm{NO}][\mathrm{RO_2}]-k_{12}[OH][NO_2][M] -k_9\left[\mathrm{O}\left(^1D\right)\right][\mathrm{H_2}O]-k_1[\mathrm{NO}][\mathrm{O_3}]-k_6[\mathrm{OH}][\mathrm{O_3}]-k_7[\mathrm{HO_2}][\mathrm{O_3}] \quad \text{, eq. 12}$$

$$\frac{d[O_3]}{dt}=k_4[\mathrm{NO}][\mathrm{HO_2}]+k_5[\mathrm{NO}][\mathrm{RO_2}]-k_{12}[OH][NO_2][M] -k_9\left[\mathrm{O}\left(^1D\right)\right][\mathrm{H_2}O]-k_6[\mathrm{OH}][\mathrm{O_3}]-k_7[\mathrm{HO_2}][\mathrm{O_3}] \quad \text{, eq. 13}$$

but

$$\left[O\left(^1D\right)\right]=\frac{j_8[O_3]}{k_{10}[N_2]+k_{11}[O_2]+k_9[H_2O]}$$

thus

$$\frac{d[O_3]}{dt}=k_4[\mathrm{NO}][\mathrm{HO_2}]+k_5[\mathrm{NO}][\mathrm{RO_2}]-k_{12}[OH][NO_2][M] -\frac{j_8[O_3]k_9[\mathrm{H_2}O]}{k_{10}[N_2]+k_{11}[O_2]+k_9[H_2O]}-k_6[\mathrm{OH}][\mathrm{O_3}]-k_7[\mathrm{HO_2}][\mathrm{O_3}]$$

Finally, shows that the production O_3 is given by

$$k_4[\mathrm{NO}][\mathrm{HO_2}] + k_5[\mathrm{NO}][\mathrm{RO_2}]$$

In the above analysis, the following processes have not been taken into consideration

a) additional chemical loss e.g. the potential reaction of halogen atoms with O_3

b) the physical processes such as, the deposition of O_3, advection in and out of the region and entrainment from above.

Appendix 2

The following figures show the hierachic structure of the BRAPHO and PHOTOST model. In addition the available reactions are shown which are separated into bimolecular, termolecular, and photolysis reactions.

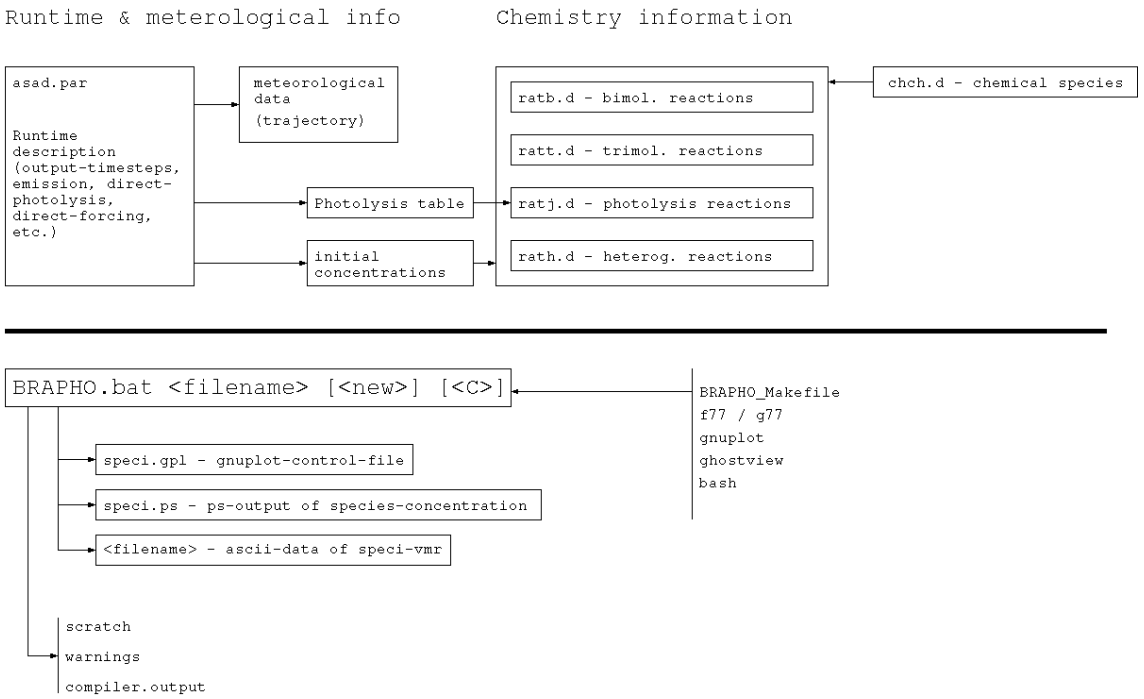

Appendix figure 1: Overview of the BRAPHO model concept.

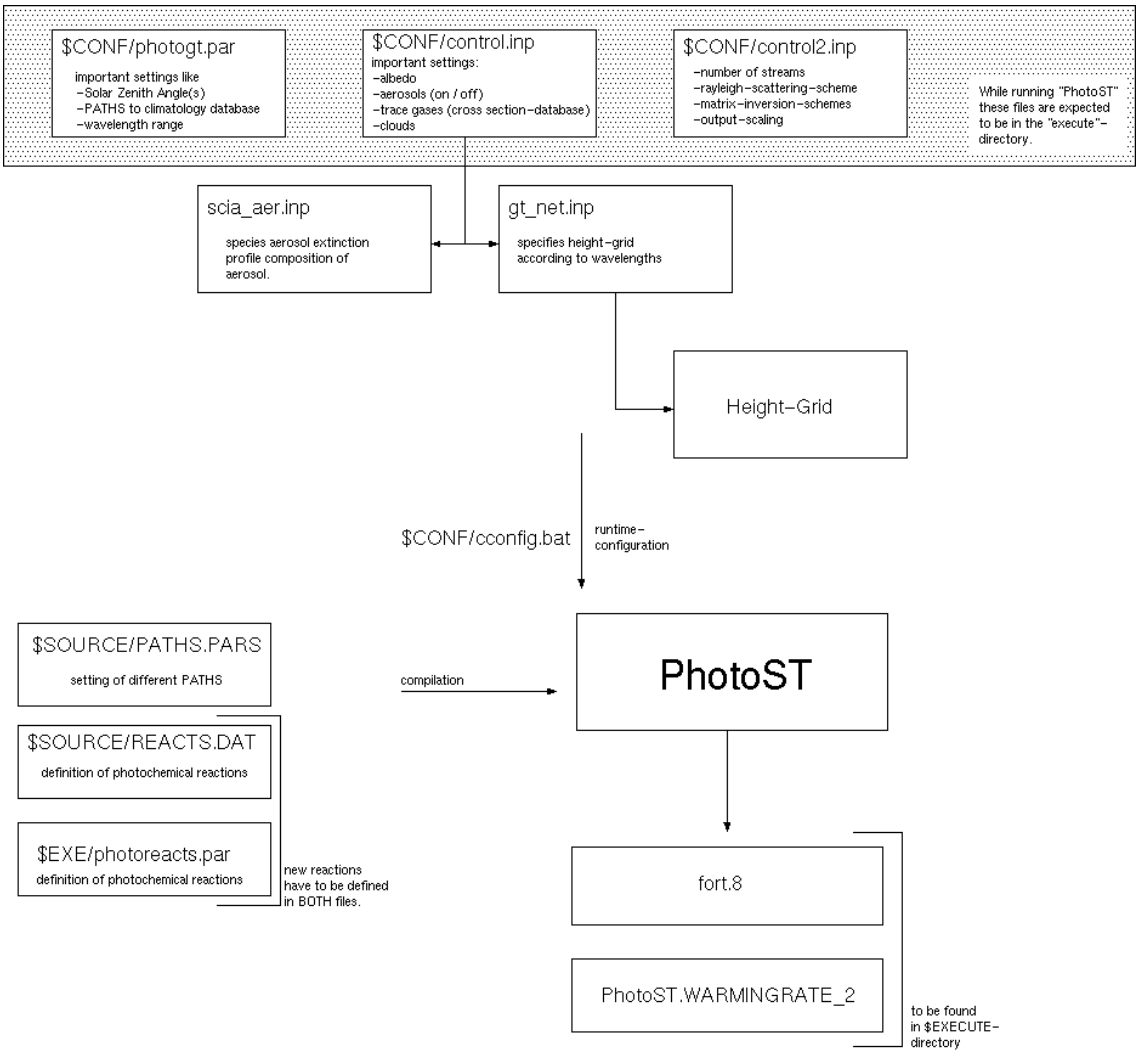

Appendix figure 2: Overview of the PHOTOST model concept.

```
# BIMOLECULAR REACTIONS - MASTER RATEFILE
# JPL 1997
# Master Rate File: Joern Burkert 04.07.00. All reactions are from both jpl97
# and Asad bimol.d original. The reactions with a 7 in front are pathways from
# IUPAC (ASAD). L+reaction is used to get a feeling for the importance of this
# reaction.
# Chemical Kinetics and Photochemical Data for Use in Stratospheric Modeling
    1 O(3P)      O3         O2         O2                  8.00E-12  0.00   2060.0
    2 O(1D)      O2         O(3P)      O2                  3.20E-11  0.00    -70.0
    3 O(1D)      O3         O2         O2                  1.20E-10  0.00      0.0
    4 O(1D)      O3         O2         O(3P)      O(3P)    1.20E-10  0.00      0.0
    5 O(1D)      H2         OH         H                   1.10E-10  0.00      0.0   JPL97
    6 O(1D)      H2O        OH         OH                  2.20E-10  0.00      0.0
    7 O(1D)      N2         O(3P)      N2                  1.80E-11  0.00   -110.0
    8 O(1D)      N2O        N2         O2                  4.90E-11  0.00      0.0
    9 O(1D)      N2O        NO         NO                  6.70E-11  0.00      0.0
   10 O(1D)      NH3        OH         NH2                 2.50E-10  0.00      0.0
   11 O(1D)      CO2        O(3P)      CO2                 7.40E-11  0.00   -120.0
   12 O(1D)      CH4        OH         CH3                 1.35E-10  0.00      0.0   Joern(NIST,mehrere Pfade)
  712 O(1D)      CH4        CH2O       H2                  1.50E-11  0.00      0.0   Joern(NIST,mehrere Pfade)
   13 O(1D)      HCl        O(3P)      HCl                 1.40E-11  0.00      0.0
  713 O(1D)      HCl        H          ClO                 3.60E-11  0.00      0.0
 7713 O(1D)      HCl        OH         Cl                  1.00E-10  0.00      0.0
   14 O(1D)      HF         OH         F                   5.00E-11  0.00      0.0
  714 O(1D)      HF         O(3P)      HF                  5.00E-11  0.00      0.0
   15 O(1D)      HBr        HBr        O(3P)               3.00E-11  0.00      0.0  Joern(?)
  715 O(1D)      HBr        Br         OH                  1.20E-10  0.00      0.0  Joern(?)
   16 O(1D)      Cl2        Cl2        O(3P)               7.00E-11  0.00      0.0
  716 O(1D)      Cl2        ClO        Cl                  2.10E-10  0.00      0.0
   17 O(1D)      CCl2O      ?          ?                   3.60E-10  0.00      0.0
   18 O(1D)      CClFO      ?          ?                   1.90E-10  0.00      0.0
   19 O(1D)      CF2O       CO2        F2                  2.20E-11  0.00      0.0
  719 O(1D)      CF2O       CF2O       O(3P)               5.20E-11  0.00      0.0
   20 O(1D)      CCl4       ?          ?                   3.30E-10  0.00      0.0  (CFC-10)
   21 O(1D)      CH3Br      O(3P)      CH3Br               1.80E-10  0.00      0.0  Joern(?)
   22 O(1D)      CH2Br2     ?          ?                   2.70E-10  0.00      0.0
   23 O(1D)      CHBr3      ?          ?                   6.60E-10  0.00      0.0
   24 O(1D)      CH3F       ?          ?                   1.50E-10  0.00      0.0  (HFC-41)
   25 O(1D)      CH2F2      ?          ?                   5.10E-11  0.00      0.0  (HFC-32)
   26 O(1D)      CHF3       ?          ?                   9.10E-12  0.00      0.0  (HFC-23)
   27 O(1D)      CHCl2F     ?          ?                   1.90E-10  0.00      0.0  (HCFC-21)
   28 O(1D)      CHClF2     ?          ?                   1.00E-10  0.00      0.0  (HCFC-22)
   29 O(1D)      CCl3F      ?          ?                   2.30E-10  0.00      0.0  (CFC-11)
   30 O(1D)      CCl2F2     ?          ?                   1.40E-10  0.00      0.0  (CFC-12)
   31 O(1D)      CClF3      ?          ?                   8.70E-11  0.00      0.0  (CFC-13)
   32 O(1D)      CClBrF2    ?          ?                   1.50E-10  0.00      0.0  (Halon-1211)
   33 O(1D)      CBr2F2     ?          ?                   2.20E-10  0.00      0.0  (Halon-1202)
   34 O(1D)      CBrF3      ?          ?                   1.00E-10  0.00      0.0  (Halon-1301)
   35 O(1D)      CF4        CF4        O(3P)               2.00E-14  0.00      0.0  (CFC-14)
   36 O(1D)      H161       ?          ?                   2.60E-10  0.00      0.0  (HFC-161)
   37 O(1D)      H152d      ?          ?                   2.00E-10  0.00      0.0  (HFC-152a),  CH3CHF2
   38 O(1D)      H1412m     ?          ?                   2.60E-10  0.00      0.0  (HCFC-141b), CH3CCl2F
   39 O(1D)      H1421d     ?          ?                   2.20E-10  0.00      0.0  (HCFC142b), CH3CClF2
   40 O(1D)      H143t      ?          ?                   1.00E-10  0.00      0.0  (HFC-143a), CH3CF3
   41 O(1D)      H1322d     ?          ?                   1.60E-10  0.00      0.0  (HCFC-132b), CH2ClCClF2
   42 O(1D)      H1331t     ?          ?                   1.20E-10  0.00      0.0  (HCFC-133a), CH2ClCF3
   43 O(1D)      H134t      ?          ?                   4.90E-11  0.00      0.0  (HFC-134a) , CH2FCF3
   44 O(1D)      H1232t     ?          ?                   2.00E-10  0.00      0.0  (HCFC-123) , CHCl2CF3
   45 O(1D)      H1241t     ?          ?                   8.60E-11  0.00      0.0  (HCFC-124) , CHClFCF3
   46 O(1D)      H125       ?          ?                   1.20E-10  0.00      0.0  (HCFC-125) , CHF2CF3
   47 O(1D)      H1133t     ?          ?                   2.00E-10  0.00      0.0  (CFC-113a) , CCl3CF3
   48 O(1D)      H1133d     ?          ?                   2.00E-10  0.00      0.0  (CFC-113)  , CCl2FCClF2
   49 O(1D)      H1142t     ?          ?                   1.00E-10  0.00      0.0  (CFC-114a) , CCl2FCF3
   50 O(1D)      H1142d     ?          ?                   1.30E-10  0.00      0.0  (CFC-114)  , CClF2CClF2
   51 O(1D)      H1151t     ?          ?                   5.00E-11  0.00      0.0  (CFC-115)  , CClF2CF3
   52 O(1D)      H11402d    ?          ?                   1.60E-10  0.00      0.0  (Halon-2402), CBrF2CBrF2
   53 O(1D)      H116       O(3P)      R116t               1.50E-13  0.00      0.0  (CFC-116)   , CF3CF3
   54 O(1D)      H338d      ?          ?                   1.80E-11  0.00      0.0  (HFC-338pcc), CHF2CF2CF2CHF2
   55 O(1D)      C4F8       ?          ?                   8.00E-13  0.00      0.0  c-C4F8
   56 O(1D)      H43-10t    ?          ?                   2.10E-10  0.00      0.0  (HFC-43-10mee),CF3CHFCHFCF2CF3
   57 O(1D)      C5F12      ?          ?                   3.90E-13  0.00      0.0  (CFC-41-12)
   58 O(1D)      C6F14      ?          ?                   1.00E-12  0.00      0.0  (CFC-51-14)
   59 O(1D)      C4F6       ?          ?                   2.80E-13  0.00      0.0  1,2-(CF3)2c-C4F6
   60 O(1D)      SF6        ?          ?                   1.80E-14  0.00      0.0
   61 O2(1D)     O(3P)      ?          ?                   2.00E-16  0.00      0.0  U
   62 O2(1D)     O2         ?          ?                   3.60E-18  0.00    220.0
   63 O2(1D)     O3         O(3P)      2O2                 5.20E-11  0.00   2840.0
   64 O2(1D)     H2O        ?          ?                   4.80E-18  0.00      0.0
   65 O2(1D)     N          NO         O(3P)               9.00E-17  0.00      0.0  U
   66 O2(1D)     N2         ?          ?                   1.00E-20  0.00      0.0  U
   67 O2(1D)     CO2        ?          ?                   2.00E-20  0.00      0.0  U
   68 O2(1S)     O(3P)      ?          ?                   8.00E-14  0.00      0.0
   69 O2(1S)     O2         ?          ?                   3.90E-17  0.00      0.0
   70 O2(1S)     O3         ?          ?                   2.20E-11  0.00      0.0
   71 O2(1S)     H2O        ?          ?                   5.40E-12  0.00      0.0
   72 O2(1S)     N          ?          ?                   1.00E-13  0.00      0.0  U
   73 O2(1S)     N2         ?          ?                   2.10E-15  0.00      0.0
   74 O2(1S)     CO2        ?          ?                   4.20E-13  0.00      0.0
   75 O(3P)      OH         O2         H                   2.20E-11  0.00   -120.0
   76 O(3P)      HO2        OH         O2                  3.00E-11  0.00   -200.0
   77 O(3P)      H2O2       OH         HO2                 1.40E-12  0.00   2000.0
   78 H          O3         OH         O2                  1.40E-10  0.00    470.0
   79 H          HO2        OH         OH                  7.20E-11  0.00      0.0  Joern(zu 90%)
  779 H          HO2        H2         O2                  8.10E-11  0.00      0.0  Joern(zu 90%)
 7779 H          HO2        H2O        O(3P)               2.40E-12  0.00      0.0  Joern(zu 90%)
   80 OH         O3         HO2        O2                  1.60E-12  0.00    940.0
   81 OH         H2         H2O        H                   5.50E-12  0.00   2000.0
   82 OH         HD         ?          ?                   5.00E-12  0.00   2130.0  JPL97
   83 OH         OH         H2O        O(3P)               4.20E-12  0.00    240.0
   84 OH         HO2        H2O        O2                  4.80E-11  0.00   -250.0
```

85	OH	H2O2	H2O	HO2		2.90E-12	0.00	160.0	
86	HO2	O3	OH	O2	O2	1.10E-14	0.00	500.0	
87	HO2	HO2	H2O2	O2		2.30E-13	0.00	-600.0	D1
88	O(3P)	NO2	NO	O2		6.50E-12	0.00	-120.0	
89	O(3P)	NO3	O2	NO2		1.00E-11	0.00	0.0	
90	O(3P)	N2O5	Lo3pn2o5			3.00E-16	0.00	0.0	U
91	O(3P)	HONO2	OH	NO3		3.00E-17	0.00	0.0	U
92	O(3P)	HO2NO2	Lo3pho2no2			7.80E-11	0.00	3400.0	
93	H	NO2	OH	NO		4.00E-10	0.00	340.0	
94	OH	NO3	HO2	NO2		2.20E-11	0.00	0.0	Joern
95	OH	HONO	H2O	NO2		1.80E-11	0.00	390.0	
96	OH	HONO2	H2O	NO3		1.50E-13	0.00	0.0	P2
97	OH	HO2NO2	Lohho2no2			1.30E-12	0.00	-380.0	JPL97
98	OH	NH3	H2O	NH2		1.70E-12	0.00	710.0	
99	HO2	NO	NO2	OH		3.50E-12	0.00	-250.0	JPL97
799	HO2	NO2	HONO	O2		5.00E-16	0.00	0.0	U JPL97
100	HO2	NO3	O2	HNO3		2.00E-12	0.00	0.0	Joern NIST
9100	HO2	NO3	OH	NO2	O2	2.00E-12	0.00	0.0	Joern NIST
101	HO2	NH2	Lho2nh2			3.40E-11	0.00	0.0	
102	N	O2	NO	O(3P)		1.50E-11	0.00	3600.0	
103	N	O3	NO	O2		2.00E-16	0.00	0.0	U
104	N	NO	N2	O(3P)		2.10E-11	0.00	-100.0	
105	N	NO2	N2O	O(3P)		5.80E-12	0.00	-220.0	
106	NO	O3	NO2	O2		2.00E-12	0.00	1400.0	
107	NO	NO3	NO2	NO2		1.50E-11	0.00	-170.0	
108	NO2	O3	NO3	O2		1.20E-13	0.00	2450.0	
109	NO2	NO3	NO	NO2	O2	4.50E-14	0.00	1260.0	b5
110	NO3	NO3	NO2	NO2	O2	8.50E-13	0.00	2450.0	
111	NH2	O2	?	?		6.00E-21	0.00	0.0	U
112	NH2	O3	?	?		4.30E-12	0.00	930.0	
113	NH2	NO	?	?		4.00E-12	0.00	-450.0	JPL97
114	NH2	NO2	?	?		2.10E-12	0.00	-650.0	
115	NH	NO	?	?		4.90E-11	0.00	0.0	
116	NH	NO2	?	?		3.50E-13	0.00	-1140.0	
117	O3	HONO	O2	HONO2		5.00E-19	0.00	0.0	U
118	N2O5	H2O	HONO2	HONO2		2.00E-21	0.00	0.0	U
119	N2(A,v)	O2	?	?		2.50E-12	0.00	0.0	
120	N2(A,v)	O3	?	?		4.10E-11	0.00	0.0	
121	O(3P)	CH3	CH2O	H		1.40E-10	0.00	0.0	Joern NIST
122	O(3P)	HCN	Lo3phcn			1.00E-11	0.00	4000.0	
123	O(3P)	C2H2	Lo3pc2h2			3.00E-11	0.00	1600.0	
124	O(3P)	CH2O	OH	HCO		3.40E-11	0.00	1600.0	JoernNISTJPL97
125	O(3P)	MeCHO	MeCO	OH		1.80E-11	0.00	1100.0	
126	O3	C2H2	CO2	CH2O		1.00E-14	0.00	4100.0	***
127	O3	C2H4	CH2O	CH2OO		1.20E-14	0.00	2630.0	***
128	O3	C3H6	CH2O	C2H4OO		6.50E-15	0.00	1900.0	***
129	OH	CO	CO2	H		1.50E-13	0.00	0.0	P1
130	OH	CH4	CH3	H2O		2.80E-14	0.00	1575.0	JPL97 D10
131	OH	MeD	?	?		3.50E-12	0.00	1950.0	
132	OH	CH2O	H2O	HCO		1.00E-11	0.00	0.0	
133	OH	MeOH	CH2OH	H2O		2.80E-12	0.00	360.0	Joern NIST
7133	OH	MeOH	MeO	H2O		5.00E-13	0.00	360.0	Joern NIST
134	OH	MeOOH	H2O	CH2OOH		1.00E-12	0.00	-190.0	Joern NIST
9134	OH	MeOOH	H2O	MeOO		1.90E-12	0.00	-190.0	Joern NIST
135	OH	HC(O)OH	?	?		4.00E-13	0.00	0.0	
136	OH	HCN	?	?		1.20E-13	0.00	400.0	
138	OH	C3H8	H2O	Pr		1.00E-11	0.00	660.0	
139	OH	MeCHO	MeCO	H2O		5.60E-12	0.00	-270.0	JPL97
141	OH	MeC(O)OH	H2O	MeCOO		4.00E-13	0.00	-200.0	
7141	OH	MeC(O)Me	MeC(O)CH2	H2O		2.20E-12	0.00	685.0	JPL97
142	OH	MeCN	?	?		7.80E-13	0.00	1050.0	
7142	OH	MeONO2	?	?		5.00E-13	0.00	890.0	JPL97
143	OH	MeC(O)O2NO2	?	?		4.00E-14	0.00	0.0	U
7143	OH	C2H5ONO2	?	?		8.20E-13	0.00	450.0	JPL97
144	HO2	CH2O	HOCH2OO			9.71E-15	0.00	-625.0	Joern NIST
145	HO2	MeOO	MeOOH	O2		3.80E-13	0.00	-800.0	
147	HO2	MeC(O)O2	O2	MeC(O)O2H		1.30E-13	0.00	-1000.0	
7147	HO2	MeC(O)O2	O3	MeCOOH		3.00E-13	0.00	-1000.0	
148	NO3	CO	NO2	CO2		4.00E-19	0.00	0.0	JOERN(?)U
149	NO3	CH2O	HNO3	HCO		5.80E-16	0.00	0.0	Joern(?)
150	NO3	MeCHO	?	?		1.40E-12	0.00	1900.0	
151	CH3	O2	MeOO			3.00E-16	0.00	0.0	U,***
152	CH3	O3	MeO	O2		5.10E-12	0.00	210.0	Joern NIST
153	HCO	O2	CO	HO2		3.50E-12	0.00	-140.0	
154	CH2OH	O2	CH2O	HO2		9.10E-12	0.00	0.0	
155	MeO	O2	CH2O	HO2		3.90E-14	0.00	900.0	
7155	MeO	NO2	CH2O	HONO		1.10D-11	0.00	1200.0	JPL97
156	MeOO	O3	MeO	O2	O2	1.00E-17	0.00	0.0	Joern NIST
157	MeOO	MeOO	MeO	MeO	O2	7.50E-14	0.00	-190.0	b3
158	MeOO	MeOO	MeOH	CH2O	O2	1.50E-13	0.00	-190.0	b3
159	MeOO	MeOO	MeOOMe	O2		2.50E-14	0.00	-190.0	b3
160	MeOO	MeOO	MeOOH	CH2O2		0.00E-00	0.00	-190.0	b3
161	MeOO	NO	MeO	NO2		4.20E-12	0.00	-180.0	
162	MeOO	MeC(O)O2	MeO	MeCO2		5.50E-12	0.00	-640.0	JPL97
7162	MeOO	MeC(O)O2	MeCO2H	CH2O		5.50E-12	0.00	-640.0	JPL97
167	MeC(O)O2	MeC(O)O2	?	?		2.90E-12	0.00	-500.0	JPL97
168	MeC(O)O2	NO	NO2	MeCOO		5.30E-12	0.00	-360.0	JPL97,***
169	O(3P)	FO	F	O2		2.70E-11	0.00	0.0	
170	O(3P)	FO2	FO	O2		5.00E-11	0.00	0.0	
171	OH	CH3F	CH2F	H2O		3.00E-12	0.00	1500.0	(HFC-41)
172	OH	CH2F2	CHF2	H2O		1.90E-12	0.00	1550.0	(HFC-32)
173	OH	CHF3	CF3	H2O		1.00E-12	0.00	2440.0	(HFC-23)
7173	OH	CF3OH	CF3O	H2O		2.00E-17	0.00	0.0	U JPL97
174	OH	H161	?	?		7.00E-12	0.00	1100.0	(HFC-161)
175	OH	H152d	?	?		2.40E-12	0.00	1260.0	(HFC-152a), CH3CHF2
176	OH	H152m	R142m	H2O		1.70E-11	0.00	1500.0	(HFC-152) , CH2FCH2F
177	OH	H143t	R133t	H2O		1.60E-12	0.00	2100.0	(HFC-143a), CH3CF3
178	OH	H143d	?	?		4.00E-12	0.00	1650.0	(HFC-143) , CH2FCHF2
179	OH	H134t	R124t	H2O		1.50E-12	0.00	1750.0	(HFC-134a), CH2FCF3
180	OH	H134d	R124d	H2O		1.60E-12	0.00	1680.0	(HFC-134) , CHF2CHF2

181	OH	H125t	R115	H2O		5.60E-13	0.00	1700.0	(HFC-125) , CHF2CF3
182	OH	CF2HOCF2H	CF2OCF2H	H2O		1.90E-12	0.00	2000.0	(HFOC-134E), JPL97
183	OH	CF3OCHF2	CF3OCF2	H2O		4.70E-13	0.00	2100.0	(HFOC-125E)
184	OH	H245d	?	?		2.40E-12	0.00	1660.0	(HFC-245ca) , CH2FCF2CHF2
185	OH	H236m	R226m	H2O		1.50E-12	0.00	1750.0	(HFC-236cb) , CF3CF2CH2F
186	OH	H236d	?	?		1.10E-12	0.00	1590.0	(HFC-236ea) , CF3CHFCHF2, JPL97
187	OH	H236t	R226t	H2O		1.30E-12	0.00	2480.0	(HFC-236fa) , CF3CH2CF3, JPL97
188	OH	H227t	R217t	H2O		5.00E-13	0.00	1700.0	(HFC-227ea) , CF3CHFCF3
189	OH	H356t	?	?		3.00E-12	0.00	1800.0	(HFC-356mff), CF3CH2CH2CF3, JPL97
190	OH	H338d	?	?		7.80E-13	0.00	1530.0	(HFC-338pcc), CHF2CF2CF2CF2H
191	OH	H43-10t	?	?		5.20E-13	0.00	1500.0	(HFC-43-10mee),CF3CHFCHFCF2CF3
192	F	O3	FO	O2		2.20E-11	0.00	230.0	
193	F	H2	HF	H		1.40E-10	0.00	500.0	
194	F	H2O	HF	OH		1.40E-11	0.00	0.0	
195	F	HONO2	HF	NO3		6.00E-12	0.00	-400.0	
196	F	CH4	HF	CH3		1.60E-10	0.00	260.0	JPL97
7196	FO	O3	?	?		1.00E-14	0.00	0.0	U JPL97
197	FO	NO	NO2	F		8.20E-12	0.00	-300.0	
198	FO	FO	F	F	O2	1.00E-11	0.00	0.0	
199	FO2	O3	?	?		3.40E-16	0.00	0.0	U
200	FO2	NO	FNO	O2		7.50E-12	0.00	690.0	JPL97
201	FO2	NO2	?	?		3.80E-11	0.00	2040.0	JPL97
202	FO2	CO	?	?		5.10E-16	0.00	0.0	U
203	FO2	CH4	?	?		2.00E-16	0.00	0.0	U JPL97
204	CF3O	O2	FO2	CF2O		3.00E-11	0.00	5000.0	U
205	CF3O	O3	CF3OO	O2		2.00E-12	0.00	1400.0	JPL97
206	CF3O	H2O	OH	CF3OH		3.00E-12	0.00	3600.0	U, LT
207	CF3O	NO	CF2O	FNO		3.70E-11	0.00	-110.0	
208	CF3O	CO	?	?		2.00E-15	0.00	0.0	U
209	CF3O	CH4	CH3	CF3OH		2.60E-12	0.00	1420.0	
210	CF3O	C2H6	C2H5	CF3OH		4.90E-12	0.00	400.0	
211	CF3OO	O3	CF3O	O2	O2	3.00E-15	0.00	0.0	U
212	CF3OO	CO	CF3O	CO2		5.00E-16	0.00	0.0	U
213	CF3OO	NO	CF3O	NO2		5.40E-12	0.00	-320.0	
214	O(3P)	ClO	Cl	O2		3.00E-11	0.00	-70.0	
215	O(3P)	OClO	ClO	O2		2.40E-12	0.00	960.0	
216	O(3P)	Cl2O	ClO	ClO		2.70E-11	0.00	530.0	
217	O(3P)	HCl	OH	Cl		1.00E-11	0.00	3300.0	
218	O(3P)	HOCl	OH	ClO		1.70E-13	0.00	0.0	JPL97
219	O(3P)	ClONO2	?	?		2.90E-12	0.00	800.0	
220	O3	OClO	?	?		2.10E-12	0.00	4700.0	
221	O3	Cl2O2	?	?		1.00E-19	0.00	0.0	U
222	OH	Cl2	HOCl	Cl		1.40E-12	0.00	900.0	
223	OH	ClO	HO2	Cl		1.10E-11	0.00	-120.0	b4
224	OH	ClO	HCl	O2		0.00E+00	0.00	0.0	b4
225	OH	OClO	HOCl	O2		4.50E-13	0.00	-800.0	
226	OH	HCl	H2O	Cl		2.60E-12	0.00	350.0	
227	OH	HOCl	H2O	ClO		3.00E-12	0.00	500.0	
228	OH	ClNO2	HOCl	NO2		2.40E-12	0.00	1250.0	
229	OH	ClONO2	?	?		1.20E-12	0.00	330.0	
230	OH	CH3Cl	CH2Cl	H2O		4.00E-12	0.00	1400.0	
231	OH	CH2Cl2	CHCl2	H2O		3.80E-12	0.00	1050.0	
232	OH	CHCl3	CCl3	H2O		2.00E-12	0.00	900.0	
233	OH	CCl4	?	?		1.00E-12	0.00	2300.0	U, LT
234	OH	CFCl3	?	?		1.00E-12	0.00	3700.0	U, LT, CFC-11)
235	OH	CF2Cl2	?	?		1.00E-12	0.00	3600.0	LT, (CFC-12)
236	OH	CH2ClF	CHClF	H2O		2.80E-12	0.00	1270.0	(HCFC-31), JPL97
237	OH	CHFCl2	CFCl2	H2O		1.70E-12	0.00	1250.0	(HCFC-21), JPL97
238	OH	CHF2Cl	CF2Cl	H2O		1.00E-12	0.00	1600.0	(HCFC-22)
7238	OH	MeOCl	?	?		2.40E-12	0.00	360.0	JPL97
239	OH	H1403t	R1303t	H2O		1.80E-12	0.00	1550.0	(HCC-140) , CH3CCl3
240	OH	C2HCl3	?	?		4.90E-13	0.00	-450.0	
241	OH	C2Cl4	?	?		9.40E-12	0.00	1200.0	
242	OH	CCl3CHO	H2O	CCl3CO		8.20E-12	0.00	600.0	
243	OH	H1412m	R1312m	H2O		1.70E-12	0.00	1700.0	(HCFC-141b) , CH3CFCl2
244	OH	H1421d	R1321d	H2O		1.30E-12	0.00	1800.0	(HCFC-142b) , CH3CF2Cl
245	OH	H1322d	R1222d	H2O		3.60E-12	0.00	1600.0	(HCFC-132b) , CH2ClCF2Cl
246	OH	H1331t	R1231t	H2O		5.20E-13	0.00	1100.0	(HCFC-133a) , CH2ClCF3
247	OH	H1232t	R1132t	H2O		7.00E-13	0.00	900.0	(HCFC-123) , CHCl2CF3
248	OH	H1241t	R1141t	H2O		8.00E-13	0.00	1350.0	(HCFC-124) , CHFClCF3
249	OH	H2432m	?	?		7.70E-13	0.00	1700.0	(HCFC-243cc), CH3CF2CFCl2
250	OH	H2252t	?	?		1.00E-12	0.00	1100.0	(HCFC-225ca), CF3CF2CHCl2
251	OH	H2252d	?	?		5.50E-13	0.00	1250.0	(HCFC-225cb), CF2ClCF2CHFCl
252	HO2	Cl	HCl	O2		1.80E-11	0.00	-170.0	
253	HO2	Cl	OH	ClO		4.10E-11	0.00	450.0	
254	HO2	ClO	HOCl	O2		4.80E-13	0.00	-700.0	b1
255	HO2	ClO	HCl	O3		0.00E+00	0.00	0.0	b1
256	H2O	ClONO2	?	?		2.00E-21	0.00	0.0	U
257	NO	OClO	NO2	ClO		2.50E-12	0.00	600.0	
258	NO	Cl2O2	?	?		2.00E-14	0.00	0.0	U
259	NO3	HCl	HONO2	Cl		5.00E-17	0.00	0.0	U
260	HO2NO2	HCl	?	?		1.00E-21	0.00	0.0	U
261	Cl	O3	ClO	O2		2.90E-11	0.00	260.0	
262	Cl	H2	HCl	H		3.70E-11	0.00	2300.0	
263	Cl	H2O2	HCl	HO2		1.10E-11	0.00	980.0	
264	Cl	NO3	ClO	NO2		2.40E-11	0.00	0.0	
265	Cl	HONO2	?	?		2.00E-16	0.00	0.0	U
266	Cl	CH4	HCl	CH3		1.10E-11	0.00	1400.0	
7266	Cl	CH3D	?	?		7.40E-14	0.00	0.0	U JPL97
267	Cl	CH2O	HCl	HCO		8.10E-11	0.00	30.0	
268	Cl	MeOO	ClO	MeO		8.00E-11	0.00	0.0	JPL97 F58
269	Cl	MeOO	HCl	CH2OO		8.00E-11	0.00	0.0	JPL97 F58
270	Cl	MeOH	CH2OH	HCl		5.40E-11	0.00	0.0	
271	Cl	C2H6	HCl	C2H5		7.70E-11	0.00	90.0	
272	Cl	C2H5O2	ClO	C2H5O		7.40E-11	0.00	0.0	
273	Cl	C2H5O2	HCl	C2H4O2		7.70E-11	0.00	0.0	
274	Cl	MeCN	?	?		1.60E-11	0.00	2140.0	JPL97
275	Cl	MeCO3NO2	?	?		1.00E-14	0.00	0.0	U
276	Cl	C3H8	HCl	Pr		1.20E-10	0.00	-40.0	JPL97
277	Cl	OClO	ClO	ClO		3.40E-11	0.00	-160.0	

278	Cl	ClOO	Cl2	O2		2.30E-10	0.00	0.0	
279	Cl	ClOO	ClO	ClO		1.20E-11	0.00	0.0	
280	Cl	Cl2O	Cl2	ClO		6.20E-11	0.00	-130.0	
281	Cl	Cl2O2	?	?		1.00E-10	0.00	0.0	
282	Cl	HOCl	?	?		2.50E-12	0.00	130.0	
283	Cl	ClNO	NO	Cl2		5.80E-11	0.00	-100.0	
284	Cl	ClONO2	?	?		6.50E-12	0.00	-135.0	JPL97
285	Cl	CH3Cl	CH2Cl	HCl		3.20E-11	0.00	1250.0	JPL97
286	Cl	CH2Cl2	HCl	CHCl2		3.10E-11	0.00	1350.0	
287	Cl	CHCl3	HCl	CCl3		8.20E-12	0.00	1325.0	JPL97
288	Cl	CH3F	HCl	CH2F		2.00E-11	0.00	1200.0	(HFC-41)
289	Cl	CH2F2	HCl	CHF2		1.20E-11	0.00	1630.0	(HFC-32), JPL97
290	Cl	CF3H	HCl	CF3		3.00E-18	0.00	0.0	(HFC-23)
291	Cl	CH2FCl	HCl	CHFCl		1.20E-11	0.00	1390.0	(HFC-31)
292	Cl	CHFCl2	HCl	CFCl2		5.50E-12	0.00	1645.0	(HCFC-21), JPL97
293	Cl	CHF2Cl	HCl	CF2Cl		5.90E-12	0.00	2430.0	(HFC-22), JPL97
294	Cl	H1403t	R1303t	HCl		2.80E-12	0.00	1790.0	U , CH3CCl3, JPL97
295	Cl	H161	HCl	R151x		1.80E-11	0.00	290.0	(HFC-161) CH3CH2F
296	Cl	H161	HCl	R151m		1.40E-11	0.00	880.0	CH3CH2F
297	Cl	H152d	HCl	R142x		6.40E-12	0.00	950.0	(HFC-152a) , CH3CHF2
298	Cl	H152d	HCl	R142d		7.20E-12	0.00	2390.0	CH3CHF2
299	Cl	H152m	HCl	R142m		2.60E-11	0.00	1060.0	(HFC-152) , CH2FCH2F
300	Cl	H1412m	HCl	R1312m		1.80E-12	0.00	2000.0	(HCFC-141b) , CH3CFCl2, JPL97
301	Cl	H1421d	HCl	R1321d		1.40E-12	0.00	2420.0	(HCFC-142b) , CH3CF2Cl, JPL97
302	Cl	H143t	HCl	R133t		1.20E-11	0.00	3880.0	(HFC-143a), CH3CF3
303	Cl	H143d	HCl	R133m		5.50E-12	0.00	1610.0	(HFC-143), CH2FCHF2
304	Cl	H143d	HCl	R133d		7.70E-12	0.00	1720.0	CH2FCHF2
305	Cl	H1331t	HCl	R1231t		1.80E-12	0.00	1710.0	(HCFC-133a) , CH2ClCF3
306	Cl	H134t	HCl	R124t		1.50E-15	0.00	0.0	(HFC-134a) , CH2FCF3
307	Cl	H134d	HCl	R124d		7.50E-12	0.00	2430.0	(HCF-134) , CHF2CHF2
308	Cl	H1232t	HCl	R1132t		4.40E-12	0.00	1750.0	(HCFC-123) , CHCl2CF3
309	Cl	H1241t	HCl	R1141t		1.10E-12	0.00	1800.0	(HCFC-124) , CHFClCF3
310	Cl	H125t	HCl	R115t		2.40E-16	0.00	0.0	(HFC-125) , CHF2CF3
311	ClO	O3	ClOO	O2		1.40E-17	0.00	0.0	U
312	ClO	O3	OClO	O2		1.00E-12	0.00	4000.0	U, LT
313	ClO	H2	?	?		1.00E-12	0.00	4800.0	U, LT
314	ClO	NO	NO2	Cl		6.40E-12	0.00	-290.0	
315	ClO	NO3	OClO	NO2		0.00E-13	0.00	0.0	
7315	ClO	NO3	ClOO	NO2		4.00E-13	0.00	0.0	
316	ClO	N2O	?	?		1.00E-12	0.00	4300.0	U, LT
317	ClO	CO	?	?		1.00E-12	0.00	3700.0	U, LT
318	ClO	CH4	?	?		1.00E-12	0.00	3700.0	U, LT
319	ClO	CH2O	?	?		1.00E-12	0.00	2100.0	U, LT
320	ClO	MeOO	ClOO	MeO		4.00E-12	0.00	115.0	JPL97 F103
321	ClO	MeOO	OClO	MeO		1.00E-15	0.00	115.0	JPL97 F103
322	ClO	ClO	Cl2	O2		1.00E-12	0.00	1590.0	
323	ClO	ClO	ClOO	Cl		3.00E-11	0.00	2450.0	
324	ClO	ClO	OClO	Cl		3.50E-13	0.00	1370.0	
325	HCl	ClONO2	?	?		1.00E-20	0.00	0.0	U
326	CH2ClO	O2	CHClO	HO2		6.00E-14	0.00	0.0	
327	CH2ClOO	HO2	CH2ClOOH	O2		3.30E-13	0.00	-820.0	
328	CH2ClOO	NO	CH2ClO	NO2		7.00E-12	0.00	-300.0	
329	CCl3OO	NO	CCl2O	NO2	Cl	7.30E-12	0.00	-270.0	
330	CCl2FO2	NO	CClFO	NO2	Cl	4.50E-12	0.00	-350.0	
331	CClF2O2	NO	CF2O	NO2	Cl	3.80E-12	0.00	-400.0	
332	O(3P)	BrO	Br	O2		1.90E-11	0.00	-230.0	JPL97
333	O(3P)	HBr	OH	Br		5.80E-12	0.00	1500.0	
334	O(3P)	HOBr	OH	BrO		1.20E-10	0.00	430.0	JPL97
335	OH	Br2	HOBr	Br		4.20E-11	0.00	0.0	
336	OH	BrO	HBr	O2		7.50E-11	0.00	0.0	Joern(?)JPL97
337	OH	HBr	H2O	Br		1.10E-11	0.00	0.0	
338	OH	CH3Br	CH2Br	H2O		4.00E-12	0.00	1470.0	
339	OH	CH2Br2	CHBr2	H2O		2.40E-12	0.00	900.0	JPL97
7339	OH	CHBr3	CBr3	H2O		1.60E-12	0.00	710.0	JPL97
340	OH	CHF2Br	CF2Br	H2O		1.10E-12	0.00	1400.0	
7340	OH	CH2ClBr	CHClBr	H2O		2.30E-12	0.00	930.0	JPL97
341	OH	CF2ClBr	?	?		1.50E-16	0.00	0.0	U
342	OH	CF2Br2	?	?		5.00E-16	0.00	0.0	U
343	OH	CF3Br	?	?		1.20E-16	0.00	0.0	U
344	OH	H11402d	?	?		1.50E-16	0.00	0.0	U, CF2BrCF2Br
345	HO2	Br	HBr	O2		1.50E-11	0.00	600.0	
346	HO2	BrO	HOBr	O2		3.40E-12	0.00	-540.0	Joern(?)JPL97
347	NO3	HBr	HONO2	Br		1.00E-16	0.00	0.0	U
348	Cl	CH2ClBr	HCl	CHClBr		4.30E-11	0.00	1370.0	
349	Cl	CH3Br	HCl	CH2Br		1.50E-11	0.00	1060.0	JPL97
350	Cl	CH2Br2	HCl	CHBr2		6.40E-12	0.00	810.0	
351	Br	O3	BrO	O2		1.70E-11	0.00	800.0	
352	Br	H2O2	HBr	HO2		5.00E-12	0.00	3000.0	U, LT
7352	Br	H2O2	HOBr	OH		5.00E-12	0.00	3000.0	U, LT
353	Br	NO3	BrO	NO2		1.60E-11	0.00	0.0	
354	Br	CH2O	HBr	HCO		1.70E-11	0.00	800.0	
355	Br	OClO	BrO	ClO		2.60E-11	0.00	1300.0	
356	Br	Cl2O	BrCl	ClO		2.10E-11	0.00	470.0	
357	Br	Cl2O2	BrCl	ClOO		3.00E-12	0.00	0.0	
358	BrO	O3	Br	O2	O2	1.00E-12	0.00	3200.0	U, LT, JPL97
359	BrO	NO	NO2	Br		8.80E-12	0.00	-260.0	
360	BrO	NO3	BrOO	NO2		1.00E-12	0.00	0.0	Joern(?)
361	BrO	ClO	Br	OClO		1.60E-12	0.00	-430.0	
362	BrO	ClO	Br	ClOO		2.90E-12	0.00	-220.0	
363	BrO	ClO	BrCl	O2		5.80E-13	0.00	-170.0	
364	BrO	BrO	Br	Br	O2	2.40E-12	0.00	-40.0	JPL97, G37
365	BrO	BrO	Br2	O2		2.80E-14	0.00	-860.0	JPL97, G37
366	CH2BrO	O2	CHBrO	HO2		6.00E-14	0.00	0.0	
367	CH2BrO2	NO	CH2BrO	NO2		4.00E-12	0.00	-300.0	
368	O(3P)	I2	IO	I		1.40E-10	0.00	0.0	
369	O(3P)	IO	O2	I		1.20E-10	0.00	0.0	JPL97
370	OH	I2	HOI	I		1.80E-10	0.00	0.0	
371	OH	HI	H2O	I		3.00E-11	0.00	0.0	
372	OH	MeI	H2O	CH2I		3.10E-12	0.00	1120.0	
373	OH	CF3I	HOI	CF3		3.10E-14	0.00	0.0	

374	HO2	I	HI	O2		1.50E-11	0.00	1090.0	
375	HO2	IO	HOI	O2		8.40E-11	0.00	0.0	
376	I	O3	IO	O2		2.30E-11	0.00	870.0	JPL97
7376	I	BrO	IO	Br		1.20E-11	0.00	0.0	JPL97
377	IO	NO	I	NO2		9.10E-12	0.00	-240.0	JPL97
7377	IO	ClO	?	?		5.10E-12	0.00	-280.0	JPL97
7377	IO	BrO	?	?		6.90E-11	0.00	0.0	JPL97
378	IO	IO	?	?		1.50E-11	0.00	-500.0	
379	INO	INO	I2	NO	NO	8.40E-11	0.00	2620.0	
380	IONO	IONO	I2	NO2	NO2	2.90E-11	0.00	2600.0	
381	O(3P)	SH	SO	H		1.60E-10	0.00	0.0	
382	O(3P)	CS	CO	S		2.70E-10	0.00	760.0	
383	O(3P)	H2S	OH	SH		9.20E-12	0.00	1800.0	
384	O(3P)	OCS	CO	SO		2.10E-11	0.00	2200.0	
385	O(3P)	CS2	CS	SO		3.20E-11	0.00	650.0	
386	O(3P)	MeSMe	MeSO	CH3		1.30E-11	0.00	-410.0	
387	O(3P)	MeSSMe	MeSO	MeS		5.50E-11	0.00	-250.0	
388	O3	H2S	?	?		2.00E-20	0.00	0.0	U
389	O3	MeSMe	MeOO	MeSO		1.00E-18	0.00	0.0	U,***
390	O3	SO2	SO3	O2		3.00E-12	0.00	7000.0	LT
391	OH	H2S	SH	H2O		6.00E-12	0.00	75.0	
392	OH	OCS	?	?		1.10E-13	0.00	1200.0	
393	OH	CS2	?	?		1.20E-12	0.00	0.0	
394	OH	MeSH	MeS	H2O		9.90E-12	0.00	-360.0	JPL97
395	OH	MeSMe	H2O	CH2SMe		1.20E-11	0.00	260.0	
396	OH	MeSSMe	?	?		6.00E-11	0.00	-400.0	
397	OH	S	H	SO		6.60E-11	0.00	0.0	
398	OH	SO	H	SO2		8.60E-11	0.00	0.0	
399	HO2	H2S	?	?		3.00E-15	0.00	0.0	U
400	HO2	MeSH	H2O	MeSO		4.00E-15	0.00	0.0	U,***
401	HO2	MeSMe	MeOO	MeSH		5.00E-15	0.00	0.0	U,***
402	HO2	SO2	OH	SO3		1.00E-18	0.00	0.0	U,***
403	NO2	SO2	?	?		2.00E-26	0.00	0.0	U
404	NO3	H2S	?	?		8.00E-16	0.00	0.0	U
405	NO3	OCS	?	?		1.00E-16	0.00	0.0	U
406	NO3	CS2	?	?		4.00E-16	0.00	0.0	U
407	NO3	MeSH	?	?		4.40E-13	0.00	-210.0	
408	NO3	MeSMe	MeSCH2	HONO2		1.90E-13	0.00	-500.0	
409	NO3	MeSSMe	?	?		1.30E-12	0.00	270.0	
410	NO3	SO2	?	?		7.00E-21	0.00	0.0	U
411	N2O5	MeSMe	?	?		1.00E-17	0.00	0.0	U
412	MeOO	SO2	?	?		5.00E-17	0.00	0.0	U
7412	F	MeSMe	?	?		2.40E-10	0.00	0.0	JPL97
413	Cl	H2S	HCl	SH		5.70E-11	0.00	0.0	
414	Cl	OCS	SCl	CO		1.00E-16	0.00	0.0	U
415	Cl	CS2	?	?		4.00E-15	0.00	0.0	U
416	Cl	MeSH	MeS	HCl		1.20E-10	0.00	-150.0	JPL97
417	Cl	MeSMe	?	?		0.00E-00	0.00	0.0	b6
418	ClO	OCS	?	?		2.00E-16	0.00	0.0	U
419	ClO	MeSMe	?	?		9.50E-15	0.00	0.0	
420	ClO	SO	Cl	SO2		2.80E-11	0.00	0.0	
421	ClO	SO2	Cl	SO3		4.00E-18	0.00	0.0	U
422	Br	H2S	HBr	SH		1.40E-11	0.00	2750.0	
423	Br	MeSH	MeS	HBr		9.20E-12	0.00	390.0	
424	BrO	MeSMe	Br	MeSOMe		1.40E-14	0.00	-850.0	Joern(?)JPL97
425	BrO	SO	Br	SO2		5.70E-11	0.00	0.0	
426	IO	MeSH	?	?		6.60E-16	0.00	0.0	
427	IO	MeSMe	?	?		1.20E-14	0.00	0.0	
428	S	O2	SO	O(3P)		2.30E-12	0.00	0.0	
429	S	O3	SO	O2		1.20E-11	0.00	0.0	
430	SO	O2	SO2	O(3P)		2.60E-13	0.00	2400.0	
431	SO	O3	SO2	O2		3.60E-12	0.00	1100.0	
432	SO	NO2	SO2	NO		1.40E-11	0.00	0.0	
433	SO	OClO	SO2	ClO		1.90E-12	0.00	0.0	
434	SO3	H2O	H2SO4			1.20E-15	0.00	0.0	Joern(NIST)
435	SO3	NH3	?	?		6.90E-11	0.00	0.0	
436	SO3	NO2	?	?		1.00E-19	0.00	0.0	
437	SH	O2	OH	SO		4.00E-19	0.00	0.0	U
438	SH	O3	HSO	O2		9.00E-12	0.00	280.0	
439	SH	H2O2	H2S	HO2		1.67E-15	0.00	0.0	JPL U
7439	SH	H2O2	HSOH	OH		1.67E-15	0.00	0.0	JPL U
77439	SH	H2O2	HSO	H2O		1.67E-15	0.00	0.0	JPL U
440	SH	NO2	HSO	NO		2.90E-11	0.00	-240.0	
441	SH	Cl2	ClSH	Cl		1.70E-11	0.00	690.0	
442	SH	BrCl	?	?		2.30E-11	0.00	-350.0	
443	SH	Br2	BrSH	Br		6.00E-11	0.00	-160.0	
444	SH	F2	FSH	F		4.30E-11	0.00	1390.0	
445	HSO	O2	?	?		2.00E-17	0.00	0.0	U
446	HSO	O3	?	?		1.00E-13	0.00	0.0	
447	HSO	NO	?	?		1.00E-15	0.00	0.0	U
448	HSO	NO2	HSO2	NO		9.60E-12	0.00	0.0	
449	HSO2	O2	HO2	SO2		3.00E-13	0.00	0.0	
450	HOSO2	O2	HO2	SO3		1.30E-12	0.00	330.0	
451	CS	O2	OCS	O(3P)		2.90E-19	0.00	0.0	
452	CS	O3	OCS	O2		3.00E-16	0.00	0.0	
453	CS	NO2	OCS	NO		7.60E-17	0.00	0.0	
454	MeS	O2	MeSO2			3.00E-18	0.00	0.0	U,***
455	MeS	O3	?	?		2.00E-12	0.00	-290.0	
456	MeS	NO	?	?		1.00E-13	0.00	0.0	U
457	MeS	NO2	MeSO	NO		2.10E-11	0.00	-320.0	
458	CH2SH	O2	?	?		6.50E-12	0.00	0.0	
459	CH2SH	O3	?	?		3.50E-11	0.00	0.0	
460	CH2SH	NO	?	?		1.90E-11	0.00	0.0	
461	CH2SH	NO2	?	?		5.20E-11	0.00	0.0	
462	MeSO	O3	SO2	MeOO		6.00E-13	0.00	0.0	Joern(?)
463	MeSO	NO2	MeSO2	NO		1.20E-11	0.00	0.0	
464	MeSOO	O3	?	?		8.00E-13	0.00	0.0	U
465	MeSOO	NO	?	?		1.10E-11	0.00	0.0	
7465	MeSOO	NO2	?	?		2.20E-11	0.00	0.0	JPL97
466	MeSOO	NO2	?	?		2.20E-11	0.00	0.0	

467	MeSCH2	NO3	?	?		3.00E-10	0.00	0.0	
468	MeSCH2OO	NO	MeSCH2O	NO2		1.90E-11	0.00	0.0	
469	MeSS	O3	?	?		4.60E-13	0.00	0.0	
470	MeSS	NO2	?	?		1.80E-11	0.00	0.0	
471	MeSSO	NO2	?	?		4.50E-12	0.00	0.0	
472	Na	O3	NaO	O2		1.00E-09	0.00	95.0	
473	Na	O3	NaO2	O(3P)		4.00E-11	0.00	0.0	U
474	Na	N2O	NaO	N2		2.80E-10	0.00	1600.0	
475	Na	Cl2	NaCl	Cl		7.30E-10	0.00	0.0	
476	NaO	O(3P)	Na	O2		3.70E-10	0.00	0.0	
477	NaO	O3	NaO2	O2		1.10E-09	0.00	570.0	
478	NaO	O3	Na	O2	O2	6.00E-11	0.00	0.0	
479	NaO	H2	NaOH	H		2.60E-11	0.00	0.0	
480	NaO	H2O	NaOH	OH		2.20E-10	0.00	0.0	
481	NaO	NO	Na	NO2		1.50E-10	0.00	0.0	
482	NaO	HCl	?	?		2.80E-10	0.00	0.0	
483	NaO2	O(3P)	NaO	O2		2.20E-11	0.00	0.0	
484	NaO2	NO	NaO	NO2		1.00E-14	0.00	0.0	U
485	NaO2	HCl	?	?		2.30E-10	0.00	0.0	
486	NaOH	HCl	NaCl	H2O		2.80E-10	0.00	0.0	
487	Br	MeCHO	HBr	MeCO		1.30E-11	0.00	360.0	
488	CN	O2	?			1.10E-11	0.00	-205.0	?
489	Cl	C2H5CHO	?			1.20E-10	0.00	0.0	?
490	Cl	C2H5OH	?			9.40E-11	0.00	0.0	?
491	Cl	C2H5ONO2	?			4.70E-12	0.00	0.0	?
492	Cl	HCO2H	?			2.00E-13	0.00	0.0	?
493	Cl	HCOCl	HCl	ClCO		1.20E-11	0.00	815.0	
494	Cl	MeCHO	HCl	MeCO		7.20E-11	0.00	0.0	
495	Cl	MeCN	?			2.00E-15	0.00	0.0	U?
496	Cl	MeONO2	?			2.40E-13	0.00	0.0	?
497	Cl	MeOOH	?			5.90E-11	0.00	0.0	?
498	Cl	i-PrOH	?			8.40E-11	0.00	0.0	?
499	Cl	i-PrONO2	?			5.80E-12	0.00	0.0	?
500	Cl	n-PrOH	?			1.50E-10	0.00	0.0	?
501	Cl	n-PrONO2	?			2.70E-11	0.00	0.0	?
502	Cl2O2	NO	?	?		2.00E-14	0.00	0.0	JPL U?
503	Cl2O2	O3	ClO	ClOO	O2	1.00E-19	0.00	0.0	U
505	HO2	HOCH2CH2OO	?			1.00E-11	0.00	0.0	?
506	HO2	HOCH2OO	O2	HOCH2OOH		2.80E-15	0.00	-2300.0	
507	HO2	HOCH2OO	O2	HCO2H	H2O	2.80E-15	0.00	-2300.0	
508	HOCH2CH2	O2	HOCH2CH2OO			3.00E-12	0.00	0.0	? ,***
509	HOCH2CH2OO	HOCH2CH2OO	HOCH2CH2OH	HOCH2CHO	O2	1.50E-12	0.00	0.0	
510	HOCH2CH2OO	HOCH2CH2OO	HOCH2CH2O	HOCH2CH2O	O2	8.30E-13	0.00	0.0	
511	HOCH2OO	HOCH2OO	HCO2H	HOCH2OH	O2	5.70E-14	0.00	-750.0	
512	HOCH2OO	HOCH2OO	HOCH2O	HOCH2O	O2	5.50E-12	0.00	0.0	
513	HOCS2	O2	?			2.80E-14	0.00	0.0	?
514	MeCOCH2OO	MeCOCH2OO	MeCOCH2OH	MeCOCHO	O2	5.00E-12	0.00	0.0	BU
515	MeCOCH2OO	MeCOCH2OO	MeCOCH2O	MeCOCH2O	O2	5.00E-12	0.00	0.0	BU
516	MeO	NO	CH2O	HNO		4.00E-12	-0.70	0.0	
517	N	OH	NO	H		3.80E-11	0.00	-85.0	
518	NH2	HO2	NH3	O2		1.70E-11	0.00	0.0	JPL B
519	NH2	HO2	HNO	H2O		1.70E-11	0.00	0.0	JPL B
520	NH2	NO	N2	H2O		1.90E-12	0.00	-450.0	JPL B
521	NO3	C2Cl4	?			1.00E-16	0.00	0.0	U?
522	NO3	C2H2	?			1.00E-16	0.00	0.0	?U
523	NO3	C2H4	?			3.30E-12	0.00	2880.0	?
524	NO3	C2HCl3	?			2.90E-16	0.00	0.0	?
525	NO3	C3H6	?			9.40E-15	0.00	0.0	?
527	NO3	MeOH	?			1.30E-12	0.00	2560.0	?
528	NO3	i-PrOH	?			5.00E-15	0.00	0.0	?U
529	OH	CHCl2CHO	?			2.40E-12	0.00	0.0	?
530	OH	COCl2	?			5.00E-15	0.00	0.0	U?
531	OH	H12311t	H2O	R11311t		5.80E-14	0.00	0.0	
532	OH	H1231mOF22	?			6.10E-13	0.00	1080.0	?
533	OH	H1231tOF22	?			2.10E-14	0.00	0.0	?
534	OH	H12401t	H2O	R11401t		1.10E-12	0.00	1250.0	
535	OH	H226iOF31	?			1.50E-12	0.00	900.0	?
536	OH	HCOCHO	?			1.10E-11	0.00	0.0	?
537	OH	HCOCl	H2O	ClCO		5.00E-13	0.00	0.0	U
538	OH	HO2NO2	?			1.50E-12	0.00	-360.0	?
539	OH	HOCH2CHO	H2O	HOCH2CO		8.00E-12	0.00	0.0	
540	OH	HOCH2CHO	H2O	HOCHCHO		2.00E-12	0.00	0.0	
542	OH	Me2CO	H2O	MeCOCH2		1.70E-12	0.00	600.0	
543	OH	MeCO2H	?			8.00E-13	0.00	0.0	?
544	OH	MeCOCH2OH	?			3.00E-12	0.00	0.0	?
545	OH	MeCOCHO	H2O	MeCOCO		1.70E-11	0.00	0.0	
546	OH	MeCOCl	H2O	CH2COCl		9.00E-15	0.00	0.0	
547	OH	i-PrOH	?			5.70E-12	0.00	0.0	?
548	OH	n-PrOH	?			5.50E-12	0.00	0.0	?
549	i-PrO	NO	Me2CO	HNO		6.50E-12	0.00	0.0	
550	i-PrO	O2	Me2CO	HO2		1.50E-14	0.00	200.0	
551	i-PrOO	NO	i-PrO	NO2		8.50E-12	0.00	0.0	
552	i-PrOO	i-PrOO	i-PrOH	Me2CO	O2	7.04E-13	0.00	2200.0	B
553	i-PrOO	i-PrOO	i-PrO	i-PrO	O2	8.96E-13	0.00	2200.0	B
554	n-PrO	O2	C2H5CHO	HO2		8.00E-15	0.00	0.0	
555	n-PrOO	NO	n-PrO	NO2		8.70E-12	0.00	0.0	
556	n-PrOO	n-PrOO	n-PrOH	C2H5CHO	O2	1.50E-13	0.00	0.0	B
557	n-PrOO	n-PrOO	n-PrO	n-PrO	O2	1.50E-13	0.00	0.0	B
9999						0.00E+00	0.00	0.0	

NOTES:

General comments
 ? - reaction products unknown
 * - user strongly advised to consult source material
 B - branching ratio assumed equal for all channels
      in the absence of more information
 C - temperature dependent branching ratio based on
      ratio st 298 K

```
 U - upper limit for rate coefficient
 LT- lower limit for temperature
 n - normal form assumed (rather than iso-)
      in the absence of more information
 *** - products of the reactions are given by Joern Burkert 04.07.00.

Specific comments
 b1 - branching ratio for ClO+HO2->HOCL+O2/HCl+O3 - second branch
      has an upper limit of between 0.3-1.5 %. Set to zero here but
      retained in ratefile in case a non-zero value is determined later.
 b2 - branching ratio for ClO+NO3->ClOO+NO2/OClO+NO2 - IUPACIV states
      that the first branch will dominate at temperatures less than 300 K
      Second branch is not in ratefile but should be implemented in case a
      non-zero value is determined later.

 b3 - brancing ratio for MeOO+MeOO->MeOH+HCHO+O2/MeO+MeO+O2/MeOOMe+O2/MeOOH+CH2O2
      is 0.6:0.3:0.1:0.0 at 298 K according to JPL94.

 b4 - branching ratio for OH+ClO->HO2+Cl/HCl+O2.
      OH + ClO.  The recommended value is based on a fit to the 219-373 K data of Hills and Howard  [671] , the
      243-298 K data of Burrows et al.  [231] , and the 298 K data of Poulet et al.  [1273] .  Data reported in the
      studies of Ravishankara et al.  [1300] , and Leu and Lin  [949]  were not used in deriving the recommended
      value because in these studies the concentration of ClO was not determined directly.  The results of Burrows
      et al. are temperature-independent while those of Hills and Howard show a slight negative temperature
      dependence.  The fraction of total reaction yielding HO2 + Cl as products has been determined by Leu and
      Lin (>0.65); Burrows et al. (0.85±0.2); Hills and Howard (0.86±0.14); and Poulet et al. (0.98±0.12).  The
      latest study gives an upper limit of 0.14 for the branching ratio to give HCl + O2 as products.  Even though
      uncertainties in all studies allow for the HCl yield to be zero, none of the current measurements can exclude a
      small, but atmospherically significant, yield of HCl.  Quantification of the HCl yield, especially at
      temperatures close to 200 K, is needed.
      Set to zero here but retained in ratefile in case a non-zero value is determined later.

 b5 - NO2 + NO3.  The existence of the reaction channel forming NO + NO2 + O2 has not been firmly
      established.  However, studies of N2O5 thermal decomposition that monitor NO2 (Daniels and Johnston;
      Johnston and Tao; Cantrell et al.) and NO (Hjorth et al., and Cantrell et al.)
      require reaction(s) that decompose NO3 into NO = O2.  The rate constant from the first three studies is
      obtained from the product kKeq where Keq is the equilibrium constant for NO2 + NO3 = N2O5 while for the
      latter two studies the rate constant is obtained from the ratio k/k(NO + NO3) where k(NO + NO3) is the rate
      constant for the reaction NO + NO3 ® 2NO2.  Using Keq and k(NO + NO3) from this evaluation, the rate
      expression that best fits the data from all five studies is 4.5 x 10-14 exp (-1260/T) cm3 molecule-1 s-1 with
      an overall uncertainty factor of 2.

 b6 - Cl + CH3SCH3.  New Entry.  Stickel et al. have used laser photolysis resonance fluorescence to
      measure the rate constant between 240-421K over the pressure range of 3-700 Torr.  The rate constant is near
      collisional but increases with increasing pressure from a low pressure limit of 1.8x10-10 to a value of
      3.3x10-10 at 700 Torr.  The yield of HCl at 297K was measured using diode laser spectroscopy to drop from
      near unity at low pressure to a value of approximately 0.5 at 203 Torr, indicating that stabilization of a
      (CH3)2SCl adduct becomes competitive with hydrogen atom abstraction with increasing pressure.  These
      investigators also observe a negative temperature dependence for the reaction.  A room temperature
      measurement at 740 Torr by Nielsen et al. agrees with the results of Stickel et al.
      Set to zero here.

 Pressure dependent reactions - require extra code in model
 to calculate rate coefficients - see source material

 P1 - OH + CO -> H + CO2  k=k(1+0.6*P/bar)

 P2 - OH + HONO2 -> H2O + NO3  (1.500E-13 = rate at 1 bar & 298 K)
      Generally, k=k1(T)+k2(T,M) where k2(M,T)=k3[M]/(1+k3[M]/k4)
      and k1=7.2e-15 exp(785/T)  cm3s-1
          k3=1.9e-33 exp(725/T)  cm6s-1    T is temperature (K)
          k4=4.1e-16 exp(1440/T) cm3s-1   [M] is tot.no.density (cm-3)


 Other dependencies:

 D1 - Depends on the concentration of H2O. See JPL 1994 and the paper
      it references: R.R.Lii et al, J.Phys.Chem 85, 1981, p2833. This
      reaction (and the trimolecular branch) need to be multiplied by
      the following factor:
      (1 + 1.40E-21[H2O]exp(2200/T).

 D10 - OH + CH4: The rate coefficient does not stricly follow the Arrhenius
          expression. A more accurate representation of the rate constant
          as a function of temperature is pbtained by using the
          three-parameter expression: k = 2.80E-14*T**0.667*exp(-1575/T).
          This three-parameter fit may be preferred for lower stratosphere
          and upper troposphere calculations. (JPL97, p. 54)

 F58 - Cl + CH3O2: 3 studies -> reaction very fast ! discrepancy in the reported
          values of the branching ratio. 50:50 bzw. 10:90 for HCl production
          The values here use the ratio 50:50, but JPL 97 does not give an
          recommendation !!!

 F103 - ClO + CH2O2: 2 production channels: ClOO + CH3O (a) and CH3OCl + O2 (b)
          There is disagreement in the branching ratio, so JPL97 does not give a
          recommendation for it !!

 G37 - BrO + BrO : The overall reaction rate is give with the parameters:
          A=1.5E-12, E/R=-230. The reaction rates for the two channels are
          derived from branching ratio measurements and are give above.

 Note: there are some other pressure dependent reactions which are
 listed as though bimolecular reactions in the IUPAC assessment,
 but which have been included in the trimolecular ratefile
 (marked 'PB'). Their pressure dependence is generally unknown.
```

```
# TRIMOLECULAR REACTIONS - MASTER RATEFILE
#
# JPL 1997,
# Chemical Kinetics and Photochemical Data for Use in Stratospheric Modeling
    1 O(3P)      O2         O3         m             0.00 6.00E-34 -2.30      0.0 0.00E+00  0.00      0.0
    2 O(1D)      N2         N2O        m             0.00 3.50E-37 -0.60      0.0 0.00E+00  0.00      0.0
    3 H          O2         HO2        m             0.60 5.70E-32 -1.60      0.0 7.50E-11  0.00      0.0
    4 OH         OH         H2O2       m             0.60 6.20E-31 -1.00      0.0 2.60E-11  0.00      0.0   JPL97
    5 O(3P)      NO         NO2        m             0.60 9.00E-32 -1.50      0.0 3.00E-11  0.00      0.0
    6 O(3P)      NO2        NO3        m             0.60 9.00E-32 -2.00      0.0 2.20E-11  0.00      0.0
    7 OH         NO         HONO       m             0.60 7.00E-31 -2.60      0.0 3.60E-11  0.00      0.0   JPL97
    8 OH         NO2        HONO2      m             0.60 2.50E-30 -4.40      0.0 1.60E-11 -1.70      0.0   JPL97
    9 HO2        NO2        HO2NO2     m             0.60 1.80E-31 -3.20      0.0 4.70E-12 -1.40      0.0
   10 HO2NO2     m          HO2        NO2           0.00 2.10E-27  0.00  10900.0 0.00E+00  0.00      0.0
   11 NO2        NO3        N2O5       m             0.60 2.20E-30 -3.90      0.0 1.50E-12 -0.70      0.0
   12 N2O5       m          NO2        NO3           0.00 2.70E-27  0.00  11000.0 0.00E+00  0.00      0.0
   13 CH3        O2         MeOO       m             0.60 4.50E-31 -3.00      0.0 1.80E-12 -1.70      0.0
   14 C2H5O      NO         C2H5ONO    m             0.60 2.80E-27 -4.00      0.0 5.00E-11 -1.00      0.0   JPL97
   15 C2H5O      NO2        C2H5ONO2   m             0.60 2.00E-27 -4.00      0.0 2.80E-11 -1.00      0.0
   16 MeOO       NO2        MeOONO2    m             0.60 1.50E-30 -4.00      0.0 6.50E-12 -2.00      0.0
   17 MeOONO2    m          MeOO       NO2           0.00 1.30E-28  0.00  11200.0 0.00E+00  0.00      0.0
   18 MeC(O)O2   NO2        PAN        m             0.60 9.70E-29 -5.60      0.0 9.30E-12 -1.50      0.0
   19 PAN        m          MeC(O)O2   NO2           0.00 9.00E-29  0.00  14000.0 0.00E+00  0.00      0.0   JPL97
   20 Cl         O2         ClOO       m             0.00 2.70E-33 -1.50      0.0 0.00E+00  0.00      0.0
   21 ClOO       m          Cl         O2            0.00 5.70E-25  0.00   2500.0 0.00E+00  0.00      0.0
   22 Cl         NO         ClNO       m             0.00 9.00E-32 -1.60      0.0 0.00E+00  0.00      0.0
   23 Cl         NO2        ClONO      m             0.60 1.30E-30 -2.00      0.0 1.00E-10 -1.00      0.0
   24 Cl         NO2        ClNO2      m             0.60 1.80E-31 -2.00      0.0 1.00E-10 -1.00      0.0
   25 Cl         CO         ClCO       m             0.00 1.30E-33 -3.80      0.0 0.00E+00  0.00      0.0
   26 ClCO       m          Cl         CO            0.00 1.60E-25  0.00   4000.0 0.00E+00  0.00      0.0
   27 Cl         C2H2       C2H2Cl     m             0.60 5.90E-30 -2.10      0.0 2.10E-10 -1.00      0.0   JPL97
   28 Cl         C2H4       C2H4Cl     m             0.60 1.60E-29 -3.30      0.0 3.10E-10 -1.00      0.0   JPL97
   29 ClO        NO2        ClONO2     m             0.60 1.80E-31 -3.40      0.0 1.50E-11 -1.90      0.0
   30 ClO        ClO        Cl2O2      m             0.60 2.20E-32 -3.10      0.0 3.50E-12 -1.00      0.0
   31 Cl2O2      m          ClO        ClO           0.00 1.30E-27  0.00   8744.0 0.00E+00  0.00      0.0
   32 ClO        OClO       Cl2O3      m             0.60 6.20E-32 -4.70      0.0 2.40E-12  0.00      0.0
   33 Cl2O3      m          ClO        OClO          0.00 1.10E-24  0.00   5455.0 0.00E+00  0.00      0.0
   34 CH2Cl      O2         CH2ClO2    m             0.60 1.90E-30 -3.20      0.0 2.90E-12 -1.20      0.0
   35 CHCl2      O2         CHCl2O2    m             0.60 1.30E-30 -4.00      0.0 2.80E-12 -1.40      0.0
   36 CCl3       O2         CCl3OO     m             0.60 6.90E-31 -6.40      0.0 2.40E-12 -2.10      0.0
   37 CFCl2      O2         CFCl2OO    m             0.60 5.00E-30 -4.00      0.0 6.00E-12 -1.00      0.0
   38 CF2Cl      O2         CF2ClOO    m             0.60 3.00E-30 -4.00      0.0 3.00E-12 -1.00      0.0
   39 CF2ClOO    NO2        CF2ClO2NO2 m             0.60 3.30E-29 -6.70      0.0 4.10E-12 -2.80      0.0
   40 Br         NO2        BrNO2      m             0.60 4.20E-31 -2.40      0.0 2.70E-11  0.00      0.0
   41 BrO        NO2        BrONO2     m             0.60 5.20E-31 -3.20      0.0 6.90E-12 -2.90      0.0
   42 CCl3O      m          COCl2      Cl            0.00 0.00E+00  0.00      0.0 3.00E+13  0.00   4600.0  M*
   43 CCl3O2NO2  m          CCl3OO     NO2           0.20 6.30E-03  0.00  10235.0 4.80E+16  0.00  11820.0
   44 CCl3OO     NO2        CCl3O2NO2  m             0.21 3.20E-28 -7.70      0.0 7.50E-12  0.00      0.0
   45 CF2ClO     m          COF2       Cl            0.00 0.00E+00  0.00      0.0 3.00E+13  0.00   5250.0  M*
   46 CF2ClO2NO  m          CF2ClOO    NO2           0.26 1.80E-03  0.00  10500.0 1.60E+16  0.00  11990.0
   47 CF3        O2         CF3OO      m             0.60 1.90E-29 -4.70      0.0 1.00E-11  0.00      0.0
   48 CF3O       m          COF2       F             0.00 0.00E+00  0.00      0.0 1.00E-05  0.00      0.0   UM*
   49 CF3O2NO2   m          CF3OO      NO2           0.28 5.00E-01 -6.00  12460.0 1.20E+17  0.00  12580.0
   50 CF3OO      NO2        CF3O2NO2   m             0.28 4.50E-29 -6.40      0.0 7.50E-12  0.00      0.0
   51 CFCl2O     m          COFCl      Cl            0.00 0.00E+00  0.00      0.0 4.00E+13  0.00   5250.0  M*
   52 CFCl2O2NO  m          CFCl2OO    NO2           0.23 1.00E-02  0.00  10860.0 6.60E+16  0.00  12240.0
   53 CFCl2OO    NO2        CFCl2O2NO2 m             0.23 1.70E-28 -6.70      0.0 7.50E-12  0.00      0.0
   54 C2H5       O2         C2H5OO     m           485.00 5.90E-29 -3.80      0.0 7.80E-12  0.00      0.0
   55 C2H5       O2         C2H4       HO2           0.00 0.00E+00  0.00      0.0 3.80E-15  0.00      0.0   M
   56 C2H5O2NO2  m          C2H5OO     NO2           0.31 4.80E-04  0.00   9285.0 8.80E+15  0.00  10440.0
   57 C2H5OO     NO         C2H5ONO2                 0.00 0.00E+00  0.00      0.0 1.30E-13  0.00      0.0   PDU
   58 C2H5OO     NO2        C2H5O2NO2  m             0.31 1.30E-29 -6.20      0.0 8.80E-12  0.00      0.0
   59 F          NO         FNO        m             0.00 5.90E-32 -1.70      0.0 0.00E+00  0.00      0.0   JPL
   60 F          NO2        FONO       m           587.00 1.00E-30 -2.00      0.0 2.00E-10  0.00      0.0   *
   61 F          O2         FO2        m             0.00 3.70E-33 -1.00      0.0 0.00E+00  0.00      0.0
   62 FO         NO2        FONO2      m           433.00 1.60E-31 -3.40      0.0 2.00E-11  0.00      0.0   *
   63 HO2        CH2O       HOCH2OO                  0.00 0.00E+00  0.00      0.0 9.70E-15  0.00   -625.0  M
   65 HOCH2OO    m          HO2        CH2O          0.00 0.00E+00  0.00      0.0 2.40E+12  0.00   7000.0  *
   66 HOCS2      m          OH         CS2           0.80 1.60E-06  0.00   5160.0 1.60E+13  0.00   5160.0
   67 HS         NO         HSNO       m             0.60 2.40E-31 -2.50      0.0 2.70E-11  0.00      0.0
   68 I          NO         INO        m          1040.00 1.80E-32 -1.00      0.0 1.70E-11  0.00      0.0   F
   69 I          NO2        IONO       m           650.00 3.00E-31 -1.00      0.0 6.60E-11  0.00      0.0   F
   70 IO         NO2        IONO2      m             0.40 7.70E-31 -5.00      0.0 1.60E-11  0.00      0.0
   71 MeCO       O2         MeCO3      m             0.00 0.00E+00  0.00      0.0 5.00E-12  0.00      0.0
   72 MeCOCH2    O2         MeCOCH2OO  m             0.00 0.00E+00  0.00      0.0 1.50E-12  0.00      0.0
   73 MeO        NO         MeONO      m             0.60 1.60E-29 -3.50      0.0 3.60E-11 -0.60      0.0
   74 MeO        NO2        MeONO2     m             0.44 2.80E-29 -4.50      0.0 2.00E-11  0.00      0.0
   75 MeS        NO         MeSNO      m           580.00 3.20E-29 -4.00      0.0 4.00E-11  0.00      0.0
   76 NO         NO         NO2        NO2           0.00 3.30E-39  0.00   -530.0 0.00E+00  0.00      0.0   *
   77 Na         O2         NaO2       m             0.60 2.40E-30 -1.20      0.0 4.00E-10  0.00      0.0   JPL
   78 NaO        CO2        NaCO3      m             0.60 8.70E-28 -2.00      0.0 6.50E-10  0.00      0.0   JPL
   79 NaO        O2         NaO3       m             0.60 3.50E-30 -2.00      0.0 5.70E-10  0.00      0.0   JPL
   80 NaOH       CO2        NaHCO3     m             0.60 1.30E-28 -2.00      0.0 6.80E-10  0.00      0.0   JPL
   81 O(3P)      OClO       ClO3       m             0.48 1.80E-31 -1.00      0.0 3.10E-11  1.00      0.0
   82 O(3P)      SO2        SO3        m             0.00 4.00E-32  0.00   1000.0 0.00E+00  0.00      0.0
   83 OH         C2H2       C2H2OH     m           623.00 5.00E-30 -1.50      0.0 9.00E-13  2.00      0.0
   84 OH         C2H4       HOCH2CH2   m             0.70 7.00E-29 -3.10      0.0 9.00E-12  0.00      0.0
   85 OH         C3H6       C3H7O      m             0.50 8.00E-27 -3.50      0.0 3.00E-11  0.00      0.0
   86 OH         CS2        HOCS2      m             0.00 8.00E-31  0.00      0.0 8.00E-12  0.00      0.0   *
   87 OH         C2H5ONO2   ?                        0.00 0.00E+00  0.00      0.0 4.40E-14  0.00   -720.0  PB?
   88 OH         HCN        ?                        0.00 0.00E+00  0.00      0.0 1.20E-13  0.00    400.0  PB?
   89 OH         MeONO2     ?                        0.00 0.00E+00  0.00      0.0 1.00E-14  0.00  -1060.0  PB?
   90 OH         SO2        HOSO2      m             0.45 4.00E-31 -3.30      0.0 2.00E-12  0.00      0.0
   91 OH         i-PrONO2   ?                        0.00 0.00E+00  0.00      0.0 4.90E-13  0.00      0.0   PB?
   92 OH         n-PrONO2   ?                        0.00 0.00E+00  0.00      0.0 7.30E-13  0.00      0.0   PB?
   93 i-Pr       O2         i-PrOO     m             0.00 0.00E+00  0.00      0.0 1.10E-11  0.00      0.0
   94 i-PrO      NO         i-PrONO    m             0.00 0.00E+00  0.00      0.0 3.40E-11  0.00      0.0
   95 i-PrO      NO2        i-PrONO2   m             0.00 0.00E+00  0.00      0.0 3.50E-11  0.00      0.0
   96 i-PrOO     NO         i-PrONO2                 0.00 0.00E+00  0.00      0.0 3.70E-13  0.00      0.0   PD
   97 n-Pr       O2         n-PrOO     m             0.00 0.00E+00  0.00      0.0 8.00E-12  0.00      0.0
```

```
   98 n-PrOO     NO         n-PrONO2               0.00 0.00E+00  0.00      0.0 1.80E-13  0.00      0.0  PD
 9999                                              0.00 0.00E+00  0.00      0.0 0.00E-00  0.00      0.0
```

Notes :

Not all JPL 97 reactions are listed. Only the important ones ! The thermal decay reaction has to follow the trimolecular reaction in order to be sure that the rate coefficient is calculated correctly !!

The HO2 HO2 reaction was removed, due to the implementation in the main program.

```
# PHOTOLYSIS REACTIONS - MASTER RATEFILE
# JPL 1994
# Chemical Kinetics and Photochemical Data for Use in Stratospheric Modeling
# and some additional reactions
# All Cross-Sections and quantum yields taken from JPL 97 unless where noted
    1 O2          PHOTON     O(3P)      O(3P)                 0.00E+00  0.00      0.0  b0
    2 O3          PHOTON     O2         O(3P)                 0.00E+00  0.00      0.0  b1
    3 O3          PHOTON     O2         O(1D)                 0.00E+00  0.00      0.0  b2
    4 H2O         PHOTON     OH         H                     0.00E+00  0.00      0.0
    5 H2O2        PHOTON     OH         OH                    0.00E+00  0.00      0.0
    6 NO          PHOTON     N          O(3P)                 0.00E+00  0.00      0.0  b3
    7 NO2         PHOTON     NO         O(3P)                 0.00E+00  0.00      0.0  b4
    8 NO3         PHOTON     NO         O2                    0.00E+00  0.00      0.0  b5
    9 NO3         PHOTON     NO2        O(3P)                 0.00E+00  0.00      0.0  b5
   10 N2O         PHOTON     N2         O(1D)                 0.00E+00  0.00      0.0
   11 N2O5        PHOTON     NO3        NO2                   0.00E+00  0.00      0.0  b6
   12 HONO        PHOTON     OH         NO                    0.00E+00  0.00      0.0
   13 HONO2       PHOTON     OH         NO2                   0.00E+00  0.00      0.0
   14 HO2NO2      PHOTON     OH         NO3                   0.00E+00  0.00      0.0
   15 HO2NO2      PHOTON     HO2        NO2                   0.00E+00  0.00      0.0
   16 HCHO        PHOTON     H          HCO                   0.00E+00  0.00      0.0  b7
   17 HCHO        PHOTON     H2         CO                    0.00E+00  0.00      0.0  b7
   18 CH3OOH      PHOTON     CH3O       OH                    0.00E+00  0.00      0.0  b8
   19 Cl2         PHOTON     Cl         Cl                    0.00E+00  0.00      0.0
   20 ClO         PHOTON     Cl         O(3P)                 0.00E+00  0.00      0.0  b9
   21 ClOO        PHOTON     ClO        O(3P)                 0.00E+00  0.00      0.0
   22 OClO        PHOTON     O(3P)      ClO                   0.00E+00  0.00      0.0
   23 Cl2O        PHOTON     Cl         ClO                   0.00E+00  0.00      0.0  b10
   24 Cl2O        PHOTON     Cl2        O(3P)                 0.00E+00  0.00      0.0  b10
   25 Cl2O2       PHOTON     Cl         ClOO                  0.00E+00  0.00      0.0
   26 HCl         PHOTON     H          Cl                    0.00E+00  0.00      0.0
   27 HOCl        PHOTON     OH         Cl                    0.00E+00  0.00      0.0
   28 ClNO2       PHOTON     Cl         NO2                   0.00E+00  0.00      0.0
   29 ClONO       PHOTON     Cl         NO2                   0.00E+00  0.00      0.0
   30 ClONO2      PHOTON     Cl         NO3                   0.00E+00  0.00      0.0
   31 ClONO2      PHOTON     ClO        NO2                   0.00E+00  0.00      0.0
   32 CCl4        PHOTON     Cl         ?                     0.00E+00  0.00      0.0
   33 CFCl3       PHOTON     Cl         ?                     0.00E+00  0.00      0.0
   34 BrO         PHOTON     Br         O(3P)                 0.00E+00  0.00      0.0  b11
   35 BrONO2      PHOTON     ?                                0.00E+00  0.00      0.0  b12
   36 BrCl        PHOTON     Br         Cl                    0.00E+00  0.00      0.0  b13
   37 Br2         PHOTON     Br         Br                    0.00E+00  0.00      0.0  b14
   38 Br2O        PHOTON     ?                                0.00E+00  0.00      0.0  b15
   39 HOBr        PHOTON     Br         OH                    0.00E+00  0.00      0.0  b16
   40 IO          PHOTON     I          O(3P)                 0.00E+00  0.00      0.0  b17
   41 CH3O2NO2    PHOTON     CH3O2      NO2                   0.00E+00  0.00      0.0  b18
   42 CH3CHO      PHOTON     CH4        CO                    0.00E+00  0.00      0.0  b19
   43 CH3CHO      PHOTON     CH3        HCO                   0.00E+00  0.00      0.0  b19
   44 CH3NO3      PHOTON     CH3O       NO2                   0.00E+00  0.00      0.0  b19
   45 C2H5OOH     PHOTON     C2H5O      OH                    0.00E+00  0.00      0.0  MCM41
   46 C2H5NO3     PHOTON     C2H5O      NO2                   0.00E+00  0.00      0.0  MCM52
   47 CH3CO3H     PHOTON     CH3        OH         CO2        0.00E+00  0.00      0.0  MCM41
   48 CH3COCH3    PHOTON     CH3CO3     CH3                   0.00E+00  0.00      0.0  MCM21
   49 C3H7O2H     PHOTON     C3H7O      OH                    0.00E+00  0.00      0.0  MCM41
   50 C3H7CHO     PHOTON     C3H7O2     CO         H          0.00E+00  0.00      0.0  MCM15
   51 C3H7CHO     PHOTON     CH3CHO     C2H4                  0.00E+00  0.00      0.0  MCM16
   52 C2H5CHO     PHOTON     C2H5O2     CO         H          0.00E+00  0.00      0.0  MCM14
   53 C4H9CHO     PHOTON     NC4H9O2    CO         H          0.00E+00  0.00      0.0  MCM15
   54 C5H11CHO    PHOTON     NC5H11O2   CO         H          0.00E+00  0.00      0.0  MCM15
   55 C5H11CHO    PHOTON     CH3CHO     BUT1ENE               0.00E+00  0.00      0.0  MCM16
   56 NC4H9O2H    PHOTON     NC4H9O     OH                    0.00E+00  0.00      0.0  MCM41
   57 NC5H11O2H   PHOTON     NC5H11O    OH                    0.00E+00  0.00      0.0  MCM41
   58 NC6H13O2H   PHOTON     NC6H13O    OH                    0.00E+00  0.00      0.0  MCM41
   59 NC7H15O2H   PHOTON     NC7H15O    OH                    0.00E+00  0.00      0.0  MCM41
 9999                                                         0.00E+00  0.00      0.0

Specific comments

 b0 - Parametrisiation for the SR-Bands taken from Minschwaner, JGR (1992), 97, p. 10103 - 10108,
     Herzberg continuum values taken from Yoshino et al.,
      Planet. Space. Sci., Vol. 40,No. 2/3,p. 185-192, 1992 (190 - 202 nm) and
      Planet. Space. Sci., Vol. 36,No. 12,p. 1469 - 1475, 1988 (205 - 240 nm)
      Both are also recommended by JPL 94-26, p.4

 b1 - Cross Sections taken from the MPI compilation, measured by Bass, Johnston, WMO 1975 ??
      Mathematical expression for the Quantum Yields taken from JPL 97-4, p.152

 b2 - Cross Sections taken from the MPI compilation, measured by Bass, Johnston, WMO 1975 ??
      For the quantum yield 5 choices can be made in PhotoGT ('photoreacts.par') :
         1) JPL 94
         2) From preprint of G. Hancock, 1994, GRL, 22, 1995, 1213-1216
         3) Michelsen et al., GRL, 21, 1994, 2227-2230
         4) JPL 97
         5) Talukdar et al, Preprint

 b3 - Cross Sections taken from Minschwaner, JGR, 1993, 98, 20401-20412

 b4 - Cross Sections from Schneider et al. (MPI), temperature dependeny from
          JPL 97, quantum yield from JPL 97

 b5 - Different choices are possible (in 'photoreacts.par'):
          - Cross Sections and quantum yield from Wayne, Atmos. Envir., 25A-1, 1991
        - Quantum yields from Johnston, H.S. et al., J Phys. Chem., 100, 4713,
            JPL 97 recomendation

 b6 - Quantum yield for NO3 is unity, but the other products can have
      different quantum yield (JPL)

 b7 - 2 Choices can be made ('photoreacts.par')
          - Cross Sections taken from the Gometran Database,
```

```
      measured by R. Meller, MPI Mainz, no T dependence
         - JPL 97 including T dependence

 b8 - Mainz Chemie-Modell benutzt CH3OOH -> HCHO + OH + H

 b9 - Cross Sections taken from Gometran Database, measured by Simon et al.

 b10 - Cross Sections taken from Simon PhD-Thesis 1989 (236.8 - 319.0 nm)
       and JPL 92-20, p. 127 ( 319 - 500 nm)

 b11 - Cross Section taken from A. Wahner

 b12 - 3 choices can be made for the Cross Sections in PhotoGT ('photoreacts.par') :
         1) JPL 94
         2) Burkholder et al., J. Geophy. Res., Vol. 100, 16793-16800, 1995 = JPL 97
         3) Deters, 1997, unpublished

 b13 - Cross Sections taken from Maric et al., J. Photochem. Photobiol. A, 83 (1994) 179-192
         recommended by JPL 97

 b14 - Cross Sections taken from Maric et al., J. Photochem. Photobiol. A, 83 (1994) 179-192

 b15 - 2 choices can be made for the Cross Sections in PhotoGT ('photoreacts.par') :
         1) Orlando & Burkholder, J. Phys. Chem., 1995, 99, 1143-1150
         2) Deters et al., 1996, Ann Geophysicae, 468-475

 b16 - 3 choices can be made for the Cross Sections in PhotoGT ('photoreacts.par') :
         1) Orlando & Burkholder, J. Phys. Chem., 1995, 99, 1143-1150
         2) Deters et al., 1996, Ann Geophysicae, 468-475
         3) JPL 97

 b17 - 2 choices can be made for the Cross Sections in PhotoGT ('photoreacts.par') :
         1) Ravishankara, 1996
         2) Himmelmann et al., 1997

 b18 - Cross Sections taken from Atkinson et al.,
       J. Phys. Chem. Ref. Data, Vol. 21,  No. 6, 1992, p. 1320
       Products taken from Jens-Uwe Grooss, Dissertation

 b19 - Cross Sections and quantum yields from Atkinson et al.,
       J. Phys. Chem. Ref. Data, Vol. 21,  No. 6, 1992, p. 1308
       This reaction is only in the troposphere relevant !

NICHT IMPLEMENTIERTE REKTIONEN aus JPL !!!


          HO2 + hn . products
          NH3 + hn . NH2 + H(1)
          CO + hn . C + O   (1)
          CO2 + hn . CO + O (1)
          CH4 + hn . products        (2)
          CH3O2 + hn . products
          C2H5O2 + hn . products
          HCN + hn . products
          CH3CN + hn . products
          ClO3 + hn . products
          Cl2O3 + hn . products
          Cl2O4 + hn . products
          Cl2O6 + hn . products
          HF + hn . H + F
*         ClNO + hn . Cl + NO
          CCl2F2 + hn . products
          CF2ClCFCl2 + hn . products
          CF2ClCF2Cl + hn . products
          CF3CF2Cl + hn . products
          CF4 + hn . products
          C2F6 + hn . products
*         CCl2O + hn . products
*         CClFO + hn . products
*         CF2O + hn . products
          CH3Cl + hn . products
          CH3CCl3 + hn . products
          CHClF2 + hn . products
          CH3CF2Cl + hn . products
          CF3CHCl2 + hn . products
          CF3CHFCl + hn . products
          CH3CFCl2 + hn . products
          CF3CF2CHCl2 + hn . products
          CF2ClCF2CHFCl + hn . products
          CH3Br + hn . products
          CHBr3 + hn . products
          CF3Br + hn . products
          CF2Br2 + hn . products
          CF2BrCF2Br + hn . products
          CF2ClBr + hn . products
#         CF3I + hn . CF3 +I
&         SO2 + hn . SO + O
          H2S + hn . HS + H (1)
&         CS2+ hn . CS + S
          OCS + hn . CO + S
          SF6 + hn . products
          NaOH + hn . Na + OH
          NaCl + hn . Na + Cl
```

Jörn Burkert

FULDASTR. 15 • 28199 BREMEN
TELEFON 0421-5967666 • MOBIL 0160-97842484 • FAX 0421-2184555
E-MAIL BURKERT@IUP.PHYSIK.UNI-BREMEN.DE

PERSÖNLICHE ANGABEN

1. Familienstand: ledig
2. Staatsangehörigkeit: deutsch
3. Alter: 30 Jahre
4. Geburtsort: Bremen
5. Eltern: Eckhard Burkert und Karla Burkert (geb. Gießmann)

PROMOTION

1999 - 2003 Wissenschaftlicher Mitarbeiter der Universität Bremen
Titel der Promotion: „Modellierung der troposphärischen Ozon- und Radikalchemie“

WEITERE BERUFSTÄTIGKEITEN

seit 02/2002 Beauftragter für Chemische Sicherheit

seit 10/2001 Beauftragter für Abwasserentsorgung
seit 04/1997 Beauftragter für das Gefahrstoffkataster

HOCHSCHULSTUDIUM

1991 - 1999 Physik an der Universität Bremen
Abschluss: Diplom (Note: 1,7)

6. Titel der Diplomarbeit: „Analyse der Rolle der Peroxyradikale in der Ozonbilanz der Atmosphäre“ (Note: 1,1)
7. Studiumschwerpunkte: Umweltphysik/-chemie, Technology Assessment

TÄTIGKEITEN NEBEN DEM STUDIUM

05/1996 - 11/1999 Studentische Hilfskraft am Institut für Umweltphysik (Universität Bremen)
06/1996 - 10/1999 Dozent am Aus- und Fortbildungszentrum in Bremen für Computeranwendungen (Microsoft Applikationen)

PRAKTIKA

06/2001 Meteorological Institute (University of Maryland, USA)

07/1997 Sommerschule (Riom, Frankreich)
02/1996 Meteorological Service of New Zealand

03/1996 - 04/1996 National Institute for Water and Atmosphere (NIWA), New Zealand

TEILNAHME AN NATIONALEN UND INTERNATIONALEN KAMPAGNEN

FIELDVOC94, EU-Projekt, 1994-1996

BROK, Umweltministerium Bremen, 1996-1999
OPTIBA, Umweltministerium Bremen, 1997-1998
ALBATROSS, Deutsche Forschungsgemeinschaft (DFG), 1996
PRICE2, EU-Projekt, 1998-2000
PRIME, EU-Projekt, 1999-2001
INDOEX, International cooperation, 1999-2002

SCHULAUSBILDUNG

19.06.1991: Abitur, Note 1,9

1984-1991: Gymnasium in Bremen

1982-1984: Orientierungsstufe in Bremen

1978-1982: Grundschule in Bremen

SPRACHKENNTNISSE

Deutsch (Muttersprache), Englisch (fließend in Wort und Schrift), Französisch (Grundkenntnisse)

HOBBYS

Handball, Surfen, Skifahren, Rollenspiele, Lesen

ERSATZDIENST

1991-1998 Arbeiter Samariter Bund

COMPUTERKENNTNISSE

Sprachen:

Turbo Pascal, Fortran, Visual Basic

Windows Applikationen:

Word, Excel, Powerpoint, Origin, Corel Draw, etc.

Unix Applikationen:

IDL, Ghostview, etc.

VERÖFFENTLICHUNGEN

Weißenmayer, M., M.D. Andrés Hernández, T. Behmann, J. Burkert, D. Schwöppe, D. Stöbener, and J.P. Burrows „Der Einfluß der Peroxyradikalkonzentration auf die Höhe der Ozon produktion“. Abschlußbericht zum Vorhaben FV058 des Bremer Senators für Umweltschutz und Stadtentwicklung in Bremen, 1995.

Burkert, J., M.D. Andrés Hernández, D. Schwöppe, D. Stöbener, M. Weißenmayer, and J.P. Burrows (1996). „Ozone production calculated by using peroxy radical measurements“. Proceedings of EUROTRAC Symposium 96, pp 627-631, 1996.

Andrés Hernández, M.D., J. Burkert, D. Stöbener, and J.P. Burrows. „Role of peroxy radicals in tropospheric ozone formation“. Proceedings of the 7th European Symposium on the physicochemical behaviour of atmospheric pollutants, pp 149-152, Venice, 1996.

Stöbener, D., M.D. Andrés Hernández, L. Reichert, J. Burkert, and J.P. Burrows. „Improvement of a H_2O calibration source for peroxy radical measurements by using the chemical amplification technique“. Proceedings of the AGU 1997 Fall meeting published as a supplement to EOS, Transaction, AGU Vol 78, Number 46, 1997.

Andrés Hernández, M.D., J. Burkert, M. Gerhard, D. Stöbener, L. Reichert, and J.P. Burrows, Role of peroxy radicals in the tropospheric ozone formation at different sites, Proceedings of the AGU 1997 Fall meeting published as a supplement to EOS, Transaction, AGU Vol 78, Number 46, 1997.

Andrés Hernández, M.D., J. Burkert, M. Gerhard, L. Reichert, D. Stöbener, and J.P. Burrows. „ Role of peroxy radicals in the tropospheric ozone formation in Bremen“ Proceedings of the XXIII General Assembly of the European Geophysical Society, Nice, 1998.

Burkert, J., M.D. Andrés Hernández, D. Stöbener, and J.P. Burrows. „ Peroxy radical measurements at the marine boundary layer“. Proceedings of the XXIII General Assembly of the European Geophysical Society, Nice, 1998.

Andrés Hernández, M.D., J. Burkert, L. Reichert, D. Stöbener and J.P. Burrows “Measurement of peroxy radicals in the remote marine boundary layer”. Poster of the XXIV EGS General Assembly, The Hague, April, 1999.

Andrés Hernández, M.D., J. Burkert, L. Reichert, D. Stöbener, J.P. Burrows, R.R. Dickerson, B.G. Doddrige „ Measurement of peroxy radicals in the Marine Boundary Layer over the Atlantic and Indian Oceans“ Proceedings of the AGU 1999 Fall meeting (San Francisco 13-17, 1999) published as a supplement to EOS, Transaction, AGU Vol 79, 1999.

Burkert, J., M.D. Andrés Hernández, L. Reichert, D. Stöbener and J.P. Burrows “Modelling of diurnal variations of Ozone and Peroxy radicals in the in the marine boundary layer”. Poster of the XXIV EGS General Assembly, Nice, April, 2000.

Krischke, U., R. Staubes, T. Brauers, M. Gautrois, J. Burkert, D. Stöbener, and W. Jaeschke, Removal of SO_2 from marine boundary layer over the Atlantic Ocean: A case study on the kinetics of the heterogenous S(IV) oxidation on marine aerosols, Journal of Geophys. Res, 105, D11, 14,413-14,422, 2000.

Andrés Hernández, M.D., J. Burkert, L. Reichert, D. Stöbener, and J.P. Burrows “Measurement of peroxy radicals in the London urban area“. Poster of the XXIV EGS General Assembly, Nice, April, 2000.

Burkert, J., M.D. Andrés Hernández, D. Stöbener, A. Kraus, M. Weissenmayer, and J.P. Burrows, " Peroxy radical and related trace gas measurement in the marine boundary layer above the Atlantic Ocean" Journal of Geophys. Res, 106, 5457-5477, 2001.

Andrés Hernández, M.D., J. Burkert, L. Reichert, D. Stöbener, J. Meyer-Arnek and J.P. Burrows, R.R. Dickerson and B. Doddridge. "Marine boundary layer peroxy radical chemistry during the AEROSOLS99 campaign: measurements and analysis". Journal of Geophys. Res, 106, D18, 20,833-20,846, 2001.

Burkert, J., T. Behmann, M.D. Andrés Hernández, M. Weißenmayer, D. Perner, and J.P. Burrows. „ Measurements of peroxy radicals in a forested area in Portugal". Chemosphere-Global change science, 3327-3338, 2001.

Andrés Hernández, M.D., J. Burkert, L. Reichert, J. Meyer-Arnek, and J.P. Burrows "Significance of Peroxy radicals for the production of O_3 in the urban troposphere". Oral presentation at the XXV EGS General Assembly, Nice, March, 2001.

Burkert, J., M.D. Andrés Hernández, L. Reichert, D. Stöbener, J. Meyer-Arnek, and J.P. Burrows, RR. Dickerson and B. Doddridge, " Modelling of the photochemistry of the marine boundary layer above the Indian Ocean". Poster presentation at the XXV EGS General Assembly, Nice, March, 2001.

Burkert, J., M.D. Andrés Hernández, L. Reichert, D. Stöbener, J. Meyer-Arnek, and J.P. Burrows, Photochemistry above the Indian Ocean: measurements and model results, Invited talk at the Annual Symposium of the Royal Meteorological Society's Atmospheric Chemistry Specialist Group (ACSG): In search of clean air, Nottingham Trent University, UK, April, 2001.

Andrés Hernández, M.D., J. Burkert, L. Reichert and J.P. Burrows, " Peroxy radical measurements in an urban plume and new characterization of the water dependence of the PERCA", Poster presentation at the IAMAS (International Association of meteorology and atmospheric sciences) Symposium, Innsbruck, July, 2001.

Burkert, J., M.D. Andrés Hernández, L. Reichert, D. Stöbener, J. Meyer-Arnek, J.P. Burrows, R.R. Dickerson and B. Doddridge, "Peroxy radicals: measurements and model results in the marine boundary layer above the Indian Ocean", Poster presentation at the IAMAS (International Association of meteorology and atmospheric sciences) Symposium, Innsbruck, July, 2001.

Andrés Hernández, M.D., J. Burkert, L. Reichert, and J.P. Burrows, "Role of Peroxy Radicals in the Photochemistry of the Urban Troposphere" Proceedings of the 8th European Symposium on the Physico-Chemical Behaviour of Atmospheric Pollutants, A Changing Atmosphere, Torino, Italy, September, 2001.

Burkert, J., M.D. Andrés Hernández, R.R. Dickerson, H. Smit, and J.P. Burrows, Photochemistry and radiative effects of aerosols in the marine boundary layer during INDOEX 1999, Oral presentation at the XXVI EGS General Assembly, Nice, April, 2002.

Andrés Hernández, M. D., J. Burkert, L. Reichert, and J.P. Burrows, Peroxy radicals in different locations: measurement and model results, Oral presentation, EXPORT-E2 workshop, Jülich, Germany, October, 2002.

Reichert, L., M.D. Andrés Hernández, D. Stöbener, J. Burkert, and J.P. Burrows Investigation of the effect of water complexes in the determination of peroxy radical ambient concentrations: implications for the atmosphere, Journal of Geophys. Res, 108, D1, 2003.

Burkert, J. Andrés Hernández, M.D., L. Reichert, J. Meyer-Arnek, J. Mühle, A.Zahn, T. Carsey, R. R. Dickerson, B. Doddridge, and J.P. Burrows, " Trace gas and radical behaviour in the marine boundary layer during INDOEX 1999", in press, Journal of Geophys. Res, 2003.

Burkert, J., M.D. Andrés Hernández, L. Reichert, J. Meyer-Arnek, R.R. Dickerson, B. Doddridge, and J.P. Burrows, Photochemistry and radiative effects of aerosols in the marine boundary layer during INDOEX 1999, submitted Journal of Geophys. Res, 2003.

Burkert, J., M.D. Andrés Hernández, L. Reichert, D. Stöbener, and J.P. Burrows, Role of peroxy radicals in the photochemistry of the urban troposphere (PRIME1999), submitted, Journal of Geophys. Res, 2003.